# A Superconducting Investigation of Nanoscale Mechanics in Niobium Quantum Point Contacts

A Thesis
Presented to
The Academic Faculty

by

**Brandon Donehoo**

In Partial Fulfillment
of the Requirements for the Degree
Doctor of Philosophy

School of Physics
Georgia Institute of Technology
August 2008

# A Superconducting Investigation of Nanoscale Mechanics in Niobium Quantum Point Contacts

Approved by:

Professor Alexei Marchenkov
School of Physics
Georgia Institute of Technology, Adviser

Professor Albert Frazier
School of Electrical Engineering
Georgia Institute of Technology

Professor Dragomir Davidovic
School of Physics
Georgia Institute of Technology

Professor Markus Kindermann
School of Physics
Georgia Institute of Technology

Professor Phillip First
School of Physics
Georgia Institute of Technology

Date Approved: June, 13 2008

*To my wife,*

*Jessica*

# ACKNOWLEDGEMENTS

First of all, I want to extend my sincerest gratitude to my advisor, Professor Alexei Marchenkov; I truly appreciate all that he has done during my time at Georgia Tech, both as an undergrad and as a graduate student. I am grateful that he took me in as an undergrad and allowed me the opportunity to experiment in a very open atmosphere where I could learn from my own mistakes; along those lines, his patience and understanding during seemingly endless strings of failures did not go unnoticed.

Secondly, I want to thank my friend and former colleague Dr. Zhenting Dai for all of his help during my Ph.D work; for all the hours he spent at the MiRC with me, as well as for always making himself available to answer any questions I might have, I am deeply indebted.

Thirdly, I want to thank our collaborators Dr. Chun Zhang, Dr. Robert N. Barnett, and Prof. Uzi Landman from the School of Physics, who performed ab-initio structure and conductance calculations related to our experiments on niobium nanowires. These simulations were performed at the Center for Computational Materials Science at Georgia Tech and the National Energy Research Scientific Computing Center (NERSC).

Next, I want to extend my appreciation to those people who worked in the lab with me over the last 4 years: John "Brooks" Howard, Sanjay Bidasaria, and Dan Benjamin. They always made the lab a fun and interesting place to be and I will always fondly remember the many talks we had about the world in general (and Josh Nichols in particular); in fact, I am pretty sure that during the course of our talks over the last few years, we have solved most socio-political problems facing the world today (though we were unable to solve any of Josh's problems). In addition to the guys in lab who not only helped me out greatly, but also kept life interesting, there were many graduate students outside of Professor Marchenkov's lab who contributed to my well-being and sanity over the last few years. Among these, I want to especially thank Patrick Bradley and Joanna Hass for all the help they have provided

me; graduate school would have been much more difficult without them.

This research was supported in part by Georgia Tech through the Nanoscience/Nanoengineering Research Program (NNRP) and the NSF CAREER Grant No. DMR - 0349110.

# TABLE OF CONTENTS

# LIST OF FIGURES

# SUMMARY

Research into molecular electronics has exploded in recent years due to a proliferation of new and exciting techniques for producing atomic level structures (e-beam lithography, self-assembled monolayers, etc.); coupling these techniques with the ability to accurately manipulate atomic systems (such as with Scanning Tunneling Microscopes (STM), Atomic Force Microscopes (AFM), or Mechanically Controllable Break Junctions (MCBJ)) opens the possibility to create novel quantum coherent devices for both engineering applications, as well as research into fundamental physics. Along these lines, presented here is a series of experiments on superconducting point contacts which were aimed at understanding the dynamics of coupling superconducting effects to the mechanical degrees of freedom of a nanowire. In addition, another series of experiments presented here explore the nature of charge transport at high biases in superconducting point contacts. Specifically, an investigation of point contacts at high voltage biases revealed a suppression of one component of the total current, which is explained through a phenomenological model.

However, before detailing the experimental results and their implications, Chapter I of this thesis covers electronic transport through mesoscopic conductors. Because mesoscopic devices are not amenable to exact calculation, approximations and phenomenological models are introduced in order to extract the relevant physics. To this end, Chapter I introduces the Fermi Liquid model of normal metals, as well as the Landauer formalism for transport through a quantum coherent device. Next, Chapter II deals with the theory of superconductivity and Josephson junctions, with an emphasis placed on transport problems in superconducting devices and weak links.

With the background theory covered, Chapter III details the aspects of the experimental design for producing, manipulating, and characterizing superconducting point contacts and nanowires. In addition to describing how the samples were microfabricated, Chapter III describes the experimental setup and measurement techniques. Furthermore, Chapter III

describes what information can be extracted from numerical simulations, including density functional theory (DFT) and Non-Equilibrium Green's Function (NEGF) methods.

Chapter IV begins the experimental results section of the thesis with measurements showing the coupling of mechanical modes in a niobium nanowire to non-equilibrium superconducting phenomena. First, data is presented which show the existence of a niobium molecule (dimer) between the superconducting electrodes. Next, through the use of DFT/NEGF calculations, the vibrational frequencies of the dimer were computed and shown to lie in the low THz range. This is advantageous because Josephson junctions easily produce AC currents and radiation in the low THz band, making coupling between the vibrational modes and the non-equilibrium phenomena possible. Lastly, experimental data is presented which conclusively shows the coupling of these two degrees of freedom for the first time.

In contrast to the experiment on nanowires which contain only a few atoms between the superconducting leads, Chapter V presents experiments done on point contacts over a wide range of contact geometries. Over the range of a bulk contact to a nanowire, a suppression feature is seen at high bias voltages in the current-voltage and the differential conductance versus voltage curves. This feature is shown to be related to suppression of supercurrent at high biases due to the magnetic field induced by the current through the contact, as well as the resistive heating of the point contact.

# CHAPTER I

# MESOSCOPIC TRANSPORT

Before transport through superconducting devices is covered, Chapter I introduces the necessary techniques for describing current flow through normal metals: Fermi liquid theory and the Landauer formalism. As it will be shown in the next chapter, the microscopic basis for superconductivity is a phonon-mediated electron-electron interaction; as such, a theory which can incorporate interactions in metallic systems is needed. Fermi liquid theory is able to bridge the gap between non-interacting systems and interacting systems by postulating the existence of quasiparticles; these particles are combinations of electrons and holes and thus behave in much the same way, though they interact much more weakly than the constituent electrons and holes. Next, the Landauer formalism is introduced as a method to perform transport calculations in mesoscopic devices. To do this, a phenomenological transmission coefficient, $\tau$, is introduced, along with the concept of transmission channels; with these in place, the transport properties of any quantum coherent device can be calculated.

## *1.1 Introduction*

> "When we get to the very, very small world, say circuits of seven atoms, we have a lot of new things that would happen that represent completely new opportunities for design. Atoms on a small scale behave like nothing on a large scale, for they satisfy the laws of quantum mechanics. So, as we go down and fiddle around with the atoms down there, we are working with different laws, and we can expect to do different things. We can manufacture in different ways. We can use, not just circuits, but some system involving the quantized energy levels, or the interactions of quantized spins, etc." –Richard Feynman

The above quote given by Richard Feynman during his 1959 talk entitled, "There's Plenty of Room at the Bottom," [77] showcases not only his remarkable foresight of new and fruitful directions in fundamental and applied physics research but also his creativity and open mindedness to the realm of physical possibility. During a time when computers such as ENIAC occupied entire rooms and required groups of people to operate, Feynman envisioned a time in the future when circuit elements would consist of small groups of atoms which could be individually manipulated to perform computations; this vision of atomic computing became one of the motivational catalysts which served to challenge the current level of technology and spearhead a push for further miniaturization of electronic devices and the exploration of physics at the quantum level. Indeed, over the last 50 years, the world's technological evolution has been defined by the ever decreasing feature size of electronic devices, as embodied by Moore's law [163]. However, as the current generation of devices approach the nanometer realm, physicists and engineers have begun to encounter fundamental obstacles which will require new innovation and creativity in the spirit of Feynman to overcome, and thus push the limits of what is physically possible further.

Currently, most microfabrication relies on optical lithography to chemically modify photosensitive resists which enables the patterning of micron size devices on chips; hence, smaller wavelengths are needed to further reduce the feature size. However, as known from elementary optics [101], the index of refraction of a material begins to diverge as the wavelength approaches approximately 200 nm; further, metals typically become transparent around this wavelength as well due to the frequency of radiation exceeding the metal's plasma frequency [120]. These two problems exemplify the types of obstacles which current researchers are facing when trying to create ever smaller devices.

However, as noted by Feynman, this struggle for smaller feature size is not in vain; in addition to decreased energy consumption, higher device density, and myriad other practical reasons for striving to fabricate smaller circuits, the transport properties begin to change in new and interesting ways as the characteristic length of the device approaches a fundamental length scale (i.e. mean free path or phase coherence length). As quantum mechanics begins to play a more pronounced role in the dynamics of the device (typically on the order of

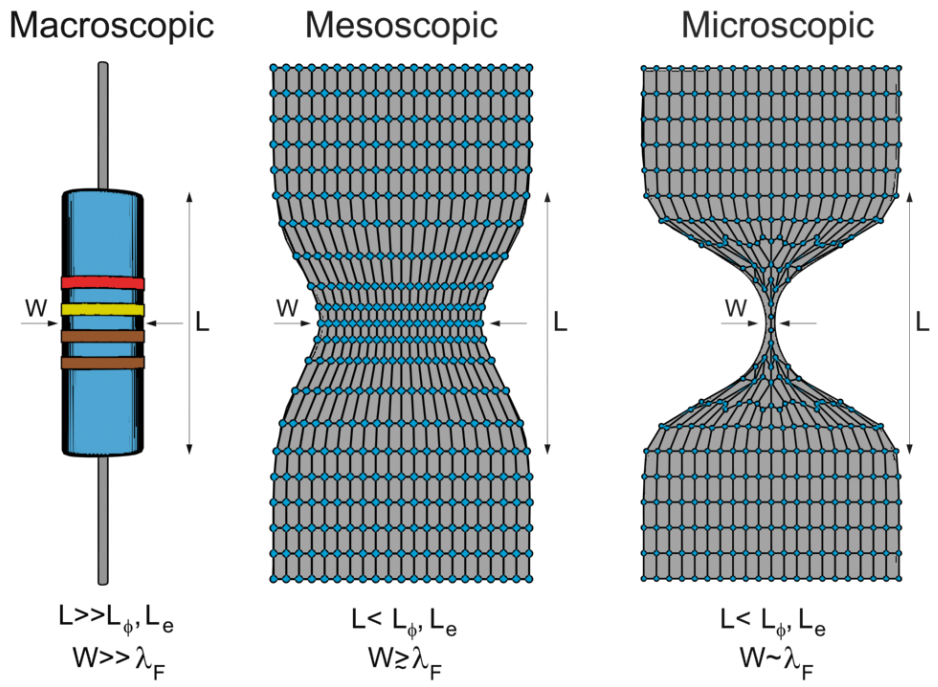


Figure 1: The characterization of the relevant length scale of a device is determined by the ratio of the length or width of the device to either the mean free path (elastic or inelastic) or the Fermi wavelength. For cases when this ratio is large (macroscopic regime), the physics of the system can be determined classically and concepts such as ensembles have a clear meaning; as the ratio approaches one (mesoscopic regime), quantum effects begin to play a larger role in the dynamics of the system, though ensemble techniques are still valid. Finally, for ratios which are less than one (microscopic regime), a fully quantum mechanical treatment is necessary for determining the device physics.

1-1000 nm), it approaches a new length scale termed mesoscopic, in that a fully quantum treatment of the transport is beyond computation but quantum mechanics is still necessary to describe the transport properties. Further, since many atoms contribute to the dynamics of the devices, the concept of ensembles is still applicable, thereby making thermodynamics and statistical mechanics calculations possible. A schematic of the crossover between the macroscopic to the microscopic scale is depicted in Fig. 1, where $L_\phi$ refers to the phase coherence length (i.e. the average length over which an electron's phase is well defined and thus exhibits wave-like character) and is generally on the order of a micron, $L_e$ is the electron's mean free path or elastic scattering length which can vary greatly but is typically on the order of a micron at low temperatures and $\lambda_F$ is the Fermi wavelength of the electron which is typically less than a nanometer.

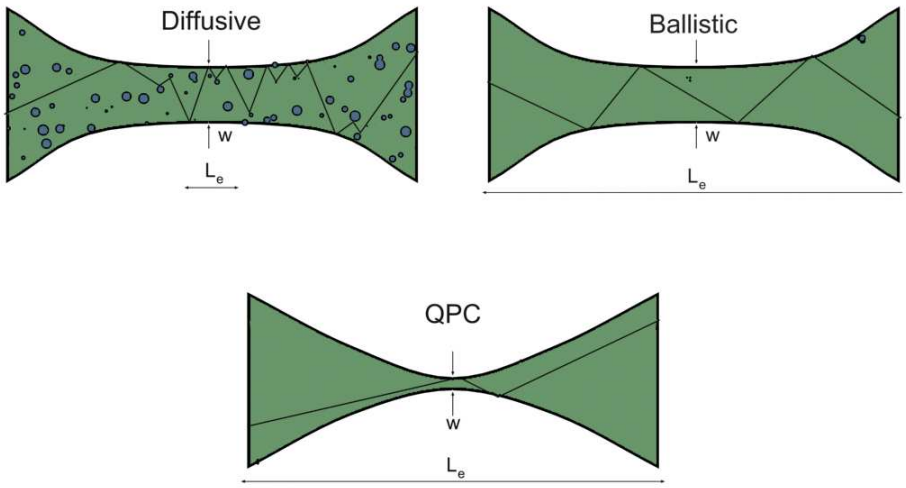


Figure 2: When dealing with mesoscopic or microscopic transport, one can realize hybrid length scales where one critical dimension is small but others are large. From this, three primary transport regimes are defined: diffusive, ballistic, and quantum point contact. For the diffusive case, the width of the device is small but the length is large when compared to the mean free path. Alternatively, for a ballistic conductor, both the width and length are small as compared to the relevant length scale, creating coherent transport. Lastly, the quantum point contact regime is characterized as being a ballistic conductor whose width is on the order of the Fermi wavelength.

Since the mesoscopic scale contains elements of both the macroscopic and the microscopic world, it is very rich with interesting phenomena such as interference of electronic wave functions (i.e. the Aharonov-Bohm effect [10, 180]) and size quantization phenomena (i.e. the Quantum Hall Effect [230] and the energy dependence of the density of states [15]). However, due to its necessarily ambiguous definition, mesoscopic transport can be further subdivided into three classes (diffusive, ballistic, and quantum point contact), as depicted in Fig. 2; diffusive transport implies that the characteristic length of the device is longer than the mean free path of the electrons which traverse the device, hence the electron undergoes scattering in the device region. On the other hand, ballistic transport is the complement to the diffusive case in that it is characterized by no scattering in the device region. Lastly, Quantum Point Contacts (QPCs) are ballistic conductors with the added constraint that the width of the device region is on the order of the Fermi wavelength; this implies that the wave nature of the electrons in the device region must be taken into account.

To describe transport through these mesoscopic conductors, exact calculations are extremely difficult to find; thus, new formalisms which are capable of effectively approximating the true nature of a mesoscopic system are required. Among these new techniques are Fermi liquid theory and Landauer formalism, both of which serve as building blocks upon which much of theoretical mesoscopic physics is based.

## *1.2 Fermi Liquid Theory*

### 1.2.1 Non-Interacting Electron Systems

In solid state physics, the most general problem is that of finding the energy eigenvalues and eigenstates to a Hamiltonian of the general form:

$$\hat{H} = \sum_i \frac{\hat{p}_i}{2m_i} + \frac{1}{2}\sum_{i \neq i'} \frac{q_i q_{i'}}{|\hat{r}_i - \hat{r}_{i'}|}, \tag{1}$$

where the index, $i$, runs over all electrons and ions in the solid. This equation is extremely deceptive in its simplicity; though it appears tractable at first sight, one soon finds that solving this type of Hamiltonian for more than a few dozen particles is computationally impractical. This forces researchers to try and approximate the full Hamiltonian of the

solid and subsequently solve a simplified Hamiltonian which will hopefully contain most of the relevant physics while easing the computational strain of the full problem.

To this end, many different approximations have been proposed for solid state systems (i.e. the Born-Oppenheimer approximation [35], pseudopotentials [15, 85], the jellium model [151], etc.), though none simpler than the non-interacting electron gas approximation which assumes that the system behaves as an electron gas where all interactions are absent except for any effects due to the Pauli exclusion principle. What is amazing about this extremely crude model is that it works remarkably well in describing conduction electrons and thus simple metals like the alkalis; nevertheless, it should be noted that the non-interacting model is incapable of explaining the existence of insulators or magnetic materials, thus showing its very limited range of applicability.

The question still arises: how can completely ignoring electron-ion effects, as well as electron-electron interactions, reflect the true state of a metal and thus be justified in any real way? The answer is twofold: first, neglecting the electron-ion potential is justified by pseudopotentials which redefine the electron's wave function in such as way as to convert non-interacting electrons into electrons that interact with weak potentials; secondly, the neglect of electron-electron interactions stems from the fact that the Pauli exclusion principle severely limits the number of states an electron can scatter into, thus effectively negating the Coulomb interaction between electrons. This suppression of scattering can be best seen through the well known expression for Fermi's Golden Rule [65, 75]:

$$T_{i\to f} = \frac{2\pi}{\hbar}|\langle f|H'|i\rangle|^2\rho, \tag{2}$$

where $\rho$ is the density of final states. In this expression, the scattering rate (and by extension, the amount of interactions) depends linearly on the number of possible final states; consequently, the constraint imposed on the possible final states by the Pauli exclusion principle counteracts the effects of electron-electron interactions, making the non-interacting electron gas more plausible. However, the above argument presumed a repulsive electron-electron interaction (i.e. the Coulomb potential between electrons) which could be incorporated into the non-interacting system through the use of standard perturbation theory.

Conversely, for the case of an electron-electron interaction which is attractive, as in the case of superconductivity, the perturbation to the non-interacting Hamiltonian is singular and thus is unamenable to standard techniques. This fact proved to be one of the most difficult obstacles for theorists to overcome during the development of a microscopic theory of superconductivity.

By placing the above plausibility argument for the use of non-interacting eigenstates in place of the more complicated interacting eigenstates in a metal on a firm theoretical foundation, Landau [133, 134] developed what is now known as Fermi liquid theory which serves as the cornerstone of our modern understanding of excitations in metallic systems.

### 1.2.2 Interacting Electron Systems

Fermi-liquid theory focuses primarily on the excitations of strongly interacting systems, not the exact nature of the interacting ground state. In doing so Landau coined the term quasiparticles for the elementary excitations of the interacting system since they behaved like standard particles in that their energies are almost additive and they do interact with one another, though not as strongly as the original particles from which they are constructed. Indeed, the very fact that quasiparticles can interact weakly with each other implies the possibility of scattering and consequently that quasiparticles have a finite lifetime.

In order to quantitatively compare normal electrons with quasiparticles, one can look at the single particle propagator [5, 80, 172], or Green's function; the utility of the Green's function comes from the fact that the pole of the propagator gives the spectrum of single particle excitations of the system. For non-interacting electrons, the Green's function is given by the expression:

$$G_0(\mathbf{k},\omega) = \frac{1}{\omega - E_{\mathbf{k}} + i\delta_{\mathbf{k}}}, \tag{3}$$

where $\delta_{\mathbf{k}} = \delta sgn(E_{\mathbf{k}} - E_F)$ and $\delta$ is an infinitesimal positive quantity, used for convergence. Interestingly, an exact expression for the propagator of the interacting electron gas can also be found using this same type of analysis, with the result:

$$G(\mathbf{k},\omega) = \frac{z_{\mathbf{k}}}{\omega - \tilde{E}_{\mathbf{k}} + \frac{i}{\tau_{\mathbf{k}}}}, \tag{4}$$

where $z_{\mathbf{k}}$ is a positive quantity related to the self-energy of the quasiparticle, $\Sigma$. Further, $\tilde{E_{\mathbf{k}}}$ is related to the excitation energy of the non-interacting gas and $\tau_{\mathbf{k}}$ is the lifetime of the quasiparticle. One can immediately see the similarities between the Green's functions for the non-interacting and the interacting electron gas: they are almost identical except for the addition of a finite lifetime for the quasiparticle and the quantity $z_{\mathbf{k}}$. This term, $\mathrm{z}_{\mathbf{k}}$, is important because it is the residue of the propagator for the interacting electron gas, in contrast to the residue for the non-interacting gas which was unity; in addition, it can be easily shown that it can only take values from zero to one. Therefore, a quasiparticle is in some sense a potentially reduced form of the original particle; thus, the most common real space description of a quasiparticle is that of an electron surrounded by a cloud of other electrons traveling through the solid, where the effect of the surrounding electrons is to shield the inner electron from interacting with other particles.

Moving to the lifetime of the quasiparticle, which is incorporated into the imaginary part of the propagator expression, one extremely important fact Landau showed concerning the lifetime of quasiparticles was that as their energy nears the Fermi surface, the scattering rate goes to zero and thus the lifetime approaches infinity; this is illustrated in Fig. 3. If we initially consider a $T = 0$ distribution of electrons with the addition of one extra particle with energy $E_1 > E_F$, then for that outlying particle to scatter, it must interact with an electron with energy $E_2 \leq E_F$ by necessity. Due to the exclusion principle, the final states after the scattering must both be outside the Fermi sphere, which is shown in the right panel of Fig. 3. If the energies of the final scattering states are denoted as $E_3$ and $E_4$, then energy conservation requires that:

$$E_1 + E_2 = E_3 + E_4. \tag{5}$$

A special case of this equation is when an electron initially at the Fermi surface is scattered; in this instance, the only way to satisfy the above equation is for all other energies to also equal the Fermi energy. Clearly then, a consequence of the exclusion principle is that electrons at the Fermi level have no states which they can be scattered into and thus the transition rate is zero; equivalently, this result can be interpreted as the lifetime of the

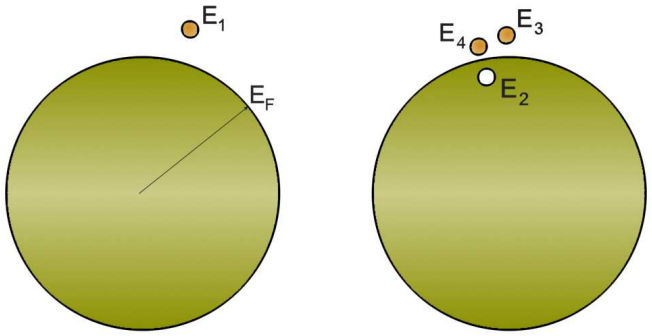


Figure 3: The figure on the left shows an electron which has been placed just outside the zero temperature Fermi sphere; for this electron to scatter, it must interact with an electron inside the sphere. The second panel shows the effect of the first electron scattering with an electron inside the sphere; as a consequence of the exclusion principle, both final electrons must be outside the sphere and have less energy than the initial electron. Furthermore, because the final electrons are closer to the sphere than the initial one, the number of scattering states available for these electrons is smaller and thus their lifetimes are larger; in fact, as a quasiparticle approaches the Fermi surface, its lifetime diverges to infinity.

electron at the Fermi level being infinite.

If instead of assuming the first electron is on the Fermi surface, it is assumed to be slightly above the Fermi energy, then after scattering with the second electron, the resulting scattered electrons outside of the Fermi surface can only occupy energies in the range $E_1 - E_F$. Thus, the scattering rate is expected to scale as $(E_1 - E_F)^2$, a hallmark of Fermi-liquid behavior. This scaling has been quantitatively proven [151, 187] to be the correct dependence. The importance of this result is that for low energy excitations, the scattering rate goes to zero and thus the lifetime of the quasiparticle goes to infinity. Further, if the energy dependence of the scattering rate is related to the temperature of the system (i.e. $(E_1 - E_F)^2 \propto (T)^2$),the lifetime of a quasiparticle due to scattering is approximately $10^{-10}$ s at room temperature, which is four orders of magnitude greater than the typical relaxation time in a metal. Thus, Fermi-liquid effects typically present themselves only at low temperatures where quasiparticle lifetimes are long and electron-electron effects are not negligible; superconductivity is a case in point of this behavior.

By dealing primarily with the low energy excitations of the interacting system, which implies excitations with a relatively long lifetime, Landau was able to draw a one-to-one correspondence between the quantum numbers of the non-interacting and the interacting case. In other words, by starting with the exact eigenstates of the non-interacting case, interactions can be added into the system perturbatively due to the direct mapping of quantum numbers. Additionally, perturbations to the system may be added adiabatically, which implies that the quantum numbers of the interacting quasiparticles are the same for the non-interacting particles; as a consequence, quasiparticles contain the same charge, spin and momentum as their constituent particles. However, one important difference between non-interacting electrons and the quasiparticles of Fermi-liquid theory is the renormalization of the effective mass of the electron, which typically ranges from 10% to 50%; this can be interpreted as another consequence of the real space picture of quasiparticles as electrons surrounded by a cloud of other electrons. Lastly, it should be noted that due to the enormous variety of low energy excitations which exist in nature, there are many different types of quasiparticles ranging from bosonic spin waves in Mott-Hubbard insulators [166, 167, 168] to fermionic bogoliubons in superconductors [219].

### 1.2.3 The Excitation Representation

Given that Fermi liquid theory is focused more on the excitations of a system and not the exact nature of that ground state, a new way of looking at complicated excited states can be introduced; to be clear, consider the general non-interacting electron excitation shown in Fig. 4 whose energy is plotted in the first panel in Fig. 5. The energy of this excited state exceeds that of the ground state by $E_\alpha - E_\beta$; however, to motivate the excitation representation, this expression can be rewritten as:

$$E = (E_\alpha - E_F) + (E_F - E_\beta). \tag{6}$$

This type of analysis can be extended to increasingly more complicated excited states by adding additional terms to the previous equation; however, to facilitate the calculation of these excitation energies, the energy spectrum of the electrons should be renormalized in terms of $\epsilon = |E - E_F|$, which is plotted in the second panel of Fig. 5. From the figure,

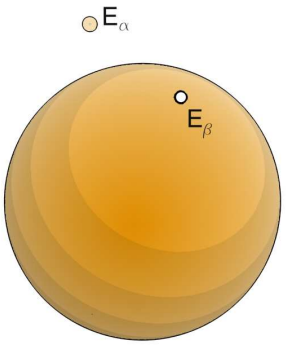


Figure 4: The most general single particle excitation from the ground state of the Fermi sphere.

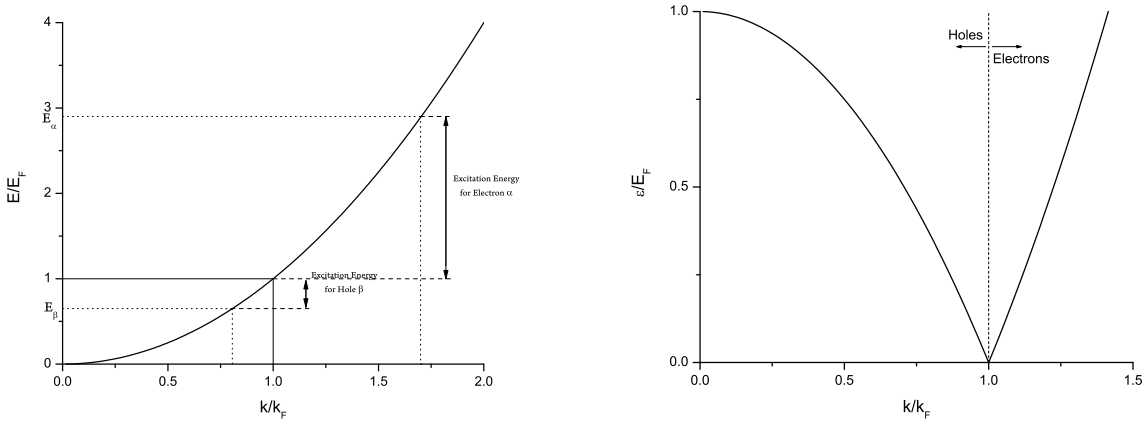


(a) (b)

Figure 5: In (a), the energy of a free electron gas is plotted as a function of wavevector in the traditional sense (i.e. $E = \hbar^2 k^2/2m$); here, excitation energies are measured as the difference between the actual energy of the excitation minus the Fermi energy. In (b), the excitation energy (i.e. $\epsilon = |E - E_F|$)is plotted as a function of wavevector, thus facilitating the calculation of excitation energies.

the effect of renormalizing the energy of a state results in a more clear description of the excitations of the system.

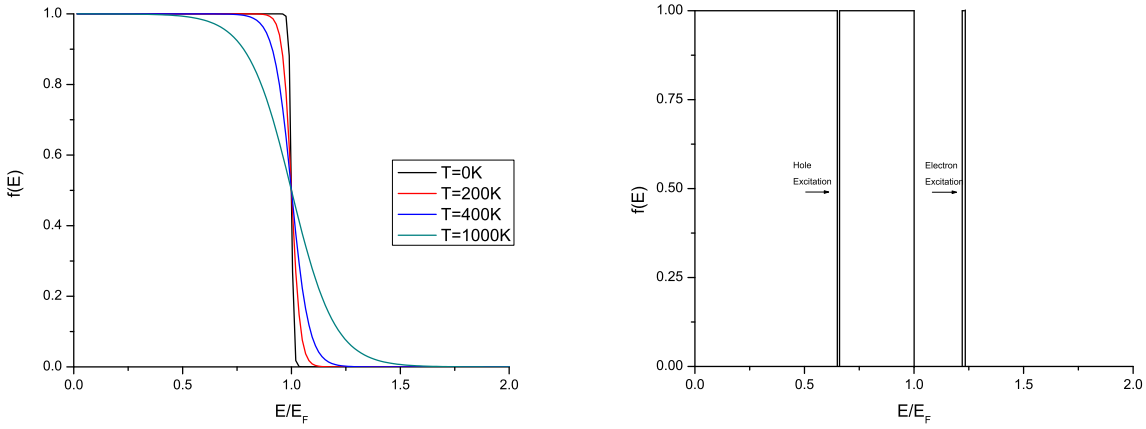


(a) (b)

Figure 6: (a) The Fermi function is plotted at various temperatures in the traditional sense, where the changing occupation probabilities are reflected by a continuous curve. (b) In contrast, in the excitation representation, the Fermi function is plotted at zero temperature but with the addition and removal of delta function peaks at the energies of excitation. Thus, changes in temperature are reflected completely through discontinuous changes in the $T = 0K$ Fermi function in the excitation representation.

Additionally, by adopting the excitation representation, changes in the occupation of a state are reflected by the addition or removal of delta function peaks at the excitation; thus, the Fermi function does not continuously evolve with additional excitations, as it does traditionally in panel (a) of Fig. 6. Instead, in using the excitation representation, the effect of excitations is to change the Fermi function in the following form:

$$f(T) = f(0) + \sum_n a_n \delta(E - E_n), \tag{7}$$

where $a_n$ is $\pm 1$, depending on whether the excitation creates a particle (excites an electron, $+1$) or removes one (excites a hole, $-1$). Though these concepts seem trivial for normal metals, they play an important conceptual role in the theory of superconductivity and how the low energy excitations of the superconducting state are accounted for.

## *1.3 The Landauer Scattering Approach*

### 1.3.1 Introduction

In order to observe phenomena such as the Aharonov-Bohm effect, not only must the characteristic length of the device be smaller than the phase coherence length, but all characteristic lengths must be smaller than the phase coherence length if phase coherence is to be maintained over all distinct paths of the device. For cases such as these, the entire circuit itself acts as a quantum scatterer of coherent electrons from the input leads, which are considered to act as perfect reservoirs for electrons. Pursuing this concept further, when the entire device region is quantum coherent, it is possible that the transport properties of the system may be obtained by using a scattering matrix approach to the problem. Indeed, Landauer [135] was the first to show that the transport properties of phase coherent circuits could be fully described by calculating the equivalent scattering matrix for the device. Moreover, Landauer was able to show that the conductance of a quantum coherent circuit is quantized and depends only on the transmission coefficients of the scattering matrix.

### 1.3.2 The Scattering Matrix Formalism

When Landauer began analyzing the problem of coherent transport in quantum devices, he considered the physical situation depicted in Fig. 7. Here, charge reservoirs inject electron waves into ideal leads that connect to the device region, which is considered as a scattering center. The reservoirs are assumed to absorb an incident electron perfectly (i.e. there is no backscattering of electrons incident on a reservoir) and the leads can be considered as electron waveguides which restrict the motion to only one dimension. By confining the electrons to move in only one dimension, the electronic states in the leads become quantized, meaning that only a finite number of modes are capable of propagating to and from the device region. This number can be estimated using the Sharvin conductance formula [203] which predicts semiclassically that the number of modes is proportional to $k_F^2$A, where $A$ is the cross-sectional area of the conductor. Furthermore, since we are considering quantum point contacts where the ideal leads are modeled as one dimensional ballistic quantum wires, as depicted in Fig. 8, the distribution of states in the leads is not described by the Fermi

distribution. This last point is especially important when considering the physical origin of quantized conductance in a ballistic device and will be discussed more fully below.

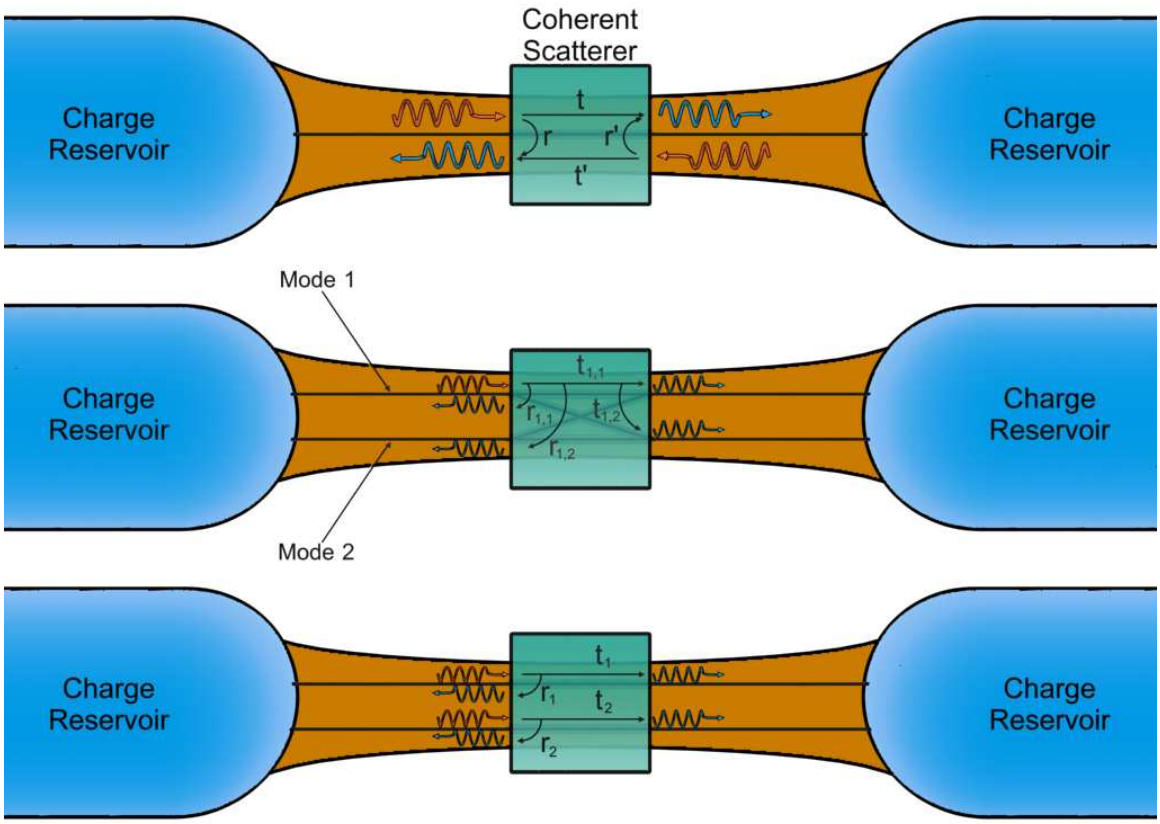


Figure 7: (a): General scattering problem dealing with incoming waves on one mode. (b): Components of the scattering matrix for an incoming wave along two modes/channels. (c): Upon diagonalization of the scattering matrix, each channel becomes decoupled and independent, thus simplifying the calculation of transport properties.

With the physical picture in place, the scattering matrix approach can now be applied in order to solve for charge transport across a coherent device. To begin, analogous to standard quantum mechanics textbooks [93], the scattering matrix is defined:

$$\mathbf{S} = \begin{pmatrix} \mathbf{s}_{11} & \mathbf{s}_{12} \\ \mathbf{s}_{21} & \mathbf{s}_{22} \end{pmatrix} = \begin{pmatrix} \mathbf{r} & \mathbf{t}' \\ \mathbf{t} & \mathbf{r}' \end{pmatrix}, \tag{8}$$

such that $\mathbf{S}$ relates the incoming probability amplitudes, $a_i$, with the outgoing amplitudes,

$b_i$, in the following fashion:

$$\begin{pmatrix} b_1 \\ b_2 \end{pmatrix} = \begin{pmatrix} \mathbf{r} & \mathbf{t}' \\ \mathbf{t} & \mathbf{r}' \end{pmatrix} \begin{pmatrix} a_1 \\ a_2 \end{pmatrix}. \tag{9}$$

Here it should be noted that in general the $\mathbf{s}_{ij}$ of the scattering matrix are matrices themselves whose entries relate the probability of an incoming electron wave on mode $i$ being scattered into mode $j$; hence, the $a_i$ and $b_i$ in the previous equation are in general vectors. Moreover, it should also be noted that the off diagonal terms in the scattering matrix relate transmission of electron waves, whereas the diagonal terms refer to reflection of a wave on mode $i$ into mode $j$ on the same lead. Additionally, the scattering matrix must be unitary (i.e. $\mathbf{SS}^\dagger=\mathbf{I}$) to ensure particle number conservation. Clearly then, the scattering matrix must have an inverse and thus it is diagonalizable; further, it has been shown [152] that the decomposition of the scattering matrix into individual, non-interacting modes is unique up to permutations. Thus, in the newly diagonalized basis, an incoming electron wave on mode $i$ is either transmitted onto mode $i$ of the other lead or is reflected back into mode $i$ of the original lead; since the different modes of the system have been decoupled from one another, one typically refers to the diagonalized modes as conduction channels. Therefore, the problem of calculating the transport properties for an entire system has been reduced to summing contributions from independent channels. Of great practical importance in transport theory is the calculation of the conductance of a device; thus, the first application of the Landauer formalism is to find the current through the quantum coherent device from which the conductance can be extracted.

### 1.3.3 Conductance of a Single Channel

The first step toward calculating the current through a quantum scatterer is introducing the creation and annihilation operators for electron waves on mode $m$ of lead $\alpha$ in the following way: $a^\dagger_{m\alpha}(\epsilon)$ and $a_{m\alpha}(\epsilon)$ refer to the energy dependent creation and annihilation operators for *incoming* electron waves; similarly we define $b^\dagger_{m\alpha}(\epsilon)$ and $b_{m\alpha}(\epsilon)$ as the creation and annihilation operators for *outgoing* electrons. With these definitions in place, Buttiker [41]

showed that the current due to mode $m$ on lead $\alpha$ is defined as:

$$I_{m\alpha} = \int_{-\infty}^{\infty} d\epsilon \left( \langle a^{\dagger}_{m\alpha}(\epsilon) a_{m\alpha}(\epsilon) \rangle - \langle b^{\dagger}_{m\alpha}(\epsilon) b_{m\alpha}(\epsilon) \rangle \right). \tag{10}$$

Clearly, the above expression shows that a net current is caused by an imbalance in the population of incoming and outgoing electrons from the device; however it can be simplified using the scattering matrix which relates the incoming and outgoing electrons. Using the relation:

$$b_{m\alpha} = \sum_{n\beta} (\mathbf{s}_{\alpha\beta})_{mn} a_{n\beta}, \tag{11}$$

and also the fact that the Fermi distribution of the reservoir imposes the condition:

$$\langle a^{\dagger}_{m\alpha}(\epsilon) a_{m\alpha}(\epsilon) \rangle = \delta_{mn} \delta_{\alpha\beta} f_{\alpha}(\epsilon), \tag{12}$$

we can then rewrite the equation for the current in lead 1 (summed over all modes) as:

$$I_1 = \frac{2e}{h} \int_{-\infty}^{\infty} d\epsilon (f_1(\epsilon) - f_2(\epsilon + eV)) \mathrm{Tr}(t^{\dagger} t). \tag{13}$$

If we look at the limiting case of small voltages ($V \ll E_F$) and at $T = 0K$, then the integral will evaluate to $eV \cdot \mathrm{Tr}(t^{\dagger} t)$. Thus, the current can be rewritten as:

$$I_1 = \frac{2e^2}{h} \mathrm{Tr}(t^{\dagger} t) V. \tag{14}$$

This, in turn, leads to a conductance of:

$$G = \frac{2e^2}{h} \mathrm{Tr}(t^{\dagger} t) = G_0 \cdot \mathrm{Tr}(t^{\dagger} t), \tag{15}$$

$$G_0 \approx 77 \mu S \approx \frac{1}{12.9 k\Omega}, \tag{16}$$

which is entirely in terms of fundamental constants and scattering matrix parameters; the fundamental constants combine to form the quantum of conductance, $G_0$. From this expression, the total conductance of the device is then given by a sum over all conductance channels:

$$G_{tot} = \sum_i G_i = G_0 \sum_i \tau_i \tag{17}$$

where $\tau_i$ is termed the transmission coefficient of channel $i$ and is given by, $\tau_i = \mathrm{Tr}(t_i^{\dagger} \mathrm{t}_i)$. Since we know that the decomposition of the scattering matrix into individual conduction

channels is unique (up to a permutation), any transport quantity of a mesoscopic device can be given in terms of the transmission coefficients of its conduction channels, which has led researchers to term the set of transmission coefficients of a coherent device as its mesoscopic PIN code. As an example of the mesoscopic PIN code's use besides the calculation of the conductance, the power spectrum of shot noise in a mesoscopic device is given by [41, 152]:

$$S_I(V, T, \tau_1, \ldots, \tau_N) = 2eG_0V \sum_{i=1}^{N} \tau_i(1 - \tau_i) \coth\left(\frac{eV}{2k_BT}\right) + 4k_BTG_0 \sum_{i=1}^{N} \tau_i^2. \tag{18}$$

### 1.3.4 Conductance of a Ballistic Channel

Even though the phenomena of conductance quantization is exotic when compared to the everyday devices our intuition is built upon, the effect can be easily predicted semiclassically; for this case, the quantization arises from the fact that in one dimension the density of states is proportional to $E^{\frac{1}{2}}$ and the velocity is proportional to $E^{-\frac{1}{2}}$, making their product independent of energy. However, though the effect can be predicted using first principles arguments, some outstanding questions still remain. For instance, if we let $\tau = 1$ (i.e. a ballistic point contact) which implies that all electrons incident on the scattering center are transmitted with a probability of one, why would the channel still have a finite conductance? One would naively suspect that for a ballistic channel the conductance should approach infinity since there are no scattering centers to impede the transmission of electrons.

The answer to this question is subtle and lies in the fact that the distribution of states in the leads is not a Fermi distribution [42]; consequently, the applied voltage across the point contact is not $eV = \mu_L - \mu_R$, but a lower value. In order to elucidate this point, assume that the applied voltage is small, making the density of states energy independent in the range of interest; additionally, let us use the model presented in Fig. 8 which presumes that the leads are one dimensional ballistic wires. Using this model, it is assumed that a left moving state on the left lead is occupied only if an electron has scattered into it by backscattering at the device or, conversely, by transmission (forward scattering) through the scattering center from the other lead. Following this further, the chemical potential of the lead must be reduced from that of the reservoir and is denoted by $\mu_L$'. Using similar arguments [102], one can show that the chemical potential on the right lead must be raised

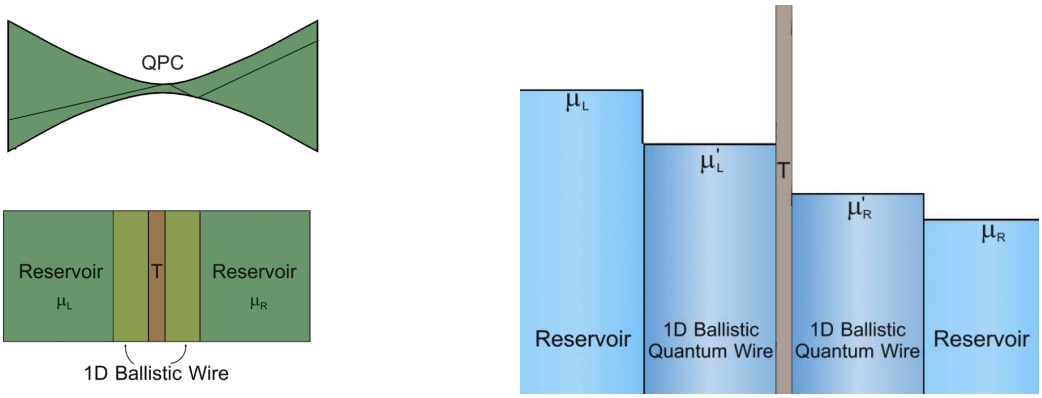


(a) (b)

Figure 8: (a): In order to explain the finite conductance of a ballistic point contact, we decompose the point contact into two reservoirs which are connected to the scattering center through one-dimensional ballistic leads. (b): For this type of decomposition of the device, there is a difference in chemical potential across both the reservoir-lead interface and also the lead-scatterer interface; the finite conductance of a ballistic contact arises from the first difference in chemical potential which is still present even for a perfectly ballistic channel.

from that of the right reservoir and is defined to be $\mu_R$'.

To quantitatively calculate what the chemical potentials are inside of the leads, recall that the chemical potential is defined as the energy for which the number of empty states below it equals the number of filled states above it. Looking at the left side of the device, the only empty states for $E < \mu'_L$ are those states which have not been occupied by reflection at the scattering center; this number can be calculated as:

$$n_{L,empty}(E < \mu'_L) = \int_{\mu_R}^{\mu'_L} dE D_L(E)\tau = D_L\tau(\mu'_L - \mu_R), \tag{19}$$

where the lower integration limit is $\mu_R$ because states below this energy on both sides cancel one another. To calculate the number of occupied states above $\mu'_L$, two different contributions must be taken into account: first, all right moving states in the range $[\mu'_L, \mu_L]$ which are occupied must be added; then, the left moving states which are occupied due to backscattering at the scattering center must be taken into account. In doing so, the result is:

$$n_{L,occ}(E > \mu'_L) = D_L(\mu_L - \mu'_L) + (1-\tau)D_L(\mu_L - \mu'_L). \tag{20}$$

Simplifying this expression and setting the last two equations equal to one another, the new

chemical potential on the left lead is:

$$\mu_L' = \mu_L - \frac{1}{2}\tau(\mu_L - \mu_R). \tag{21}$$

Similarly, the chemical potential for the right lead becomes:

$$\mu_R' = \mu_R + \frac{1}{2}\tau(\mu_L - \mu_R). \tag{22}$$

Hence, the voltage drop across the quantum point contact itself is only:

$$V' = \frac{1}{e}(\mu_L' - \mu_R') - \frac{1}{e}(1-\tau)(\mu_L - \mu_R). \tag{23}$$

Thus, the conductance of the barrier itself is given by the expression:

$$G_b = \frac{2e^2}{h}\frac{\tau}{1-\tau} = G_0\frac{\tau}{1-\tau}. \tag{24}$$

Furthermore, since the total conductance of the system (device plus leads) is equal to $G = G_0\tau$, there must be a residual resistance associated with the leads which is given by:

$$R_{contact} = \frac{1}{G} - \frac{1}{G_b} = \frac{1}{G_0}. \tag{25}$$

This resistance is a contact resistance which arises from the fact that the distribution of states is different in the ballistic leads than in the reservoir. Specifically, electrons which are emitted from the left contact impinge on the right contact with energies above $\mu_R'$ and relax back to a Fermi distribution inside the right contact through inelastic scattering processes. In the process, these electrons create an additional contact resistance which is equal to that calculated above. By looking at the expression for the conductance of the barrier region alone, it is clear that the conductance diverges for $\tau \to 1$, as expected for a ballistic wire.

Now, having a formalism in place which is capable of handling quantum coherent devices and their excitations, the next step toward quantum point contacts is to detail the nature of the superconducting state itself. To that end, the next chapter covers the well-established BCS theory of superconductivity, leading to a discussion of the physics of Josephson junctions.

# CHAPTER II

# MESOSCOPIC SUPERCONDUCTIVITY

Chapter II begins with a survey of the early experimental work on superconductivity, leading to the introduction of the London theory which is one of the first phenomenological theories of superconductivity. From this point, the major results of the BCS theory of low $T_c$ superconductors are presented; among these are the concept of an effective electron-electron interaction which allows electrons to condense in pairs to a single ground state at low temperatures, and the introduction of an energy gap, $\Delta$, in the quasiparticle energy spectrum. However, one major drawback of the BCS theory is its inability to handle inhomogeneous superconductors where the energy gap is spatially varying. For cases such as these, the Bogoliubov-de Gennes formalism is required. In addition, altogether new physics emerge at normal-superconductor interfaces which complicate the transport calculations; specifically, the process of Andreev reflection is introduced and shown to be the key to understanding transport phenomena in superconductors. Moreover, it is shown that the well-known Josephson effect is a result of Andreev reflection at the interface between a superconductor and other material (normal metal, insulator, etc.). Lastly, a digression is made on the different types of superconductors which are characterized by their response to a magnetic field; it is shown that there are two types of superconductors and that they differ greatly in applied magnetic fields.

## *2.1 Survey of BCS Theory*

### 2.1.1 Historical Overview and Early Observations

Generally speaking, thermodynamics is the study of the evolution of state variables (temperature, pressure, entropy, etc.) in a given physical system, typically in order to attain some form of equilibrium which may be achieved by simply raising the temperature of the system (i.e. upon an increase in the pressure of an ideal gas) or it may require that the

system undergoes a drastic phase transition to reclaim equilibrium and thus lower its energy (i.e. eutectic transformations or Bose-Einstein condensation). With such a wide range of system responses to changes in state, it is no wonder that there is a perpetual push toward the extremes of these thermodynamic variables: higher pressures, more disorder, lower temperature, high magnetic fields, etc.

Moreover, since temperature reigns as the most universal variable by which equilibrium is defined, it is natural to assume that much work, both experimental and theoretical, would be done in this realm. For example, leading physicists of the 1800's were extremely puzzled by why there was such a strong similarity between the temperature dependence of the thermal and electrical conductivities. Questions such as this led to a surge in experimental activity to reach the lowest possible temperatures and thus, be the first to measure these quantities near absolute zero. However, one large obstacle which initially impeded progress for the experimentalist was the lack of cryogenic methods and technology required to obtain lower temperatures; in fact, it was not until 1799 that scientists were able to even freeze water in commercial quantities.

Nevertheless, much progress was made over the next hundred years, culminating in H. Kamerlingh Onnes at Leiden successfully liquefying helium [176], reaching temperatures only a few degrees from absolute zero. Being the first researcher with this capability, he was in a prime position to discover new physical phenomenon which only appear at cryogenic temperatures; in fact, upon measuring the resistivity of a mercury filament at low temperatures Onnes observed a sudden drop in resistance by orders of magnitude from the previous reading around 4 K [177, 178, 179], as seen in Fig. 9. Through repeated trials he discovered that this jump to a zero resistance state was reversible and also occurred in lead and tin; this property of perfect conductivity below a critical temperature is the hallmark of the transition to the superconducting state.

From the initial observation of superconductivity in mercury, Onnes immediately began considering how magnets could be constructed with this new state of matter [62] since perfect conductivity implies that currents in superconductors would flow indefinitely with no

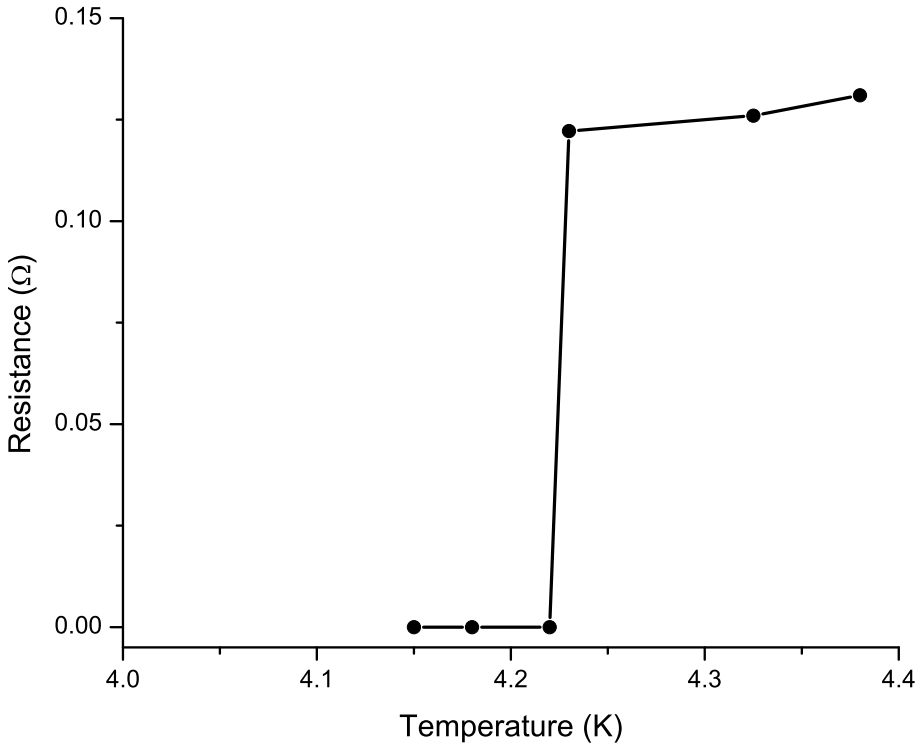


Figure 9: Adaptation of the original data from Kamerlingh-Onnes regarding the superconducting transition in mercury.

measurable change in magnitude (i.e. persistent currents). However, upon further investigation he observed that even moderate currents in superconducting coils would destroy the superconducting state and prevent their use as magnets. As an aside, persistent currents have been extensively studied using state of the art equipment and researchers [146, 240] have put a lower bound on the half-life of persistent currents to be $10^{23}$ years; this modern study further confirms the observations of Onnes in 1911 that the DC resistance of the mercury filament had essentially zero resistance, not some small but finite value which could not be resolved by his instrumentation.

Over the next twenty years, the magnetic properties of superconductors were heavily explored, culminating in the famous Meissner-Ochsenfeld experiment [160] which is schematically illustrated in Fig. 10. In the figure, panels (a) and (b) correspond to the expected behavior of a material which develops perfect conductivity below a certain critical temperature $T_c$, in contrast to panels (c) and (d) which show the results which Meissner and Ochsenfeld actually obtained.

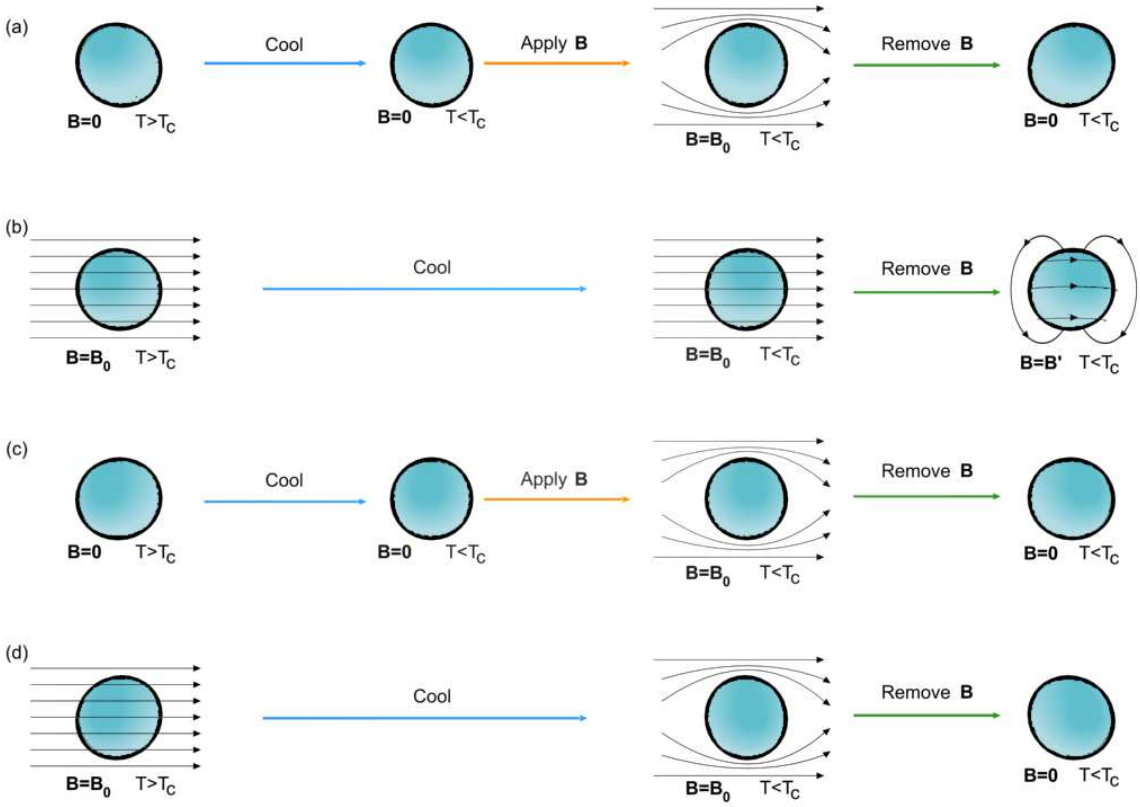


Figure 10: The top two panels of the figure graphically describe two different thermodynamic paths for a perfectly conducting material; similarly, the same two paths are shown for a superconductor in the bottom two panels. It can be seen that for a perfectly conducting material, the effect of cooling and then applying a magnetic field results in a different final state than if a magnetic field is applied and then the temperature is lowered below the critical value; thus, this does not constitute a true thermodynamic state since the final state of the system depends on the path. Instead of observing this behavior, the Meissner-Ochsenfeld experiment demonstrated that the superconducting state is a true thermodynamic state in that the final state of the system is independent of the path taken, as shown in the bottom two panels.

In panel (a), the material is cooled below its critical temperature and is then subjected to a magnetic field $\mathbf{B}_0$; since it is assumed that the material is perfectly conducting once the temperature is lowered below the critical temperature, the addition of the magnetic field does not result in any flux penetrating the sphere, which is a consequence of Lenz's Law. Therefore, by the end of panel (a), when the magnetic field is removed, there is no residual flux contained in the material. In contrast, panel (b) shows the same situation except that the magnetic field is applied before the perfectly conducting material is cooled below its critical temperature; in this case, magnetic flux will penetrate the material because it is initially not perfectly conducting. Upon cooling down, the internal magnetic flux is trapped inside the sphere and circulates while the external flux lines are unable to penetrate; at this stage, if the external field is removed, the induced persistent currents will maintain the internal flux of the sphere. Thus, the magnetization of a perfectly conducting material is path dependent, implying that it is not a thermodynamic state.

Panels (c) and (d) describe what Meissner and his colleagues actually measured; panel (c) illustrates that when the superconducting material is cooled below the critical temperature and subsequently a magnetic field is applied, the predicted behavior for a perfectly conducting material is observed. In contrast, upon traversing the opposite thermodynamic path (i.e. applying a magnetic field and subsequently cooling the sample), Meissner observed that the internal magnetic flux was completely expelled from the material; in other words, the material has a relative magnetic permeability, $\mu_r$, of zero or similarly, a magnetic susceptibility, $\chi$, of -1. This unexpected result of complete flux expulsion from a superconductor is now known as the Meissner effect. A consequence of this effect is that the magnetization of a superconductor is path independent and thus superconductivity is a new thermodynamic state of matter; thus, the Meissner experiments laid the foundation for a full thermodynamic treatment of superconductors which was eventually given by Abrikosov [1, 2]. Over the course of the next twenty years, many experimentalists focused on uncovering more about the superconducting state while theorists worked diligently to apply the experimental findings to an appropriate formalism which could account for the

existence of the superconducting state; in particular, experimentalists observed strong evidence that the charge carriers in superconductors were electron pairs and also that an energy gap forms during the transition to superconductivity, both of which must be incorporated into any microscopic theory of superconductors.

On the theoretical side, the first accepted theory which described superconductivity in a phenomenological way was proposed by London and London [147] and consisted of the following equations:

$$\mathbf{E} = \lambda \frac{\partial \mathbf{J}_s}{\partial t}, \tag{26}$$

$$\mathbf{B} = -\lambda \nabla \times \mathbf{J}_s, \tag{27}$$

$$\lambda = \frac{m^*}{n_s e^2}, \tag{28}$$

where $\lambda$ is the phenomenological parameter, $\mathbf{J}_s$ is the current density of superconducting electrons, $m^*$ is the electron's effective mass and $n_s$ is the number density of superconducting electrons. The first equation describes the acceleration of superconducting electrons in an applied AC electric field (it is unphysical to assume that a DC field would accelerate charge indefinitely). Further, by using both the first and second equation it is simple to show that all electric fields (AC and DC) are screened in superconductors and as well, that AC magnetic fields are screened. Although the London equations are useful in solving some practical problems, these phenomenological equations do not describe the disappearance of superconductivity in high magnetic fields; thus, they are valid only for weak magnetic fields and in situations where the spatial variation of fields is small.

Working from a thermodynamic perspective, Ginzburg and Landau [90] developed a phenomenological theory which extended Landau's previous work on second order phase transitions by postulating the existence of a complex, superconducting order parameter. In addition, they assumed a series expansion for the free energy and, by using the variational principle, were able to minimize the energy to obtain two differential equations which accurately describe the superconducting state in the vicinity of the critical temperature. However, through continued theoretical work on this phenomenological approach, the GL theory has been extended to include more general situations; moreover, after the publication

of the BCS theory of superconductors, which occurred the same year as the publication of the Ginzburg-Landau theory, Gor'kov [92] proved that the GL theory is a limiting case of the completely microscopic BCS theory, thus fully substantiating the phenomenological GL theory.

As mentioned above, on the same year as the publication of the Ginzburg-Landau theory of superconductivity, a new theory was proposed which explained not only the observable phenomena associated with superconductivity, but also the origin of the effect itself. This microscopic theory of superconductivity [18, 19] was published by Bardeen, Cooper and Schrieffer (BCS) and is the foundation of most subsequent work on low temperature superconductors; BCS theory does not describe high temperature superconductors because the underlying mechanism is somewhat different for these materials.

### 2.1.2 Cooper Pairing

Before a coherent theory of superconductivity could be formulated, theorists first had to discover the mechanism for electron pairing in superconductors. Additionally, the proposed interaction must be strong enough to cause an instability in the Fermi sea of electrons, thereby making electron pairing energetically advantageous under certain conditions. Cooper was the first to discover a pairing mechanism [46] and prove that it lowers the energy of the many-body system; to do so, he postulated an attractive electron-electron interaction which was mediated by phonons, as seen schematically in Fig. 11.

Furthermore, by looking at the panels in Fig. 12, one can see a crude real-space representation of the Cooper pairing mechanism; from the second panel of the figure, an electron traveling through a crystal lattice will locally distort the ion's positions due to Coulomb attraction. Moreover, since the ions are much more massive compared to an electron, the distortion created by the incoming electron will last long after that electron leaves the distorted region; therefore a local region of greater positive charge will be formed. Subsequently, it is an electron traveling from the opposite direction to the incoming electron that will be most attracted to the newly created line of ion distortions left by the first electron. As well, electrons traveling in opposite directions also minimize the repulsive effects

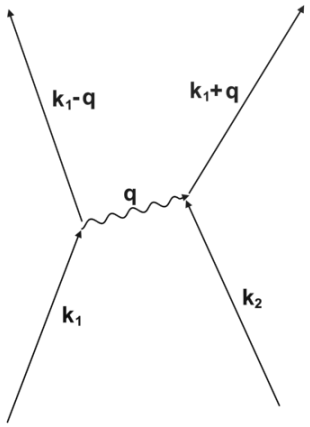


Figure 11: A generic interaction between two particles which is mediated by a phonon; in the specific case of superconductors, the k states must take on specific values for the attractive interaction to be maximized.

incurred due to the Coulomb interaction since they travel away from each other the fastest. For these reasons, if electron pairing does exist, the electron states most likely to form a pair will be of opposite momentum.

This conclusion was quantified by Cooper who showed that the amount of energy reduction gained by electron pairing is proportional to the number of available scattering states for the electrons, as shown in Fig. 13. In both panels of the figure, the total wavevector, $\mathbf{K}$, is conserved and the shell around the Fermi sphere contains all the states electrons may scatter into as a result of interactions with phonons (the shell thickness is assumed to be $\hbar\omega_d$, i.e. the largest phonon energy in the Debye model). With this in mind, the first panel describes the general situation where $\mathbf{k}_1$ and $\mathbf{k}_2$ are not collinear; thus, the two electrons can scatter only into the small shaded region if momentum is to be conserved. However, the hatched area can be greatly increased if the two momentum vectors are opposite, $\mathbf{k}_2 = -\mathbf{k}_1$; in this case, all possible states are available by phonon scattering, thereby making pairs in this configuration the most energetically favorable for superconductivity.

With the above considerations in mind, Cooper constructed an artificial, yet instructive model of electron pairing in superconductors; specifically, he assumed that the entire Fermi sphere of the metal was filled up to $\mathbf{k}_F$ and that two additional electrons were added above the Fermi energy. These additional electrons are assumed to have opposite spins and also

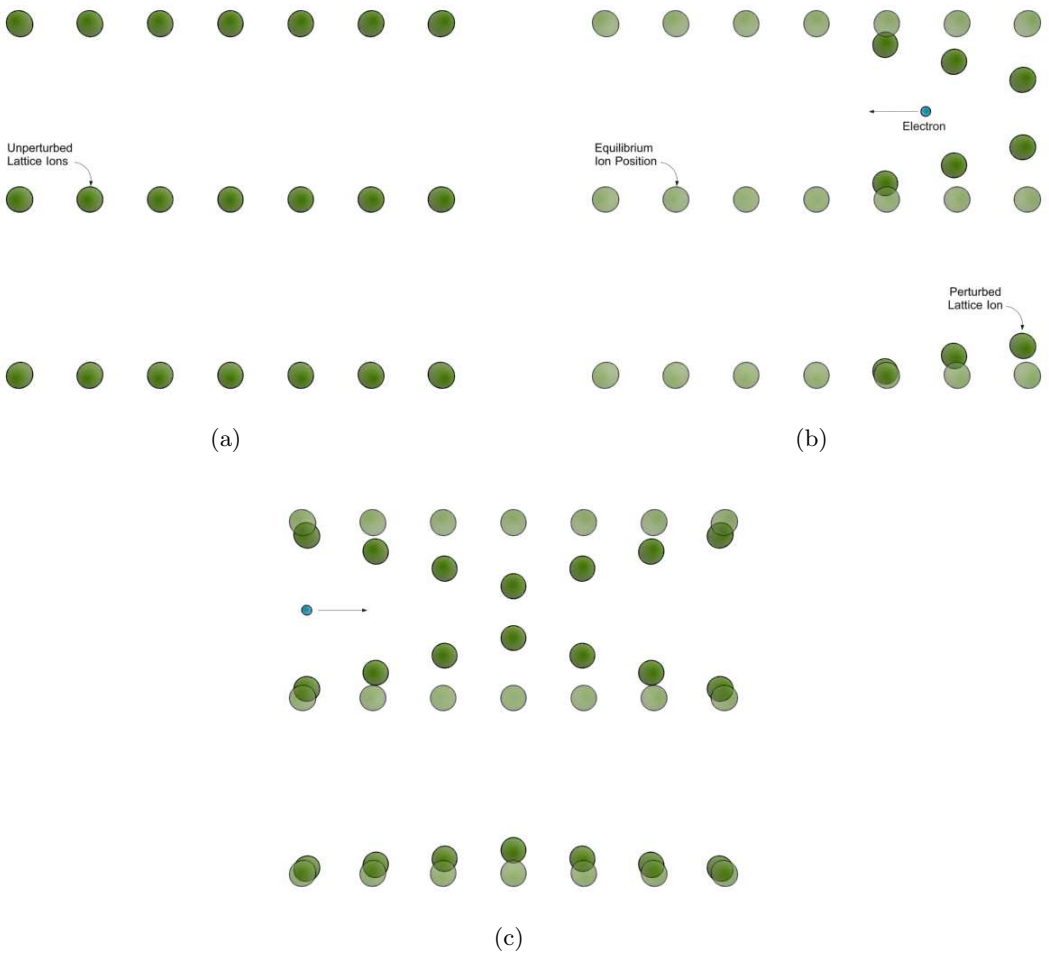


Figure 12: (a): The equilibrium position of a lattice in real space. (b): As an electron passes by these lattice ions , they are displaced from equilibrium. Since the ions are much larger than the electron, even after the electron has left the proximity of these ions, they are still displaced which creates a net positive charge. (c): Hence, if another electron travels through the same region after the first electron, it will be attracted to this local center of positive charge, creating an effective electron-electron interaction which is mediated by the lattice ions. Additionally, it should be noted that this interaction will be maximized if the two electrons have opposite wave vectors since then the Coulomb repulsion will be minimized.

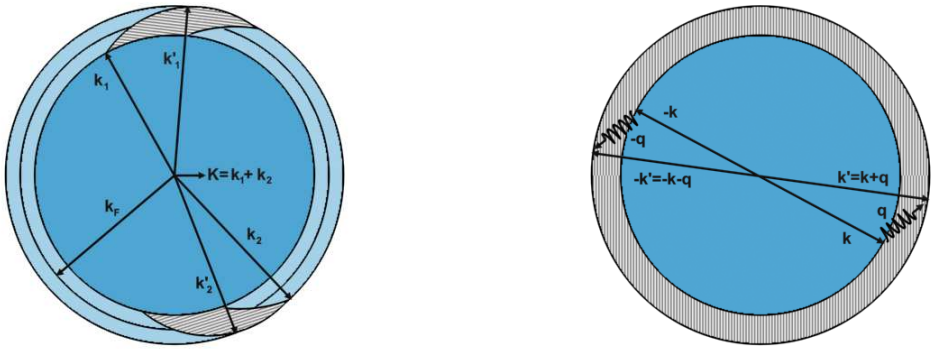


(a) (b)

Figure 13: Here we see a schematic of two pair interactions in k-space; the two interacting electrons have wave vectors which lie close to the Fermi surface and have a net wavevector of $\mathbf{K} = \mathbf{k_1} + \mathbf{k_2}$. In order to conserve momentum, there is a limited set of final states which the particles may be scattered into, as shown by the hatched region. The second panel shows the same interaction, but with zero center of mass momentum; here it is clear that the number of available states has been maximized. As noted in the text, since the strength of the interaction between the particles is dependent upon the number of final scattering states, states with opposite momentum are the most likely to have an attractive interaction.

opposite momenta; further, Cooper assumed no Coulomb interaction, only an attractive electron-electron interaction, V($\mathbf{r}_1$,$\mathbf{r}_2$), whose k-space matrix element was given by:

$$\langle \mathbf{k}, -\mathbf{k}|V(\mathbf{r_1}, \mathbf{r_2})|\mathbf{k}, -\mathbf{k}\rangle = -V. \tag{29}$$

Solving for the energy eigenvalue of the system, Cooper found it to be:

$$W = -2\hbar\omega_d e^{\frac{1}{\lambda}}, \tag{30}$$

where $\lambda$ is a measure of the strength of the attractive interaction. This result shows that an arbitrarily small attractive interaction will lower the energy of the system below the Fermi energy, thereby causing a collapse of the Fermi sphere; more importantly, this calculation explains why superconductivity could not be explained using standard perturbation theory. Specifically, since the energy eigenvalue has an essential singularity as $\lambda$ approaches zero, it could not possibly be obtained by using perturbation theory; additionally, we see that the effect of electron pairing is purely quantum mechanical in nature, given the $\hbar$ in the expression for the energy. In the same way, since the energy is below the Fermi energy,

which is expressly prohibited by the Pauli exclusion principle, this gives an indication that the bound pairs of electrons may not obey Fermi statistics like their constituents.

Although Cooper's model clearly has many inherent assumptions, some of which were not *a priori* justified, it served as a solid foundation to be built upon in that it described a physically sound pairing mechanism for electrons. However, showing that two electrons outside of the Fermi sphere would condense into pairs in the presence of an attractive interaction does not necessarily imply that the entire Fermi sea would condense as well. By assuming no repulsive Coulomb interaction, Cooper used an inherently unphysical model which must be corrected before a physically compelling argument for phonon-mediated attraction can be made. Thus, the next logical step must be to show that under certain circumstances, the attractive interaction between the electrons is stronger than the Coulomb interaction; this was accomplished through the use of dielectric functions, where it can be shown that the true potential of the electrons, including the screened Coulomb potential, is given by:

$$V_{\mathbf{k},\mathbf{k}'} = \gamma \left( 1 + \frac{1}{\left(\frac{\omega}{\omega_q}\right)^2 - 1} \right), \tag{31}$$

where $\gamma$ is a constant involving the dielectric constant and the magnitude of the phonon wave vector, $\mathbf{q}$, and $\omega_q$ is the frequency of the scattered phonon. This potential is plotted in Fig. 14 with the simplified Cooper model for comparison. From the figure, one can see that for energies less than that of the phonon, bound pairs are energetically favorable due to the stronger influence of the attractive interaction.

### 2.1.3 The BCS Ground State

By proving that in some cases a net attractive interaction exists between electrons in a metal, a huge step was taken toward a consistent theoretical formulation of superconductivity; however, at this point there remains no way to determine how many pairs of electrons will condense into the superconducting state (i.e. when does the pair binding energy go to zero). It is this problem which was solved via the variational method by BCS [18] in 1957; in using the formalism of second quantization [196], the authors postulated a ground state wave function and subsequently minimized the system's energy, thereby obtaining the

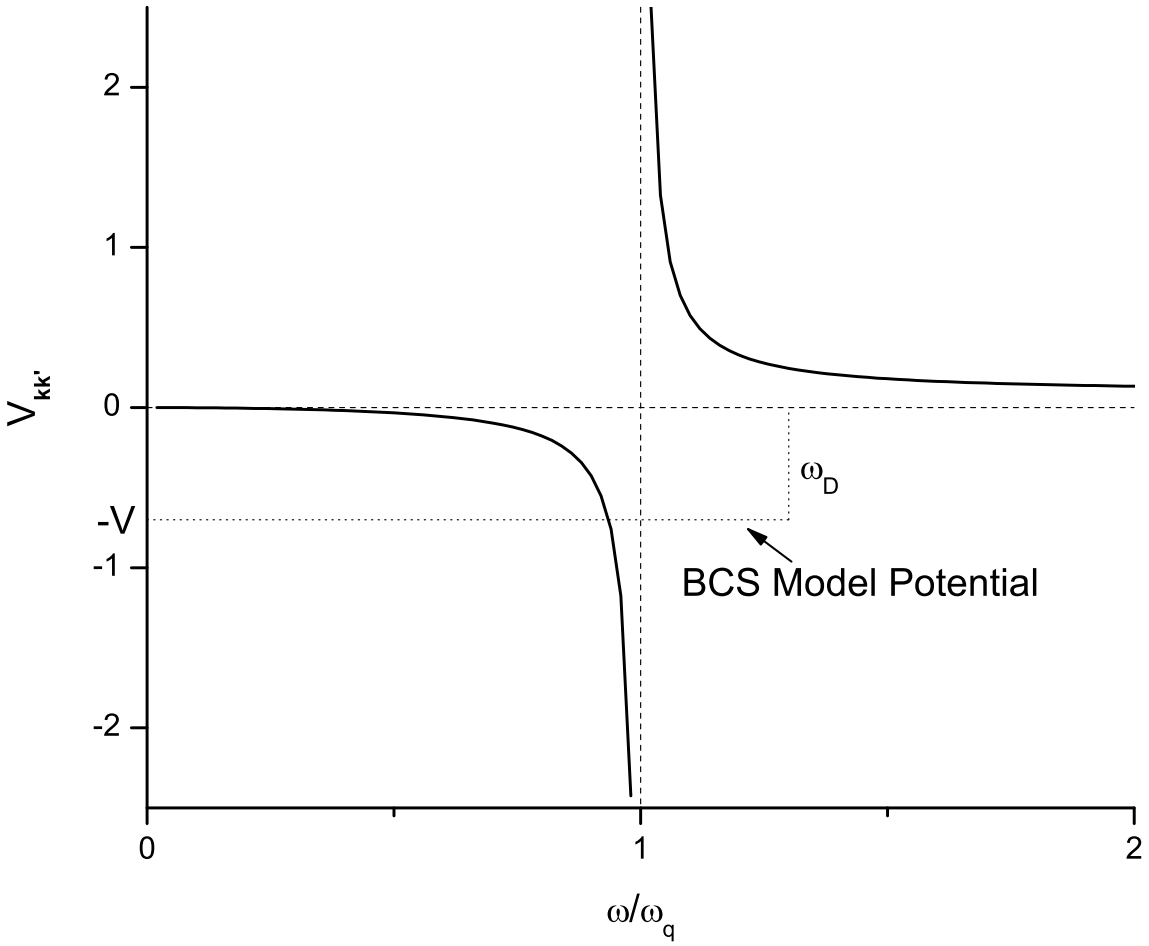


Figure 14: Here, the solid line refers to the total potential of the electrons which includes the contribution due to the screened Coulomb potential. Also shown in the figure for comparison is the BCS approximation to the true electron potential, which is simply a negative constant up to the Debye frequency and zero elsewhere.

condensation energy of the superconductor.

In keeping with standard second quantization notation, we introduce the creation operator, $c^{\dagger}_{\mathbf{k}}$, for an electron with wave vector $\mathbf{k}$ such that:

$$c^{\dagger}_{\mathbf{k}}|0\rangle = |1\rangle. \tag{32}$$

Likewise we introduce the annihilation operator, $c_{\mathbf{k},\uparrow}$, which satisfies the relation:

$$c_{\mathbf{k}}|1\rangle = |0\rangle. \tag{33}$$

Because electrons obey Fermi statistics, these creation and annihilation operators must satisfy the fermion anticommutation relations:

$$[c_{\mathbf{k},\sigma}, c^{\dagger}_{\mathbf{k}',\sigma'}]_{+} = c_{\mathbf{k},\sigma}c^{\dagger}_{\mathbf{k}',\sigma'} + c^{\dagger}_{\mathbf{k}',\sigma'}c_{\mathbf{k},\sigma} = \delta_{\mathbf{k},\mathbf{k}'}\delta_{\sigma,\sigma'}, \tag{34}$$

where $\sigma$ is a generic spin index. Furthermore, recall that the particle number operator can be expressed through the composite operator, $n_{\mathbf{k},\sigma} = c^{\dagger}_{\mathbf{k},\sigma}c_{\mathbf{k},\sigma}$; additionally, a general pair transition for electron's of opposite spin (as in the case of superconductivity) can be represented by the following composite operator, $c^{\dagger}_{\mathbf{k}+\mathbf{q},\uparrow}c^{\dagger}_{-\mathbf{k}-\mathbf{q},\downarrow}c_{-\mathbf{k},\downarrow}c_{\mathbf{k},\uparrow}$, which destroys a pair with momentum, $|\mathbf{k}|$, and creates another pair with new wave vector $|\mathbf{k}+\mathbf{q}|$.

By applying the notation presented above, a general pairing Hamiltonian for the system can be written as:

$$\hat{H} = \sum_{\mathbf{k},\sigma} \epsilon_{\mathbf{k}} n_{\mathbf{k},\sigma} + \sum_{\mathbf{k},\mathbf{m}} V_{\mathbf{k},\mathbf{m}} c^{\dagger}_{\mathbf{k},\uparrow} c^{\dagger}_{-\mathbf{k},\downarrow} c_{-\mathbf{m},\downarrow} c_{\mathbf{m},\uparrow}, \tag{35}$$

where the aim is to include those terms in the Hamiltonian which are directly relevant to superconductivity (i.e. terms involving pair creation and annihilation) and omit others. With a general Hamiltonian for the system in place, the next step is hypothesizing a ground state for the system; to this end, BCS assumed a ground state wave function of the form:

$$|\psi\rangle = \prod_{\mathbf{k}=\mathbf{k_1},\ldots,\mathbf{k_n}} \left(u_{\mathbf{k}} + v_{\mathbf{k}} c^{\dagger}_{\mathbf{k},\uparrow} c^{\dagger}_{-\mathbf{k},\downarrow}\right)|0\rangle, \tag{36}$$

where the first term of the sum is required for the normalization of $|\psi\rangle$, $|0\rangle$ is the vacuum state of the system with no pairs present, $v_{\mathbf{k}}$ is the probability of pair occupancy for state $\mathbf{k}$ and similarly, $u_{\mathbf{k}}$ is the probability for pair vacancy of state $\mathbf{k}$ (conservation of probability implies that $u^2_{\mathbf{k}} + v^2_{\mathbf{k}} = 1$).

With the Hamiltonian and ground state wave function in place, if the variational method is used to minimize the ground state energy of the system, a system of two equations is obtained which relate the amplitudes of pair occupation and vacancy:

$$2u_{\mathbf{k}}v_{\mathbf{k}} = \frac{\Delta_{\mathbf{k}}}{E_{\mathbf{k}}}, \tag{37}$$

$$v_{\mathbf{k}}^2 - u_{\mathbf{k}}^2 = -\frac{\xi_{\mathbf{k}}}{E_{\mathbf{k}}}, \tag{38}$$

where $\Delta_{\mathbf{k}}$ is a quantity which must be solved for self-consistently through the following expression:

$$\Delta_{\mathbf{k}} = -\frac{1}{2}\sum_{\mathbf{m}}\left(\frac{\Delta_{\mathbf{m}}}{E_{\mathbf{m}}}\right)V_{\mathbf{km}}, \tag{39}$$

Further, $E_{\mathbf{k}}$ is given by the formula:

$$E_{\mathbf{k}} = (\Delta_{\mathbf{k}}^2 + \xi_{\mathbf{k}}^2)^{\frac{1}{2}}, \tag{40}$$

where the quantity $\xi_{\mathbf{k}} = \epsilon_{\mathbf{k}} - \mu$ is simply the energy of a single particle referenced from the Fermi energy, i.e. in the excitation representation. From equation (37) and knowing that the energy can only take on real values, the term $\Delta_{\mathbf{k}}/u_{\mathbf{k}}v_{\mathbf{k}}$ must also be real; further, since this is the only constraint on the phases of the three quantities, $\phi_\Delta - \phi_u - \phi_v = 0$. Hence, any one of the three quantities can be set to zero with generality, realizing then that the other two must have a fixed relative phase; typically speaking, it is customary to set the electron's coherence factor, $\mathrm{u}_{\mathbf{k}}$, zero. By using this convention, the gap parameter becomes complex, along with the hole's coherence factor, $\mathrm{v}_{\mathbf{k}}$, and furthermore, they have opposite phases; as seen more clearly later, the phase of the gap parameter is a quantity of fundamental importance in superconducting devices.

Because the expression for $\Delta_{\mathbf{k}}$ must be solved self-consistently, solutions will be difficult to obtain in general; thus, a simplifying approximation is made by using the Cooper potential, $-V$, in place of the more complicated $V_{\mathbf{km}}$. In doing so, the expression for $\Delta_{\mathbf{k}}$ simply becomes a constant, $\Delta$, whose value is approximately 1meV for most metals; consequently, the pair amplitudes then can be rewritten as:

$$v_{\mathbf{k}}^2 = \frac{1}{2}\left(1 - \frac{\xi_{\mathbf{k}}}{(\Delta^2 + \xi_{\mathbf{k}}^2)^{\frac{1}{2}}}\right), \tag{41}$$

$$u_{\mathbf{k}}^2 = 1 - v_{\mathbf{k}}^2 = \frac{1}{2}\left(1 + \frac{\xi_{\mathbf{k}}}{(\Delta^2 + \xi_{\mathbf{k}}^2)^{\frac{1}{2}}}\right), \tag{42}$$

where the probability for pair occupancy is plotted in Fig. 15. From the figure, a striking similarity to the Fermi function for normal metals at $T \neq 0K$ is seen, though this result is for $T = 0K$; additionally, it should be noted that the probability of pair occupancy changes significantly only in the range of a few $\Delta$ (i.e. $\Delta$ is a characteristic energy scale of superconductors). This qualitative form of the pair occupancy can be understood by considering that pairs will have a tendency to move towards states of higher kinetic energy since that will maximize the amount of final scattering states which lowers the potential energy of the system, see Fig. 14. Following this further, there is an initial decrease in potential energy which more than offsets the increase in kinetic energy of the pairs, thus they will continue to move toward states of higher kinetic energy. However, an equilibrium will eventually be reached when the decrease in potential energy is fully compensated by the increase in kinetic energy, resulting in a curve qualitatively similar to the Fermi function at a non-zero temperature.

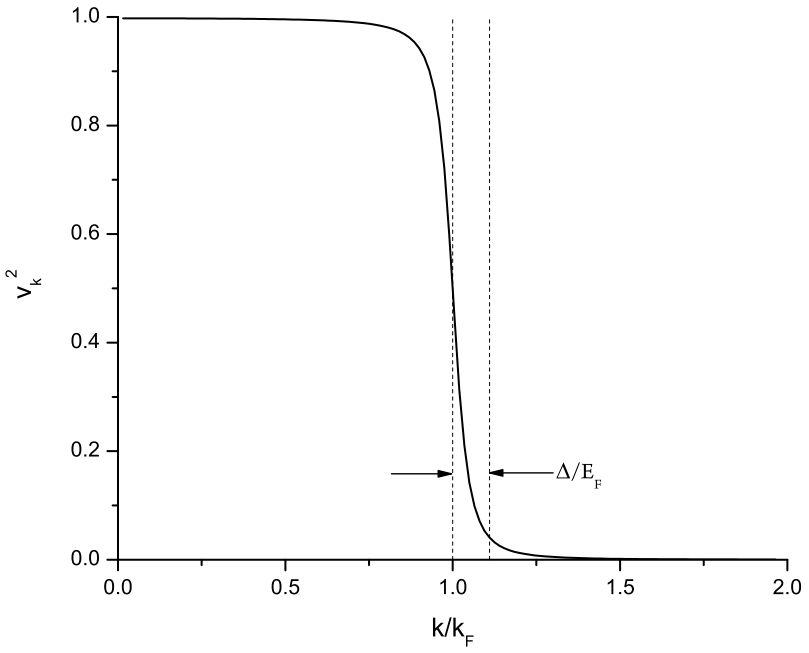


Figure 15: Plotted here is probability of pair occupation in a superconductor; the functional form of the probability is very similar to Fermi function for electron occupation in normal metals

With the probability of pair occupancy calculated, the condensation energy (i.e. the difference in energy between the normal ground state and the superconducting ground state) can be calculated [227] as:

$$E_n - E_s = \frac{1}{2}N(0)\Delta^2, \tag{43}$$

where N(0) is the normal density of states at the Fermi level. This approximation is justified since the characteristic energy scale of superconductivity is $\Delta$, which is typically around 1meV, as opposed to a typical Fermi energy on the order of eV. This result is not totally surprising given that the energy range of pairing interactions is $\Delta$ and thus the number of pairs in this region is approximately $N(0)\Delta$; furthermore, if the binding energy of pairs is considered to be $2\Delta$, then the condensation energy will be on the order of the correct value ($2\mathrm{N}(0)\Delta^2$ as opposed to $1/2\mathrm{N}(0)\Delta^2$). From this physical argument, only those electrons whose energy lie in the narrow range of $\Delta$ about the Fermi energy may contribute to pairing interactions; however, the electrons which are farther below the Fermi surface may be considered as pairs for mathematical convenience (as BCS did), but they are too far removed from the Fermi energy to participate in the phonon mediated attractive interaction which leads to pairing.

The wave functions of these paired states exhibit an interesting phenomenon known as the proximity effect [63] which allows the wave functions of two spatially separated superconductors to overlap and interact. Consequently, this phenomenon will be of fundamental importance in the study of Josephson junctions. Nevertheless, though the condensate wave function may extend outside of the superconductor itself, one Cooper pair only has a spatial extent of typically 100 nm, as this is the region over which a pair is phase coherent; thus, this length is termed the superconducting coherence length, $\xi$, and a general expression was given by BCS [18] as:

$$\xi_0 = 0.18\frac{\hbar v_F}{k_B T_c}. \tag{44}$$

From the symmetry of Fig. 15 around $\mathrm{k}_F$, as well as the above argument for the existence of pair states only around a small energy range centered on the Fermi energy, we can see that the phase coherent pairs form a wave packet, much like a de Broglie wave packet, which

oscillates at $f = 2E_F/h$.

Additionally, the relatively large size of a single Cooper pair implies that many pairs must overlap in a superconductor; consequently, it is energetically advantageous for the pairs to lock relative phases. Specifically, for the case of zero center of mass motion of the pairs (i.e. no applied bias), all pairs lock phases and oscillate at the same frequency and the collective wave function of the condensed pairs can be represented simply as an ensemble average function, $\psi = |\psi(\mathbf{r})|$. However, if there is a non-zero center of mass momentum, $\mathbf{K}$, then the expression for the wave function contains an additional phase factor given by:

$$\psi = |\psi(\mathbf{r})|e^{i\mathbf{K}\cdot\mathbf{r}} \longrightarrow, |\psi|e^{i\theta(\mathbf{r})} \tag{45}$$

where $\theta(\mathbf{r})$ is the phase of the electron pairs and is a quantity of fundamental importance in the study of superconducting devices.

### 2.1.4 Excitations from the Ground State

In modern treatments of excitations in superconductors, theorists rarely employ the variational principle as introduced initially by BCS; instead, a more sophisticated approach is adopted which uses a linear transformation to diagonalize the BCS Hamiltonian, as initially discovered independently by Bogoliubov [34] and Valatin [224]. The appropriate linear transformation of the original creation and annihilation operators to reduce the model Hamiltonian into diagonal form is given by:

$$c_{\mathbf{k},\uparrow} = u^*_{\mathbf{k}}\gamma_{\mathbf{k},0} + v_{\mathbf{k}}\gamma^*_{\mathbf{k},1}, \tag{46}$$

$$c^*_{-\mathbf{k},\downarrow} = -v^*_{\mathbf{k}}\gamma_{\mathbf{k},0} + u_{\mathbf{k}}\gamma^*_{\mathbf{k},1}, \tag{47}$$

With these definitions in place, the model Hamiltonian becomes:

$$H = H_{s,0} + \sum_{\mathbf{k}} E_{\mathbf{k}}(\gamma^*_{\mathbf{k},0}\gamma_{\mathbf{k},0} + \gamma^*_{\mathbf{k},1}\gamma_{\mathbf{k},1}), \tag{48}$$

where $\mathrm{H}_{s,0}$ is a constant and equal to the energy of the normal state minus the condensation energy of the superconductor and the operator $\gamma^*_{\mathbf{k},0}\gamma_{\mathbf{k},0}$ has the form of a new number operator. Evidently, the new operators, $\gamma_{\mathbf{k}}$, correspond to the quasiparticle excitations of

the superconducting state and are known as bogoliubons; by inverting the transformation given above, the composition of the quasiparticles are observed to be:

$$\gamma^*_{\mathbf{k},0} = u^*_{\mathbf{k}} c^\dagger_{\mathbf{k},\uparrow} - v^*_{\mathbf{k}} c_{-\mathbf{k},\downarrow}, \tag{49}$$

$$\gamma^*_{\mathbf{k},1} = u^*_{\mathbf{k}} c^\dagger_{-\mathbf{k},\downarrow} + v^*_{\mathbf{k}} c_{\mathbf{k},\uparrow}. \tag{50}$$

Clearly then, the effect of exciting a superconducting quasiparticle is to create a normal state electron plus with its time-reversed counterpart, a hole of opposite spin; moreover, the probabilities $u_{\mathbf{k}}$ and $v_{\mathbf{k}}$ acquire a new interpretation: $u_{\mathbf{k}}$ represents the extent to which a superconducting quasiparticle excitation is "electron-like." Similarly, $v_{\mathbf{k}}$ represents the probability that the quasiparticle is "hole-like." As such, an excitation which has a large $u_{\mathbf{k}}$ (and thus a small $v_{\mathbf{k}}$ since $v^2_{\mathbf{k}} + u^2_{\mathbf{k}} = 1$) can be termed a quasi-electron; likewise, an excitation whose $v_{\mathbf{k}}$ is large compared to $u_{\mathbf{k}}$ is termed a quasi-hole. However, the values of $u_{\mathbf{k}}$ and $v_{\mathbf{k}}$ are ensemble averages and thus refer only to the tendency of a specific system of the ensemble to have an excitation in state $\mathbf{k}$; more importantly, fractional $u_{\mathbf{k}}$ or $v_{\mathbf{k}}$ in no way imply that the electrons or holes which comprise the excitation are fractional. Looking at the diagonalized Hamiltonian, the excitation energies of the quasiparticles are seen to be:

$$E_{\mathbf{k}} = (\Delta^2_{\mathbf{k}} + \xi^2_{\mathbf{k}})^{\frac{1}{2}}, \tag{51}$$

This result explains the previously mentioned experimental discovery that superconducting quasiparticles cannot be excited with arbitrarily low energy; instead, an energy gap of $2\Delta$ opens in the excitation spectrum upon lowering the temperature below $T_c$, which is shown in Fig. 16 for a highly exaggerated gap. However, experimentalists had also observed that the gap in the spectrum of excitation energies is temperature dependent and that it goes smoothly to zero as the temperature is increased to $T_c$. To quantify this experimental fact, note that the constituents of superconducting quasiparticles are fermions; consequently, the probability of one being thermally excited is still the Fermi function. This implies that a temperature dependent expression for the gap can be obtained by extending equation (39)

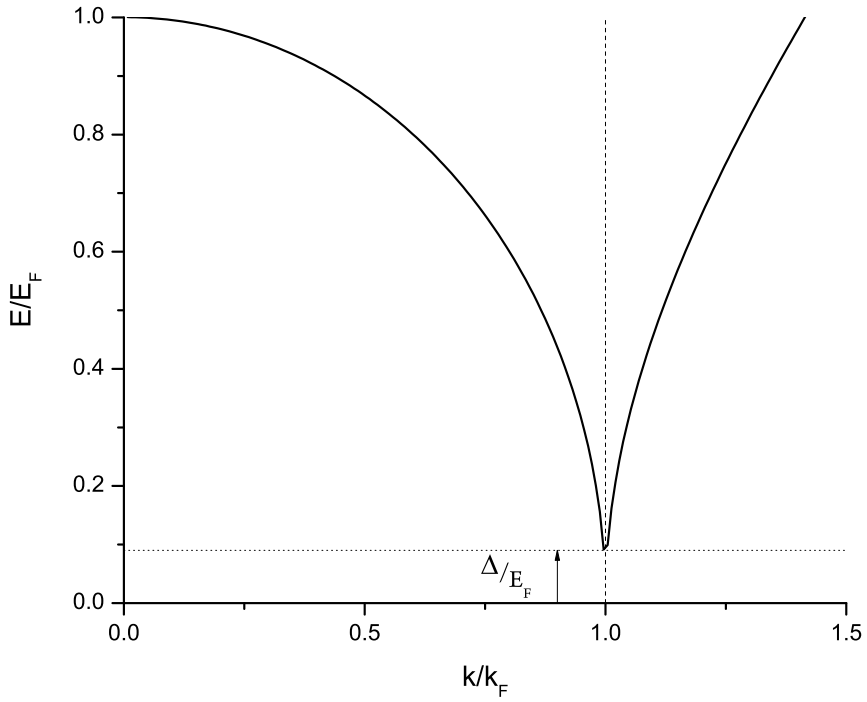


Figure 16: The excitation spectrum for superconductors; note the similarity to that of normal metals, with the important exception of a gap which develops for low lying excitations. This quasiparticle excitation gap is a central feature of superconductors which provides the physical basis for many of the interesting phenomena in superconductivity.

to include the probability of thermally exciting quasiparticles from the ground state:

$$\Delta_{\mathbf{k}} = -\sum_{\mathbf{m}} V_{\mathbf{km}} u^*_{\mathbf{m}} v_{\mathbf{m}} [1 - 2f(E_{\mathbf{m}})] \rightarrow \frac{V}{2} \sum_{\mathbf{m}} \frac{\tanh(\frac{\beta E_{\mathbf{m}}}{2})}{E_{\mathbf{m}}}, \tag{52}$$

where the second expression is derived under the approximation of $V_{\mathbf{km}} = -V$. From this equation the temperature dependence of the gap must be determined self-consistently due to the implicit dependence of the gap by $\mathrm{E}_K$; for computational purposes, the expression can be transformed into an integral where the density of states is considered a constant, N(0), due to the small energy range considered:

$$\frac{1}{N(0)V} = \int_0^{\hbar\omega_D} d\xi \frac{\tanh\left(\frac{1}{2}\beta\sqrt{\xi^2 + \Delta^2}\right)}{\sqrt{\xi^2 + \Delta^2}}. \tag{53}$$

However, this integral can be approximated using a mean field expression for temperatures

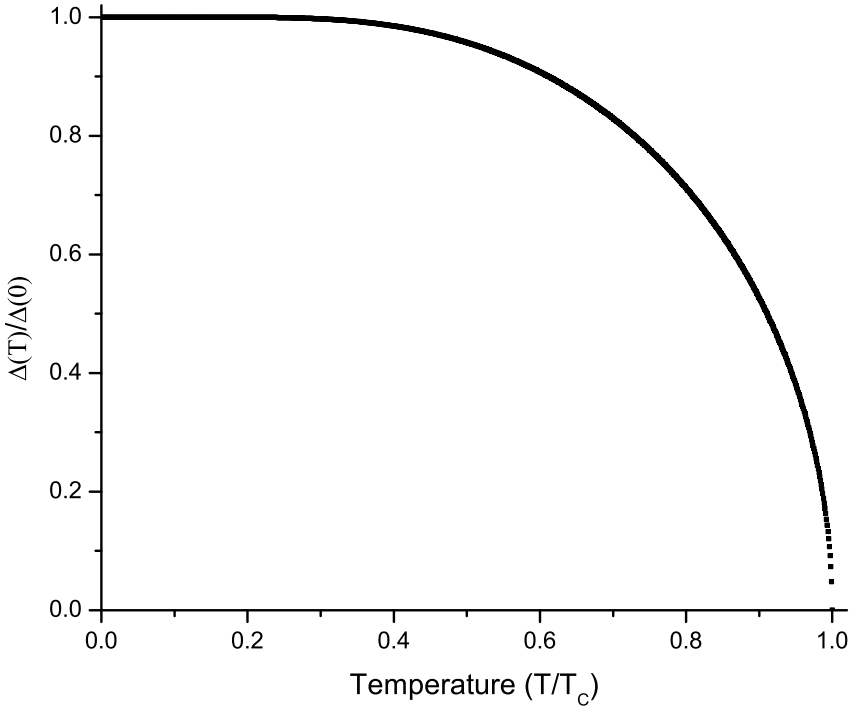


Figure 17: Here we see that the magnitude of the superconducting gap parameter decreases sharply only near the critical temperature.

approaching $T_c$ from below; specifically, in the region near the critical temperature, the

kernel of the integral is slowly varying, leading to the approximate result:

$$\frac{\Delta(T)}{\Delta(0)} \approx 1.74 \left(1 - \frac{T}{T_c}\right)^{\frac{1}{2}}, \tag{54}$$

which is plotted in Fig. 17.

In addition to the energy gap which was observed for superconductors, experimentalists also noted that the density of states was altered as the temperature was decreased below the critical temperature; to explain this result, the one-to-one correspondence of the superconducting quasiparticles with the original electrons of a normal metal (i.e. Fermi liquid theory) can be exploited to obtain an analytical expression for the superconducting density of states:

$$N_s dE = N_n d\xi. \tag{55}$$

In the usual way, the normal density of states, $N_n$, is approximated to be a constant, N(0); consequently, the superconducting density of states becomes:

$$\frac{N_s(E)}{N(0)} = \frac{d\xi}{dE} = \begin{cases} 0 & \text{for } E < \Delta \\ \frac{E}{\sqrt{E^2 - |\Delta|^2}} & \text{for } E > \Delta \end{cases}$$

which is plotted in Fig. 18 in the form of a "semiconductor diagram." However, one caveat about the use of these types of diagrams for the density of states is that the energies are measured positive in each direction from the center; furthermore, the lower part of the graph corresponds to the density of states for quasiholes, whereas and the upper half corresponds to the density of quasi-electrons in the superconductor. Physically, the structure of the density of states reflects the fact that pair breaking takes an energy of $2\Delta$ in a superconductor; thus, there can be no quasiparticle states in a region of $2\Delta$ about the Fermi energy; however, once the energy is raised above $\Delta$ from the Fermi energy, the density of states quickly reduces back to that of a normal metal over a range of a few $\Delta$, as seen in the figure.

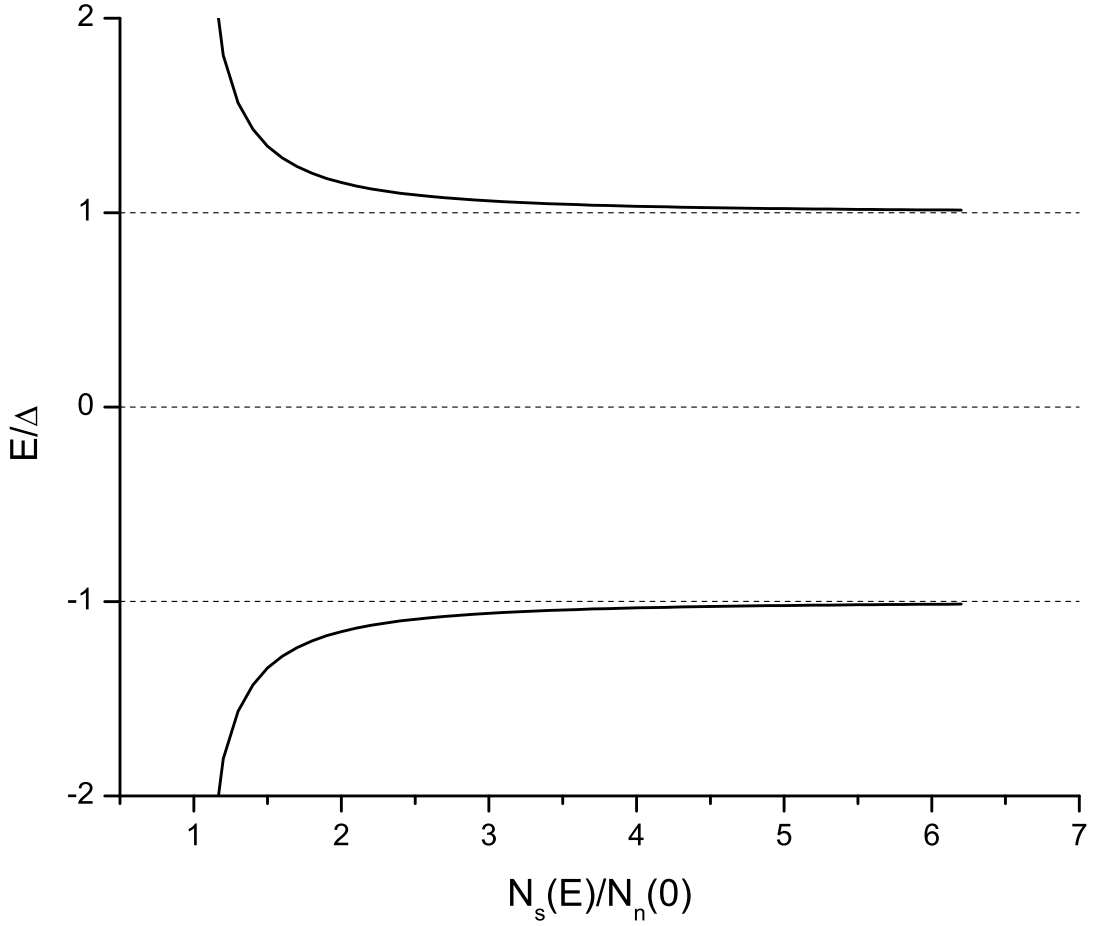


Figure 18: The BCS density of states deviates very strongly from normal metal behavior for energies which are comparable to the gap parameter; specifically, a gap opens up for energies within $\pm\Delta$ of the Fermi energy, followed by a sudden increase in density. From this point, the density of states slowly relaxes back to the normal metal value, $N_0$.

## 2.2 Inhomogeneous Superconductivity

### 2.2.1 Bogoliubov-de Gennes Formalism

Up to this point, the superconducting gap parameter, $\Delta$, has been assumed to be a constant, $\Delta(\mathbf{r}, t) = \Delta_0$; however, in many cases of interest (dirty superconductors, normal-superconductor interfaces, etc.), this assertion breaks down completely and a more general formalism which can explicitly handle inhomogeneities in the gap parameter must be employed.

To this end, the Bogoliubov-de Gennes equations [63] were derived as an approximate form of the BCS Hamiltonian in which spatial variation was included; upon projecting the simplified Hamiltonian onto real space, the following equations are obtained:

$$\begin{pmatrix} H_n(x) & \Delta(x) \\ \Delta^*(x) & H_n^*(x) \end{pmatrix} \begin{pmatrix} u(x) \\ v(x) \end{pmatrix} = E \begin{pmatrix} u(x) \\ v(x) \end{pmatrix}, \tag{56}$$

where $H_n$ is the normal state Hamiltonian and the vector which consists of u(x) and v(x) describes the state of the superconducting quasiparticle. In fact, u(x) and v(x) are the Fourier transforms of $u_{\mathbf{k}}$ and $v_k$, meaning the association of these functions with the electron and hole amplitudes of a quasiparticle remains.

In order to more clearly see the effect a non-homogeneous pairing potential has on the system, the potential energy, U(x), contained within the normal state Hamiltonian will initially be set to zero. In doing so, the non-interacting electron gas approximation can be employed, allowing electron's to be represented by plane waves. However, it is typically not advantageous to take the superconducting gap to be real, though it is possible by looking at equation (37).

With these considerations in mind, the pairing potential is assumed to be of the form depicted in Fig. 19 which corresponds to a superconductor-normal-superconductor(SNS) sandwich; the first panel of the figure takes into account the proximity effect, forcing the gap parameter to gradually decrease to zero. In this case, the Bogoliubov-de Gennes equations must be solved self-consistently, implying that considerable computational effort must be used to arrive at solutions. However, if a simpler model is assumed where the proximity

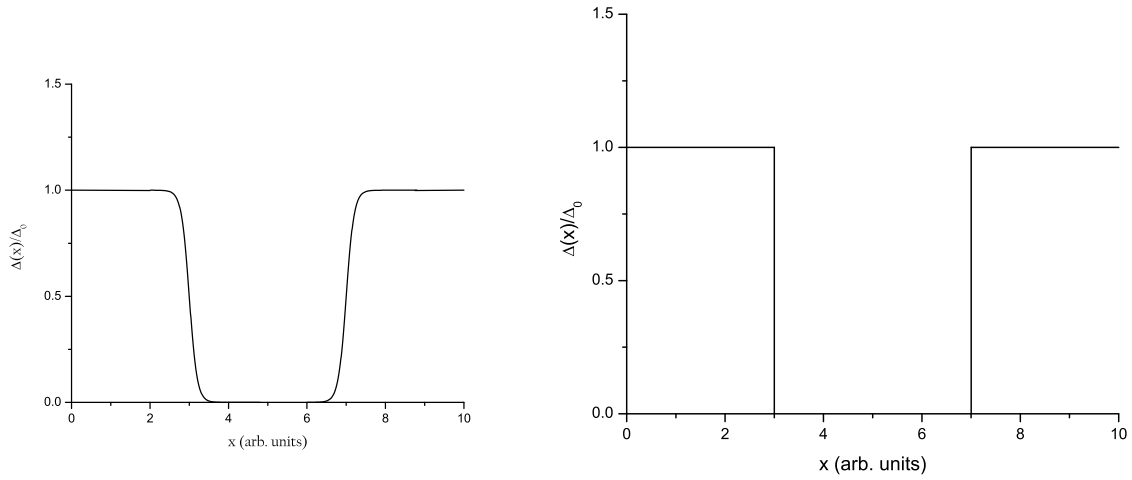


Figure 19: In the first panel, a superconductor-normal-superconductor (SNS) interface is shown with the proximity effect taken into account. For this case, the magnitude of the gap decreases continuously from its bulk value, meaning that there is some penetration of the condensate wave function into the normal material. In contrast, the second panel describes an idealized version of the first panel where the size effects of a Cooper pair are neglected; this step model of a SNS junction is advantageous for calculation due to its similarity with the finite square well problem of elementary quantum mechanics.

effect is suppressed, as shown in the second panel of Fig. 19, the gap develops a discontinuity at the interfaces between the normal and superconducting regions:

$$\Delta(x) = \begin{cases} 0 & \text{inside normal region} \\ |\Delta| e^{i\phi} & \text{inside superconducting region} \end{cases}$$

where $\phi$ is the relative phase of the gap with respect to $\mathrm{u}_{\mathbf{k}}$ which satisfies equation (37).

### 2.2.2 Andreev Reflection

Before the full problem of a SNS device is discussed, the simpler case of a single NS interface is considered, which can be generalized to more complicated geometries. To begin, Fig. 18 shows that the density of states of a superconductor is very different from a normal metal, at least for low excitation energies. Thus, a high energy electron (with respect to $\Delta$) in the normal metal which impinges on the NS interface should transmit with a very high probability; only for lower energies should electrons have a non-negligible chance of reflection at the interface. However, this simple picture is significantly changed when the energy of the incident electron is less than the energy gap; in this case, there are no states available for

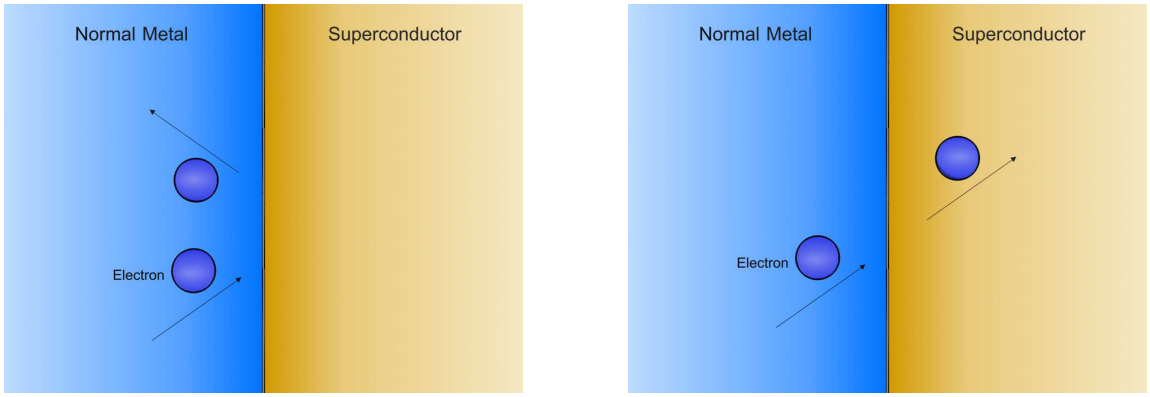


(a) (b)

Figure 20: The first panel shows the situation of an electron being reflected upon hitting a NS interface; for the second panel, the electron is transmitted through the superconductor. In normal systems, an incident electron has only two possibilities upon impinging upon a barrier; however, more exotic phenomena must be considered when the barrier includes a superconductor.

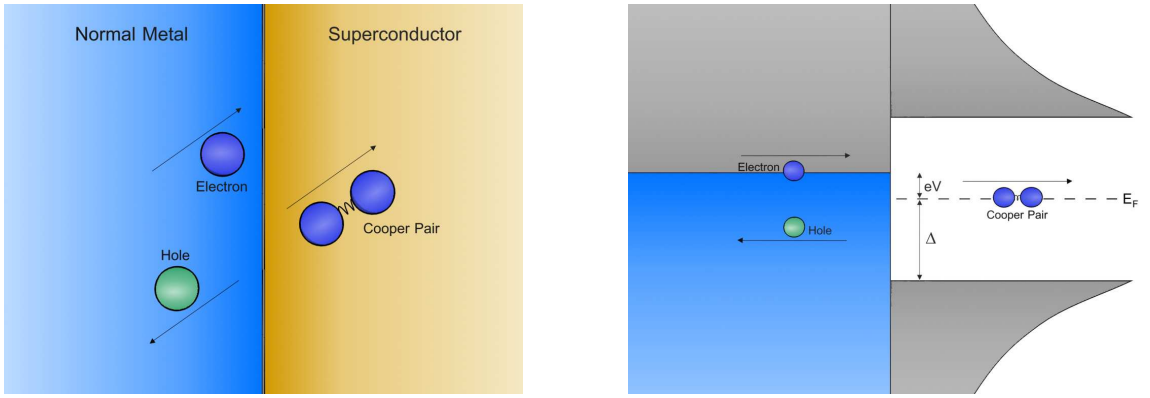


(a) (b)

Figure 21: The first panel shows the mechanism of Andreev reflection; when a normal electron is incident on a normal-superconductor interface, the superconductor is unable to reverse the momentum of the electron (normal reflection). Instead, a hole is retroreflected from the interface in order to conserve momentum (almost). The second panel describes how a Cooper pair is injected into the superconductor through the mechanism of Andreev reflection; by taking into account only the interaction on the normal side of the interface, neither charge nor energy are conserved. To account for the missing charge of 2e, as well as the difference in energy, a Cooper pair is created on the superconducting side of the interface.

the electron to occupy in the superconductor and thus it must be reflected. Furthermore, because the energy scale of the superconductor, $\Delta$, is very small when compared to the Fermi energy, the superconductor does not possess the necessary energy to reverse the momentum of the electron, as occurs during normal reflection [4]; instead, a new mechanism must be used which, at least approximately, conserves momentum. This new process was first detailed by Andreev [13] and is depicted schematically in Fig. 21. From the figure, when an electron whose energy is less than $\Delta$ impinges on a superconductor, the electron must retroreflect (Andreev reflect) as a hole with the opposite spin, thus conserving momentum to first order in $\Delta/E_F$ [219]. Moreover, in order to comply with conservation of charge, the missing charge of 2e which is created by the process of Andreev reflection appears as a Cooper pair on the superconducting side of the interface [23]; thus, charge transport is possible for energies less than $2\Delta$, which appears forbidden from the density of states of a superconductor. The second panel in Fig. 21 describes how Andreev reflection takes place with respect to energy; specifically, the incoming electron has an energy eV above the Fermi energy (but below $2\Delta$), and is Andreev reflected as a hole with energy eV below the Fermi energy. Thus, when the Cooper pair in the superconductor (which resides at the Fermi energy) is taken into account, energy is conserved during the Andreev reflection process. On a side note, an interesting analog to the Andreev reflection process exists in optics and is known as a phase conjugating mirror [185].

### 2.2.3 Probability of Andreev Reflection

With the process of Andreev reflection in place, the Bogoliubov-de Gennes formalism can be used to compute the probability of Andreev reflection at a NS interface; specifically, from the Bogoliubov-de Gennes equations, four quasiparticle solutions are expected for $E > \Delta$ which should reduce to normal electron and hole solutions (propagating in both directions) for large energies or $\Delta \to 0$. By inspection, the form of these solutions should be the following:

$$\psi_{e,\mathbf{k}} = \begin{pmatrix} u^e_{\mathbf{k}_e} \\ v^e_{\mathbf{k}_e} \end{pmatrix} e^{i\mathbf{k}_e \cdot \mathbf{x}}, \tag{57}$$

$$\psi_{h,\mathbf{k}} = \begin{pmatrix} u^h_{\mathbf{k}_h} \\ v^h_{\mathbf{k}_h} \end{pmatrix} e^{i\mathbf{k}_h \cdot \mathbf{x}}. \tag{58}$$

With this assumption, solving the Bogoliubov-de Gennes equations gives for the wave vectors:

$$k_e(E) = \frac{1}{\hbar}\sqrt{2m(\mu + sgn(E)\sqrt{E^2 - |\Delta|^2})}, \tag{59}$$

$$k_e(E) = \frac{1}{\hbar}\sqrt{2m(\mu - sgn(E)\sqrt{E^2 - |\Delta|^2})}. \tag{60}$$

Additionally, the components of the electron eigenvector satisfy the relation:

$$\frac{v_e}{u_e} = \frac{1}{|\Delta|e^{i\phi}}\left(E - sgn(E)\sqrt{E^2 - |\Delta|^2}\right), \tag{61}$$

whereas the components of the hole eigenvector satisfy:

$$\frac{v_h}{u_h} = \frac{1}{|\Delta|e^{i\phi}}\left(E + sgn(E)\sqrt{E^2 - |\Delta|^2}\right), \tag{62}$$

and are plotted in Fig. 22. From the figure, the eigenvectors are seen to reduce back to the normal electron or hole eigenvectors for large energies or a vanishing superconducting gap; more specifically, as the energy of the quasiparticle is increased, the fraction $v_e/u_e$ decreases towards zero. This implies that the hole coherence factor (i.e. the hole contribution to the quasiparticle) decays to zero. Additionally, the charge of these excitations varies continuously from zero at $E = \Delta$ to $E = \pm e$ for large energies, owing to the decreased mixing of electron and hole states as the energy rises.

The above analysis, which is valid for E> $\Delta$, changes considerably for E< $\Delta$ due to the addition of Andreev reflection. In addition to the extra processes which must be taken into account, Andreev reflection does not strictly conserve momentum, no longer making $\mathbf{k}$ a good quantum number. Instead, it is better to use energy as a variable and to introduce the probability of each of the four distinct processes which can occur at a NS interface:

- A(E): The probability that an incident particle will Andreev reflect from the interface
- B(E): The probability of normal reflection at the interface
- C(E): The probability of normal transmission through the NS interface

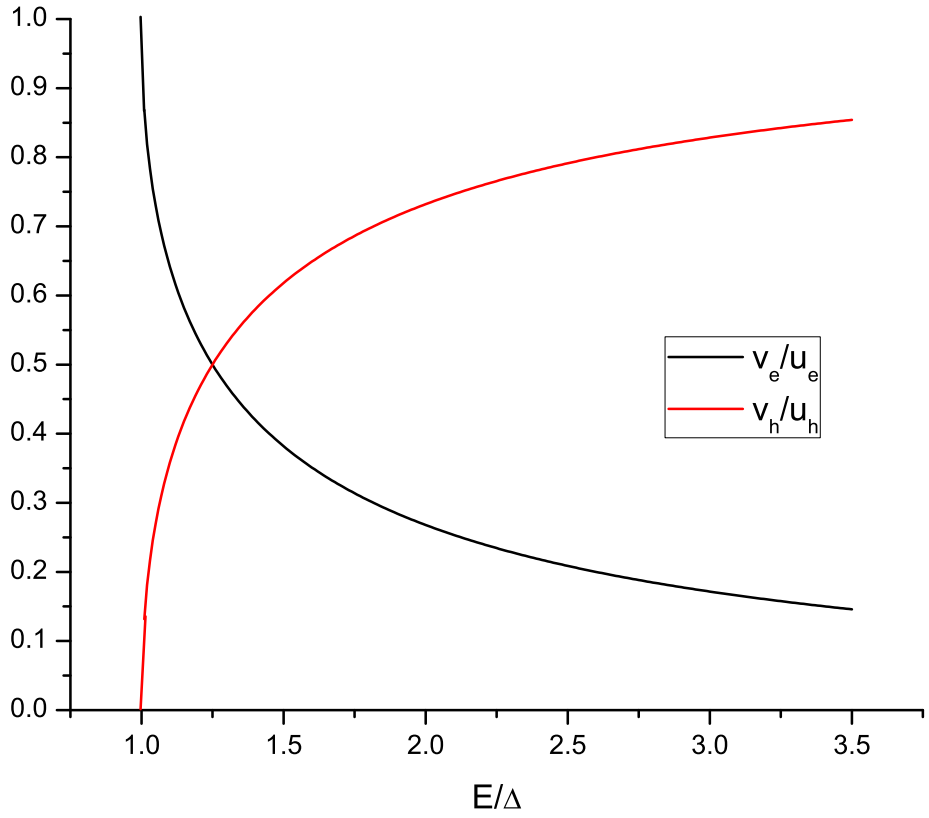


Figure 22: Plotted in the graph is the ratio of the two eigenvector components for both the electron-like and hole-like quasiparticles of the system; by looking at the asymptotic behavior of the curves we can see that for large energies, the quasiparticles reduce back to the standard electrons and holes of normally conducting systems.

- D(E): The probability of transmission and branch crossing[19] whereby the transmitted particle has its wave vector reversed upon transmission

Due to the nature of the density of states inside the superconductor, both C(E) and D(E) will be zero for energies less than the gap, as no states are available to the incoming electron. In addition, B(E) will be zero for energies less than the gap when no barrier is present (i.e. a clean NS interface cannot support normal reflection, a thin oxide layer or other barrier region must be present for the probability of normal reflection to be non-zero). Thus, if we assume a normal electron is incident on a clean interface with an energy less than the gap, we can write the expression:

$$\psi_N = \begin{pmatrix} 1 \\ 0 \end{pmatrix} e^{ik_e x} + A(E) \begin{pmatrix} 0 \\ 1 \end{pmatrix} e^{-k_h x} = \begin{pmatrix} u_e \\ v_e \end{pmatrix} e^{ik_e x}. \tag{63}$$

By solving this equation using standard techniques for transmission and reflection, the probability of Andreev reflection for a clean interface is given by:

$$A(E) = \begin{cases} \frac{1}{|\Delta|e^{i\phi}} \left( E - i\sqrt{|\Delta|^2 - E^2} \right) & \text{for } E < \Delta \\ \frac{1}{|\Delta|e^{i\phi}} \left( E - sgn(E)\sqrt{E^2 - |\Delta|^2} \right) & \text{for } E > \Delta \end{cases}$$

By separating the above expression for A(E) when the energy is less than the gap, one can see that it is unity for all energies up to the gap, and then decreases down to zero as the energy is further increased. To include the effects of a barrier region, the condition of U(x)=0 must be relaxed; this has been done [31, 174] for the situation depicted in Fig. 23 which adds a delta function barrier to each NS interface. By solving the semiclassical Boltzmann equation in the presence of these potential barriers, whose strength is parameterized by the quantity Z, general expressions for how each of the four quantities listed above (A,B,C,D) evolve with increasing barrier strength and energy can be calculated, the result of which is plotted for two different cases in Fig. 24. As expected, the effect of the barrier is to decrease the probability of Andreev reflection and enable normal reflection to occur. Additionally for large energies, the probability of Andreev reflection quickly decreases back to zero, thus reducing the physics back to the standard barrier problem.

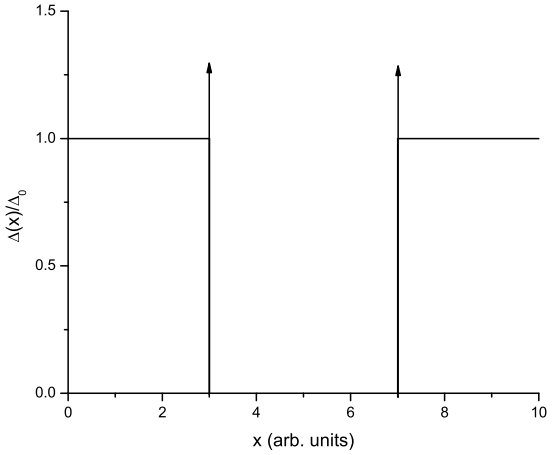


Figure 23: Here we see a more general SNS potential which includes a delta function potential at each interface; the additional barriers allow for normal reflection of quasiparticles at the NS interface. By explicitly including normal reflection in the system, a coupling exists between the two Andreev reflection processes (electron retroreflects into a hole and vice versa).

### 2.2.4 Andreev Bound States

In the above analysis for a SNS structure, no mention of the thickness of the normal region was made, though it does play an important role in determining the level of coupling between the two superconducting leads; specifically, if the normal region is too thick, no coherent effects will be observed because the two superconducting wave functions will be unable to overlap. Furthermore, if the region is too thin, the superconductors strongly couple and the effects due to the normal region are not observed (i.e. the superconducting wave functions significantly overlap, creating only a small change in the bulk value of $\Delta$); thus, to observe coherent effects through the structure while still preserving the additional phenomena due to the normal region, the weak coupling regime is ideal. For weak coupling to exist, the wave functions of the superconductors must slightly overlap, creating a large change in the gap parameter, as seen in the first panel of Fig. 25. However, due to the complexities involved in solving the fully self-consistent problem imposed by the addition of the proximity effect, two simplifications are typically used: the first is to neglect the proximity effect and the second is to employ the Landauer formalism to reduce the problem to that of a coherent quantum

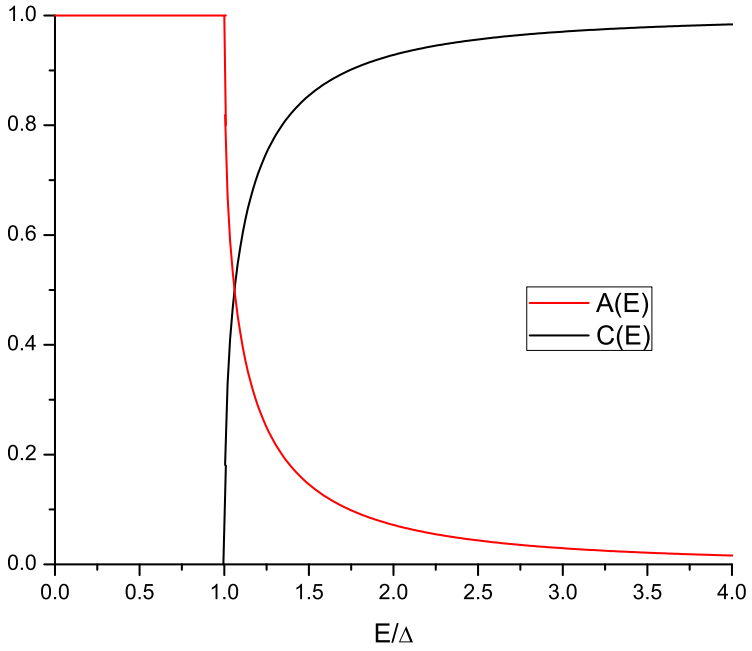


(a)

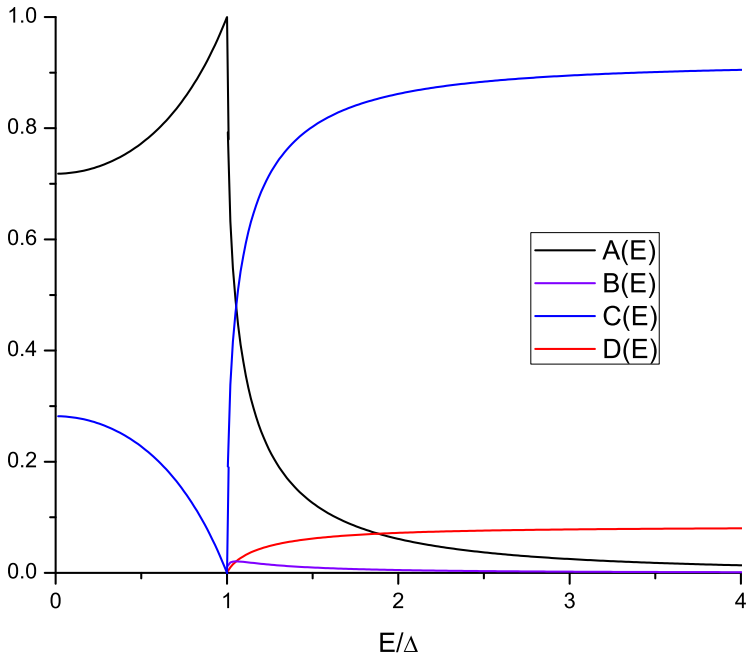


(b)

Figure 24: The first panel shows the probabilities of Andreev reflection (A) and normal transmission (B) for a clean interface; for energies inside the superconducting gap, Andreev reflection is the only possibility of the system, whereas above the gap, the probability of Andreev reflection decreases significantly. In the second panel, the barrier has a strength of Z=0.3 and the probabilities of transmission with branch crossing (C) and normal reflection (D) are taken into account. Clearly, the effect of the barrier is to suppress Andreev reflection in the system. However, the probability of the quasiparticle being Andreev reflected always increases for energies up to the gap (where it is always unity) and then decays rapidly as the more traditional processes take over, above the gap.

scattering problem. In making these approximations, the phenomenological transmission coefficient, $\tau$, is introduced which creates a much simpler problem to solve; however, the tradeoff is that the mesoscopic theory is unable to determine the transport properties of the system in terms of only material and geometrical parameters, as in a fully microscopic derivation. Furthermore, in reframing the problem of transport through a SNS device in terms of the Landauer formalism and conductance channels, the effect of Andreev reflection on the conductance channels must be carefully considered (i.e. does Andreev reflection causes channel mixing?). To this end, it has been shown [17, 40] that Andreev reflection does not cause channel mixing, thus the full power of the scattering approach (reduction of the problem to independent conduction channels) can be utilized. Under the simplification

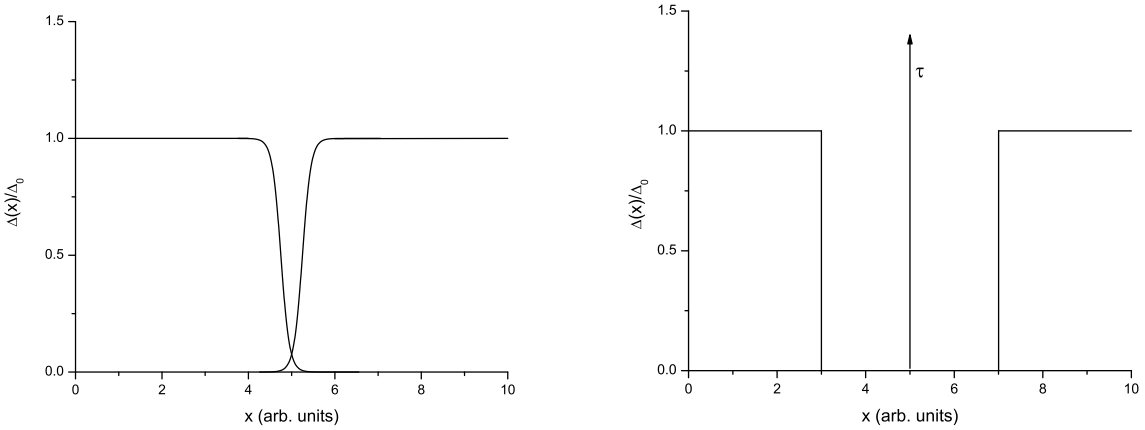


Figure 25: Shown in the first panel is a weakly coupled SNS structure which incorporates the proximity effect; because the normal region is thin compared to the amount of the superconducting wave function which leaks into the region, the two superconducting wave functions can overlap and create coherent physical effects. Due to the inherently mesoscopic nature of this structure, the Landauer scattering approach is well suited to model the system; in this case, the complexity of the first panel is replaced with the situation shown in the second panel.

that the proximity effect is neglected, the general problem of coherent scattering in a SNS device is schematically given by the second panel of Fig. 25; however, the assumption of a ballistic normal region (i.e. $\tau \to 1$) will be made initially and then subsequently relaxed. By assuming a ballistic normal region between the two superconducting leads, a right moving electron will be Andreev reflected with probability one as a hole moving to the left, creating

a Cooper pair in the right superconductor. When the hole reaches the left NS interface, it is again Andreev reflected back into an electron, equivalently destroying a Cooper pair in the left superconductor; this process will continue indefinitely, thereby creating a bound state in the normal region. This bound state will exist if and only if the phases acquired during the two Andreev reflections equal 0(mod $2\pi$); keeping in mind that the phase difference gained by Andreev reflection of a hole is the opposite of the phase gained by Andreev reflection of an electron. Specifically, this additional phase due to Andreev reflection of an electron is given by $arg[A(E,\phi_i)]$, where i represents either the left or right superconductor; for a hole which is Andreev reflected, the phase difference is $arg[A(E,-\phi_i)]$. Explicitly, this expression is given by:

$$arg[A(E,\phi_R)] = -\phi_R + \arctan\left(-\frac{\sqrt{|\Delta|^2 - E^2}}{E}\right), \tag{64}$$

and the expression for a hole which is Andreev reflected at the opposite side of the SNS structure is:

$$arg[A(E,\phi_L)] = \phi_L + \arctan\left(-\frac{\sqrt{|\Delta|^2 - E^2}}{E}\right). \tag{65}$$

Thus, the resonance condition for the existence of a bound state is:

$$\arctan\left(-\frac{\sqrt{|\Delta|^2 - E^2}}{E}\right) = \phi_R - \phi_L = \delta, \tag{66}$$

where we introduce the new quantity, $\delta$, which is the phase difference between the two sides of the SNS structure. Solving this equation for the energy,it is clear that two bound states exist in the normal region with energies given by:

$$E = \pm\Delta\cos\left(\frac{\delta}{2}\right). \tag{67}$$

Using this equation, the current through the device can also be calculated:

$$I_{\pm}(\delta) = \frac{1}{\phi_0}\frac{\partial E}{\partial \delta} = \pm\frac{e\Delta}{\hbar}\sin\left(\frac{\delta}{2}\right), \tag{68}$$

where $\phi_0$ is the flux quantum, $\phi_0 = \hbar/2e$; thus, the two current carrying states (Andreev bound states [81, 131]) in the normal region carry an equal magnitude of current in opposite directions, as depicted in Fig. 26. This analysis for a ballistic normal region can be extended

to regions with arbitrary transmission coefficient using the Landauer formalism; however, a major complication to this generalization is that the two Andreev bound states will be coupled due to the possibility of normal reflection at a NS interface for $\tau < 1$. This coupling manifests primarily as an energy gap which opens at $\delta = \pi/2$, which can be seen from the full expression for the energy of an Andreev bound state:

$$E_{\pm}(\delta) = \pm\Delta\sqrt{1 - \tau\sin^2\left(\frac{\delta}{2}\right)}, \tag{69}$$

which reduces to the ballistic case derived above for $\tau = 1$. Using this expression, the current through the device is now given by [21]:

$$I_{\pm}(\delta) = \pm\frac{\tau e\Delta}{2\hbar}\frac{\sin(\delta)}{\sqrt{1 - \tau\sin^2\left(\frac{\delta}{2}\right)}}, \tag{70}$$

and is plotted along with the energy in Fig. 27 for three different transmission coefficients. Clearly, as the transmission decreases, an ever larger energy gap is created between the two bound states. This analysis can be further generalized to include non-zero temperatures, the result of which is [153, 14, 22, 95]:

$$I_{\pm}(\delta) = \pm\frac{\tau e\Delta}{2\hbar}\frac{\sin(\delta)}{\sqrt{1 - \tau\sin^2\left(\frac{\delta}{2}\right)}}\tanh\left(\frac{E}{2k_BT}\right), \tag{71}$$

giving a maximum, sustainable supercurrent of [239]:

$$I_{max}(\tau) = \frac{e\Delta}{\hbar}(1 - \sqrt{1 - \tau}). \tag{72}$$

With a general expression for the current calculated for a single conductance channel, the total current is found by summing this general result over all conductance channels; thus, the set of transmission coefficients (i.e. the mesoscopic PIN code) fully characterizes the transport through the device.

On a side note, the importance of Andreev reflection goes well beyond its role in charge transport through coherent structures; in fact, the coupling of electron and hole dynamics, which is mediated by Andreev reflection, is responsible for many of the distinct phenomena of superconductivity. Exemplifying the role of Andreev reflection in superconductors is the proximity effect [64], by which normal materials in close contact with a superconductor

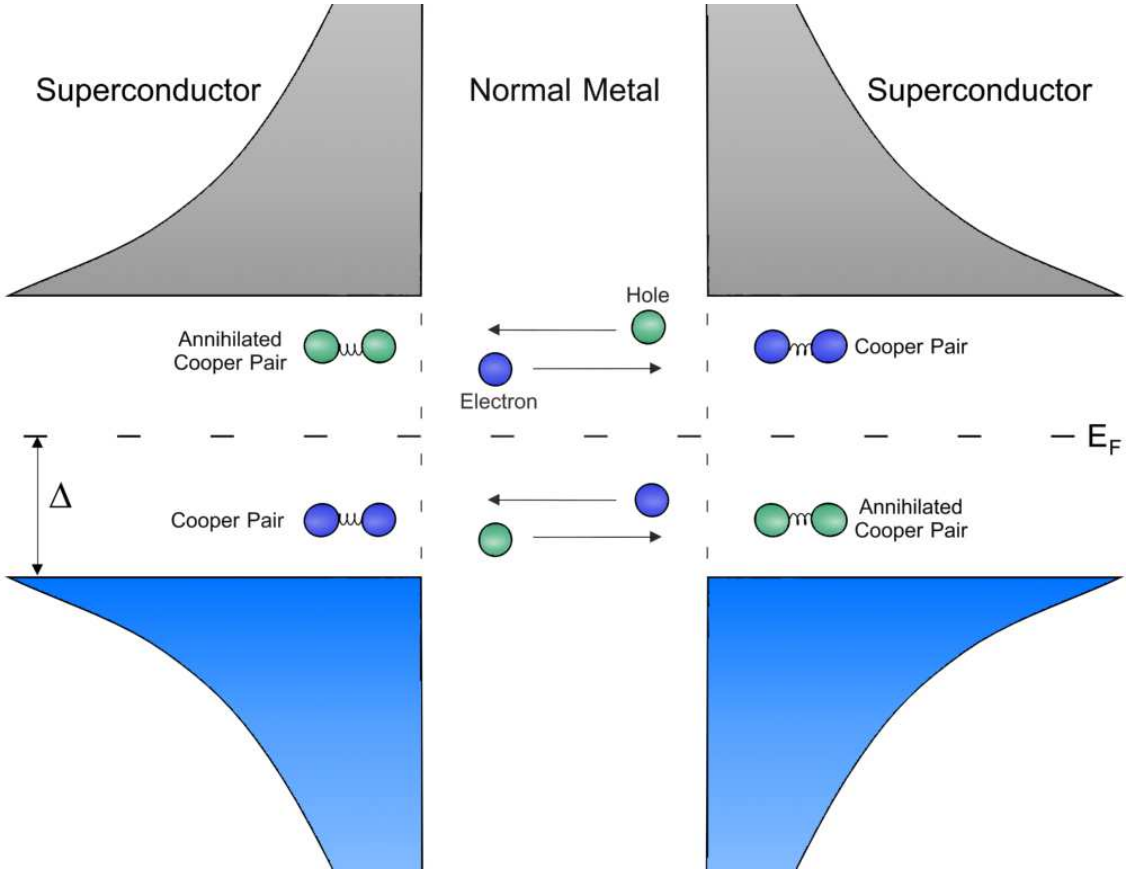


Figure 26: Shown schematically in the figure are the two Andreev bound states of the SNS structure; supercurrent is able to flow across the weakly coupled SNS structure by using successive Andreev reflections in the normal region. A net supercurrent will flow only when there is an imbalance in the population of these two states.

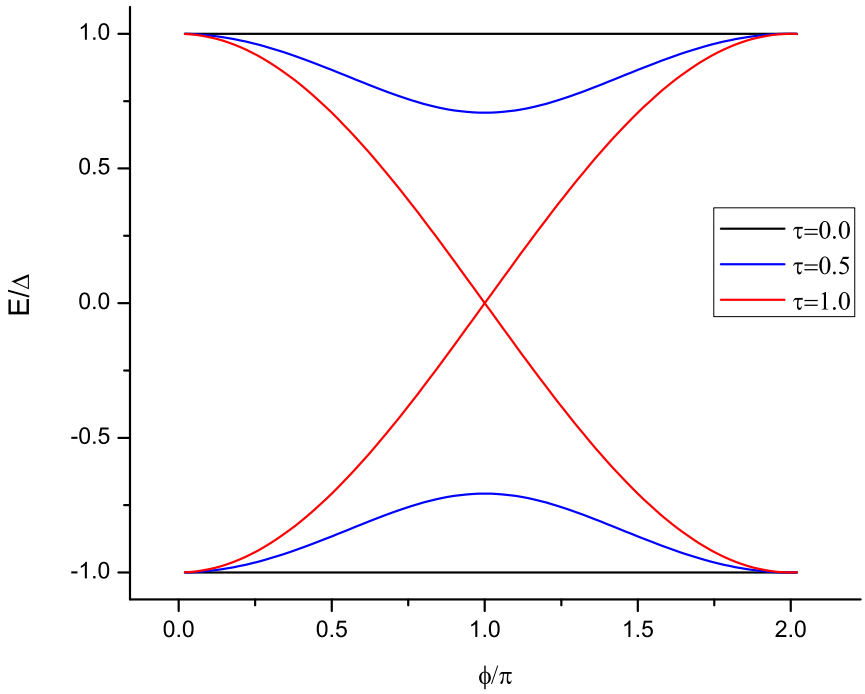


(a)

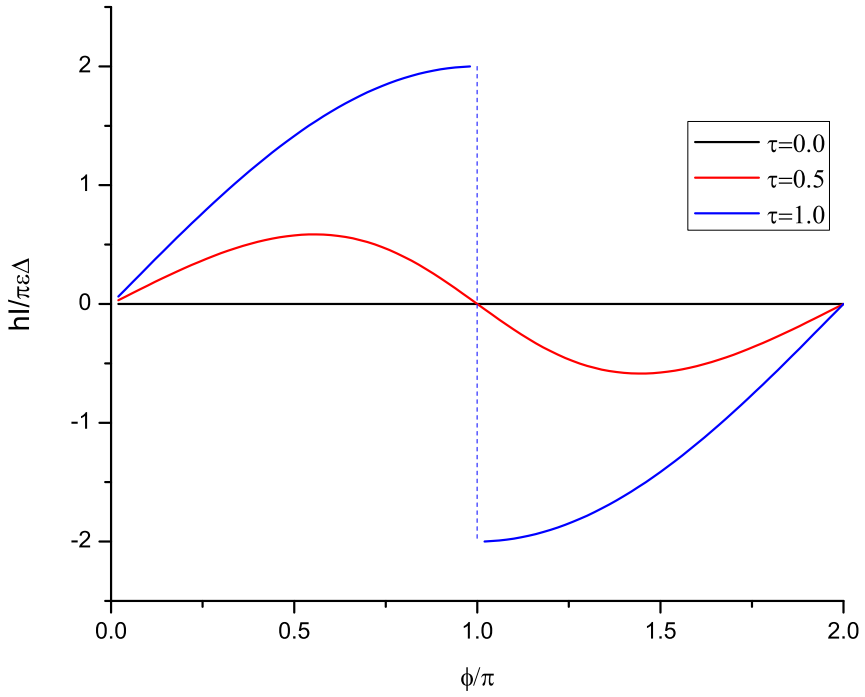


(b)

Figure 27: The first panel shows the energy of the two Andreev bound states as a function of the phase difference across the structure for three different transmission coefficients; clearly, the barrier creates an energy gap between the two states which widens as the transmission decreases. The second panel shows the resulting Andreev supercurrent for the same three transmission coefficients, which is $2\pi$ periodic with respect to the superconducting phase difference.

exhibit superconducting behavior over a certain penetration depth; in fact, it has been established in recent years that the proximity effect and Andreev reflection are one in the same phenomena [181]. More specifically, the process of Andreev reflecting a normal particle at a NS interface creates a correlated electron-hole pair (specifically, a phase conjugated pair), which maintains phase coherence for some distance into the normal metal [121]; this length is determined by inelastic scattering and other processes which destroy phase coherence between particles.

### 2.2.5 Multiple Andreev Reflection

The previous section focused solely on Andreev reflection and the calculation of current through a SNS structure from the point of view of phase biasing (i.e. setting of the superconducting phase on both sides of the SNS structure); though phase biasing is an important transport regime for devices such as SQUIDs, a more conventional way to bias the device is by voltage. However, when the normal region has an applied potential, the Andreev bound states which appear in the phase biased case no longer exist due to inelastic scattering in the normal region, though current does still flow through the structure. In fact, brand new phenomena are seen for voltage biased SNS devices [6, 214]; specifically, new and highly nonlinear features emerge on the I-V curve at voltages below $2\Delta/e$. These features manifest as a series of peaks in the differential conductance curve for small biases and have become known as the subgap structure for the device. To explain this phenomena of subgap structure for voltage biased SNS devices, theorists initially used a perturbative approach, known as multi-particle tunneling theory [201], which was able to calculate the current to second order in the tunneling Hamiltonian. However, only one of the peaks in the differential conductance curve appeared and only at the cost of a diverging current for $eV = 2\Delta$. Thus, the other peaks in the differential conductance must come from higher order processes which the second order calculation ignored; as such, in order to obtain the full structure of the I-V curve, the current must be calculated to all orders in the perturbation. This calculation was first done by Klapwijk et al. [122] and later generalized by Octavio et al. [174]; the physical mechanism underlying these two papers is known as multiple Andreev reflection(MAR),

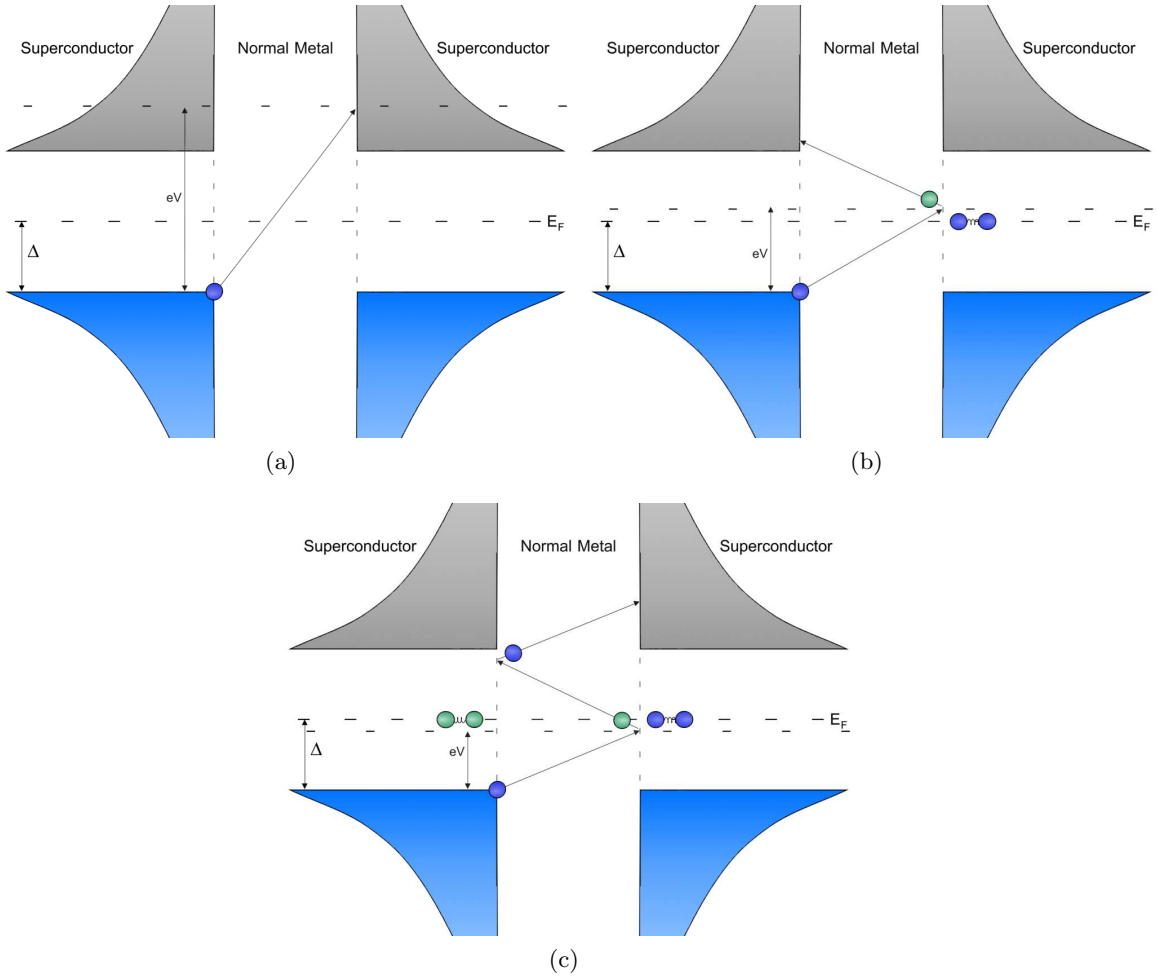


Figure 28: The first panel describes the situation where the applied voltage is large enough for an electron to pass through the structure to a state on the other side of the junction, whereas the second panel shows what happens when the energy of the particle satisfies $\Delta < eV < 2\Delta$). In this case, an electron is Andreev reflected inside of the normal region, creating a Cooper pair inside of the second superconductor; the resulting hole which is generated from the Andreev reflection continues to gain energy as it crosses back across the normal region, where it is absorbed in the first superconductor. The last panel shows the next highest order process of multiple Andreev reflection where it takes two successive Andreev reflections for the single particle to gain enough energy to overcome the gap in the density of states.

which is depicted in Fig. 28. During the MAR process, an electron initially gains energy as it travels through the normal region; upon Andreev reflection at the NS interface, the newly created hole also gains energy from the voltage bias as it travels in the opposite direction. Once the hole reaches the opposite NS interface, it can either be absorbed into the superconductor, if its energy is sufficient, or it will be Andreev reflected once again. This type of ladder process enables an incoming electron whose energy is initially less than the gap to be Andreev reflected multiple times, gaining an energy of eV for every reflection, until its energy is above the gap and thus can be absorbed by the superconductor, as seen in Fig. 28. In the first panel of the figure, a voltage bias is placed across the normal metal which is sufficient for the electron to be directly transmitted across the device (i.e. $eV \geq 2\Delta$); in the second panel, the electron does not have enough energy initially to be transmitted through the device, so it is Andreev reflected at the first interface. Upon reflection, the newly created hole continues to gain energy until it reaches the left interface where it can be absorbed if $eV \geq \Delta$; in the third panel, the incoming electron must be Andreev reflected twice before it has gained enough energy to be transmitted (i.e. $eV \geq 2\Delta/3$). This type of process can continue to all orders, with the n$^{th}$ order process creating a contribution to the IV curve beginning at a voltage of $eV = 2\Delta/n$. This multiple threshold behavior explains the series of peaks of the subgap structure, with each peak corresponding to the activation of a new Andreev process. However, if the normal metal has a transmission coefficient less than unity, each crossing of the normal region carries with it a probability of normal reflection, 1-$\tau$, due to scattering events. As such, for a n$^{th}$ order process, the particle must successfully traverse the normal region n times and thus has a probability of occurrence which goes as $\tau^n$.

Following the early theoretical work which focused on semi-classical approaches to the subgap structure, researchers began to develop a greater understanding of the problem by creating a fully quantum mechanical framework of transport through SNS structures and Andreev reflection. For example, in the small bias regime, transport is considered due to a population imbalance between the two Andreev bound states of the phase biased case [17]. Additionally, as the voltage is increased, the Andreev bound state picture does not

completely break down; instead, transport is modeled as the two Andreev bound states being connected via Landau-Zener transitions [51].

### 2.2.6 The Josephson Effect

Previously, it was shown (equation (45)) that the wave function of an isolated superconductor is simply a complex constant with a phase given by $\phi$; in addition, equation (70) demonstrated that the phase difference, $\delta$, across a SNS device provided a driving mechanism for the flow of supercurrent. In fact, this phenomenon of a phase biased current is a general feature of weak superconductivity (different examples of which are shown in Fig. 29), where weak implies that the phase on each side of the structure is well defined though the wave functions of the two sides do overlap. The first panel shows the familiar SNS structure which was analyzed in the previous chapter, the second shows a SIS structure which incorporates a thin insulating layer as the weak link; the third is of a Dayem bridge [61] which exploits a narrow constriction on the order of the coherence length to quench superconductivity locally, and the last example is relevant to the high $T_c$ superconductors, which uses a grain boundary as the weak link. These are only a few examples of the plethora of different weak link structures which researchers have discovered [143]; in fact, even more exotic weak links have been discovered in systems such as superfluids [16] and Bose-Einstein condensates [195].

Historically, the transfer of supercurrent across a weak link was first discovered in SIS junctions theoretically by Josephson [113] in 1962 and later confirmed experimentally by Anderson and Rowell [12]. By examining SIS junctions, Josephson was able to straightforwardly calculate the current through the device since the barrier created by the insulating layer inhibited Andreev reflection; in fact, the only transport mechanism which Josephson considered was Cooper pair tunneling across the barrier region, implying that only the ground state of each superconductor need be considered. To begin the analysis of the SIS junction, a method [76] due to Feynman will be used which is simpler than Josephson's original work [114]; as in most quantum mechanical problems, the starting place is the time

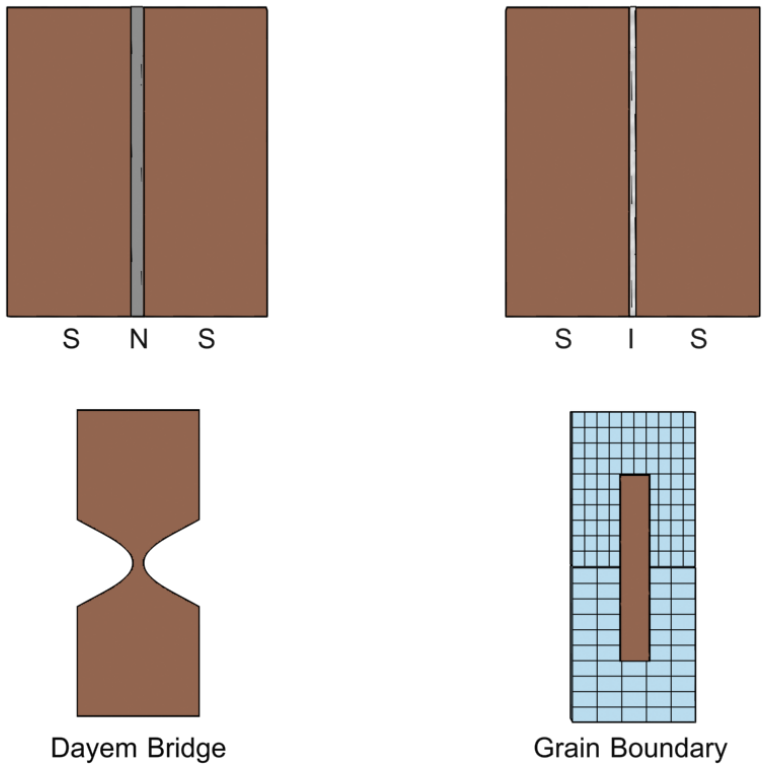


Figure 29: (a): SNS weak link created by bridging two superconducting electrodes with a normal metal. (b): SIS weak link which substitutes the normal metal of the SNS structure with a thin insulating layer; it is this type of junction which Josephson first considered. (c): A Dayem bridge utilizes a narrow constriction to create a weak link; if the width of the region is less than the coherence length of the superconductor, then the region itself will not be superconducting, thereby creating a weak link. (d): For high temperature superconductors made of cuprates, a common technique for creating Josephson junctions is to exploit a grain boundary of the material.

dependent Schrödinger equation [196]:

$$i\hbar\frac{\partial\psi}{\partial t} = E\psi, \tag{73}$$

with the wave function of an isolated superconductor being given by, $\psi = |\psi|e^{i\phi} = \rho_s^{\frac{1}{2}}e^{i\phi}$ where $\rho_s$ is the density of Cooper pairs. However, due to the presumed overlap of the two isolated wave functions, we must modify the above equation to include a leakage term; this results in the two following equations (one for each side of the device):

$$i\hbar\frac{\partial\psi_L}{\partial t} = E\psi_L + K\psi_R, \tag{74}$$

$$i\hbar\frac{\partial\psi_R}{\partial t} = E\psi_R + K\psi_L, \tag{75}$$

where L,R refer to the left and right side of the device respectively and K is a coupling constant which quantifies the strength of the overlap of the two wave functions. Further, it is assumed that $E_L$=$E_R$ for $K = 0$ (i.e. identical superconductors) and that the junction is voltage biased $E_L - E_R = -2eV$, where the factor of two accounts for the effects of pair tunneling. If the zero of energy is taken to be halfway between $E_L$ and $E_R$, then the applied voltage will be split evenly between the two sides of the device, resulting in the equations:

$$i\hbar\frac{\partial\psi_L}{\partial t} = eV\psi_L + K\psi_R, \tag{76}$$

$$i\hbar\frac{\partial\psi_R}{\partial t} = -eV\psi_R + K\psi_L. \tag{77}$$

Now, if the wave function of the superconductors is inserted into these equations and the real and imaginary parts are equated, the following four equations result:

$$\frac{\partial\phi_R}{\partial t} = -\frac{K}{\hbar}\left(\frac{\rho_L}{\rho_R}\right)^{\frac{1}{2}}\cos(\delta) + \frac{eV}{\hbar}, \tag{78}$$

$$\frac{\partial\phi_L}{\partial t} = -\frac{K}{\hbar}\left(\frac{\rho_R}{\rho_L}\right)^{\frac{1}{2}}\cos(\delta) - \frac{eV}{\hbar}, \tag{79}$$

$$\frac{\partial\rho_R}{\partial t} = -\frac{2K}{\hbar}(\rho_L\rho_R)^{\frac{1}{2}}\sin(\delta), \tag{80}$$

$$\frac{\partial\rho_L}{\partial t} = \frac{2K}{\hbar}(\rho_L\rho_R)^{\frac{1}{2}}\sin(\delta). \tag{81}$$

From the last two equations, an expression for the current density through the SIS structure is found:

$$J = -2e\frac{\partial\rho_L}{\partial t} = -2e\frac{\partial\rho_R}{\partial t} = \frac{4Ke}{\hbar}(\rho_L\rho_R)^{\frac{1}{2}}\sin(\delta), \tag{82}$$

In most cases, the constants in front are combined into one term, making the current density simply:

$$J = J_0 \sin(\delta), \tag{83}$$

which is known as the first Josephson relation or the DC Josephson effect. This expression predicts that in the absence of an applied voltage, a supercurrent can still flow from one side to the other; in fact, the flow of supercurrent is governed solely by the phase difference across the structure. This is not surprising since current which flows under an applied bias voltage is inherently dissipative by nature, whereas supercurrent is dissipationless by definition. However, in addition to phase gradients, the magnetic vector potential, **A**, can also induce supercurrent to flow, as seen by the Ginzburg-Landau equations [90, 227]. One of the most important consequences of the DC Josephson effect is the existence of a maximum supercurrent density, $J_0$, which is given by the material and geometrical properties of the junction. In addition to the DC Josephson effect, there also exists an AC Josephson effect which can be obtained by subtracting the last two equations above:

$$\frac{\partial \delta}{\partial t} = \frac{\partial}{\partial t}(\phi_R - \phi_L) = \omega_J = \frac{2e}{\hbar}V, \tag{84}$$

where $\omega_J = 483 MHz/mV$ and is known as the Josephson frequency; the AC Josephson effect implies that in response to an applied voltage, the phase difference of the junction oscillates at the Josephson frequency. Furthermore, since the phase difference of the junction mediates supercurrent through the device, the effect of applying a DC voltage is to create an AC supercurrent. Additionally, the application of an AC voltage to the junction, $V = V_0 + V_s \cos(\omega_s t)$, results in the following current:

$$I = I_c \sin\left(\frac{2eV}{\hbar}t + \frac{2eV_s}{\hbar\omega_s}\sin(\omega_s t) + \phi_0\right), \tag{85}$$

where $\phi_0$ is a constant of integration. By using both standard trigonometric and Bessel function identities [32], this expression can be cast into a more useful form:

$$I = I_c \sum_{n=-\infty}^{n=\infty} (-1)^n J_n\left(\frac{2eV_s}{\hbar\omega_s}\right) \sin[\phi_0 + (\omega_J - n\omega_s)t], \tag{86}$$

where $J_n$ is the $n^{th}$ order Bessel function of the first kind. The key factor of this expression is that the time dependence of the $n^{th}$ term of the summation will be zero if $\omega_J - n\omega_s$, thus

adding an additional DC component to the current; as such, a step feature will be created on the DC I-V curve which is known as a Shapiro step [202].

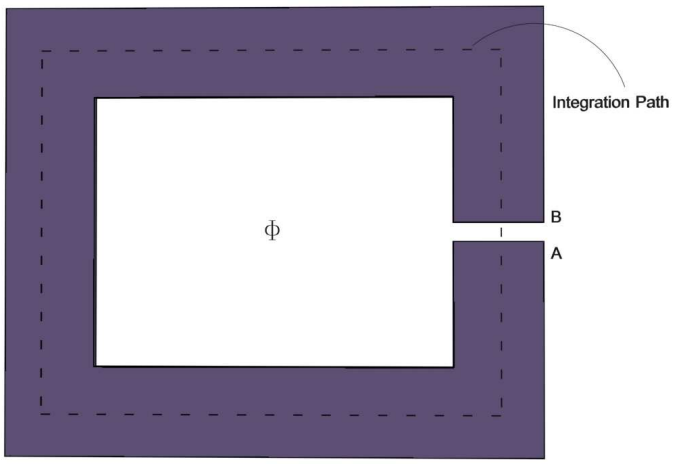


Figure 30: Flux quantization in a superconductor. Given here is a superconducting loop which is weakly broken in one section, creating a coherent phase difference between the two sides of the junction; in addition, a magnetic flux, $\Phi$, penetrates the loop.

In addition to Shapiro steps, Josephson junctions also exhibit interesting phenomena when a magnetic field is applied perpendicular to the superconducting loop, as shown in Fig. 30. However, before solving the problem of a Josephson junction in a magnetic field, it is instructive to begin with a closed superconducting loop in a magnetic field; in the figure, this would correspond to extending the loop such that A=B. To begin, consider the classical canonical momentum of a particle:

$$\mathbf{p} = m^*\mathbf{v} + e^*\mathbf{A}, \tag{87}$$

where the asterisks denote effective quantities and $\mathbf{A}$ is the magnetic vector potential. Next, by using the quantum mechanical formula for momentum, $\mathbf{p} = -i\hbar\nabla$, and the expression for the superconducting wave function given previously, this formula for the momentum becomes:

$$\mathbf{p} = \hbar\nabla\phi = m^*v + e^*\mathbf{A}, \tag{88}$$

where $\phi$ is the phase of the superconducting wave function. Taking this formula and inserting the expression for the parameter $\Lambda$ given previously, the equation becomes:

$$\mathbf{p} = \hbar\nabla\phi = e^*\Lambda\mathbf{J} + e^*\mathbf{A}, \tag{89}$$

where $\mathbf{J}$ is the superconducting current density. Now, if this equation is integrated over the path shown in Fig. 30, the result is:

$$\hbar \oint \nabla\phi \cdot \mathbf{dl} = e^* \oint (\Lambda\mathbf{J} + \mathbf{A}) \cdot \mathbf{dl}. \tag{90}$$

However, the expression can be simplified since the integration path is taken deep inside the superconductor which means that the current density is zero. Furthermore, the second term on the right hand side can be expressed as:

$$e^* \oint \mathbf{A} \cdot \mathbf{dl} = e \int_S (\nabla \times \mathbf{A}) dS = e^* \int_S \mathbf{B} \cdot \mathbf{dS} = e^*\Phi, \tag{91}$$

where $\Phi$ is the total flux enclosed by the superconducting loop. Lastly, the line integral on the left hand side is simply $2n\pi$ since it is a closed loop and the phase difference must be single-valued. Combining these simplifications together gives:

$$\Phi = \frac{nh}{2e}, \tag{92}$$

where the effective charge was replaced with 2e due to the effect of Cooper pairs. This equation shows that magnetic flux is quantized in a superconducting loop to be an integer value of $\Phi_0 = h/2e = 2.07 \cdot 10^{-15}$Wb.

This analysis can be easily extended to Josephson junctions where there exists a phase difference between the two sides of the junction. To do this, the phase difference must undergo a transformation in order to make the quantity gauge-invariant; the result is that the phase difference across a Josephson junction in a magnetic field is given by:

$$\delta = 2n\pi - \frac{2\pi\Phi}{\Phi_0}. \tag{93}$$

Since it is the phase difference across the junction which determines the current, this equation shows that the effect of a magnetic field on a Josephson junction is to modulate the current. It is this principle which is exploited in DC and RF SQUIDs to detect extremely weak magnetic fields.

### 2.2.7 Connection with Andreev Bound States

In the last section, the current through a tunnel junction (i.e. SIS structure) was considered and by using a simple phenomenological argument, shown to be given as $I = I_c \sin(\delta)$; however, this result is readily obtained from the analysis given in the last chapter on current through mesoscopic SNS structures. Indeed, in taking the limit of $\tau \to 0$ in equation (71), which is consistent with the transmission of a tunnel junction, the current through a single channel is found to be:

$$I = \frac{e\tau\Delta}{2\hbar} \sin(\delta) = I_c \sin(\delta), \tag{94}$$

which is the DC Josephson effect. From this result, the dependence of the critical current through the junction on the gap is seen, which is not present in the analysis due to Feynman. However, the mesoscopic derivation still includes the phenomenological parameter, $\tau$, instead of the full dependencies on material and geometrical parameters. As such, there is a need for a fully microscopic derivation of the DC Josephson effect, which has been done [11] and yields the result:

$$I(\delta, T) = \frac{\pi\Delta(T)}{2eR_N} \sin(\delta) \tanh\left(\frac{\Delta(T)}{k_B T}\right), \tag{95}$$

where $R_N$ is the normal state resistance of the junction; this is known as the Ambegaokar-Baratoff relation which is in agreement with the mesoscopic derivation given in the last chapter for a general transparency junction.

This connection between the Josephson effect for a SIS junction and the theory of mesoscopic superconductivity hint at the possibility of the Josephson effect being a manifestation of mesoscopic superconductivity (i.e. conduction channels and Andreev bound states); indeed, it turns out that through the formalism of mesoscopic superconductivity a unifying framework [103] exists which is capable of treating the Josephson effect in all types of coherent coupling structures. From this perspective, the Josephson effect is mediated by the two Andreev bound states which couple the two sides of the structure. Furthermore, since each bound state carries current in the opposite direction, a non-zero net current is created through an imbalance of the population of these two states.

## 2.3 Magnetic Properties of Superconductors

### 2.3.1 Ginzburg-Landau Theory

During the discussion of the BCS theory of superconductivity, the wave function of the condensate was assumed to be of the form:

$$\psi(\mathbf{r}) = |\psi(\mathbf{r})|e^{i\Delta(\mathbf{r})}, \tag{96}$$

where $|\psi(\mathbf{r})|$ denotes the density of Cooper pairs and was assumed to be spatially invariant in the development of the BCS theory, as was $\Delta(\mathbf{r})$; however, the Bogoliubov-de Gennes formalism relaxed this restriction on the gap parameter, allowing for the calculation of the currents through SNS structures. In order to relax the constraint of spatial invariance on the density of Cooper pairs, as well as add the effects of magnetic fields on superconductors, the previously mentioned Ginzburg-Laudau (GL) theory can be applied. From the GL theory, it is discovered that more complex and interesting states exist besides the normal and Meissner states which have been covered previously and are pictured in Fig. 31.

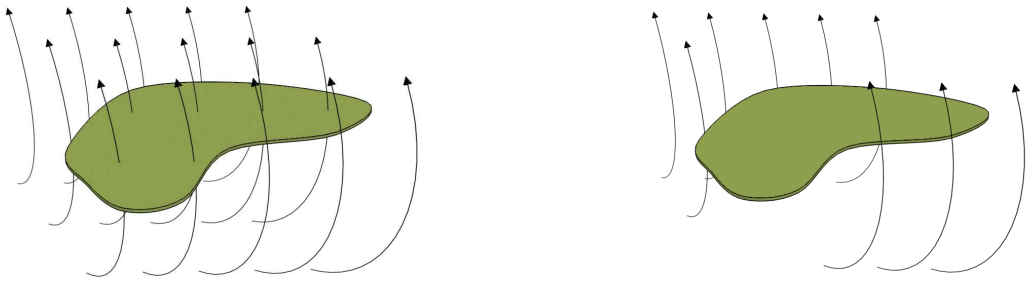

(a) (b)

Figure 31: (a): For a normal metal, the extent to which magnetic flux is capable of penetrating the material is determined by the material's relative permeability, $\mu_r$, which can range over many orders of magnitude. (b): On the other hand, superconductors have a relative permeability of exactly zero, implying that magnetic flux is unable to penetrate the material.

In the GL theory, an order parameter is postulated which is able to quantify the amount of Cooper pair condensation in a superconductor; this quantity is unlike order parameters needed to describe the spatial order of atoms or the spin alignment of a ferromagnet in

that the superconducting order parameter must be considered a complex quantity. For a uniform system in the absence of a magnetic field, this order parameter is simply the gap parameter, $\Delta$, which is also known as the pair potential in the literature; more generally, the order parameter is taken to be $\psi(\mathbf{r})$ itself, which is intuitive in that the absence of Cooper pairs implies that the material is normal.

To arrive at the GL differential equations which describe the variation of the Cooper pair density with magnetic fields, the standard approach is to set up the Gibbs free energy in terms of the order parameter and then subsequently minimize the resulting functional to obtain the necessary equations. To begin, the Gibbs free energy per unit volume, g, can be written as:

$$g = f - b(\mathbf{r})H \tag{97}$$

where f is the Helmholtz free energy per unit volume, b($\mathbf{r}$) is the magnetic flux density, and H is the magnetic field. Upon calculating the Helmholtz free energy for the system [227], the Gibbs free energy functional can be written as:

$$g_s = g_{n,0} + \nabla f(|\psi|^2) + \frac{1}{2m^*}|(i\hbar\nabla + e^*\mathbf{A})\psi|^2 + \frac{b^2}{2\mu_0} - bH, \tag{98}$$

where the asterisk denotes effective quantities and $g_{n,0}$ refers to the Gibbs free energy per unit volume for a normal material. Upon assuming that the free energy functional can be expanded as a power series in $|\psi|^2$ and that only the first two terms of the series need be considered, the above equation can be rewritten in the following form:

$$\Delta g(|\psi|^2) = g_s - g_{n,0} = \alpha(T)|\psi|^2 + \frac{1}{2}\beta(T)|\psi|^4, \tag{99}$$

where the two new parameters, $\alpha(T)$ and $\beta(T)$ can be expressed as:

$$\alpha(T) = \frac{\mu_0 H_c^2(T)}{|\psi_0(T)|^2}, \tag{100}$$

$$\beta(T) = \frac{\mu_0 H_c^2(T)}{|\psi_0(T)|^4}, \tag{101}$$

where $\psi_0$ refers to the equilibrium value of the order parameter. With these definitions in place, the energy function can be minimized with respect to both the magnetic vector

potential and the order parameter given the GL differential equations:

$$-\mathbf{J}_s = \frac{ie^*\hbar}{2m^*}(\psi^*\nabla\psi - \psi\nabla\psi^*) + \frac{e^{*2}}{m^*}|\psi|^*\mathbf{A}, \tag{102}$$

$$\alpha(T)\psi + \beta(T)|\psi|^2\psi + \frac{1}{2m^*}(i\hbar\nabla + e^*\mathbf{A})^2\psi = 0. \tag{103}$$

Upon normalizing these equations, a new length scale is introduced, $\xi_{GL}$ which is defined as:

$$\xi_{GL} = \frac{\hbar}{|2m^*\alpha(T)|^{\frac{1}{2}}}, \tag{104}$$

and signifies the smallest distance over which the order parameter can change significantly; it should be noted that this coherence length is separate from the BCS coherence length or the mean free path of the material, though they are related. In addition to this length scale, a separate length scale exists which is termed the penetration depth, $\lambda(T)$, and is given by:

$$\lambda(T) = \sqrt{\frac{m^*}{\mu_0 e^{*2}|\psi_0|^2}}, \tag{105}$$

and is the characteristic length over which a magnetic field is screened inside of a superconductor. In the GL theory, as well as superconductivity in general, a quantity of imminent importance is the ratio between these two length scales; this quantity is simply termed the GL parameter, $\kappa$, and is:

$$\kappa = \frac{\lambda(T)}{\xi_{GL}(T)}, \tag{106}$$

The GL parameter is very important in the theory of superconductivity because it distinguishes two different types of superconductors: type I superconductors satisfy the relation, $\xi_{GL} < 1/\sqrt{2}$, while type II superconductors satisfy $\xi_{GL} > 1/\sqrt{2}$. Up to this point, the discussion has primarily been on type I superconductors whose defining property is the complete expulsion of magnetic flux up to a certain critical field, $H_c$; above this field, the superconductor is unable to counter the rising magnetic field and it is energetically favorable to allow flux to enter. In contrast, type II superconductors expel flux completely up to a certain field, $H_{c1}$; above this value, there exists a mixed state where flux is able to partially penetrate the superconductor. Only at a higher field, $H_{c2}$, is flux able to fully thread the superconductor.

### 2.3.2 Type II Superconductors

To see this more clearly, if it is assumed that the applied field is close to $H_{c2}$, the order parameter will be very close to zero; as such, higher order terms in the GL equations can be neglected. In this case, the second GL equation becomes:

$$\frac{1}{2m}(-i\hbar\nabla - 2e\mathbf{A})^2\psi = -\alpha\psi, \tag{107}$$

where the effective quantities are replaced with the actual values for a Cooper pair and the temperature is assumed to be constant, meaning that $\alpha(T)$ may be replaced with $\alpha$. This equation is a Schrödinger equation for a particle in a magnetic field with energy eigenvalue $\alpha$. The resulting energy can be written as:

$$E_{n,v_z} = \frac{1}{2m}mv_z^2 + \left(n + \frac{1}{2}\right)\hbar\omega_c, \tag{108}$$

where $v_z$ is the velocity of the particle parallel to the applied field and unaffected by it, and the second term is due to cyclotron motion of the particle in the plane perpendicular to the field. Neglecting the velocity term since it is independent of the magnetic field, the lowest energy eigenvalue is given by:

$$-\alpha = \frac{1}{2}\hbar\frac{2eB}{m} = \hbar\omega_c, \tag{109}$$

where $\omega_c$ is the cyclotron frequency. Because this analysis is only valid for fields near $B_{c2}$, the above expression can be rewritten as:

$$-\alpha = \frac{\hbar eB_{c2}}{m}. \tag{110}$$

From GL theory, it is known that the following two relations exist:

$$\frac{\alpha^2}{2\beta^2} = \frac{B_c^2}{2\mu_0}, \tag{111}$$

$$\beta = \frac{(4e^2)^2\mu_0^3 H_c^2\lambda^4}{m^2}. \tag{112}$$

Thus, using these two relations, the expression for the upper critical field, $B_{c2}$ can be simplified to:

$$B_{c2} = \kappa\sqrt{2}B_c, \tag{113}$$

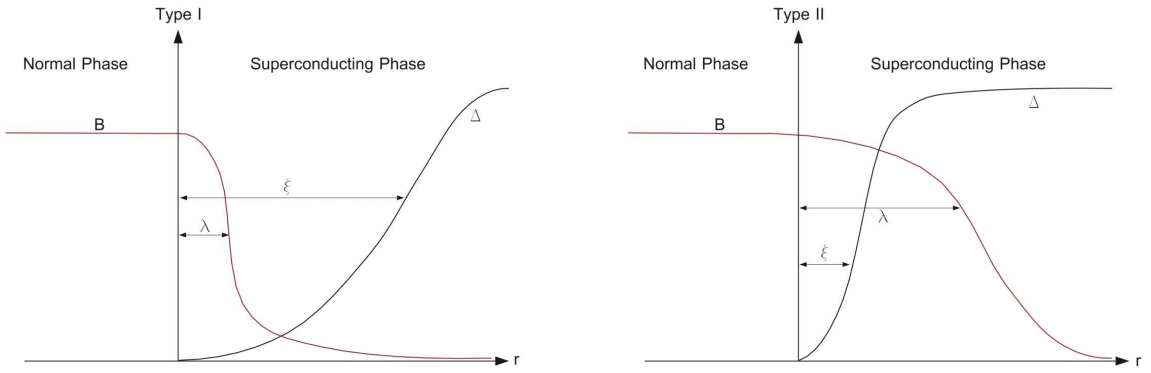


(a) (b)

Figure 32: (a): For a type one superconductor, the magnetic field is unable to penetrate deeply in to the material, leading to a Meissner state of complete flux expulsion. (b): On the other hand, a type two superconductor allows magnetic fields to penetrate more deeply into the material, with the wave function being suppressed primarily in the vicinity of the vortex core. The ratio of the two length scales shown on the graph determines what type of superconductor a specific material is.

where $\kappa$ is the ration of the penetration depth to the GL coherence length. From this equation it is clear that materials that have a value of $\kappa$ greater $1/\sqrt{2}$ will have an upper critical field greater than $B_c$; in other words, a mixed state of some sort exists for fields between $B_c$ and $B_{c2}$ for superconductors with $\kappa > 1/\sqrt{2}$. For the other case when $\kappa < 1/\sqrt{2}$, as the field is lowered from above $B_c$, the Meissner effect sets in before $B_{c2}$ is ever reached, implying that the standard results which were derived previously still hold. The differences between type I and type II superconductors are outlined in Fig. 32; shown in the figure is a N-S boundary with a magnetic field applied. For the type I material, the field is quickly screened due to the Meissner effect, whereas the order parameter slowly rises to its bulk value. Conversely, the penetration depth is much larger for a type II material, as well as having a correspondingly small GL coherence length. In both cases, there is a strong interplay between the normal and superconducting state; this can be seen very vividly at the N-S boundary. For instance, there are two energetic processes occurring at the boundary between a normal metal and a superconductor when magnetic fields are present: one is the energy it takes for the superconductor to expel the applied field over a distance $\lambda$, and the second is the energy it takes to break up Cooper pairs over a distance of $\xi_{GL}$. Thus, via

simple energy arguments it can be shown that it is energetically advantageous for type I materials to expel flux from the inside of the superconductor (i.e. the N-S boundary has positive surface energy). In contrast, a type II material has a negative surface energy at the N-S boundary and so normal domains are introduced into the superconductor when the field reaches $B_{c1}$. These domains are not allowed to increase without bound at a given magnetic field; instead of spreading through the material when the field exceeds $B_{c1}$, the normal regions nucleate in a lattice of vortices, as seen in Fig. 33.

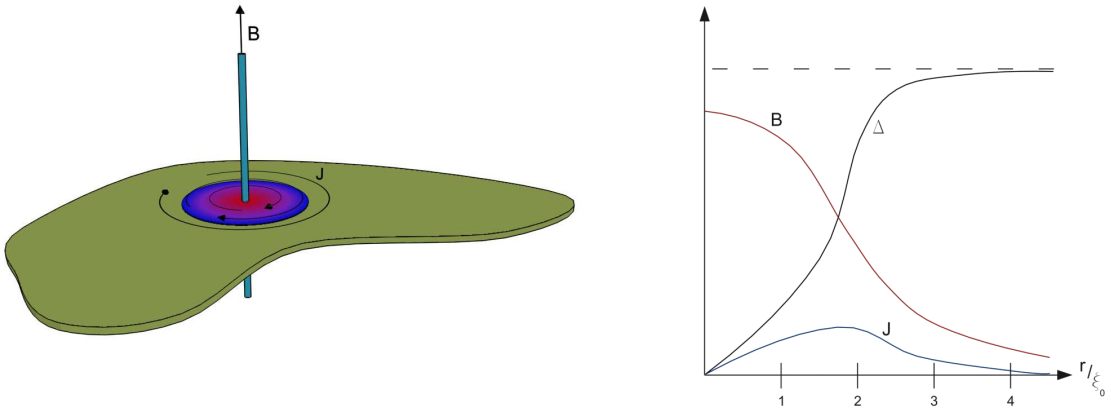


(a) (b)

Figure 33: (a): Schematic of a Single Vortex in a Superconductor. When the applied magnetic field exceeds $H_{c1}$, a type 2 superconductor will allow flux to partially penetrate the superconductor, creating a mixed state. This mixed state is characterized by regions of flux penetration which create vortices of current. (b): Graph showing the effect of a vortex on superconductivity. The graph assumes that a vortex lies on the y-axis; as such, the gap parameter is totally suppressed on this line, while the magnetic field is highest. In contrast, as the distance from the vortex is increased, the magnitude of the gap asymptotically approaches its bulk value, while both the magnetic field and its induced current decay to zero.

Because flux is quantized in a superconductor, it is energetically favorable for many individual vortices to be created inside the superconductor, as opposed to large domains of normal material. Inside these vortices is a region of high field and circulating supercurrent which maintains the vortex; as well, the density of Cooper pairs is reduced from the bulk value near a vortex and it is exactly zero at the center of a vortex. It has been shown both theoretically [3] and experimentally [220] that the vortices in the mixed state form a triangular lattice in order to minimize the total energy of the system, as shown in Fig. 34.

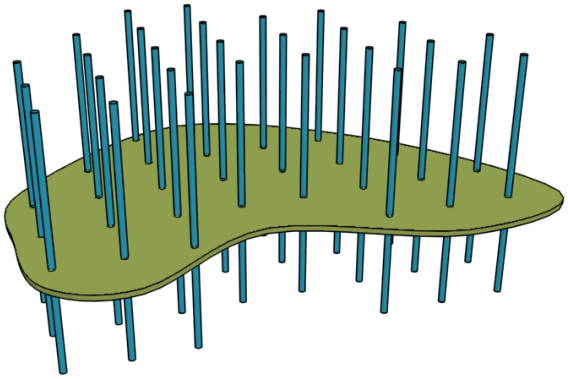

(a)

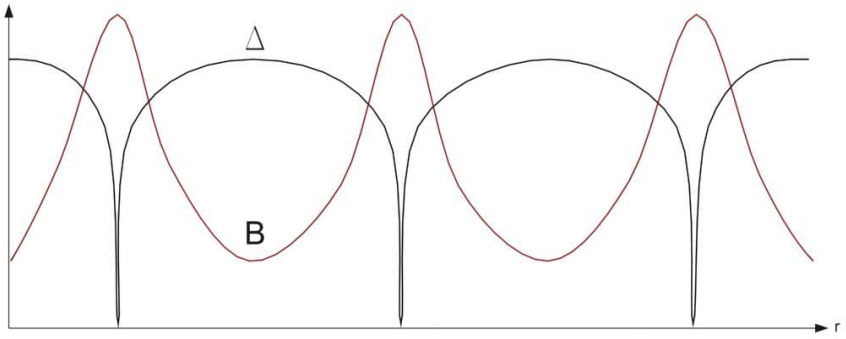


(b)

Figure 34: (a): Vortex Lattice for a type 2 superconductor. When a superconductor enters the mixed state, the regions of suppressed order parameter form a lattice in order to minimize the total energy of the system. This vortex lattice does not follow the periodicity of the underlying real space lattice; rather, it is triangular for all type 2 superconductors. (b): Magnetic field and order parameter of a vortex lattice for an applied field which is just above $H_{c1}$. As the magnetic field just exceeds $H_{c1}$, the vortex lattice appears and the order parameter is suppressed at the sites of the cores. Away from the lattice sites, the order parameter returns to its bulk value; however, as the magnetic field increased, the penetration of the cores increases and leads to a bulk suppression of the superconducting wave function.

However, the vortices of a type II superconductor are capable of movement through the material; in doing so, dissipation is created in the material which can catalyze the transition of the material to fully normal (an extremely important practical problem in superconducting magnet technology). Specifically, if a current is passed through the superconductor when it is in the mixed state, there exists a Lorentz force on the vortex given by:

$$\mathbf{F} = \mathbf{J} \times \frac{\mathbf{B}}{c}, \tag{114}$$

where gaussian cgs units are used. In forcing the vortices to move, an electric field is induced which is parallel to the flow of current:

$$\mathbf{E} = \mathbf{B} \times \frac{\mathbf{v}}{c}, \tag{115}$$

where $\mathbf{v}$ is the velocity of the vortex. In this way, a moving vortex creates a longitudinal voltage difference in the superconductor which carries with it dissipation. However, due to impurities and defects in the superconducting material, the vortices may be pinned and unable to flow and create dissipation. In this case, there exists a threshold force that is dependent on the nature of the pinning site below which the vortex will be pinned. However, there also exists thermally assisted flux flow which can cause vortices to jump from one pinning site to the next. Because the presence of vortices locally destroys superconductivity, they are potentially detrimental to superconducting devices and magnets; as well, the added dissipation caused by flux flow can create unwanted heating effects in devices.

# CHAPTER III

# EXPERIMENTAL TECHNIQUES

Chapter III begins with a description of the history of atomic contacts and the advantages of the Mechanically Controllable Break Junction (MCBJ) method over other similar techniques. Next, the fabrication of our point contact devices is detailed, as well as the fabrication of a cryogenic filter which can be used in conjunction with the other circuitry presented. The next section covers how the MCBJ is implemented and also the measurement circuits for the point contact devices. Lastly, some of the numerical techniques used in point contact experiments are presented, mainly focusing on the extraction of the Landauer transmission coefficients and the DFT/NEGF simulations which were used.

## *3.1 History of Atomic Contacts*

Over the last two chapters, the rich framework of mesoscopic physics and weak superconductivity have been detailed, resulting with many new and interesting physical phenomena such as quantized conductance and the Josephson effect; however, the focus has primarily been on the theoretical aspects of these topics, with the experimental side of mesoscopic physics and how these effects are measured being neglected [9]. Among mesoscopic systems, atomic point contacts serve as an ideal testbed for transport measurements due to their inherently small number of conductance channels and the ability to accurately control many different atomic configurations; as such, the aim of this chapter is to focus on the experimental techniques which are necessary for transport measurements on atomic point contact systems. However, it is advantageous to understand the origins of experimental mesoscopic physics so as to further appreciate the current state of the field; thus, before detailing the current techniques used by our lab to probe atomic contacts, a small historical digression will be made.

To begin, much of the early work in atomic contacts was instigated by two landmark

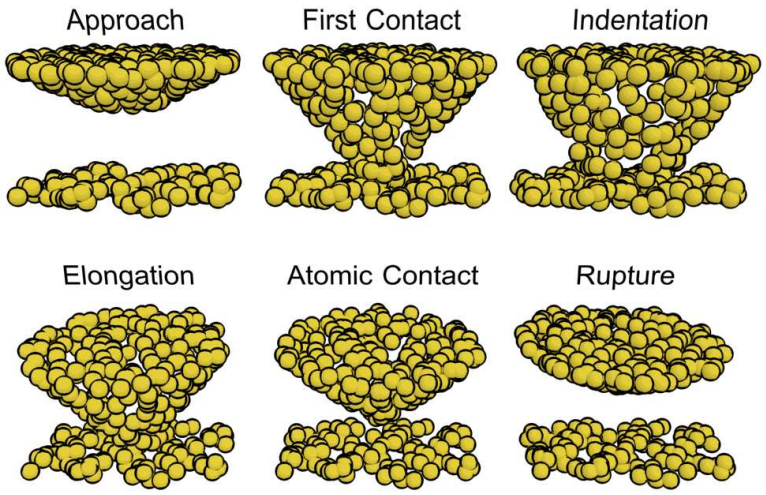


Figure 35: Here we can see the evolution of a point contact in an STM as the tip is brought into the surface and subsequently retracted; molecular dynamics simulations have shown that during the retraction phase of the STM tip, both atomically thin nanowires and single atomic contacts are able to be created and measured.

molecular dynamics papers [212, 138] which focused on the structural evolution of an atomically sharp, metallic tip during retraction from the surface of a metal, as pictured in Fig. 35. Here, the authors were interested in investigating the mechanical properties of atomic systems, specifically the elastic deformations which lead to structural rearrangements of the contact, as they apply to problems such as adhesion and friction. However, one of the most interesting results of the study was that the metallic tip naturally forms an atomic contact during the final stages of retraction before breakup of the contact, shedding light on how atomic size contacts could be experimentally made.

During this time, reliable atomic contacts were not able to be fabricated; instead, only point contacts which consisted of tens to hundreds of atoms could be faithfully reproduced using a method known as the spear-anvil technique [238], which is pictured in Fig. 36. Here, a metallic needle (spear) is brought slowly into contact with a metallic surface (anvil) through the use of a differential screw. With this method, researchers were able to reliably produce ballistic contacts as small as 10 nm, attracting much experimental interest. By

operating in the ballistic regime, experimentalists realized that the strength of the electron-phonon interaction in a material could be measured via the second derivative of the voltage with respect to current, $d^2V/dI^2$, thus creating a new technique which is known as point contact spectroscopy [112] and that is used extensively in measuring the phonon spectra of different materials. However, the spear-anvil technique lacked the stability and fine control necessary to produce truly atomic contacts and observe atomic level phenomena; as such, new techniques were needed which could effectively manipulate structures composed of a few atoms.

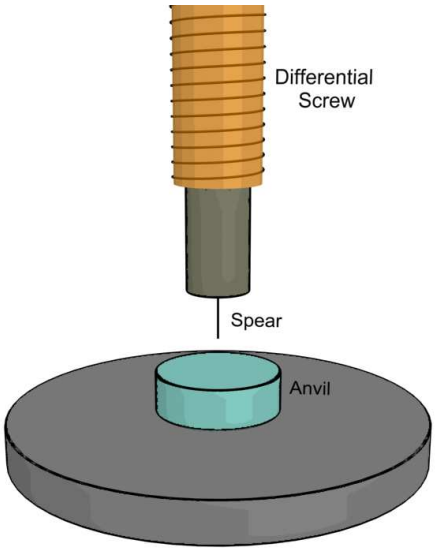


Figure 36: In the spear-anvil technique, a thin needle (the spear) is attached to a differential screw which is actuated in order to drive the needle through a sample (the anvil); because the actuation mechanism is relatively coarse, the spear-anvil technique is generally unable to form stable atomic contacts.

The first device which afforded experimentalists the ability to dynamically control atomic level structures was the Scanning Tunneling Microscope (STM) [25] and it is from this point in history that a veritable explosion in mesoscopic research started as groups began to apply the STM technique to problems such as the measurement of atomic conductances [89] and forces [72]. In addition, many other types of atomic microscopy were developed in conjunction with scanning tunneling microscopy. Among these, atomic force microscopy [26, 87] remains as one of the foremost high-resolution imaging techniques, which

has the added capability of atomic level positioning and patterning [48], as shown schematically in Fig. 37. Moreover, complementing the range of techniques which came from the idea of STM were other novel mesoscopic systems which presented unique advantages over STM; for instance, research into the physics of two dimensional electron gases provided the first experimental evidence of conductance quantization [228] by utilizing a gate electrode which could alter the width of the electron gas in the device region. This concept of dynamic control over the width of a quantum conductor proved to be one of the central ideas which would drive experimental work in mesoscopic transport; by gaining the ability to actively manipulate the structure of devices at the sub-nanometer level, a variety of atomic level interactions can be experimentally probed under dynamic conditions, as well as allowing devices to operate in multiple transport regimes.

However, it became evident early on that direct application of an STM to atomic contact studies (i.e. pushing the tip into the substrate and subsequently retracting to form a contact) was very difficult. For instance, creating a clean metallic contact can be difficult with an STM due to adsorbates on the substrate surface, though it is possible to *in-situ* clean the tip-substrate interface [89]. Additionally, the stability of STM atomic contacts remained a large problem for many researchers, and new custom vibration stages were needed to control the coupling to the outside environment. For these and other reasons, many different techniques were developed to reliably create atomic contacts for mesoscopic electrical and mechanical studies [9]. Among these, a powerful method for atomic contact fabrication was developed by Moreland and Ekin [164] and later refined by Muller [170] and is known as the Mechanically Controllable Break Junction (MCBJ) technique and is shown schematically in Fig. 38.

The essence of the MCBJ technique is the use of a bendable substrate which, when placed in a three point bending configuration, enables the width of the contact to be dynamically changed through piezoelectric actuation. Indeed, the MCBJ method allows complete control over the width of device region from that of a bulk contact to a single atom contact to a tunnel junction. However, not only do MCBJ's have an extensive range of possible atomic configurations, they are also naturally robust against mechanical vibrations, which implies

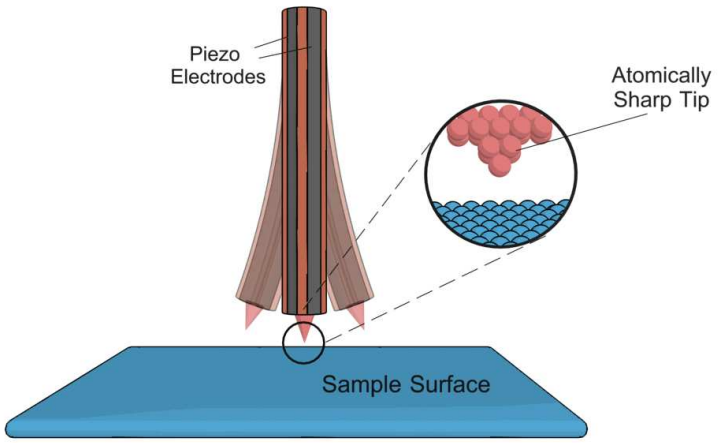


(a)

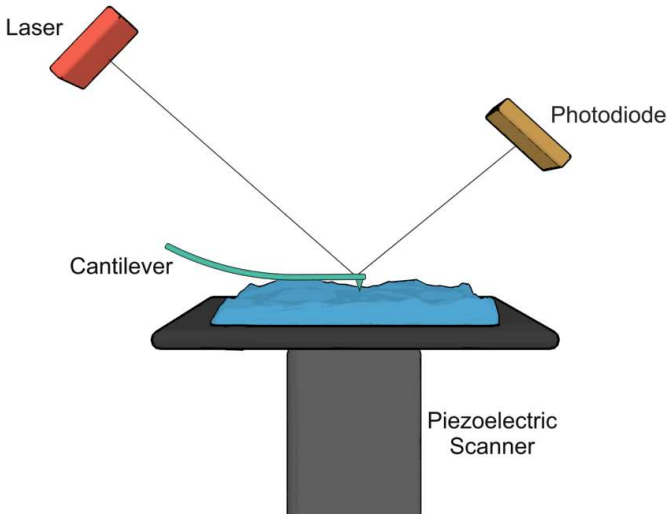


(b)

Figure 37: (a): The STM technique exploits the ability of electrons to tunnel from one electrode to another in order to perform surface studies; because the tunneling current depends exponentially on the distance between the two electrodes, the STM methods offers a very sensitive surface measurement. (b): The AFM technique is used to measure forces by measuring the deflection of a cantilever beam which is scanned across the surface of a sample; the deflection is typically measured by reflecting a laser pulse off of the cantilever beam which is detected by a photodiode.

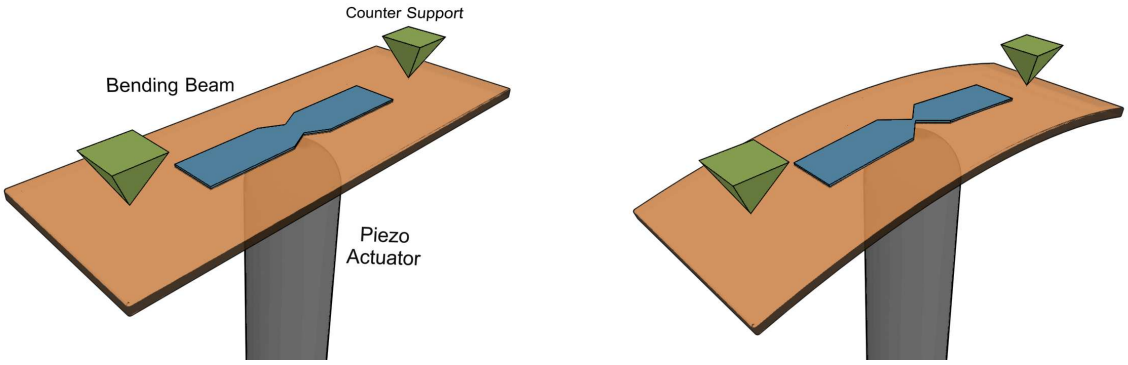


(a) (b)

Figure 38: (a): The MCBJ relies on a point contact which is prepared on a flexible substrate; this device is placed in a three point bending mechanism as shown. (b): Upon actuating the piezo, the point contact is elongated through the bending of the substrate, thereby effectively controlling the width of the atomic contact.

that one can easily maintain single atom contacts for long lengths of time. This combination of range and stability provided an ideal testbed for mesoscopic system physics; in fact, soon after the introduction of the technique, researchers were able to show conductance quantization in Nb and Pt MCBJ's [169]. Nb was chosen as the device material since it has the largest superconducting critical temperature of any metal ($\approx$ 9 K); hence, theories of normal mesoscopic transport (i.e. the Landauer formalism) could be tested, as well as the more exotic theories of mesoscopic superconductivity (i.e. Andreev reflection, Josephson effects, etc.). Indeed, by using a Nb MCBJ in the tunnel junction mode, researchers were able to confirm [226] the theoretical idea of multiple Andreev reflection being responsible for the subgap structure. However, during these studies it was also noticed that the conductance of these junctions was not quite one conductance quantum, $G_0$. This observation led to a systematic study [200] of superconducting MCBJ point contacts and the evolution of the conductance in order to determine the reason for the discrepancy between the measured and expected conductance values. In the end, it was determined that instead of a single conductance channel being present in the device, a few, weakly transmitting channels provided for the transport across the junction, whose total conductance was approximately $G_0$. Furthermore, it was shown that by exploiting the highly non-linear I-V relation of

the subgap structure in superconducting point contacts, one could extract that mesoscopic PIN code of the device; however, the major question of how to determine the number of channels in a given device remained. The answer, which was provided by Cuevas et al. [52] and confirmed experimentally by Scheer et al. [199] was shown to be that the number of channels in a mesoscopic conductor is given by its chemical valence; hence, for aluminum there are three conduction channels, whereas Nb has five conduction channels.

## *3.2 Fabrication of Niobium Quantum Point Contacts*

### 3.2.1 Niobium Point Contact Junction

For the fabrication of mechanically controllable break junctions, the major design goal is to create a metallic structure whose smallest dimensions can be altered through elastic deformation of the underlying substrate; to that end, our design employs the widely used technique of suspending a narrow metallic bridge between two contacts on a flexible substrate. Using this configuration, the width of the bridge can be precisely varied from hundreds of nanometers down to a single atom by bending the substrate with a piezoelectric actuator.

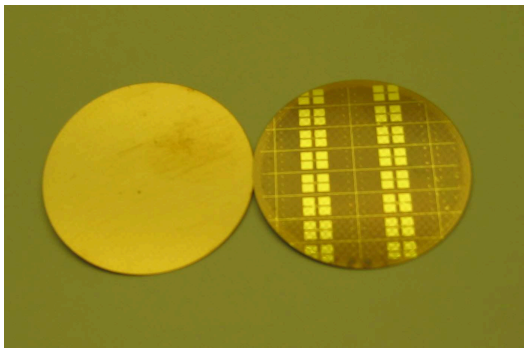

Figure 39: Shown here are the top and bottom of two wafers prior to backside etching.

For the substrate material, silicon is not an appropriate choice due to its lack of flexibility; instead our group began with 250 $\mu$m thick by 50 mm diameter phosphor bronze discs bought from Goodfellow Inc., which acts as both a ground plane and flexible substrate for the finished device. Next, an insulating layer must be deposited which will not only separate the ground plane from the device layer, but also serve to planarize the surface; for this, a

2 $\mu$m layer of polyimide (PI2610 bought from HD Microsystems) is spun and cured onto the wafer. In addition to planarizing and insulating, polyimide also has the advantages of a low thermal expansion coefficient and the capability to be dry etched in oxygen to free the bridge region of the device. However, polyimides tend to suffer from problems with adhesion, though they typically can be remedied by roughening or chemically modifying the surface to increase adhesion. To deposit the polyimide, a coat of VM652 adhesion promoter from HD Microsystems is spun onto the wafer to improve the substrate-insulator bonding; then, the PI2610 is spun on and cured to convert the dissolved polyamic acid into a fully aromatic polyimide and remove any solvents. With the insulation for the ground plane completed, the metallization layers of the device can now be deposited.

First, a 150 nm layer of niobium is magnetron sputtered onto the sample using a *in situ* cold trap to reduce the amount of water vapor and other contaminants in the vacuum chamber; as well, the introduction of the cold trap aided in removing excessive compressive stresses which can occur during the deposition process, as seen in Fig. 41. Sputtering was chosen over evaporation due to the high melting point of the metal (2750 K), as well as to limit the amount of radiation incident on the polyimide layer. After sputtering, Shipley 1813 photoresist is spun onto the sample, baked to remove any remaining solvents, and then exposed in a mask aligner. Once complete, the wafer is put into a chlorobenzene bath for 20 minutes to harden the surface layer of the photoresist which will make for a better undercut and hence a cleaner liftoff. Once the surface layer has been hardened, the wafer is then developed in Microposit MF-319 developer for approximately 70 seconds and then is ready for metal deposition; for our samples, 15 nm of Ti was first evaporated onto the sample to act as an adhesion layer, followed by 135 nm of Au. Once deposited, the unwanted metal is lifted off by soaking the wafer in heated Microposit 1165 remover for approximately 2 hours, thus completing the patterning of the contact pads.

Now the break junction itself must be fabricated; since the smallest dimension of the bridge is approximately 200 nm, the junction must be patterned using e-beam lithography. Since niobium was sputtered over the entire wafer, the bridge region must be protected while the unwanted metal is removed via dry etching; to do this, an Al dry etch mask is

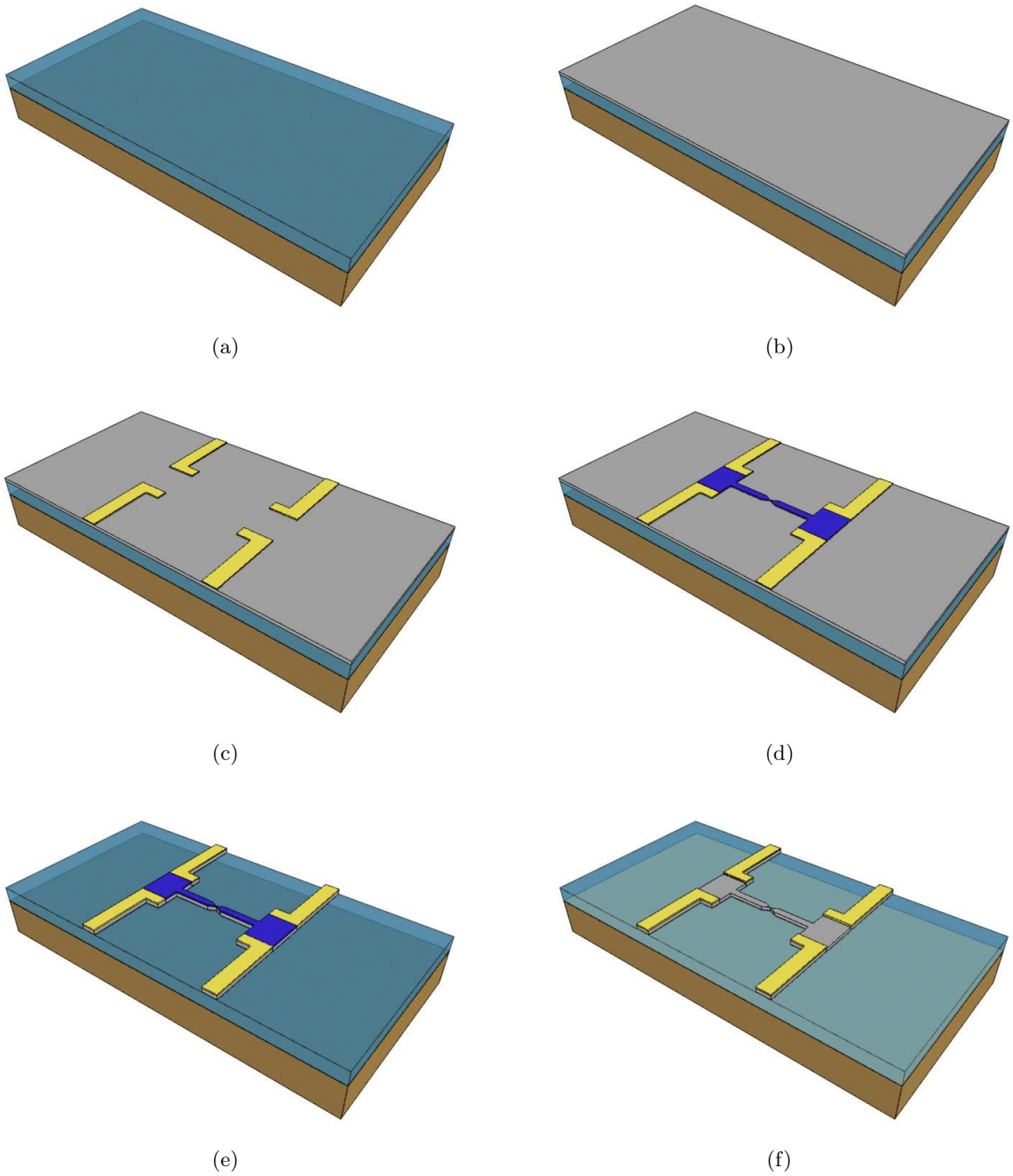

Figure 40: (a) Deposit insulating polyimide layer; (b) sputter Nb onto wafer; (c) pattern Au contact pads; (d) use e-beam lithography to pattern Al etch mask; (e) anisotropically dry etch Nb; (f) remove etch mask and isotropically dry etch the polyimide to free the bridge.

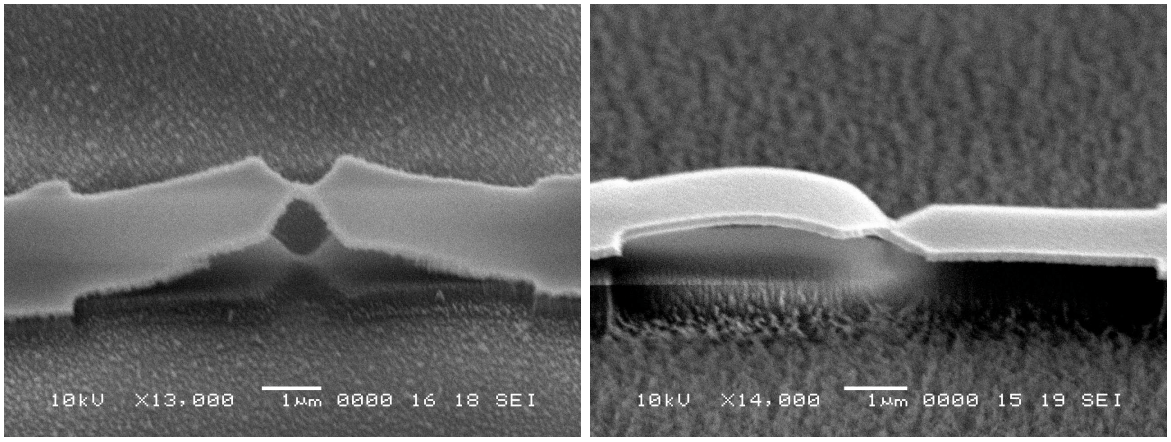


(a) (b)

Figure 41: Here, both panels show SEM micrographs of the junction region which have been lifted due to a lack of stress control during the niobium deposition step; to remedy the large intrinsic compressive stresses of the material deposition, a liquid nitrogen cold trap was incorporated into the sputterer.

patterned over the break junction area using e-beam lithography, followed by etching of the niobium in a RIE. Specifically, a PMMA/MMA bilayer was spun over the sample, the break junction geometry was exposed in a modified SEM/EBL tool, and then the pattern was developed in 1:3 MIBK/IPA; next, Al was evaporated over the sample and subsequently lifted off in an acetone bath, creating the dry etch mask. For the dry etch, a two step RIE process was used to remove the unwanted niobium: first, the sample was exposed to a short $BCl_3$ plasma in order to remove any native oxide which may have grown on the surface and which could compromise the etch uniformity; second, a longer, anisotropic $SF_6$ plasma was used to etch the Nb not covered by the Al etch mask. With the break junction patterned, the dry etch mask may be removed by either wet etching of Al or by adding an additional $Cl_2$+$BCl_3$ RIE step. The last step of the MCBJ fabrication is to isotropically dry etch the polyimide in order to free the break junction. To accomplish this, an oxygen plasma (under a higher RIE pressure than for the other steps) was used to free the bridge region, thus completing the device; SEM micrographs of the finished device can be seen in Fig. 66.

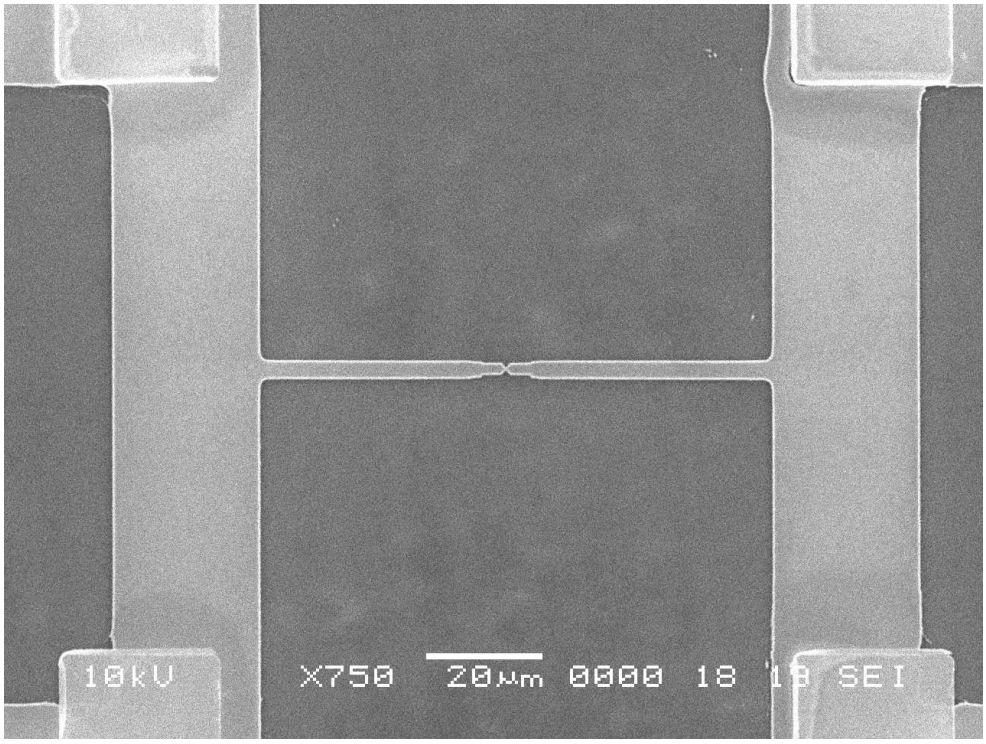


(a)

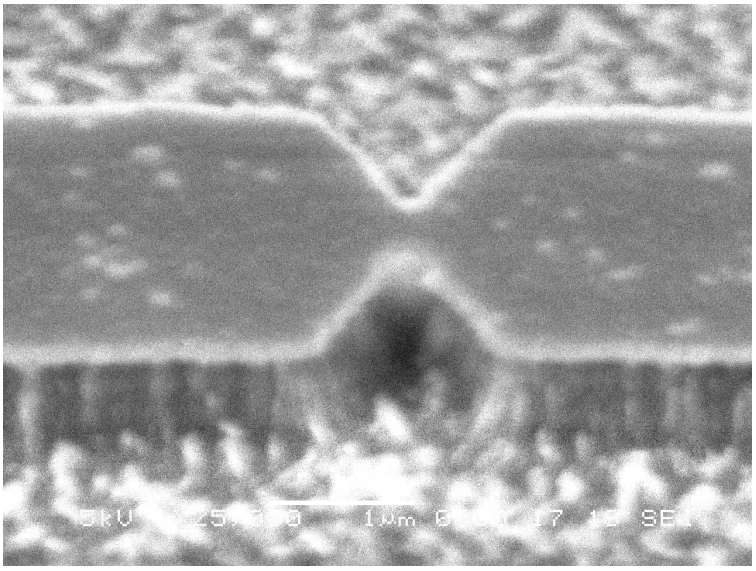

(b)

Figure 42: (a): Here, a SEM micrograph of the completed device can be seen, along with the interconnects to the gold contact pads. (b): Zoomed view of a completed junction, showing the undercut of the polyimide to free the bridge region.

### 3.2.2 Shunted Point Contact Junction

With the fabrication of a single point contact completed, we next sought to extend our measurement capability by fabricating a geometry which would enable not only the PIN code to be measured, but also the current-phase relation of the junction. The advantage gained by measuring both of these quantities is that the theoretical I-V curve, which depends on both the transmission for each conduction channel (and hence the PIN code) and the current-phase relation for the junction, could be tested. A schematic for the this type of device, along with the principles of operation are detailed in Fig. 43.

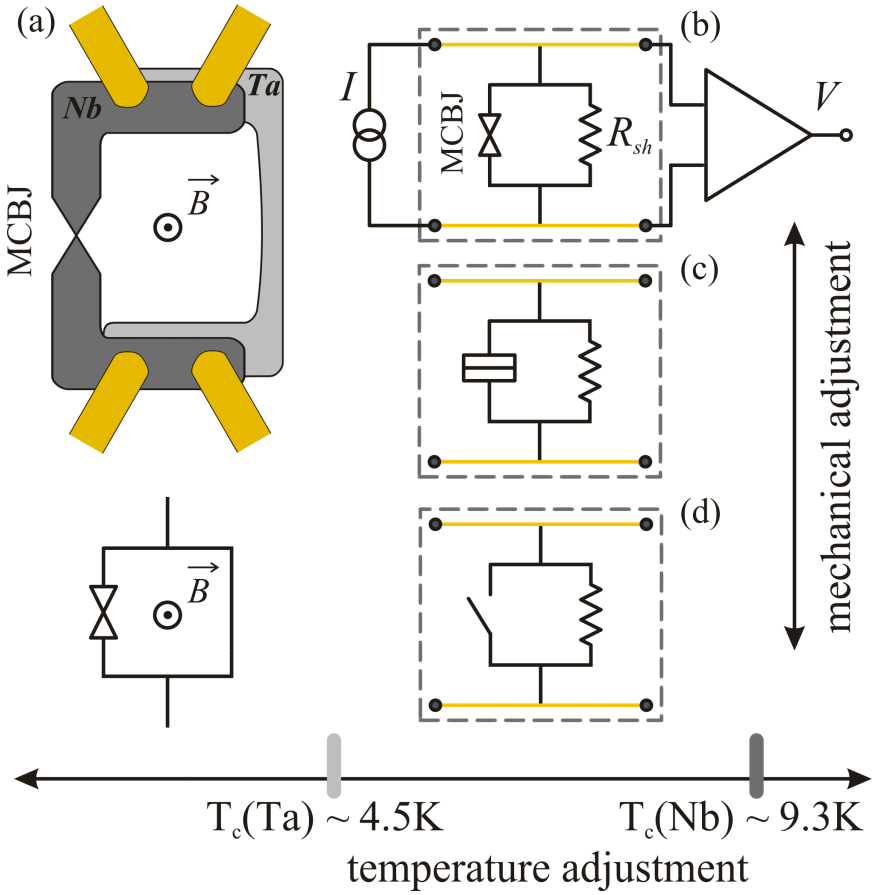


Figure 43: Principle of operation for the shunted junction device. (a): Here, a mock-up of the desired device is shown with both the point contact, shunt, and contacts. (b): Resistively shunted junction (RSJ) configuration with the MCBJ in the contact mode and the shunting segment in the normal state. (c): Stretching the MCBJ into the tunnel mode allows for the measurement of the superconducting gap of the junction material. (d): By stretching even further, the junction breaks and is considered an open circuit ($R_{MCBJ>2G}$)

With this goal in mind, the integration of a Ta shunt was pursued; the reason being that since Ta has a different superconducting critical temperature than Nb, the device can operate in different regimes. More specifically, if the device temperature is below the Ta critical temperature, the device operates as an RF SQUID since the entire device region is superconducting; however, if the temperature is between the two critical points, the Ta will act as a resistive shunt to the Nb junction. Nevertheless, though this extra degree of freedom afforded by using different materials for the device enables the measurement of both the conductance channel composition and the current-phase relation, the cost is an increase in fabrication complexity. This added complexity is due to the high melting temperature of Ta, which like Nb, must be sputtered onto the sample; if not for this, the material of interest could simply be evaporated onto existing samples and the shunt would be completed.

The process begins, as before, with a bronze wafer which is coated with polyimide and then subsequently cured in a furnace; after this, the Nb and Ta are then sputtered onto the wafer. Ta is sputtered over the Nb to insure that $\alpha$-Ta, not $\beta$-Ta, is deposited since $\beta$-Ta has a much lower transition temperature and much higher resistivity. After the two metals are sputtered, Au contact pads are patterned onto the sample in the same way as for straight junctions.

Next, the bridge region of the sample is fabricated. To do this, an additional step of selectively removing Ta from the bridge region is required since a Ta layer is covering the Nb; to remove the Ta, e-beam lithography is used to open a rectangle in the junction region and subsequently, the Ta layer is dry etched. Because $SF_6$ is used as the etch gas during the RIE step (which etches both Nb and Ta), it must be ensured that only Ta is removed from the area; to do this, Energy Dispersive X-Ray Spectroscopy (EDS) is used to measure the amount of Ta remaining after dry etching. With the Ta over the bridge region removed, another layer of PMMA/MMA is applied to the sample and the junction and shunt region are patterned with an Al etch mask which is lifted off. After patterning the new dry etch mask, the Nb and Ta which is not covered is removed using another dry etch step.

With the device regions patterned, the only remaining steps are to remove the Nb

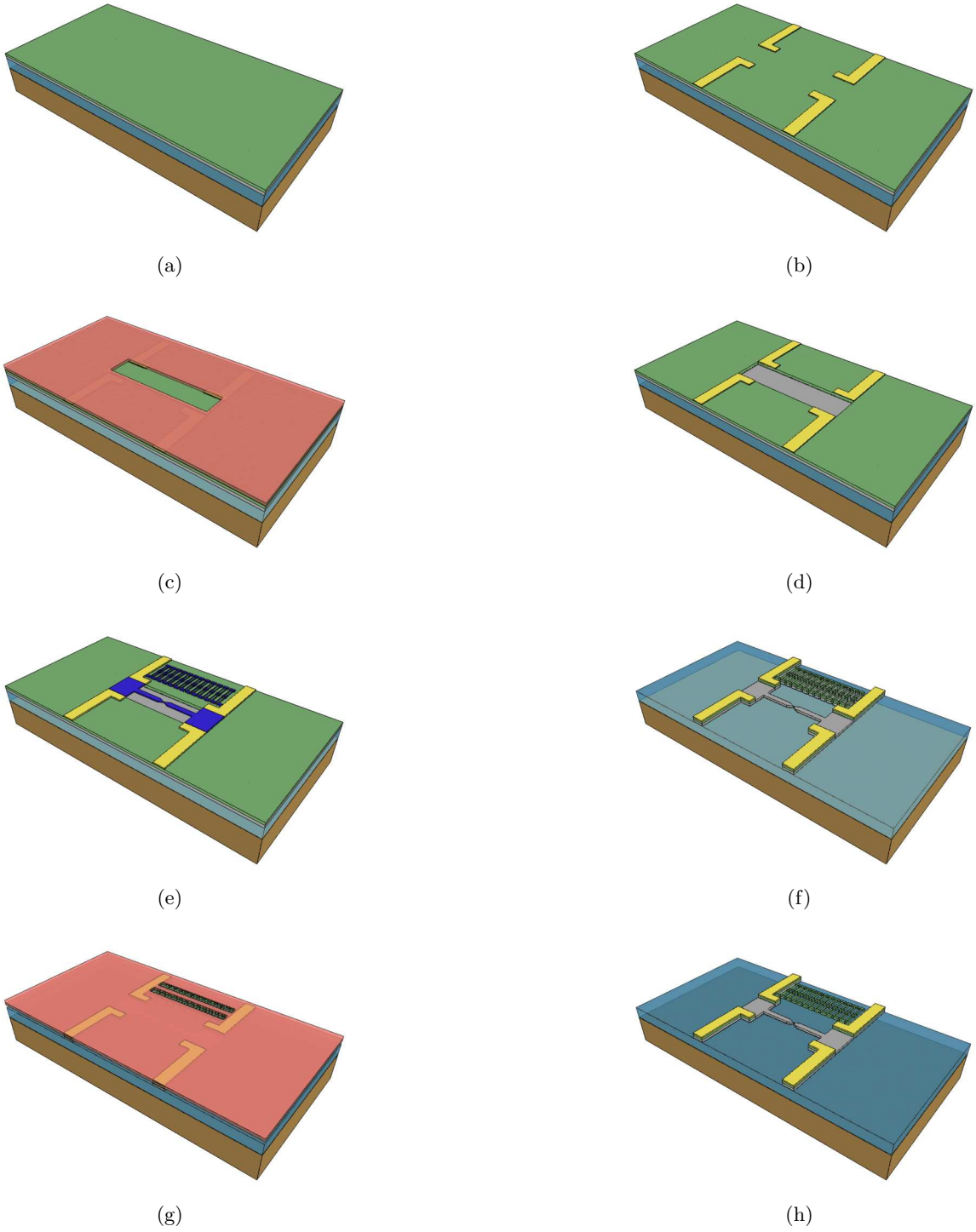

Figure 44: (a) Deposit polyimide layer and sputter the Nb and Ta layers; (b) pattern Au contact pads; (c) open a window over the junction region; (d) dry etch Ta; (e) pattern new Al dry etch mask; (f) anisotropically dry etch both Nb and Ta; (g) expose shunt in order to wet etch the underlying Nb; (h) isotropically dry etch polyimide.

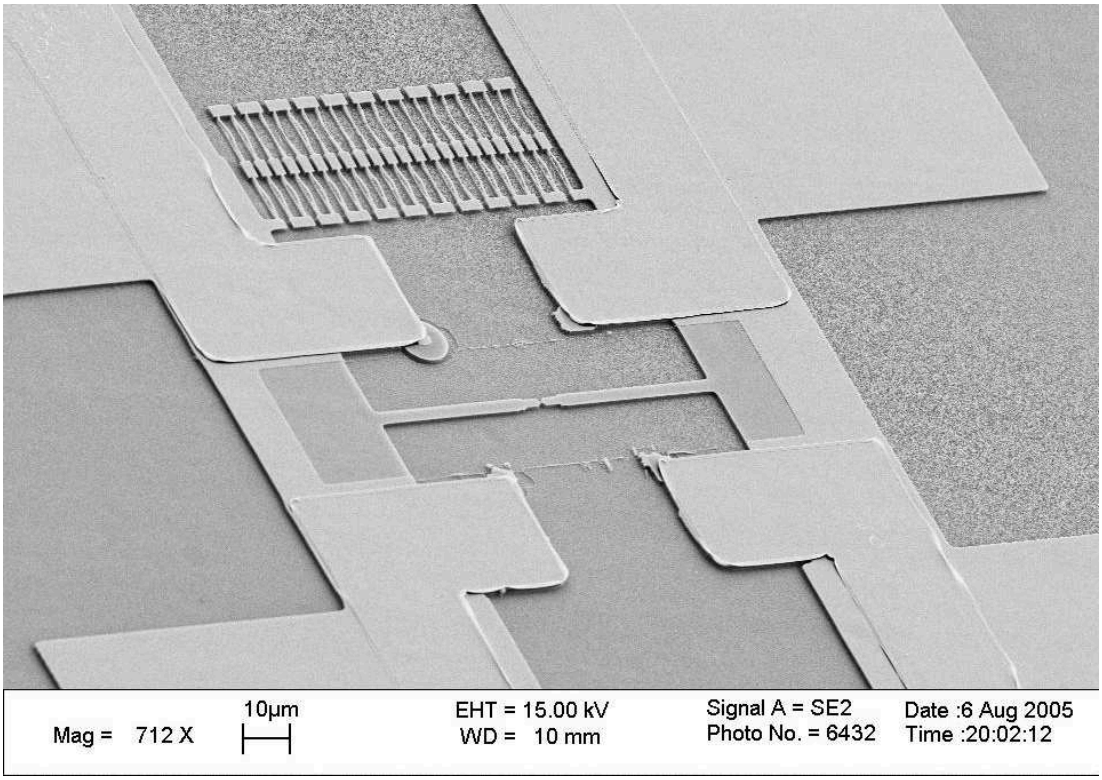


(a)

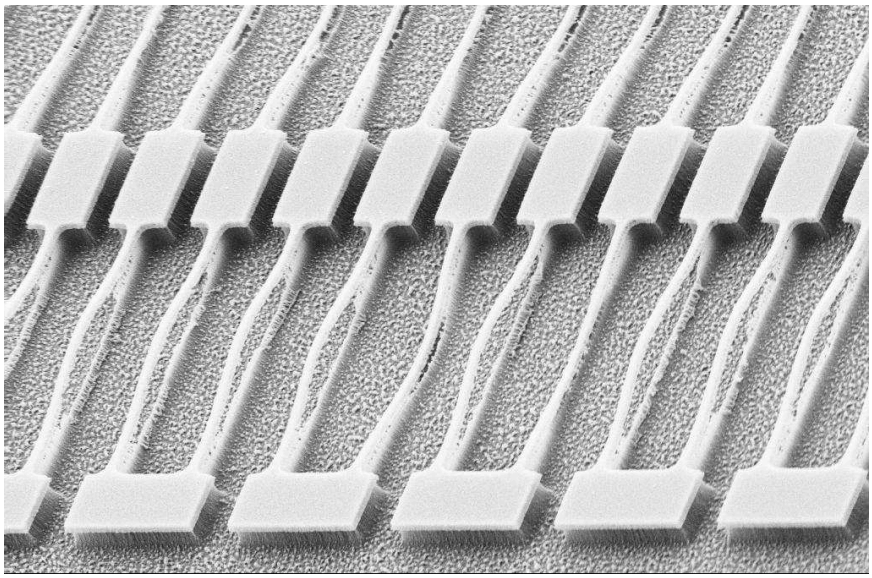

(b)

Figure 45: (a): Here, a SEM micrograph of the completed device can be seen with the shunt and point contact. (b): SEM micrograph of the shunt region; from the figure, the effect of underetching the Nb layer is clear, as well as the compressive stress which the shunt wires are under.

underneath the Ta shunt and etch the polyimide layer to free the bridge region. To remove the Nb under the shunt, another PMMA/MMA layer is applied and the shunt region is opened; then the underlying polyimide of the shunt region is partially etched to create an undercut where the underlying Nb can be easily wet etched. Finally, after removing the remaining resist in an acetone bath, the entire sample is dry etched in an oxygen plasma to to free the bridge and complete the device; the completed device can be seen in Fig. 45

### 3.2.3 Niobium Point Contact Spectrometer

From the BCS theory of superconductors it is well known that all Cooper pairs condense into a ground state at the Fermi level of the superconductor. This fact implies that when a voltage is applied across a Josephson junction, a Cooper pair which travels from the side of higher potential to the other has to release an amount of energy equal 2eV in order to reach the new Fermi level. To do this, the pair emits a photon of the appropriate frequency, $\omega = 2eV/\hbar$. Hence, by applying a moderately small DC voltage across a Josephson junction, one is able to control the emission of electromagnetic radiation from the GHz to the low THz region. This ability to easily emit photons in the lower THz spectrum is especially important because there are few reliable sources of radiation at those frequencies, which is why researchers frequently refer to the lower THz region as the "Terahertz Gap." Furthermore, radiation in this spectrum has many properties similar to x-rays; however, photons emitted at lower THz frequencies are non-ionizing, implying that they are much safer for both imaging and communication.

The major design goal behind the fabrication of a double point contact spectrometer is to have one point contact emit a characteristic spectrum of radiation (as given by the Josephson relation); then, the second point contact is used as a receiver and is able to reconstruct the spectrum of incident radiation. This is done by measuring the modifications of the receiver's IV curve when the radiation is applied. It has been shown [66] that there is a direct mapping of these changes in current to the spectrum of incident radiation on a Josephson junction, much in the same way as Shapiro steps modify the DC IV curve in a specified manner. This type of analysis is termed Hilbert spectroscopy and has been successfully applied to both

tunnel junctions [27], as well as high $T_c$ superconducting junctions [66, 129] In our case, the goal is to embed a molecule between the two point contacts and measure the spectrum of radiation absorbed by the molecule by knowing the transmitted spectrum and measuring the received spectrum.

To fabricate such devices, the steps outlined in Fig. 46 were followed, which begin with a polished silicon substrate, in contrast to the bronze substrate used in the MCBJ devices; the reason being that there is no need to dynamically change the width of the device once completed. However, an insulating layer still must be grown to isolate the device; as such, 1 $\mu$m of $SiO_2$ was next grown via PECVD using the following conditions: a temperature of 250℃, a pressure of 900 mTorr, a power of 25 W, a silane flow rate of 400sccm and a $N_2O$ flow rate of 900 sccm.

After the oxide layer has been deposited, a 100 nm layer of Nb is sputtered in the same way as for the other devices; similarly, gold contact pads are patterned next. Specifically, Shipley 1813 photoresist is spun over the wafer, it is exposed in a mask aligner, soaked in chlorobenzene for 15 minutes and finally developed using Microposit 354. Next, a 15 nm layer of Ti is evaporated as an adhesion layer, followed by a 135 nm layer of Au. Lastly, the excess photoresist is removed by soaking in 1165 stripper for approximately an hour.

In much the same way as for the other devices, the next step involves dry etching the Nb in order to pattern the device layer of the sample. To begin, a bilayer of PMMA/MMA is spun using the same recipe as for the other devices, exposed using an e-beam lithography tool, developed first in 3:1 MIBK:IPA for 60 seconds and then IPA for 20 seconds. Next, a filament evaporator is used to deposit 75 nm of Al over the surface of the wafer. Then, after lifting off in acetone for approximately 30 minutes, the dry etch mask is complete and the sample is ready to be dry etched by RIE. Using the same recipe for dry etching as for the previous devices, the oxidized portions of the surface are etched away to enable a more uniform subsequent etch. Next, the Nb is removed using an $SF_6$ precursor gas and lastly, the Al etch mask is removed using a combination of $BCl_3$ and $Cl_2$ gas, thus completing the device. SEM micrographs of the completed device can be seen in Fig. 47.

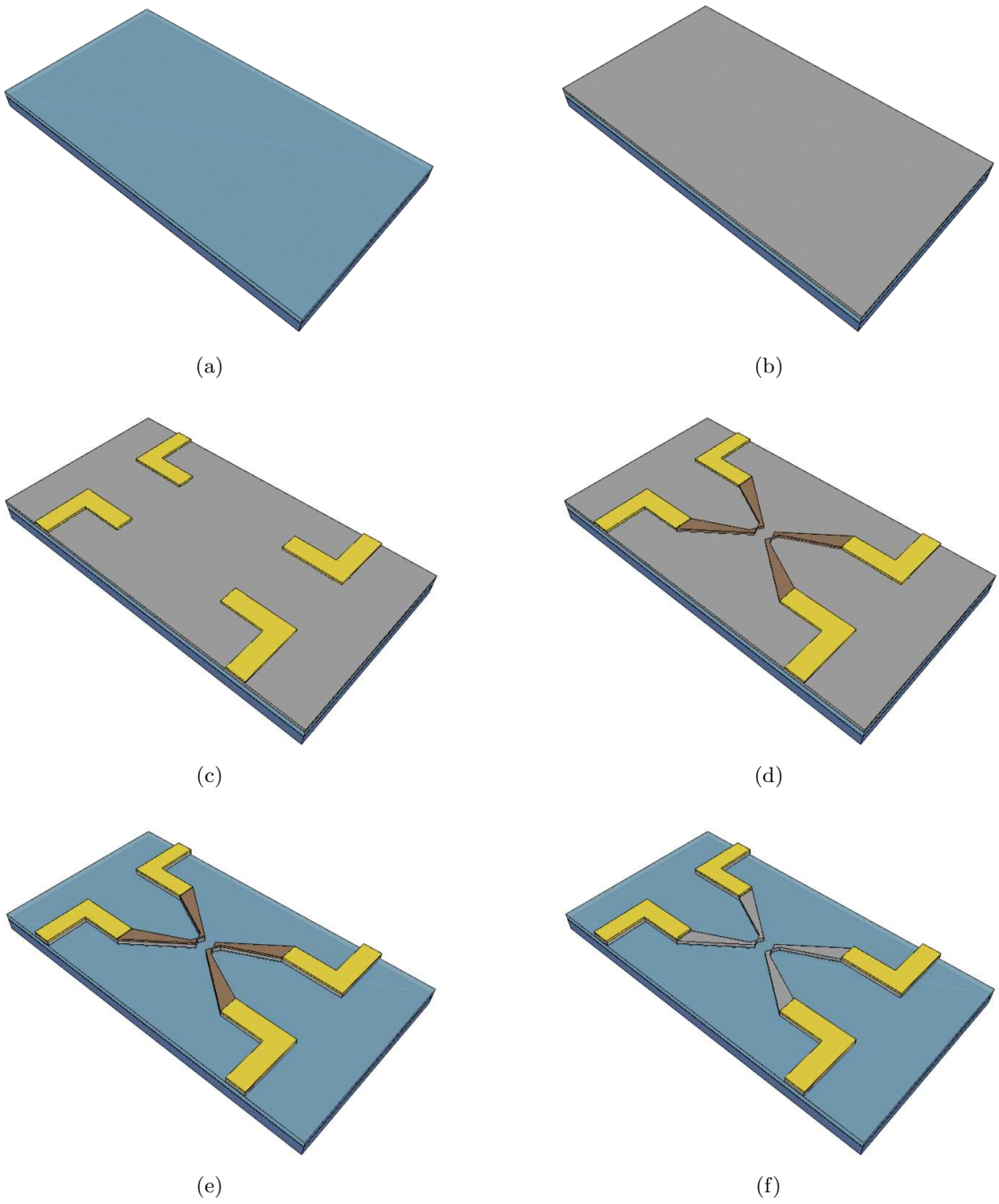


Figure 46: Two Junction Spectrometer Fabrication. (a) A layer of PECVD silicon dioxide is first grown on a silicon substrate; (b) this is followed by DC magnetron sputtering of a niobium layer. (c) Next, gold contact pads are patterned over the niobium and (d) subsequently an aluminum etch mask is fabricated. (e) Following this, the niobium is dry etched to pattern the device area; (f) lastly, the etch mask is removed using another dry etch step, finishing the device.

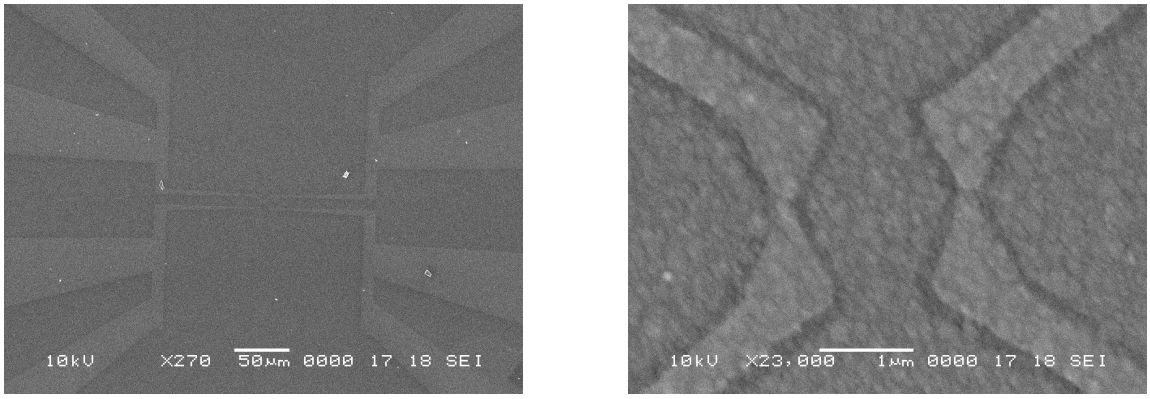


(a) (b)

Figure 47: (a): Zoomed out view of the device, showing how the contact pads, which are defined via photolithography, are connected to the device, which is fabricated using e-beam lithography. (b): View of the device region, showing both point contacts, as well as the central region for embedding molecules.

## *3.3 Microfabricated Cryogenic Filter*

### 3.3.1 Introduction

Attaining complete thermal equilibrium at cryogenic temperatures has been a long standing issue with experimentalists; the use of room temperature instruments to measure device properties near absolute zero necessarily creates an out-of-equilibrium situation. Indeed, there are many instances when experimental results can be explained only by assuming a higher temperature than the refrigerator itself. Furthermore, though the use of heat sinks on electrical lines entering the refrigerator can reduce the noise coupled to the system, electromagnetic noise from regions of higher temperature can still propagate to the device unless more complete measures are taken.

To combat this problem, many different solutions have been used with varying degrees of success; among these are copper powder filters [154, 161], lossy coaxes such as Thermocoax®[242, 91] and also microfabricated distributed RC filters [211, 229, 189]. With copper powder filters, a coiled wire is inserted into an enclosure filled with a metal powder (typically copper or stainless steel); the attenuation comes from the eddy current dissipation created by the metal powder and thus is increased as the number of coils of wire is increased. However, by creating a filter which has a large number of turns (and hence high

attenuation), it becomes impossible to fix the characteristic impedance of the filter around 50Ω; this potential impedance mismatch between the source and the filter can be the cause of spurious transmission resonances which degrade the performance of the device.

Lossy coax offers an alternative to copper powder and is something which is utilized in our own measurement setup to increase the attenuation of high frequency noise signals. The major advantage of these lossy coaxes is the ease of use since they act as both the line and the filter and are readily bought through commercial suppliers (i.e. Thermocoax®). However, because it is the electrical lines themselves that act as a distributed RC filter, in order to lower the cutoff frequency of the filter, more lossy coax must be used. In many applications the cutoff frequency is such that it would require meters of lossy coax to adequately filter the electrical lines, which is an impractical requirement for most modern refrigerators; further, since the filter is distributed from room temperature down to the refrigerator's base temperature, estimating the output noise from the filter can be difficult.

Lastly, there are microfabricated distributed RC filters which can be used to provide filtering of electrical lines and which do not suffer from many of the disadvantages of copper powder filters and lossy coaxes. Specifically, since the microfabricated filter is by nature extremely small and thus at only one temperature, the output noise can be easily characterized. Further, since it is not reflective like a copper powder filter (i.e. it is a dissipative filter), it does not suffer from spurious transmission resonances, thereby ensuring a predictable performance over a wide range of experimental situations. Additionally, the characteristic impedance of the microfabricated filter can be easily tailored to 50Ω; thus, it is experimentally advantageous to employ cryogenic distributed RC filters for use in high precision transport measurements.

### 3.3.2 Fabrication

The fabrication process for cryogenic filters follows steps that are very similar to those of straight junctions since a bronze substrate was incorporated as a ground plane for the device. As with the straight junction process, an insulating polyimide layer is first deposited over the surface of the wafer; specifically, the VM652 primer is spun on at a rate of 2000rpm

for 30 seconds, followed by a soft bake for 60 seconds at 110℃. Next, the polyimide is spun over the sample at 2000rpm for 45 seconds and subsequently softbaked for 2 minutes at 90℃ and then 2 minutes at 150℃. With the polyimide layer deposited, the sample is then annealed in a nitrogen environment for 3 hours at 350℃ to convert the remaining polyamic acid into polyimide.

Following this, the meander pattern is ready to be fabricated, with being chosen as the meander material NiCr for its large resistivity ($\rho = 1.1\mu\Omega m$) [191] and relatively low temperature coefficient of resistance ($\alpha = 0.0004/℃$) [86]. To pattern the metal, a standard liftoff process was used:

- Spin Shipley 1813 over the wafer for 30 seconds at 5000 rpm
- Softbake at 115℃ for 2 minutes
- Expose the wafer at 22 mW/cm$^2$ and 405 nm for 10.5 seconds using the meander mask
- Soak the wafer in chlorobenzene for 15 minutes
- Without rinsing the wafer, develop in Microposit 354 for approximately 45 seconds
- Evaporate 400 nm of NiCr over the wafer
- Liftoff the unwanted NiCr by soaking in 1165 stripper at 70℃ for approximately 1 hour

Now that the device area of the filter has been patterned, it must be encased in an insulator and sheathed to decouple the adjacent arms; for the insulator, another layer of polyimide is deposited using the same set of steps outlined above. For the ground sheath, a 1 $\mu$m layer of Au is lifted off using the same process as for the NiCr step; the only difference being the addition of a 15 nm layer of Ti which acts as an adhesion layer for the sheath.

Once the sheath is completed, the last microfabrication step is to remove the insulator covering the NiCr contact pads. To accomplish this, an oxygen plasma dry etch is used to isotropically remove the polyimide. Specifically, 40 sccm of oxygen at 200 mTorr and an

RF power of 125W is used for approximately 7 minutes to free the contact pads; because the layer of polyimide can shrink up to 15% during annealing, the etch time may vary from wafer to wafer.

## *3.4 Measurement Setup*

When performing experiments on superconducting mechanically controllable break junctions, many environmental factors come into play which must be properly accounted for during the experimental setup if high precision measurements are to be taken. For instance, in order to reliably maintain a single atom contact for the length of an entire measurement cycle ($\approx$ 12hr.), a very high degree of mechanical stability is required; also, as many of the properties of a superconducting material are dependent of the temperature, thermal stability is a must for reproducible transport features. Additionally, in order to avoid contamination of the metallic surfaces during the experiment, the sample region should be under ultra-high vacuum to avoid compromising the quality of the contact.

To satisfy these constraints, a custom-built dipstick refrigerator was constructed whose purpose is to house the sample, electronics, and bending mechanism for the MCBJ, as seen in Fig. 49. In order to have access to these various components, as well as to provide access to the sample for pumping, a manifold is attached on top of the dip-stick which supports all of the vacuum, mechanical, and electrical feedthroughs which are necessary to pump down, actuate, and measure the sample. Furthermore, by building the manifold from UHV rated Conflat®components and using OFE copper gaskets to connect the various parts, a pressure of $10^{-7}$ Torr at room temperature is easily achieved, thus ensuring that our samples will not be contaminated during the breaking process.

Once the sample space has been evacuated and base pressure achieved, the sample is ready to be begin the cooling cycle. To begin, the dipstick is precooled to liquid nitrogen temperatures in a separate dewar from where the liquid helium will be used. The reason is that if the nitrogen is not fully removed before liquid helium is introduced into the dewar, the latent heat of the remaining liquid nitrogen (about sixty times that of liquid helium [188]) can cause significant boil off of the liquid helium; thus, an intermediate dewar is

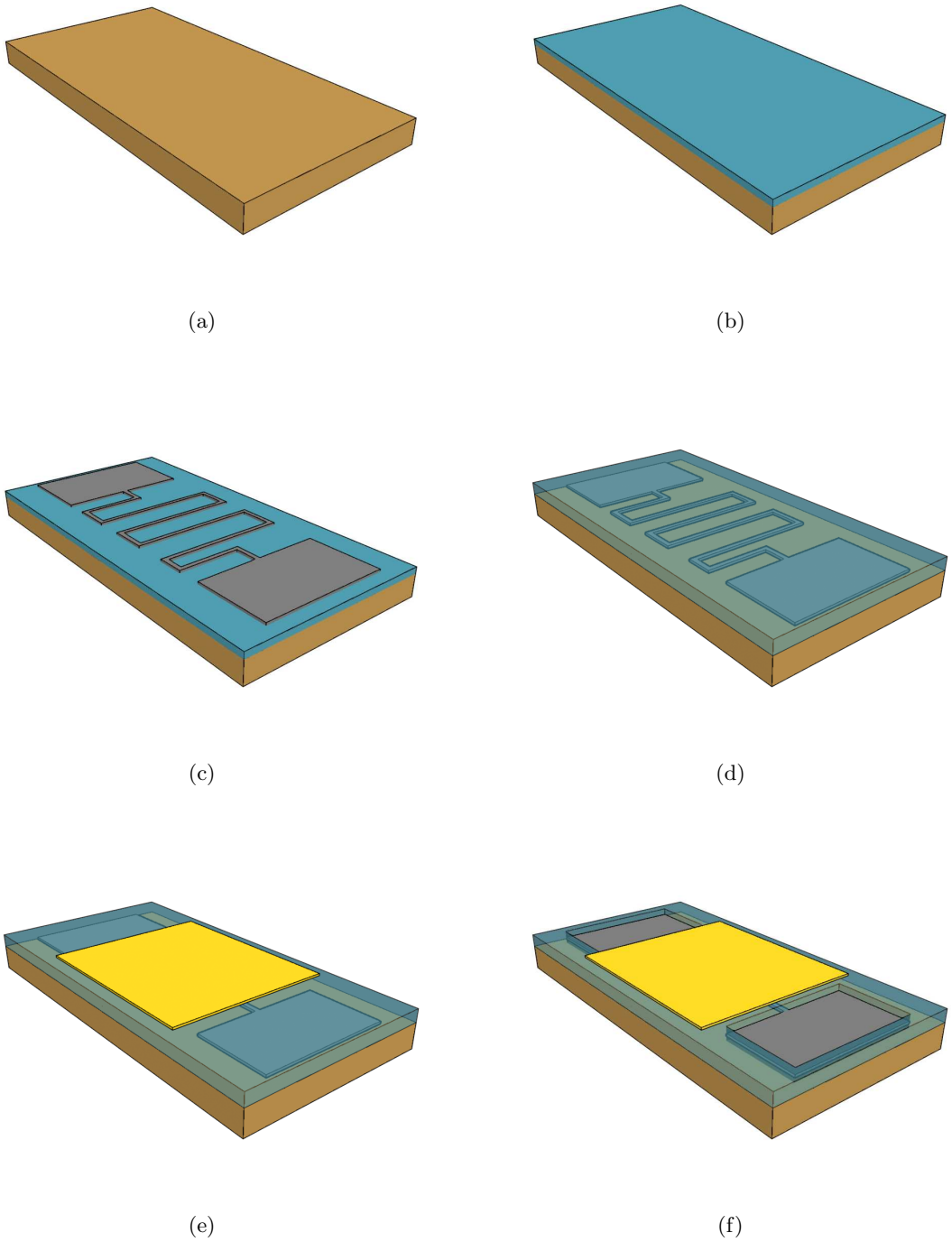

(a) (b)

(c) (d)

(e) (f)

Figure 48: First, a layer of polyimide is deposited on top of the brass substrate; this is followed by the patterning of a NiCr layer which will be the device layer of the filter and consists of a meandering pattern. Next, the patterned NiCr is insulated by another insulating polyimide layer; once the polyimide has been cured, a Au sheath is placed over the meandering pattern for protection from stray signals, as well as to prevent leakage from the device. Lastly (not shown), the contact pads of the NiCr are opened through the polyimide using a dry etch of the insulating layer.


(a)

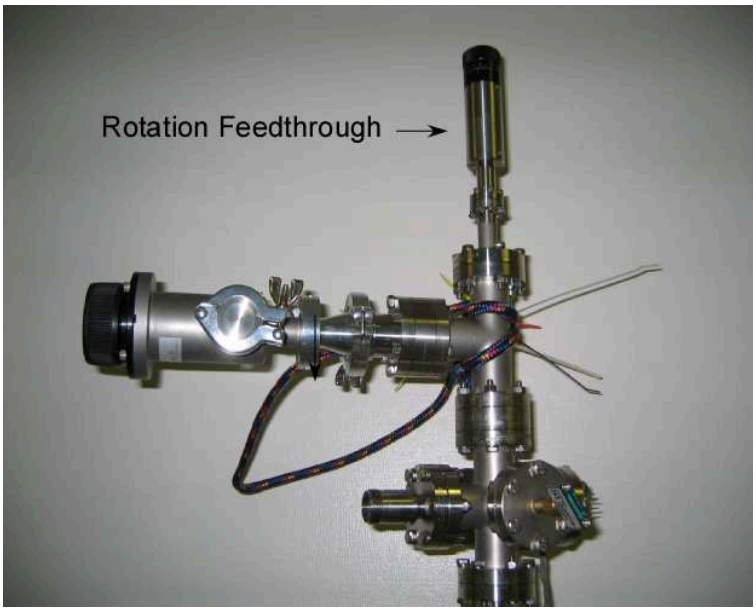


(b)

Figure 49: (a): Shown here is the custom dipstick for the sample, as well as the liquid helium dewar used for housing the dipstick during measurement. (b): Shown here is a zoomed view of the dipstick which displays the rotational actuator which actuates the sample; rotation at the top of the dipstick is coupled to linear elongation of the sample through the bending mechanism.

utilized to conserve as much liquid helium as possible. After the dipstick has been cooled to liquid nitrogen, it is inserted in a liquid helium grade, super-insulated, nitrogen-free dewar which was manufactured by Precision Cryogenic Systems (model PVS-4.0/54); upon transferring liquid helium into the dewar, the dipstick will continue to cool until it reaches 4.2 K. When operating at base temperature, the system has a helium boil off rate of less than 0.8 liters/hr., implying that the system is overall very thermally stable, thus adding to the mechanical stability as well since excess boiling of helium could compromise the sensitive atomic configurations studied. However, though most of our experiments are done in the range of 4.2 K to 10 K (temperature cycling is accomplished through the use of a 150Ω heater resistor), it is possible to pump on the liquid helium bath to further cool the sample space down to approximately 1.5 K.

### 3.4.1 Mechanics and Actuation

With the sample space evacuated and cooled down to liquid helium temperatures, the break junction can finally be elongated to create an atomic contact; to accomplish this, a bending mechanism is used whose operation is detailed in Fig. 50. From the figure, the coarse control is provided by manual actuation at the top of the dipstick, coupled to the sample through a fork and blade mechanism [49] to a 0.5"x40 custom brass microscrew; the microscrew is fed through a fixed stainless steel nut, thereby causing an elongation of the contact, as seen in Fig. 51. The nut for the brass microscrew is made of stainless steel to avoid jamming during coarse actuation. Similarly, the dipstick is normally pumped on for at least 12 hours prior to being cooled down to dehumidify the sample space and prevent freezing from occurring, which could compromise the coarse actuation.

When the coarse actuation has elongated the contact sufficiently, fine control is provided by a cryogenically rated piezoelectric actuator (made by Staveley Sensors) which can very accurately control the bending of the sample substrate. To incorporate both the coarse and fine actuation into one mechanical system, macor pieces were secured to both ends of the piezo with Stycast 2850. These insulating layers provide electrical isolation for the piezo electrodes and prevent potential grounding problems between the sample substrate

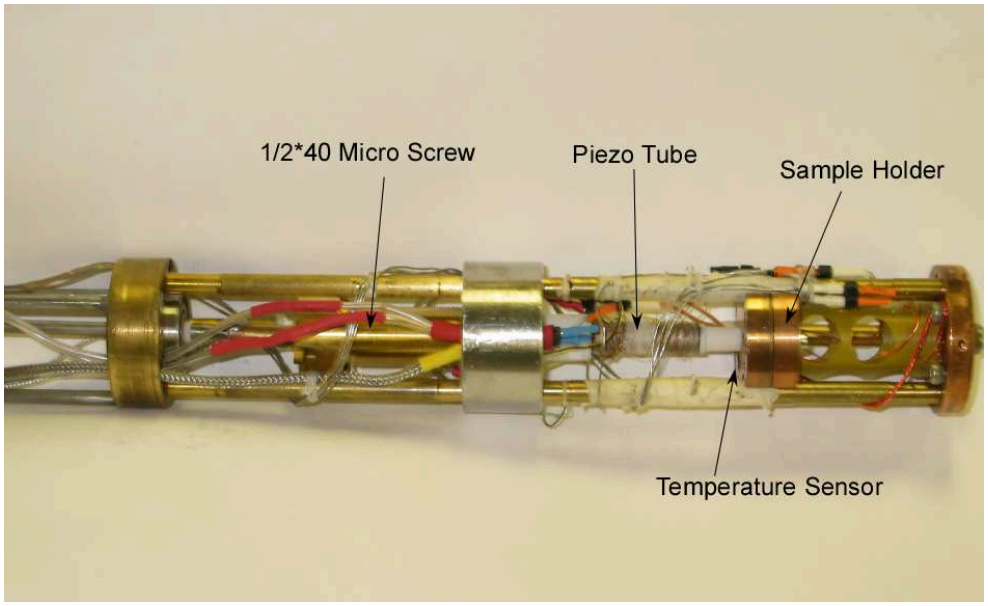


(a)

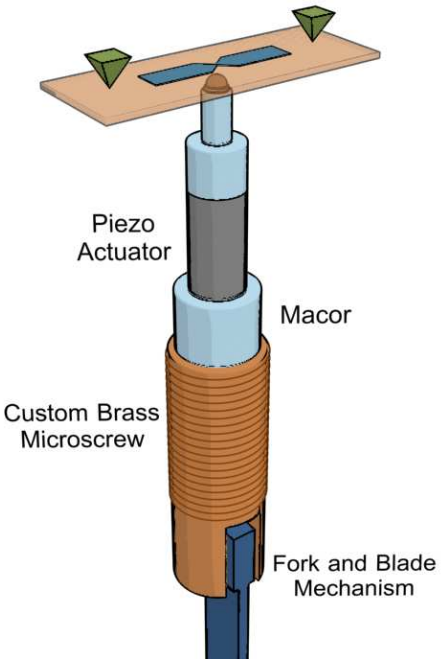


(b)

Figure 50: (a): Here, the actuation mechanism, as well as the sample space can be seen. (b): To couple the rotational motion at the top of the dipstick to the sample, a fork and blade mechanism is used; by rotating the feedthrough at the top of the dipstick, the brass microscrew is fed through a fixed stainless steel nut, creating a coarse actuation of the sample. For finer control of the sample's elongation, a piezoelectric element is incorporated onto the microscrew; to do this, macor pieces are epoxied onto each end of the piezo for electrical isolation from the screw and sample.

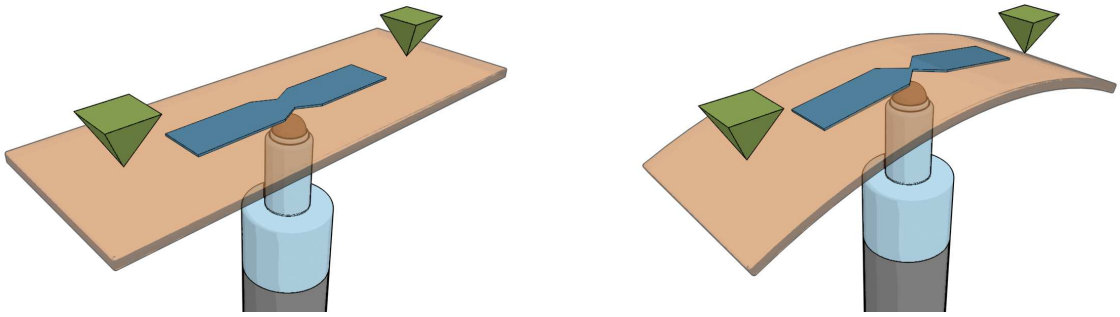

(a) (b)

Figure 51: Shown here is a mock-up of how the point contact is elongated by the bending mechanism; by either coarse actuation via the microscrew or fine actuation via the piezo, the flexible substrate bend, thus elongating the sample.

and the other metallic components of the bending system. From the data provided by the manufacturer of the piezo, the estimated elongation is given as:

$$\Delta L = \frac{|d_{31} L}{t} \cdot V, \tag{116}$$

where $\Delta L$ is the elongation of the piezo tube, $d_{31}$ is the elongation constant for PZT-5A at 4.2 K and is $-0.031$ nm/V, L is the tube length and t is the wall thickness of the piezo; using the values provided by the manufacturer, the total elongation of the piezo is approximately 1.2 $\mu$m over the voltage range of $\pm 400$ V.

### 3.4.2 Elongation Calibration

Due to the fact that the spacing of the two contacts in an MCBJ is dynamically controlled by a piezoelectric actuator which bends the sample substrate from below, the actual displacement of the contact is less than the accompanying piezo elongation. Though this implies that longer piezo elongations are required to extend the sample a given distance, greater mechanical stability is achieved. Specifically, for a given reduction ratio (i.e. the ratio between the contact displacement and the piezo elongation), which depends on the geometry of the sample, external vibrations couple to the contact through the same ratio; thus implying that small reduction ratios are preferred in order to maximize stability.

To calculate the reduction ratio for a given sample geometry, there are two main approaches which are used for calibration. The first, and crudest, approach is to use the expression for the reduction ratio caused by a homogeneous strain in a bending beam:

$$r_d = \frac{3uh}{L^2}, \tag{117}$$

where $r_d$ is the reduction ratio, u is the bridge length, h is the thickness of the sample, and L is the length between the counter supports. In our samples, representative values for these parameters are: u=2 $\mu$m, h=250 $\mu$m, and L=1.5 cm; consequently, these values give a reduction ratio of $2.7 \cdot 10^{-5}$. Given this, plus the specification of our piezo that $\Delta L_{piezo} = 1.55$ nm/V for piezo elongation, a relationship between the applied piezo voltage and contact displacement is found as $\Delta x_c = 4.14 \cdot 10^{-5}$ nm/V; additionally, since the piezo is rated for operation in a range of 400 volts ($\pm$200 V), the total fine adjustment of the contact is approximately 20pm, less than the radius of a hydrogen atom [93]. Thus, this approximate approach is of little practical value due to the incredibly small value obtained.

As such, a more accurate *in-situ* approach is more desirable for high-precision experiments; to this end, the exponential nature of the tunneling current can be exploited to determine the reduction ratio. From elementary quantum theory it is known that the tunneling resistance has the following proportionality:

$$R \propto e^{\frac{\sqrt{8m\Phi}}{\hbar}\delta}, \tag{118}$$

where m is the mass of an electron, $\Phi$ is the work function of the metal, and $\delta$ is the distance between the contacts. Thus, by measuring the tunneling resistance as a function of piezo voltage, the stretch rate of the sample, k, can be found. To do this, another quantity, $\alpha$, is defined such that:

$$\alpha = \frac{\partial \ln(R)}{\partial V} = \frac{2}{\hbar}\sqrt{2m\Phi} \cdot k, \tag{119}$$

Then, the stretch rate is found to be:

$$k = \frac{\hbar}{\sqrt{8m}}\frac{\alpha}{\sqrt{\Phi}} \approx 0.97\frac{\alpha}{\Phi_{eV}}, \tag{120}$$

where $\Phi_{eV}$ is the metal's work function measured in electron-volts. Thus, upon doing a linear fit of tunneling resistance as a function of piezo voltage on a semi-log plot, the resulting

slope is $\alpha$; in our measurements, $\alpha = 0.0042$, which when combined with the work function for niobium (4.3 eV [108]), gives a sample stretch rate of $k = 1.96 \cdot 10^{-4}$ nm/V. However, due to variations in the work function of the metal in the vicinity of the junction, this method could overestimate the actual result by as much as 30%; as such, an ideal calibration would not only measure the reduction ratio *in-situ*, but would also independently measure the work function of the metal. To do this, the most accurate method for calibration involves the measurement of Gundlach oscillations during field emission [126] and which allows an accurate calibration of the displacement, but also a simultaneous measurement of the contact's work function [127]. Nevertheless, using field emission resonance is clearly the preferred method of calibration. Our lab typically resorted to the easier method of measuring the tunneling resistance as a function of piezo voltage and subsequently factored this additional uncertainty into calculations.

### 3.4.3 Circuitry

With the mechanical system in place and calibrated, the next major component of the experimental setup is the circuitry required to perform transport measurements on atomic contacts. For this, the major design consideration is that both the IV and dI/dV must be measured simultaneously while adding as little noise as possible. To do this, a small AC signal is applied over a larger DC bias current, then the resulting voltage across the junction and the differential conductance are subsequently measured. To measure the differential conductance, the AC voltage, which develops across the junction in response to small applied AC bias current, is measured using a lock-in amplifier. Specifically, since the AC signal is assumed to be small, the total voltage across the junction can be Taylor expanded about the DC bias point as:

$$V(I) = V(I_0) + \left(\frac{dV}{dI}\right)_{I_0} (I - I_0) + \left(\frac{d^2V}{dI^2}\right)_{I_0} (I - I_0)^2 + \ldots, \tag{121}$$

where $I_0$ is the DC bias current, I is the total current ($I = I_0 + I_{AC}\sin[\omega_{ac}t + \theta_{ac}]$)and all derivatives are evaluated at the DC bias point. Clearly then, by feeding a signal of this form into a lock-in amplifier whose reference frequency is the AC bias frequency, the output of the lock-in will be proportional to the differential resistance. In actuality, the output

of the lock-in amplifier is simply dV and thus must be divided by dI (which is set by the applied bias) in order to obtain the differential resistance, dV/dI, which is the inverse of the differential conductance. To calculate dI, the following formula is used:

$$|dI| = \frac{|V_{AC}|}{R_{MCBJ} + R_{bias}}, \tag{122}$$

where $R_{MCBJ}$ is the sample's resistance and $R_{bias}$ is the bias resistance which converts the applied voltage into a current.

Extending this analysis to higher orders shows that any derivative of voltage with respect to current can be experimentally measured by a lock-in amplifier by setting the reference signal to the $n^{th}$ harmonic of the applied AC signal.

With the general idea behind the transport measurements given, the specifics of the electronic setup can be seen in Fig. 52. To begin, the AC and DC current bias for the sample must be generated and subsequently combined to form one signal (in combining the two signals, a high pass filter is put into the AC line in order to avoid loading problems from the DC source). This merging is done by using a separate AC and DC voltage source, then combining the two signals into one and passing it through a large bias resistor (in the range of 1MΩ-1GΩ); the specific value is set by the need to have the bias resistor be much larger than the sample resistance. For instance, a larger bias resistor will be needed for tunnel junctions ($R_{MCBJ} \approx 100k\Omega$) in order to satisfy the biasing requirement.

The DC voltage source is a Stanford Research Systems (SRS) SIM928 rechargeable, isolated voltage source which is controlled through a GPIB connection via Labview; additionally, the AC voltage is supplied by a SRS DS345 function generator which is also controlled by Labview through a GPIB connection. In order to minimize losses in the bias current, the bias resistor is positioned on the electrical flange of the dipstick; in this way, the current path is shortest and thus cable losses from the resistor to the sample are minimized. Furthermore, due to the inherently small AC signal ($\approx 1mV$), care must be given to ensure that the signal to noise ratio is sufficiently large from the source to the bias resistor. To do this, a large AC voltage is applied at the function generator which is able to propagate down the signal wire with a relatively large signal to noise ratio. Then, the signal undergoes

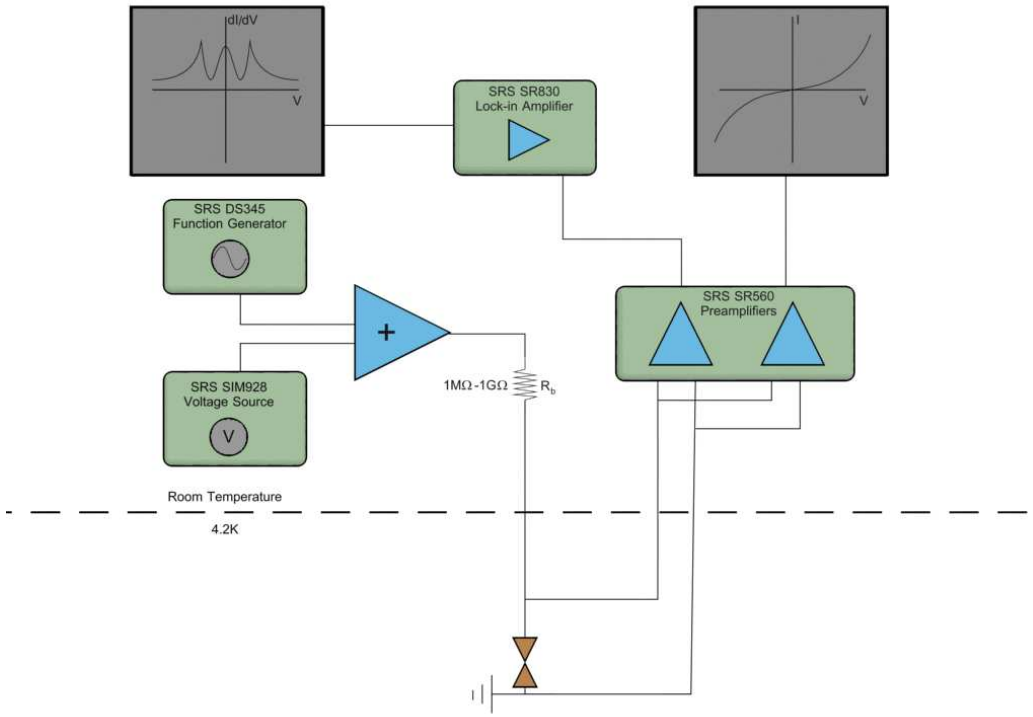


(a)

(b)

Figure 52: (a): In our experimental setup, the point contact is current biased by passing a combined DC and AC voltage across a large bias resistor; the resulting voltage which develops across the junction is measured, amplified, and processed in order to obtain both the DC voltage across the junction, as well as dV for differential conductance measurements. (b): Photograph of the experimental setup.

-40 dB of attenuation when it reaches the bias resistor, which brings the voltage down to the appropriate level.

Once the bias voltages have been converted into a current, the resulting signal is applied to the sample and the voltage drop across the junction is measured. In order to simultaneously measure both the voltage and differential conductance of the sample, the voltage leads from the dipstick are split and fed into separate AC and DC preamps (both are SRS SR560 low noise, voltage preamplifiers). For the AC signal, the preamp is AC coupled and the integrated bandpass filter is used with a rolloff of -6 dB/octave and cutoff frequencies of 100 Hz and 300 Hz respectively (the AC frequency of the current is typically 200 Hz). For the DC signal, DC coupling is used with a low pass filter whose cutoff frequency is 3 Hz with -6 dB/octave as well. Once the DC signal has been amplified and filtered, it is fed directly into a National Instruments BNC-2090 connector block which interfaces with a National Instruments PCI-6221 data acquisition board; because the only operation performed on the DC voltage is amplification, it is simply a matter of dividing our the DC gain to reclaim the original signal. In contrast, the AC signal must undergo an additional step of phase sensitive detection at the lock-in amplifier (SRS830) to extract the component of the signal at the bias frequency; once this is completed, the resulting signal is transmitted via GPIB to the control computer. In this case, not only must the AC amplification be taken into account, scaling due to the lock-in amplifier itself must also be considered. Specifically, the expression for calculating the original signal from the output of the lock-in amplifier is given by:

$$V_{real} = S\left(\frac{V_{meas}}{10E} + O\right), \tag{123}$$

where $V_{real}$ refers to the actual voltage one wants to measure, S is the sensitivity of the lock-in, $V_{meas}$ is the signal which is output by the lock-in, E is the expand parameter of the device, and O refers to the offset of the lock-in. In addition to this scaling, the gain due to the AC amplifier must be taken into account; thus, the total expression relating the AC voltage measured by the lock-in to the real AC voltage across the junction is given by:

$$V_{real} = \frac{S}{G_{AC}}\left(\frac{V_{meas}}{10E} + O\right), \tag{124}$$

where $G_{AC}$ is the AC gain of the system. With dV measured, the differential conductance of the sample can be found by calculating dI, as given previously, and forming the ratio of dI and dV.

## *3.5 Extraction of the Conductance Channel Composition*

### 3.5.1 Background

From both the Landauer and the multiple Andreev reflection formalism detailed in previous chapters, it is clear that the mesoscopic PIN code of a device is a fundamental quantity in terms of calculating the transport properties of the device. With this in mind, a systematic method of determining the PIN code of a device from experimental data is necessary. However, using the normal state effect of conductance quantization is not sufficient to accurately determine the PIN code, there is not enough unique information contained in the data to unambiguously calculate the PIN code. On the other hand, by utilizing the highly nonlinear current-voltage curves of the subgap structure in SNS devices, the PIN code of the device can be completely extracted.

To do this, the experimental data must be fit to a sum of theoretical IV curves:

$$I(V) = \sum_{j=1}^{N} i(V, \tau_j, \Delta), \tag{125}$$

where N is the number of channels in the contact, $\tau_j$ is the transmission coefficient of the $j^{th}$ channel and $\Delta$ is the superconducting gap parameter. This method of extracting the PIN code by decomposing the subgap structure into individual channels was first experimentally demonstrated by Scheer et.al. [200] on Al contacts. For our fits, the theoretical curves were calculated using a FORTRAN code provided by Åke Ingerman and John Lantz at Chalmers University, which itself uses the model given by Bratus', Shumeiko, and Wendin [40] for a BCS superconductor. Representative curves given by this code can be seen in Fig. 53. One significant advantage our code has over others [49] is that the IV curves can be calculated at any temperature up to $T_c$, as can be seen in Fig. 54, thereby eliminating any errors associated with thermal broadening of the MAR steps. However, one disadvantage and potential source of error in the fits is that the theoretical curves are calculated for an

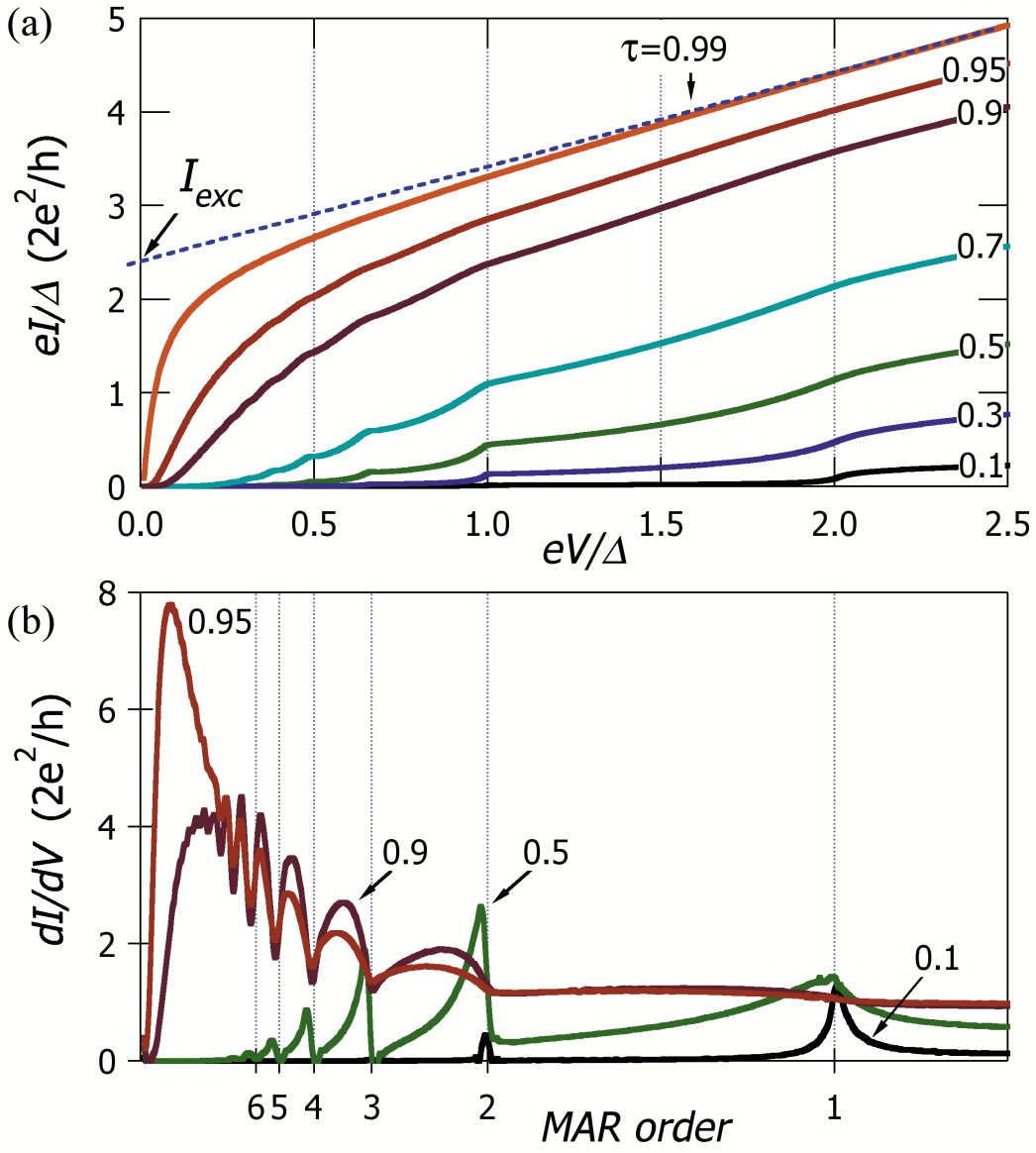


Figure 53: (a): Shown above are numerically calculated current-voltage curves for point contacts of various transmissions. Notice the transition from tunnel junction to a ballistic point contact as the transmission is increased. (b) Here, we see numerically calculated differential conductance curves plotted with different transmission coefficients. For low voltages, the only peak in the differential conductance occurs at eV=2Δ, allowing a simple experimental observation of the gap.

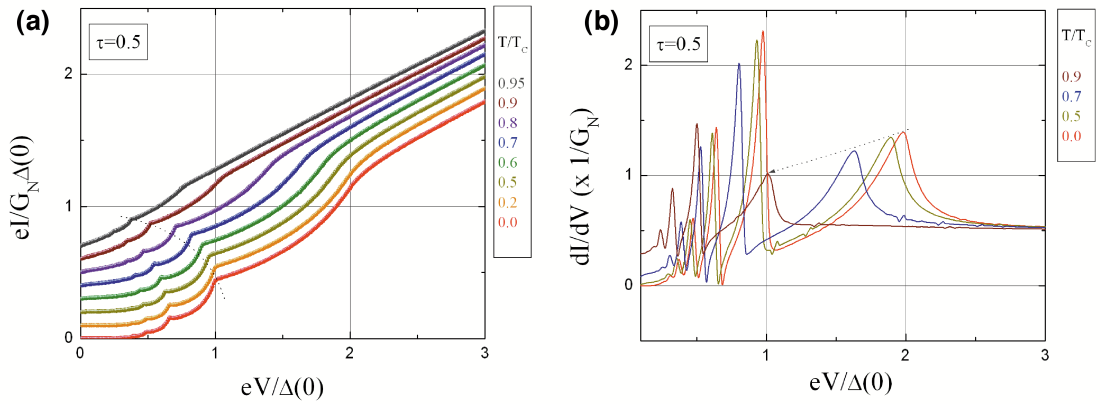


Figure 54: Here the effect of temperature on both the current-voltage and the differential conductance curves for a point contact can be seen; for low temperatures, the curves are dominated by the highly non-linear features associated with MAR. However, as the temperature is raised to $T_c$, the curves become more ohmic in nature, signifying the onset of dissipative processes inside the junction.

ideal BCS superconductor, which is an idealization of true behavior. Nevertheless, elements such as aluminum deviate little from ideal BCS behavior, whereas elements such as niobium show small to moderate deviation from ideal behavior. Furthermore, there are additional systematic errors produced by the A/D conversion of our data acquisition board, as well as an additional error which is incurred due to the necessity of interpolating our data. Specifically, since the theoretical curves are calculated by assuming a voltage bias across the junction, instead of a current bias as in our experiments, there will be some error associated with the need to interpolate our data to compare the theoretical curves and the experimental data sets.

However, before the actual fitting procedure can be employed, the experimental data must be appropriately scaled to the dimensionless units which the theoretical curves use. Specifically, the dimensionless voltage, $eV/\Delta$, and the dimensionless current, $eI/G_0\Delta$ are used. Since both of these quantities rely on scaling the superconducting gap parameter, $\Delta$, the gap must either be approximated or measured experimentally. To approximate it, the following BCS result can be used: $\Delta = 1.76 k_B T_c$ [219]. However, the gap parameter is always experimentally measured, in practice, by fitting a deep tunneling curve, as in Fig. 55. Deep tunneling implies that the channel composition is reduced to one weakly

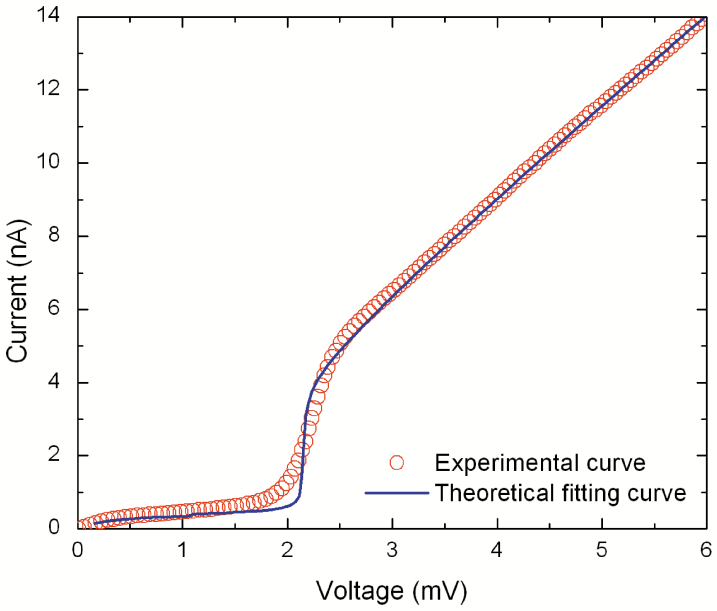


Figure 55: A characteristic current-voltage curve for a tunnel junction, along with the best fit obtained from the numerically calculated data; for this curve, only one channel is required to accurately fit the experimental data.

transmitting channel, thereby leaving only 2 degrees of freedom for the curve: $\Delta$ and $\tau$.

### 3.5.2 Fitting Procedure

To find the best fit for the experimental data, a metric must first be constructed to measure how good of a fit has been achieved with a set of transmission coefficients. For our code, the metric is the norm of the difference between the experimental results and the theoretical set of IV curves, known as $\chi^2$:

$$\chi^2 = \frac{1}{M}\sum_{j=1}^{M}\left(I(V_j) - \sum_{k=1}^{N} i(V_j, \tau_k, \Delta)\right). \tag{126}$$

Hence, the problem reduces to finding a vector of transmission coefficients which minimizes $\chi^2$, given the number of channels and the superconducting gap for the data. By the very nature of atomic contacts, there are only a few conductance channels for the system (typically 1 to 6). In fact, it has been shown [198] that the number of channels is directly related to the chemical valence of the constituent atoms for atomic contacts. Thus for aluminum, three channels typically suffice to accurately describe the transport properties, whereas five

channels are generally necessary to achieve a sufficiently small $\chi^2$ for niobium. Though fits with higher channel numbers can be done, the quality of the fit increases negligibly.

The fitting procedure begins with the calculation of 1000 model theoretical curves, at a given temperature, with transmission ranging from 0.001 to 0.999. With this many model curves to choose from, the calculation of $\chi^2$ for all possible transmission vectors would require the determination of $1000^n$ combinations, where n is the number of channels. For six channels, there would then be $10^{18}$ possible combinations of transmission coefficients that the system could take, which is far too great to be computed by brute force, even when the 6-fold degeneracy of the vectors is taken into account, i.e. $\chi^2([\ldots,\tau_i,\ldots,\tau_j,\ldots]) = \chi^2([\ldots,\tau_j,\ldots,\tau_i,\ldots])$. Thus, other methods must be found which can quickly and accurately determine the PIN code of a sample.

Many standard optimization techniques were tried in order to accurately extract the PIN code: Monte Carlo simulations, Steepest Descent methods and also hybrid codes which employed both Monte Carlo and Steepest Descent algorithms, to name a few. In the end, a modified Steepest Descent procedure gave accurate results in a reasonable length of time ($\approx$ 5 minutes) for the PIN code of a niobium contact. The fitting procedure is schematically outlined in Fig. 56, where blocks are used to represent a three channel transmission vector. Here each block corresponds to a set, $[\tau_i, \tau_j, \tau_k]$), over which the $\chi^2$ can be determined. Furthermore, clear blocks represent a set whose $\chi^2$ has not been determined yet, whereas blocks with color represent sets which have been calculated.

Following the procedure outlined in the figure, the major computational steps involved in determining the PIN code are:

- First, perform a $\chi^2$ line search over the transmission vector $[\tau_i, 0, 0, \ldots, 0]$ to determine the local minimum of that subset.

- With the first minimum determined, throw away all other calculated points and search the vicinity of that point to determine if a new minimum exists.

- Continue this process until no new minimum is found; at that point the code has found a global minimum of the $\chi^2$ metric.

One point which should be mentioned is that the $\chi^2$ function itself is continuous and contains no local minima, which has been determined via a full calculation of $\chi^2$ for multiple data sets. If this were not the case, it would not be guaranteed that a true global minimum of $\chi^2$ was found. Further, since there is an n-fold degeneracy of $\chi^2$, the minimization only needs to be performed over a subset of the entire range of transmission vectors. Additionally, by restricting the support set of $\chi^2$ to only unique values, we ensure that there will be only one global minimum.

### 3.5.3 Results

With a systematic procedure in place to extract the PIN code from experimental data, the quality of fits can be compared as the number of channels is increased, the result of which can be seen in Fig. 57. Clearly, as the channel number increases, the fit becomes increasingly better. However, the fit does not appear to become significantly better as the channel number is increased above 4 channels. This observation can be quantified by using the values of $\chi^2$ to determine how much the fit error decreases as the channel number increases; which is seen in Fig. 58. Here, the values of $\chi^2$ are normalized to the value for the one-channel case, thereby making numerical comparisons between fits of different channel numbers more meaningful. From the figure, it is apparent that the decrease in $\chi^2$ becomes almost negligible above four channels, confirming the observation made earlier concerning Fig. 57. Additionally, this corroborates studies which reported that niobium can be characterized as having five conductance channels which contribute to mesoscopic transport. Another interesting feature, which can be seen in Fig. 57, is the tendency for the channel transmission vector to be degenerate in a particular transmission coefficient. From the figure, whether there are either 3, 4, or 5 channels, a degenerate or nearly degenerate pair of transmission coefficients exist. This peculiar observation is echoed in current literature [55, 49, 50], though never mentioned specifically; this fact implies that the degeneracy is not imposed by the computational algorithm used to extract the code. Moreover, multiple optimization algorithms used to determine the PIN code all show signs of this degeneracy. Further, a brute force calculation of the PIN code for one sample which showed degeneracy

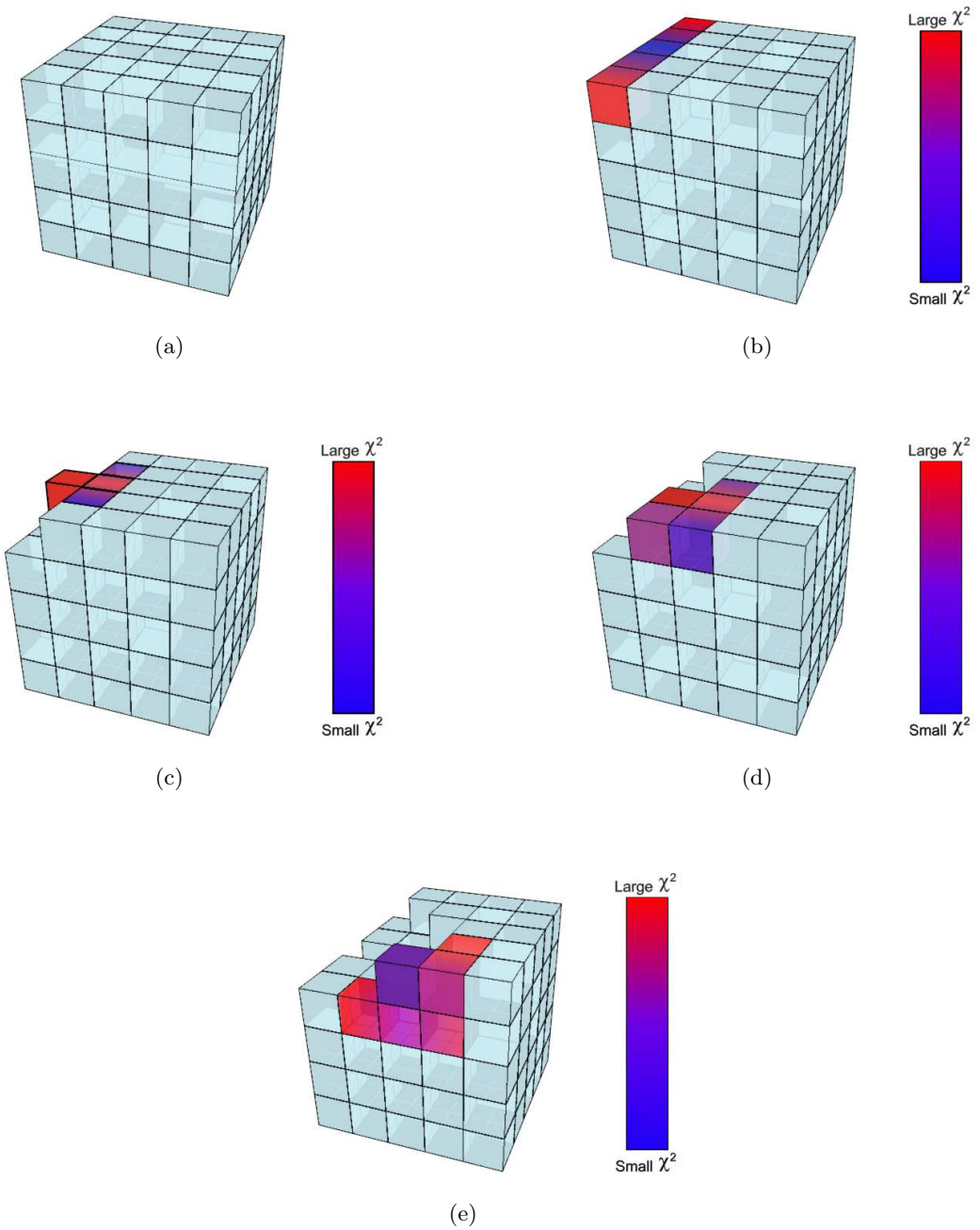


Figure 56: Here, the basic process underlying the evaluation of the PIN code is shown, where each block represents a set of transmission coefficients with the number of elements of the set being given by the number of conductance channels of the system (typically 5 for niobium). The clear blocks represent sets which have not been calculated yet, whereas the colored blocks represent sets for which the $\chi^2$ has been calculated; by following the procedure outlined in the text, one can successively follow the line of steepest descent until a minimum in $\chi^2$ is found.

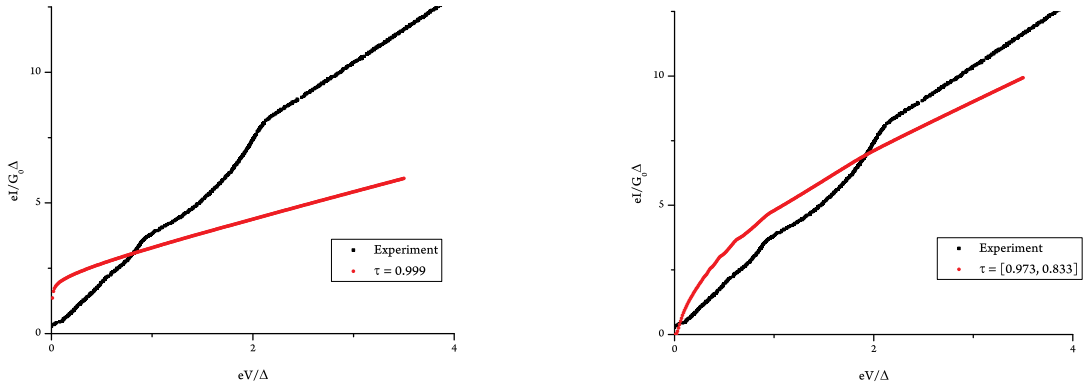


(a)




(b)

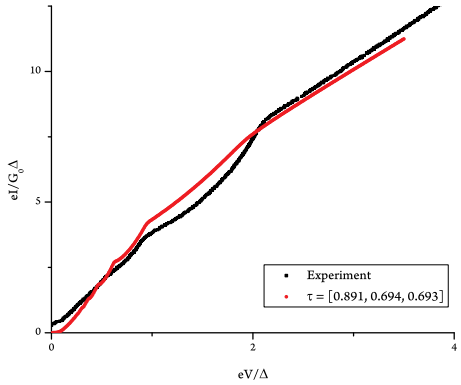


(c)

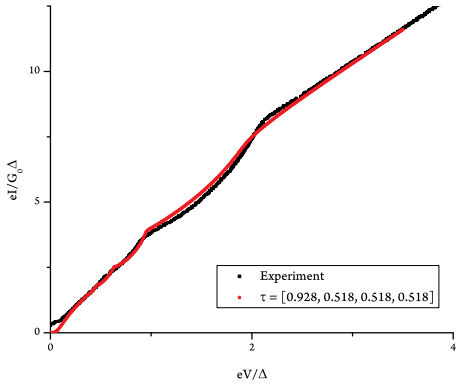


(d)

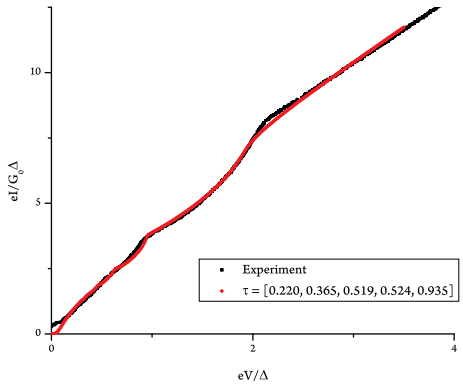


(e)

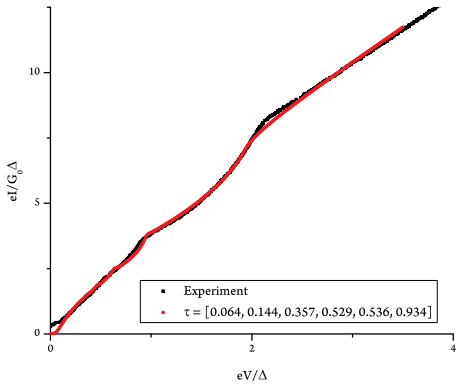


(f)

Figure 57: Here we see the evolution of the curve fit as the number of channels is increased for a set of experimental data; one can see that above 4 channels, the numerically determined curve fit gives a good representation of the experimental data.

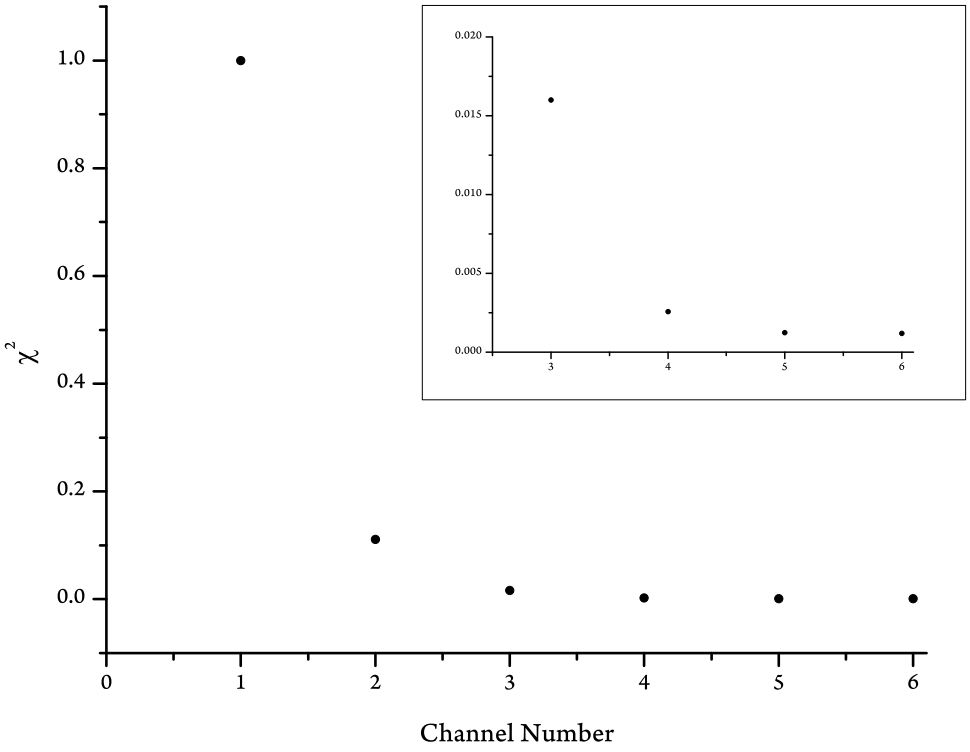


Figure 58: Here the value of $\chi^2$ as a function of channel number is plotted for the same data presented in the previous figure; to make comparisons easier, the $\chi^2$ are normalized to the value obtained for a one channel fit. From the inset of the figure, the quality of the fit does not appreciably change above four channels; this confirms earlier studies which postulated that niobium can be considered as having five conductance channels.

in the transmission vector has been done and confirms the existence of a degenerate pair. Additionally, for the four and five channel cases in the figure, a degenerate channel can be broken into two less conducting channels of almost the same overall magnitude by adding an extra conductance channel. However, though degeneracy is apparent in much of the experimental data our group has taken, as well as in other groups working on mesoscopic physics, the degeneracy does not appear in all samples and does not seem to appear in any systematic way. Hence, for now it seems that the tendency of these mesoscopic systems to prefer degenerate transmission vectors is an interesting observation which will require more in-depth analysis before concrete conclusions can be drawn.

## *3.6 Structural and Transport Calculations*

### 3.6.1 Density Functional Theory

As is well known from elementary quantum mechanics, all observable properties of a system can be calculated if its wave function is given; furthermore, the Schrödinger equation gives a prescription for calculating the wave function, given the setup of the system:

$$\left[\sum_{i}^{N}\left(\frac{-\hbar^2\nabla_i^2}{2m}+v(\mathbf{r}_i)\right)+\sum_{i<j}U(\mathbf{r}_i,\mathbf{r}_j)\right]\Psi(\mathbf{r}_1,\mathbf{r}_2,\ldots,\mathbf{r}_N)=E\Psi(\mathbf{r}_1,\mathbf{r}_2,\ldots,\mathbf{r}_N), \quad (127)$$

where N is the number of electrons, U($\mathbf{r}_i,\mathbf{r}_j$) is the electron-electron interaction, and v($\mathbf{r}_i$) specifies the external potential of the system (including electron-ion interactions). If only Coulomb interactions are considered, both U and v share the same form:

$$\hat{U}=\sum_{i<j}U(\mathbf{r}_i,\mathbf{r}_j)=\sum_{i<j}\frac{q^2}{|\mathbf{r}_i-\mathbf{r}_j|}, \quad (128)$$

$$\hat{V}=\sum_{i}v(\mathbf{r}_i)=\sum_{ik}\frac{qQ_k}{|\mathbf{r}_i-\mathbf{R}_k|}, \quad (129)$$

where $Q_k = Z_k e$, $Z_k$ is the valence of the $k^{th}$ ion and $R_k$ is the position of the $k^{th}$ ion. Because the expression for $\hat{U}$ is a sum over pairs of electrons, the wave function which results from this Hamiltonian will be drastically different from the standard single-particle wave-function; in fact, it is only through $\hat{U}$ that many-body effects enter into the Hamiltonian. In addition, from the structure of the Hamiltonian, only three parameters are needed to completely specify the system: the number of electrons, the positions of the lattice ions, and

the charge of each lattice ion. Given these three quantities which specify the Hamiltonian, and thus the wave function, any observable can be computed. This progression can be represented in the following way:

$$v(\mathbf{r}) \Rightarrow \Psi(\mathbf{r}_1, \mathbf{r}_2, \ldots, \mathbf{r}_N) \Rightarrow \hat{O} = \langle\Psi| \ldots |\Psi\rangle. \tag{130}$$

However, calculating observables using this method of first finding the wave function is prohibitively complex for almost any system; in fact, exact solutions exist only for systems of less than ten atoms. As such, approximate methods are necessary to compute the wave function of any real system. As an example, by simply discretizing a 10 electron wave function over a mesh of 20 points per degree of freedom (a very coarse approximation), there would need to be $20^{30}$ values calculated in order to describe $\Psi$ over the mesh. Thus, considering the amount of storage space and computation power necessary for calculating the wave function of a system, better methods than simply discretizing the wave function over a mesh are necessary. Ideally, instead of making drastic approximations to the wave function at the outset (as in the Hartree-Fock approximation [47, 213]), one would be able to only eliminate the unnecessary or redundant information contained in the wave function.

One way of doing this is by neglecting the wave function altogether, and instead promoting the electron density, n($\mathbf{r}$), to the role of the key computational variable. In doing so, a function of 3 variables is substituted for a function of 3N (neglecting spin) variables. If the electron density is a valid computational variable (i.e. if all observables are able to be computed from the electron density), then it would require $10^{35}$ less storage space than the wave function in the example given above, a considerable computational savings. However, the question of plausibility still remains: is it possible to calculate observables from the electron density? First, the electron density is given by the expression:

$$n(\mathbf{r}) = N \int d^3r_2 \int d^3r_3 \ldots \int d^3r_N \Psi^*(\mathbf{r}_1, \mathbf{r}_2, \ldots, \mathbf{r}_N)\Psi(\mathbf{r}_1, \mathbf{r}_2, \ldots, \mathbf{r}_N). \tag{131}$$

From this definition, it is clear that:

$$\int n(\mathbf{r}) d^3r_1 = N. \tag{132}$$

Furthermore, the density has the property that its maxima occur only at the positions of the lattice ions, $\mathbf{R}_i$, and that the maxima are cusps [123]; also, the density at the position of the nucleus follows the expression:

$$\lim_{r\to 0}\left[\frac{\partial}{\partial r}+2Z_i\right]n(\mathbf{r})=0. \tag{133}$$

From these three properties, the electron density is intimately related to the three parameters which are required to unambiguously define v($\mathbf{r}$). Knowledge of v($\mathbf{r}$) implies knowledge of the many-body wave function and thus any observable, which can be written as:

$$n(\mathbf{r})\Rightarrow v(\mathbf{r})\Rightarrow \Psi(\mathbf{r}_1,\mathbf{r}_2,\ldots,\mathbf{r}_N)\Rightarrow \langle\Psi|\ldots|\Psi\rangle. \tag{134}$$

However, by taking the electron density as the key variable, a paradigm shift has been made whereby the energy of the system is a functional of the density, E=E[n]; thus, the kinetic and potential energy of the system must also be functionals of the density. Specifically, the external potential can be expressed as:

$$\hat{V}=\int d^3r n(\mathbf{r})v(\mathbf{r}), \tag{135}$$

which is system-specific, but easily calculated once an electron density is given. On the other hand, even though the kinetic energy, $\hat{T}$, and potential energy, $\hat{U}$, are universal functionals in that they are not system specific, there are no explicit functional forms for $\hat{T}$ or $\hat{U}$ in terms of the density. Thus, though it is certainly probable that the electron density is sufficient to describe the observables of a system, these arguments must first be placed on a more formal footing and then a procedure must be put into place whereby the universal functionals can be computed.

The first step was taken by Hohenberg and Kohn in their landmark paper [107] which began the field of density functional theory by showing that there cannot be two external potentials which yield the same electron density. In other words, the first Hohenberg-Kohn theorem shows that the ground state electron density uniquely determines the external potential, the wave function, and all observables of a system. Thus, the ground state energy of a system can be expressed as:

$$E_0[n_0]=T[n_0]+U[n_0]+V[n_0], \tag{136}$$

where brackets denote functional notation. Next, Hohenberg and Kohn showed in their second theorem that any trial density must produce a ground state energy which is greater than or equal to the true density (i.e. $\mathrm{E}_{trial} \geq E_0$), which is nothing more than the variational principle applied to densities instead of wave functions. However, though they showed that the density can be elevated to the status of a key variable, Hohenberg and Kohn gave no prescription for dealing with the energy functionals which their approach utilized; in fact, the exact forms of the energy functionals are unknowable in all likelihood. As such, approximate methods are required to move forward with calculating observables with the electron density.

To that end, Kohn and Sham developed an approach [125] for dealing with the density functionals in an efficient way; the key to their approach centered on the largest contribution to the energy of the system, the kinetic energy. The Kohn-Sham approach begins with breaking the kinetic energy functional into two parts: one which is the kinetic energy for a set of non-interacting particles, $\mathrm{T}_s$, and the remainder term which includes correlation effects, $\mathrm{T}_c$. This set of non-interacting particles are imaginary in the sense that they do not refer to the true physical system; instead, they are a set of wave functions, called Kohn-Sham orbitals, which satisfy the following equation:

$$n_0(\mathbf{r}) = \sum_{i}^{N} \sum_{s} |\phi_i(\mathbf{r}, s)|^2. \tag{137}$$

Thus, there is considerable freedom in choosing an appropriate basis set of Kohn-Sham orbitals: as long as the basis set meets the above criteria, it is a valid basis.

In addition to the kinetic energy, the potential energy is separated into two terms: one being the standard Coulomb potential, $\mathrm{U}_c$, and the other being the remainder term, $\mathrm{U}_r$. By grouping the unknown quantities into one term, the total energy functional can be expressed as:

$$E[n] = T_s[n] + U_c[n] + E_{xc}[n] + V[n], \tag{138}$$

where $\mathrm{E}_{xc}$ is known as the exchange-correlation energy and is, by definition, the sum of the two remainder terms mentioned above. A more physically intuitive description of the exchange-correlation energy is the amount of energy lowering which is associated with both

electrostatic repulsion and the Pauli exclusion principle. Because electrons cannot be in the same state (Pauli principle) and are much less likely to be near one another (electrostatic repulsion), the many-body system is correlated and a subsequent reduction in total energy ensues.

Of major importance to density functional theory is the fact that the formula for the energy is a formally exact expression. Given an expression for the exchange-correlation energy, all terms could be computed exactly with no approximations necessary. This is in stark contrast to other methods such as Hartree-Fock which presume an approximate wave function at the outset and subsequently suffer in accuracy. Although the energy functional in DFT is technically exact, due to the unknown nature of the exchange-correlation functional, approximations must be made in order to calculate the total energy of the system. However, the advantage in not making approximations until this point is that the exchange-correlation energy is presumed to be small in comparison to the other terms in the energy functional which are capable of being computed exactly. Many different approximations exist for the exchange-correlation energy, though by far the two more common are the Local Density Approximation (LDA) and the Generalized Gradient Approximation (GGA). The LDA assumes a density functional for the exchange-correlation energy which depends solely on the density at a given point, whereas the GGA assumes an additional gradient term for the density. In this way, the GGA can be considered as the second order term in a power series approximation, though GGA can be expanded to include functional forms which are not consistent with the power series approximations (true power series approximations are typically known as Generalized Expansion Approximations (GEA)).

In addition to redefining the energy functional, Kohn and Sham were able to map the true many-body problem into a single-particle problem by defining the exchange-correlation potential, $V_{xc}$, of the system as:

$$V_{xc} = \frac{\partial E_{xc}}{\partial n}. \tag{139}$$

With this definition, the effective one-body problem for a Kohn-Sham orbital is given by:

$$\left( -\frac{1}{2}\nabla^2 + \int \frac{n(\mathbf{r}_2)}{|\mathbf{r}_1 - \mathbf{r}_2|} d^3 r_2 + V_{xc}(\mathbf{r}_1) - \sum_j^M \frac{Z_j}{|\mathbf{r}_1 - \mathbf{r}_j|} \right) \phi_I = \epsilon_i \phi_i. \tag{140}$$

Thus, once the terms in the above equations are known, the equivalent Kohn-Sham orbitals can be calculated, from which the ground state density can be found using equation (137). However, the above equation already implicity depends on the ground state density through the Coulomb term, meaning that the energy must be determined self-consistently.

Now, with a general prescription for determining the ground state energy of a system, given the ground state electron density, are there other quantities besides the energy which DFT can calculate? The answer is that many other important quantities can be computed by using the DFT formalism. For instance, if the lattice constant of a solid, a, is varied over a given range and the resulting energies are calculated, the minimum of energy for these points gives the correct lattice constant for the system. By extending this approach, more complicated geometries, bond angles, and charge distributions can be computed using the DFT approach. Furthermore, by comparing the total energy of a system with that of its constituents, the disassociation energy can be found; as well, atomic forces can be calculated using the Hellman-Feynman theorem. Thus, without having to solve the full many-body problem or having to appeal to approximate wave function methods, DFT provides a way to efficiently calculate many important physical quantities.

### 3.6.2 Non-Equilibrium Green's Function Formalism

With an approach in place for determining the ground state electron density of a system, the next step is to use this information to determine the transport properties of the system. To do this, a technique known as Non-Equilibrium Green's Functions (NEGF) calculations are employed [37, 216, 59]. This method is advantageous in that it is easier to implement than solving the full Schrödinger equation (as with DFT) and most of the properties of a system can be calculated from Green's functions, specifically transport related quantities such as the current.

To begin, given a system with a constant perturbation:

$$\hat{H}|\psi\rangle = E|\psi\rangle + |v\rangle, \tag{141}$$

where $|v\rangle$ is the perturbation to the system and the Green's function for the system is

defined as:

$$(E - \hat{H})|\psi\rangle = -|v\rangle \Rightarrow |\psi\rangle = -G(E)|v\rangle, \tag{142}$$

Furthermore, for most transport calculations, the system is broken down into three parts

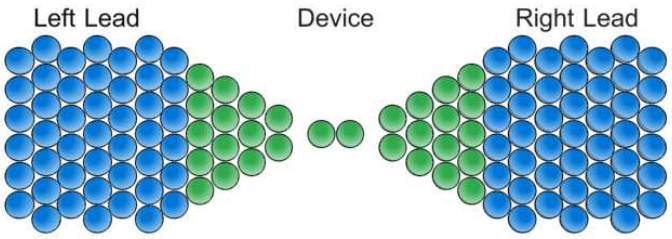


Figure 59: Schematic of the way a NEGF calculation is set up; the total system is broken down into three parts: each of the leads and the device region.

as seen in Fig. 59, with two of them being the leads and the third being the device itself. In this way, the Hamiltonian for the system can be written as:

$$\begin{pmatrix} H_1 & \tau_1 & 0 \\ \tau_1^\dagger & H_d & \tau_2^\dagger \\ 0 & \tau_2 & H_2 \end{pmatrix} \begin{pmatrix} |\psi_1\rangle \\ |\psi_d\rangle \\ |\psi_2\rangle \end{pmatrix} = E \begin{pmatrix} |\psi_1\rangle \\ |\psi_d\rangle \\ |\psi_2\rangle \end{pmatrix}. \tag{143}$$

Next, the wave functions in the above equation can be substituted for the Green's function, yielding:

$$\begin{pmatrix} E - H_1 & -\tau_1 & 0 \\ -\tau_1^\dagger & E - H_d & -\tau_2^\dagger \\ 0 & -\tau_2 & E - H_2 \end{pmatrix} \begin{pmatrix} G_1 & G_{1d} & G_{12} \\ G_{d1} & G_d & G_{d2} \\ G_{21} & G_{2d} & G_2 \end{pmatrix} = \begin{pmatrix} I & 0 & 0 \\ 0 & I & 0 \\ 0 & 0 & I \end{pmatrix}, \tag{144}$$

where each $G_{ij}$ is a matrix itself. By solving the above system of equations for the Green's function of the device, the following expression is found:

$$G_d = (E - H_d - \Sigma_1 - \Sigma_2)^{-1}, \tag{145}$$

$$\Sigma_j = \tau_j^\dagger g_j \tau_j, \tag{146}$$

where $\Sigma_j$ is the self energy of contact j. Thus, the Green's function for the device in the presence of the leads is changed from its isolated value by the addition of the two self energy terms. In addition to the Green's function and the self-energy, another useful quantity is given in terms of the self-energy matrices:

$$\Gamma_j = i(\Sigma_j - \Sigma_j^\dagger). \tag{147}$$

With this definition, the total charge density of the system can be expressed as:

$$\rho = \frac{2}{2\pi} \int_{E=-\infty}^{\infty} dE \sum_i f(E, \mu_i) G_d \Gamma_i G_d^\dagger, \tag{148}$$

where the factor of two in the numerator comes from accounting for the electron's spin and the factor f(E,$\mu_i$) is the Fermi function. Similarly, an expression for the current through the device can be calculated as:

$$I = \frac{e}{\pi\hbar} \int_{E=-\infty}^{\infty} dE[f(E, \mu_1) - f(E, \mu_2)] Tr(G_d^\dagger \Gamma_2 G_d \Gamma_1), \tag{149}$$

which has the same form as the Landauer formula for the current through a mesoscopic device without reference to transmission coefficients.

Using the formula for the charge density given above, a self-consistent DFT-NEGF loop can be created in order to calculate transport properties of a system [39]. By assuming a specific charge density, the resulting structure and potential can be found; from this, NEGF can calculate the charge density which results from this potential. If the resulting density is within the specified tolerance of the initial density, a self-consistent solution has been found and the NEGF formalism can be applied to calculating the current or other transport properties of the system.

# CHAPTER IV

# VIBRONIC EFFECTS IN NIOBIUM NANOWIRES

Chapter IV details experimental results which show coupling of a nanowire's vibrational mode to a superconducting degree of freedom for the first time. Previously, similar experiments have shown vibronic (vibrational+electronic) coupling between a normal metal and a nanowire; however, the effect described here has a completely separate origin from that of normal vibronic coupling. To begin, the frequency range of the AC Josephson effect must be investigated, since that will determine the efficacy of vibronic coupling in superconducting point contacts. Specifically, because vibrational modes typically lie in the low THz band, the AC Josephson effect must be capable of producing frequencies in this band for coupling to exist. Once this is proven, the next step is to show that niobium naturally forms a dimer during the final stages of elongation of the point contact. In this regime, the vibrational modes of the system were calculated using DFT simulations and shown to lie in the low THz range, as expected. Because niobium point contacts have an intrinsic molecule which bridges the gap between the superconducting electrodes, they are ideal systems for testing vibronic coupling. As such, with the vibrational frequencies calculated, the next step was to calculate the corresponding resonant voltages and experimentally investigate the possibility of vibronic coupling. In this way, it was shown for the first time that a superconducting degree of freedom can excite a vibrational mode of a nanowire.

## *4.1 Motivation*

### 4.1.1 Vibronic Coupling in Normal Systems

It has been well established that for normally conducting systems containing a small number of atoms, electrical degrees of freedom can interact with the mechanical modes of the atomic system [210, 82, 182, 106, 74, 241]. This interplay between different degrees of freedom manifests itself as changes in the transport properties of the system, as shown schematically in

Fig. 60. This type of system and the associated modifications in the current-voltage curves are shown in Fig. 60 for a model system. From the figure, when the applied voltage satisfies

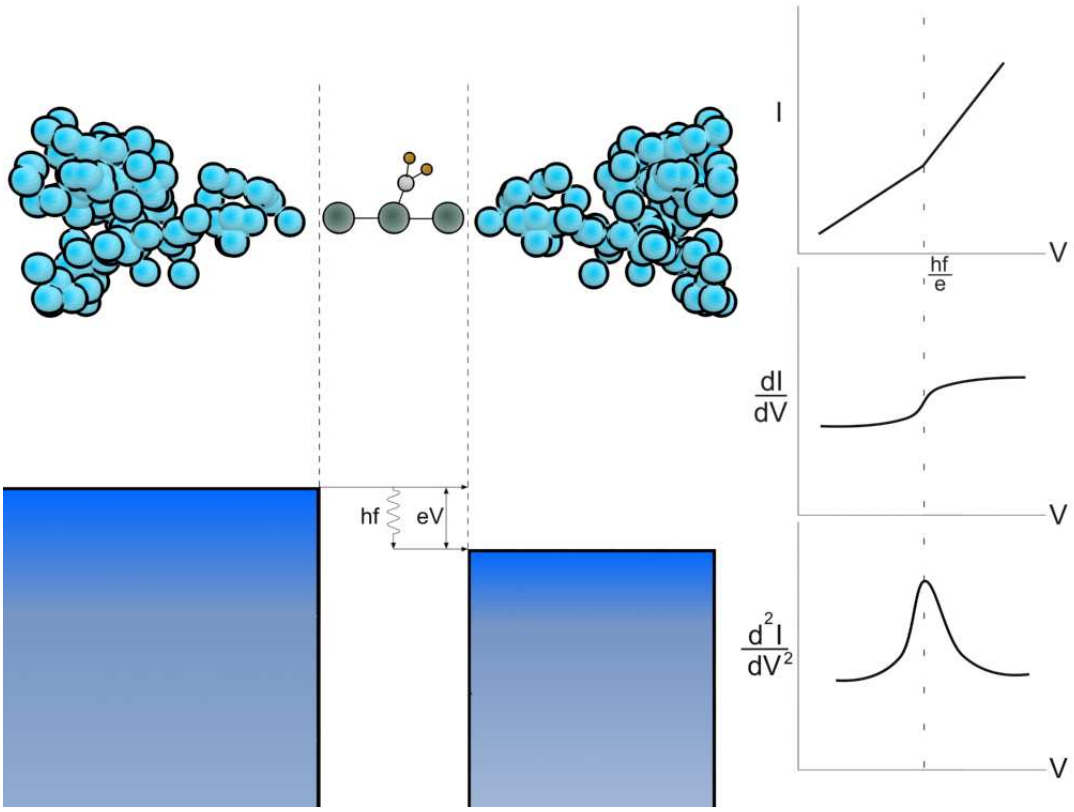


Figure 60: (a): A mock-up of a molecular junction with the resulting energy diagram. When the applied voltage reaches the threshold for a specific vibrational mode, a new, inelastic current path is created which typically results in an enhancement of the conductance (in some cases, the net effect of opening a new path is to reduce the current through the junction). (b): The effect of opening an inelastic path on the electrical properties of the system.

the resonance condition with the vibrational mode, i.e. $eV = \hbar\omega$, a new current pathway is created such that incoming electrons can inelastically scatter off of the molecular junction before crossing to the other lead, thereby exciting a vibrational mode of the molecule. It is natural to assume that the additional, inelastic pathway for electrons would always constitute an increase in the magnitude of the current. However, for many systems the net effect of opening an inelastic path is to reduce the current [68, 206, 97] or create more complex features [232]. The reason has not been unambiguously determined [82], though it is certain that the answer lies in the many-body aspect of the problem. Two possible explanations

are that there is a renormalization of the elastic path upon opening an inelastic pathway [60], or possibly that if the transmission coefficient of a certain channel is close to unity, the only possible effect of an inelastic path is to decrease the current through it [132, 7].

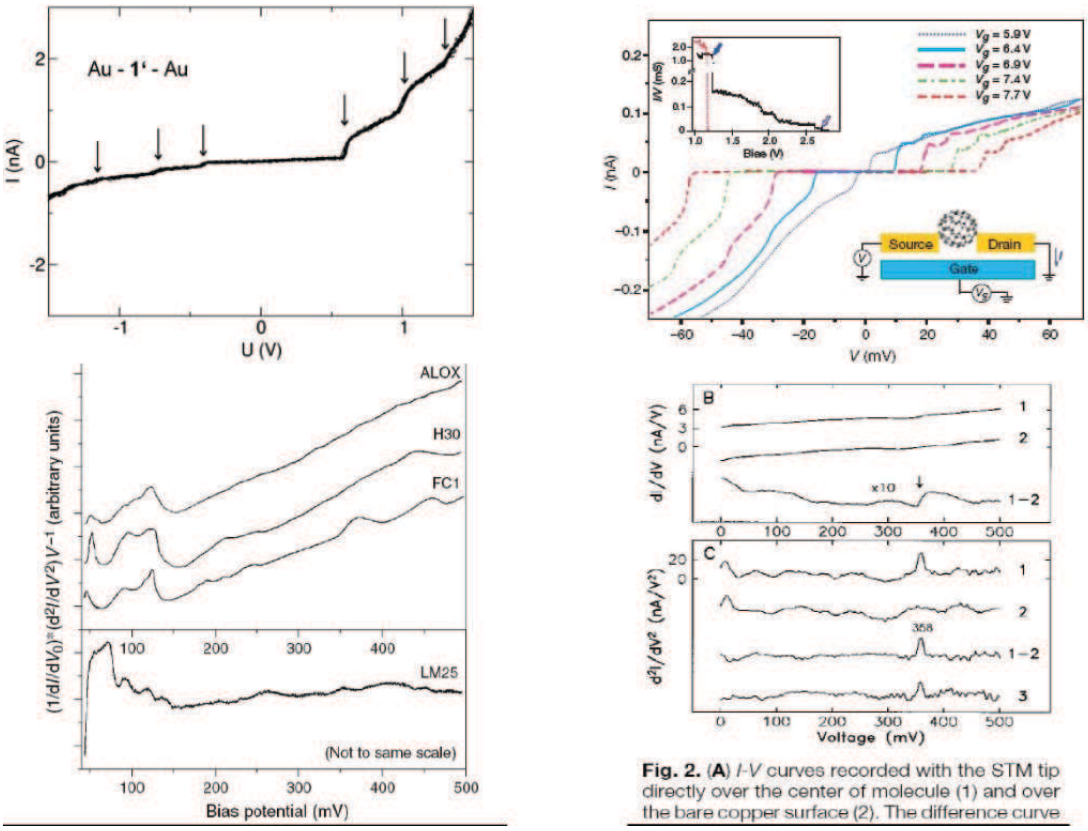


**Fig. 2.** (**A**) *I-V* curves recorded with the STM tip directly over the center of molecule (1) and over the bare copper surface (2). The difference curve

Figure 61: Here we see transport data taken from [210, 44, 74, 182] where a molecule is embedded between two normal leads; the top two panels show the resulting current-voltage curves which have obvious enhancements due to the presence of the molecular bridge. These features are more distinguished in the first and second derivatives of the current with respect to voltage, making peaks which can be easily resolved against the normal background. For this reason, electronic spectroscopy (as in IETS or PCS for example) makes an interesting and viable alternative to traditional light based spectroscopy methods.

Fig. 61 shows a few examples of actual data taken from molecular junction experiments. These examples are just a few of the wide range of systems which have been experimentally realized; to name just a few, vibronic coupling has been observed in $C_{60}$ transistors [182], carbon nanotubes [142, 197], molecular hydrogen and its isotopes [206], organic molecules [241, 210], and gold atomic chains [8].

In each of these cases, new conductance features are seen which correspond to the excitation of a vibrational mode of the system; thus, this type of experiment is capable of

performing spectroscopy of atomic systems. The main driving forces behind this form of spectroscopy are the advantages it presents over the more traditional infrared or Raman spectroscopy of molecules, as well as the wide range of successful applications. Two major advantages of vibronic spectroscopy over its optical counterparts are that overtone and combination bands are very weak [100, 119]; in addition, vibronic spectroscopy is capable of detecting optically forbidden transitions [104, 105]. As far as applications, two examples where this type of analysis has been successfully applied is in surface chemistry [231] and the study of adhesion and corrosion [145]. However, though vibronic spectroscopy allows for characterization of optically forbidden transitions, it does have its share of disadvantages as well; primarily, the amount of level broadening created by the coupling of the molecule to leads of the device [165] results in decreased resolution.

Nevertheless, it is clear that performing spectroscopic measurements by coupling electrical degrees of freedom to the mechanical modes of the system yields results which nicely complement the host of other spectroscopy methods. However, a natural question to ask is whether this technique can still be applied if the leads connecting the molecule are superconducting? Moreover, is there any new information or advantages to using superconductors instead of normal metals as electrodes?

First however, is the question of plausibility: is it even feasible that coupling could exist between superconducting degrees of freedom and the vibrational modes of a molecule? To answer this question, it is known from the Josephson relation that for a DC voltage bias, an AC current exists in the junction and oscillates at $f_J = 0.484 THz/mV$. Furthermore, the lowest vibrational frequencies of molecules lie in the low THz range, thus implying that coupling to superconducting degrees of freedom is plausible. However, there must be a maximum frequency at which the supercurrent can oscillate and it is this frequency which determines the plausibility of using superconducting leads for spectroscopy.

### 4.1.2 AC Effects in Point Contacts

Understandably so, there is considerable interest in the generation of frequencies in the low THz due to the spectroscopic data which can be obtained for molecules; however, the potential uses of THz radiation far exceed this one application. For instance, low THz radiation can penetrate fabrics and plastics, making it useful for security and surveillance purposes [162]; moreover, it is non-ionizing to biological tissues, making it attractive for medical imaging purposes [109, 110, 141]. Yet, although there are many potential applications for low THz radiation, only in the last decade have real strides been made in harnessing systems which can coherently produce it Among these are the gyrotron [204], the backward wave oscillator [70], the far infrared laser ("FIR laser") [43], and the quantum cascade laser [149].

In contrast to these highly engineered systems which are capable of producing low THz radiation, Josephson junctions are incredibly simple systems which naturally produce THz radiation (as seen through the Josephson relation). Moreover, Josephson junctions are ideal systems for converting voltage to frequency and vice versa; in fact, the volt standard used currently by NIST based on arrays of Josephson junctions [215]. In addition, one major advantage of using Josephson junctions for the creation of low THz radiation is that very small voltages (on the order of mV) can create very large frequency shifts (on the order of THz), making it an ideal transducer. Indeed, this property, when combined with the highly nonlinear nature of Josephson junctions, has been exploited for some time now in the creation of Josephson junction mixers [227]. In fact, mixers using Josephson junctions have been realized using both low $T_c$ [28] and high $T_c$ superconductors [234], with some being capable of near quantum-limited performance [116, 128] in the low THz range.

Looking at the low $T_c$ mixers, they typically use either tunnel junctions [111] or point contacts [29] to create the Josephson element of the circuit, both of which are pictured for comparison in Fig. 62. In these devices, the upper limit to the usable frequency range is determined by the maximum frequency for which AC supercurrent can flow through the junction. In tunnel junctions, this frequency is given by the expression [222], $f_{max} = 0.484 \cdot V_{gap}$, where $f_{max}$ is the maximum supercurrent frequency, measured in THz, and $V_{gap}$ is the superconducting gap voltage of the junction, measured in mV. Given that most mixers

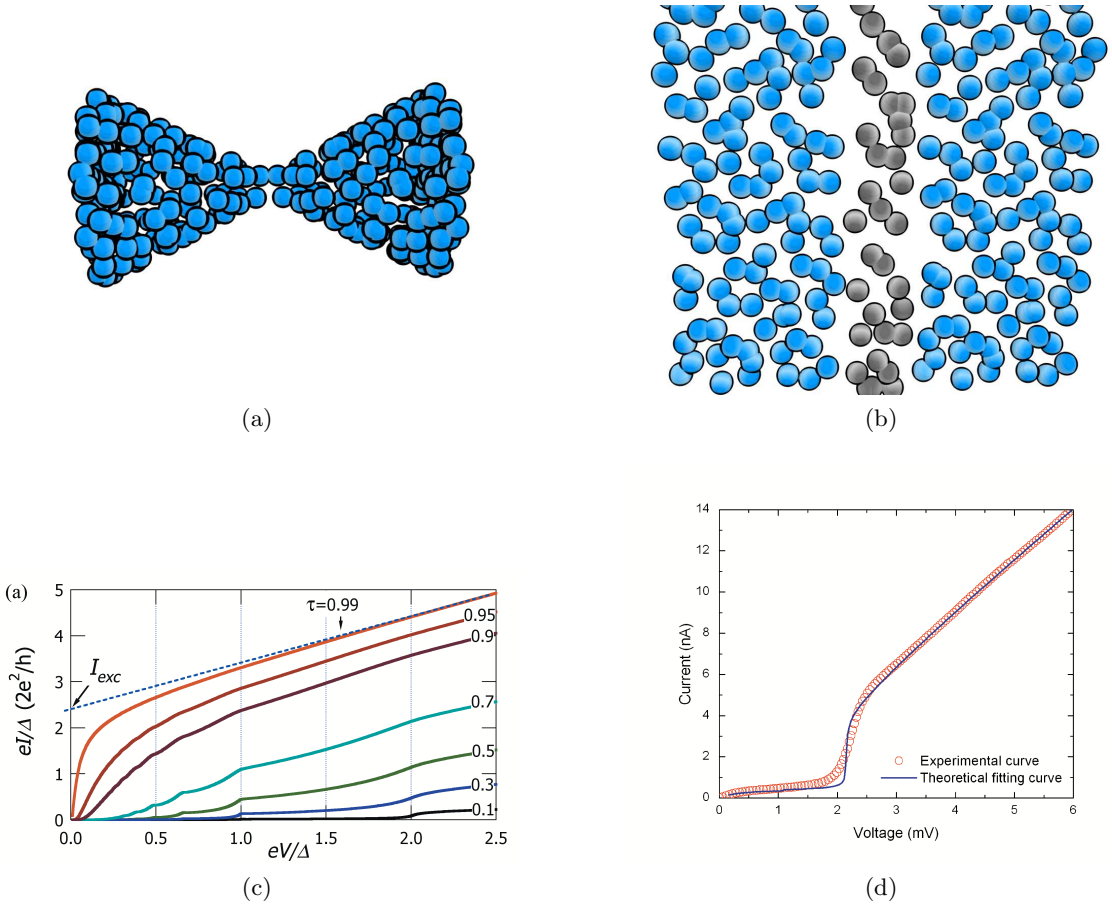


Figure 62: (a) and (c): A schematic of a superconducting quantum point contact and a typical set of current-voltage curves. (b) and (d): Mock-up of a tunnel junction with a barrier region and its associated current-voltage relation. Due to the larger number and higher transmission of the conductance channels in quantum point contacts, it is expected that the Josephson coupling between the superconducting electrodes will last well above the gap value; conversely, a tunnel junction by definition contains only a weakly transmitting channel which inhibits Josephson coupling at higher energies.

use niobium as the superconducting material and that it has a gap value typically around 2.8 mV, we see that the upper frequency limit of tunnel junctions is approximately 1.4 THz. In contrast, point contact junctions are able to sustain AC current oscillations at much higher frequencies due to the increased Josephson coupling between the two superconducting leads. However, no analytic results are available, meaning that the maximum AC frequency can only be determined through either numerical simulations or experimental investigation.

Analytical calculations for point contacts are difficult due to the onset of MAR in channels with higher transmission coefficients; this is especially true for the low voltage characteristics since an increasingly large number of MAR processes must be taken into account. However, by performing the full calculation, it has been discovered that the current through a point contact junction can be written as a sum of harmonics of the Josephson frequency in the following way [17, 51]:

$$I = \sum_n I_n(V) e^{in\omega_J t}, \tag{150}$$

where $I_n$ is the amplitude of the $n^{th}$ harmonic of the Josephson current and is a function of voltage. In Fig. 63, the first three harmonics of both the supercurrent and quasiparticle current can be seen. In contrast to what would be expected for tunnel junctions, the amplitude of the first harmonic of the current does not decay to zero quickly as a function of the applied voltage; in fact, it is non-zero well above the energy gap for the superconductor, in contrast to the higher harmonics which decay to zero relatively quickly. This result confirms the assumption that the AC Josephson effect should be active above the gap due to the stronger Josephson coupling in point contacts; stated another way, it shows that point contact junctions are capable of much higher mixing frequencies than tunnel junctions. This numerical result has been confirmed through many experiments by using the effect of Shapiro steps [202] in Josephson junctions [30, 158, 29, 28]. Here, monochromatic laser radiation is incident on the junction and the number of resonant voltage steps are measured (resonance occurs for $\hbar\omega_J = 2eV/h = n\hbar\omega_{inc}$, where $\omega_{inc}$ is the angular frequency of the incident radiation). By observing the number of harmonics which can be resolved using this technique, a very sensitive measurement for the high frequency limit of the AC Josephson effect can be made. The result of one of the experiments is shown in Fig. 64, where the top

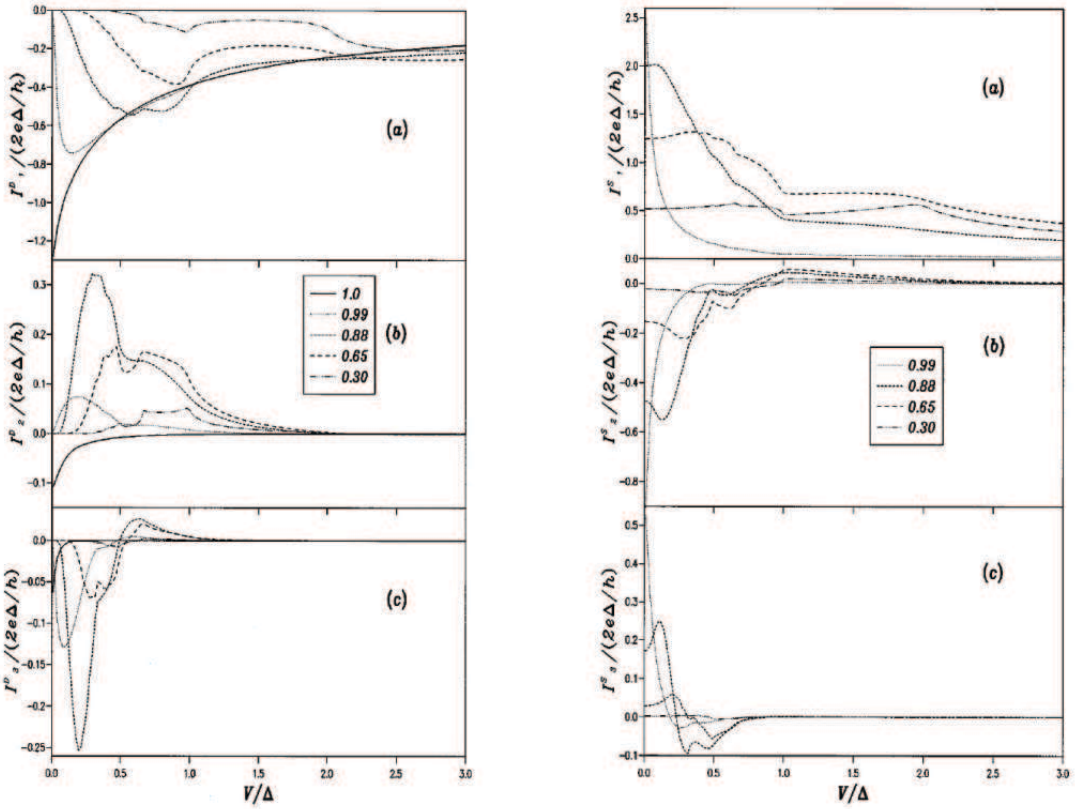


Figure 63: Left Panel: Here we see the amplitudes of the first three harmonics of the AC dissipative current through a point contact, which was numerically computed from [51]; the different curves for each graph correspond to varying the transmission coefficient of the channel. Right Panel: Similar to the left panel, here are the amplitudes of the first three harmonics of the AC supercurrent through a point contact; the key feature to note for both graphs is that the amplitude for the first harmonic does not decay to zero as quickly as the higher harmonics. In fact, the amplitude for the first harmonic of the supercurrent is still non-negligible well above the superconducting gap, implying that the AC Josephson effect extends well above the gap due to the strong Josephson coupling between the two superconducting leads.

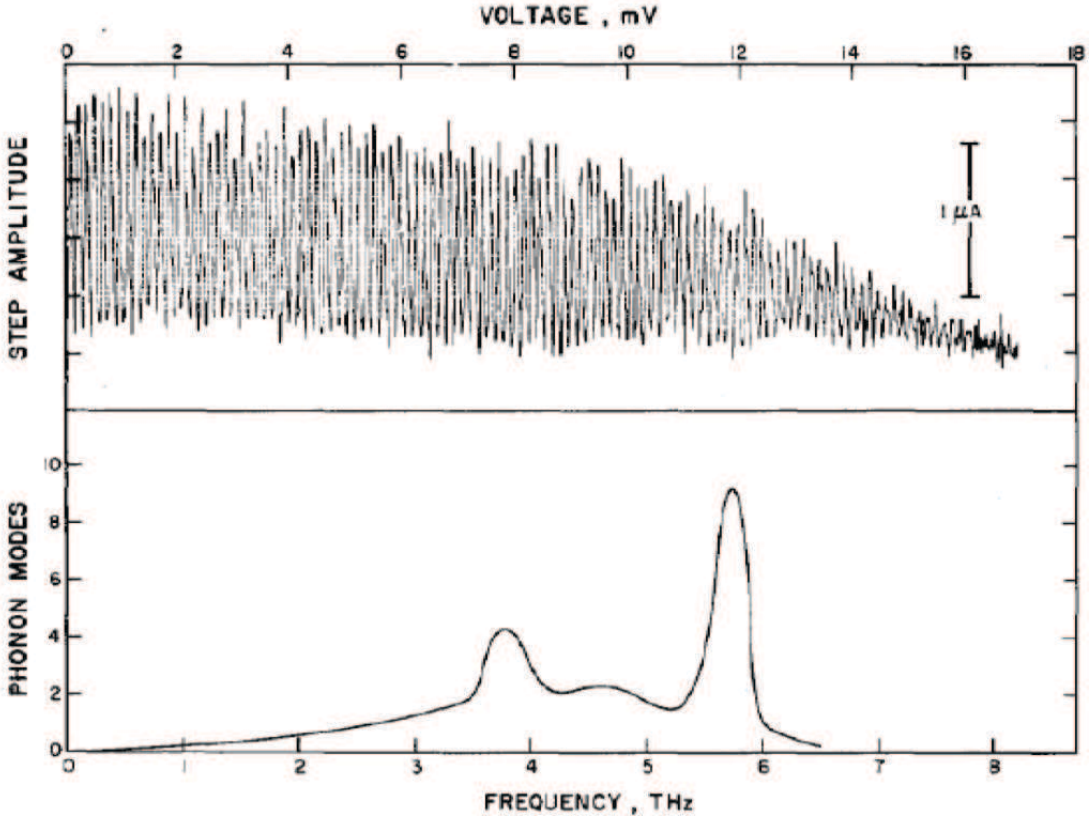


Figure 64: Shown here is experimental data taken from [159] which shows the result of irradiating a point contact with a 70 GHz laser; due to the resonance condition, $n\hbar\omega = 2eV$, Shapiro steps [202] appear when the voltage across the junction matches one of the harmonics of the applied radiation. These current steps are a sensitive detector of the AC Josephson effect in systems and show the range of the AC Josephson effect. For the case of point contacts, it is clear that the AC currents through the junction were able to couple to the applied radiation well above 10 mV or about 5 THz. Shown below the Shapiro steps data is the phonon density of states for niobium, where clear correlations can be seen between the highest Shapiro step and the saturation of phonon modes.

panel shows the current response of the system and the bottom shows the phonon modes in niobium for comparison. The major result of this experiment is that the AC Josephson effect in point contacts extends above 7 THz, in comparison to the high frequency limit of approximately 1.4 THz in tunnel junction mixers. Additionally, there seems to be a clear correlation between the saturation of the phonon modes and the high frequency limit of the Josephson effect; this could mean that some type of damping mechanism exists which is activated only when a significant portion of the phonon modes of the system are excited. Continuing further, various other mechanisms have been proposed in the literature to describe this suppression of the AC amplitude of the supercurrent such as damping due to the relaxation of the order parameter in the superconductor [118] or attenuation due to the anomalous skin effect [157]. However, though the AC Josephson effect is attenuated above approximately 7-8 THz, this range of frequencies is suitable for our purposes of attempting to excite the lowest vibrational modes of molecules; thus, the problem now becomes testing the system by embedding a molecule into a superconducting point contact and performing spectroscopic measurements. A very fortuitous consequence of using niobium point contacts is that during elongation of the contact, the system forms an intrinsic molecule (a niobium dimer) during the final stages of elongation; thus, testing the spectroscopic technique is straightforward in our case. However, it still must be shown that a dimer does, in fact, exist between the two superconducting leads during the final stage of elongation.

## *4.2 Structure of Niobium Nanowires*

### 4.2.1 Introduction

As noted in Chapter III, and covered much more thoroughly elsewhere [9], it is possible to form a nanowire between two electrodes by any number of methods such as STM, spear-anvil, or mechanically controllable break junction(MCBJ). This was first shown through molecular dynamics simulations [138] which were aimed at exploring contact formation, nano-indentation, the atomic origins of frictional processes, and tip-substrate interactions [24, 136, 137]. It is from these beginnings that the experimental realization of molecular electronics [144] began. Thus, soon after the first seminal paper, many experimental and

theoretical studies were performed in order to shed light on the structural, mechanical, electrical, and chemical properties of atomic-size contacts and nanowires [236, 207, 209, 139]. Among these studies, one of the most interesting aspects considered was the formation of

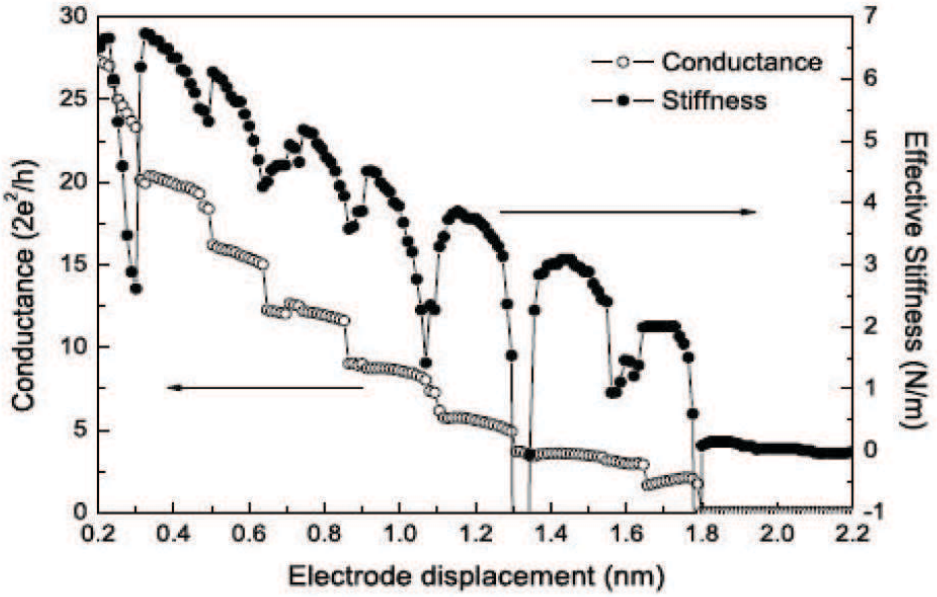


Figure 65: This plot shows the result of simultaneously measuring the stiffness and the conductance of an atomic contact as a function of the elongation [205]; clearly, a direct correlation exists between atomic rearrangements and changes in conductance of the junction.

atomic contacts and switches at the final stages of elongation before breakage occurs [73, 33, 88, 218]. Specifically, as the contact is elongated, it undergoes a sequence of structural instabilities which are caused by stress accumulation and subsequent yielding to a new atomic configuration. On a side note, it is intriguing that simulations have shown [138] that the patterns of structural evolution of the contact create oscillations in the elongation force, with a period approximately equal to the crystal interlayer spacing. These oscillations reflect the changes in stress which the contact undergoes during elongation. In addition, these same simulations predicted the existence of atomically thin gold nanowires during the last stages of elongation. These results have been experimentally confirmed by High Resolution Transmission Electron Microscopy (HRTEM) of a gold STM tip as it was retracted from a

gold surface [175]. Furthermore, these atomic rearrangements which the contact undergoes have a profound impact of the conductance through the junction, as can be seen from simultaneous measurements of the force and conductance of an atomic point contact [225, 193, 194, 7, 205]. In Fig. 65, the stiffness of the junction was measured simultaneously with the conductance of the contact using an MCBJ coupled to a tuning fork which acted as a force sensor [205]. Clearly, during periods of atomic rearrangement, the contact abruptly changes its conductance as well, showing how the release of accumulated stress in the junction plays an important role in determining the electrical properties of the contact. Hence, there is a strong correlation between the structural and electronic properties of nanowires. Therefore, it is advantageous to understand the structural evolution of niobium nanowires during elongation, as these changes in atomic structure directly relate to changes in transport properties. Moreover, by investigating the elongation of the contact and what specific atomic configurations the nanowire takes, it is possible to use these intrinsic systems as an ideal testbed for vibronic coupling studies.

### 4.2.2 Experimental Results

As detailed in Chapter III, our samples are microfabricated niobium point contacts, seen in the left panel of Fig. 66, which are placed in a cryogenic MCBJ setup under UHV conditions. The combination of using microfabricated samples, coupled with the inherent rigidity of MCBJ technique, produces remarkably stable contacts which allow for reversible atomic manipulation over a range of approximately one angstrom. In fact, it is possible to accurately restore the length of a contact to within a picometer using this system, thus enabling the faithful reproduction of highly non-linear IV curves even after hours of experimentation.

To prepare the samples [53], approximately 1 $\mu$m of insulating polyimide is spun and cured onto a flexible bronze substrate, followed by DC magnetron sputtering of niobium in the presence of a liquid nitrogen cold trap to remove contaminants from the system. This sputtering step was optimized to produce high quality superconducting samples which tend to form microcrystalline thin films [99]. The right panel of Fig. 66 shows an SEM micrograph of a typical sample after breaking, where it appears to be cleaved along a

microcrystalline boundary. Upon subsequent pattering of the sample, which is detailed in Chapter III, the samples are ready to be placed into our custom dipstick for testing. During this phase, all measurements were performed under ultra-high vacuum conditions and either at 4.2 K or 9 K, depending on whether superconducting or normal transport properties were desired.

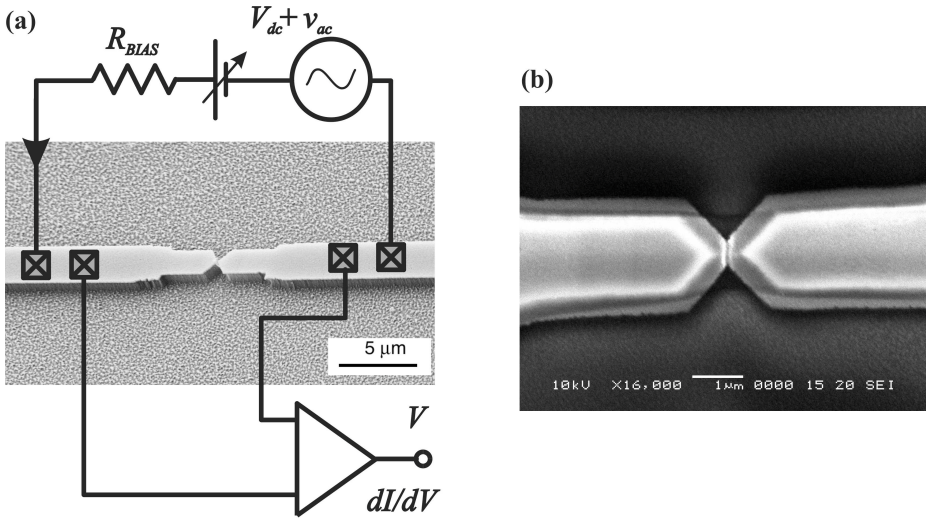


Figure 66: (a): Shown here is an SEM micrograph of a niobium break junction with the basic measurement circuit superimposed. (b): Here is an MCBJ sample after it has been broken; note that niobium samples appear to cleave along microcrystalline facets, unlike tensile materials such as gold or aluminum.

Initially, the evolution of the conductance during contact elongation was studied, as seen in Fig. 67. Here, the left panel shows the result of measuring the conductance of niobium point contacts at 4.2 K as a function of the contact elongation during the final stages before the contact is broken. In these measurements, the conductance can be measured one of two different ways: one is by increasing the temperature of the sample above $T_c$ and measuring the conductance directly. In this case, the fact that suppression of superconductivity, due to either increases in temperature or magnetic field, does not change the conductance channel composition [200], which has been experimentally verified using our microfabricated samples is. In contrast, an alternate method which does not involve ramping the temperature of the sample is to measure the differential conductance of the contact at voltages above $2\Delta$, corresponding to the resistive/dissipative branch of the curve.

The elongation cycle of Fig. 67 begins at an atomic configuration whose conductance is

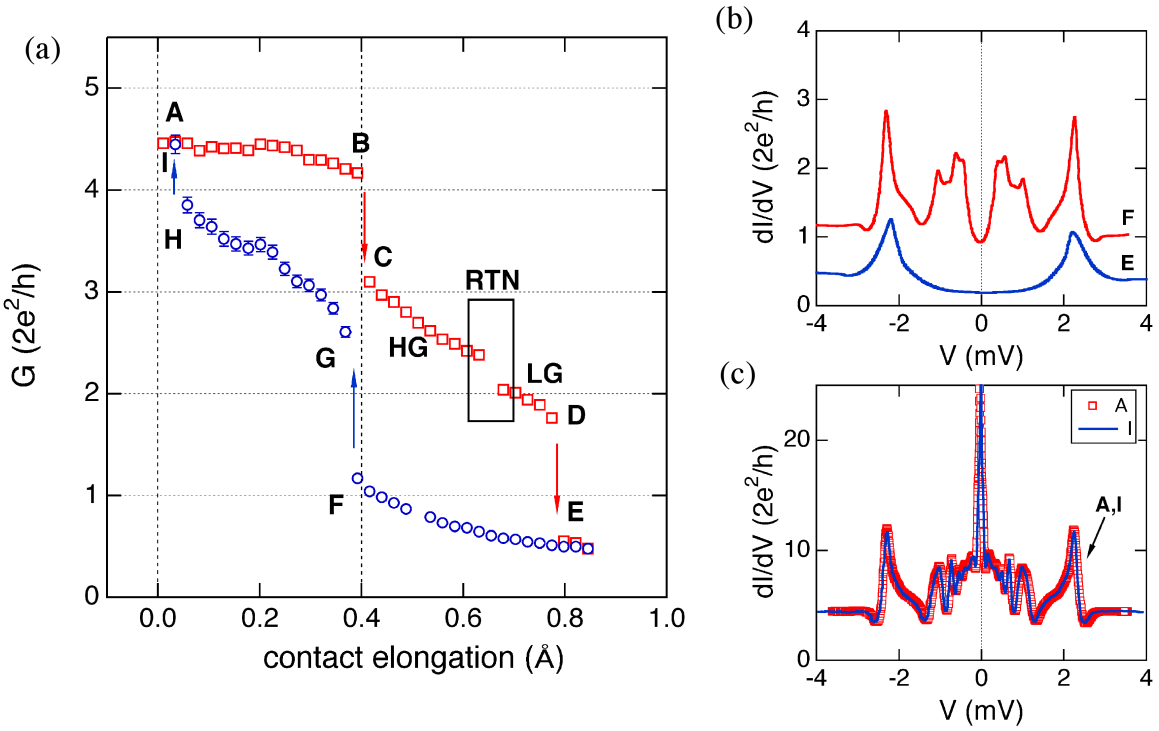


Figure 67: (a): Shown here is an elongation (red) and contraction (blue) cycle for Nb point contacts at 4.2 K; the sudden jumps which occur at places such as (B) are indicative of the contact rearranging itself into a lower energy structure. The key region of interest is marked by the black box labeled RTN for Random Telegraph Noise; in this region, switching between two distinct conductance states is observed. (b): Plotted here are the conductance traces for both points E and F. Clearly, E is in the tunnel mode, whereas at F, contact has been made between the two sides, creating Multiple Andreev Reflection (MAR) features. The tunnel nature of the EF transition can be inferred as well from the exponential characteristic of the conductance as the piezo is retracted. (c): To demonstrate the stability of our experimental setup, two conductance traces (A and I) are shown which correspond to the first and last trace measured; the total time between the two traces was approximately 12 hours. Though much time had elapsed and many atomic configurations were measured, the same configuration is still faithfully reproduced after 12 hours, showcasing the high degree of mechanical stability of our system.

approximately 4.4 $G_0$, which is initially obtained via coarse actuation of the brass micro-screw. However, after the initial setting of the conductance, the piezo is used exclusively for fine control of the system. Thus, the piezo is used to stretch the contact another 0.4 angstroms before another atomic configuration is obtained, as evidenced by the jump in conductance from B to C in the figure. Upon further stretching of the contact, the conductance goes through a small region of random telegraph noise before finally breaking at approximately 0.8 angstroms (the D-E transition). This transition marks the jump from contact to tunnel junction, which is seen through not only the qualitative differences in the differential conductance curves between points E and F in Fig. 67, but also the exponential behavior of the conductance during the retraction step (E-F). Once the sample is retracted to approximately the same point as the B-C transition, contact between the two sides is reestablished and the piezo is still further compressed until the initial configuration is recovered. This last configuration, I, is identical to the starting configuration, as seen by the two differential conductance curves given in Fig. 67. The total time between the initial and final conductance measurements was approximately 12 hours, thus exemplifying the high degree of mechanical stability attained through the use of microfabricated samples and the MCBJ technique.

During this elongation-retraction cycle, the main feature of interest is the area of random telegraph noise (RTN) which is seen during the C-D step of the cycle. In Fig. 68, similar behavior is shown for a different sample, where the noise was investigated more thoroughly. As is characteristic of RTN, slow two level fluctuations of conductance states are observed inside the region, as evidenced by the upper right panel of Fig. 68. Additionally, these fluctuations were seen during both elongation and retraction of the contact, occurring without any noticeable hysteresis during multiple scans. It should be noted that in order to plot the conductance of the contact inside the RTN region, a time average of the two level fluctuations was taken over multiple time constants of the system; in this way, the overall trend of the conductance can be seen, even though the contact does not adopt one configuration.

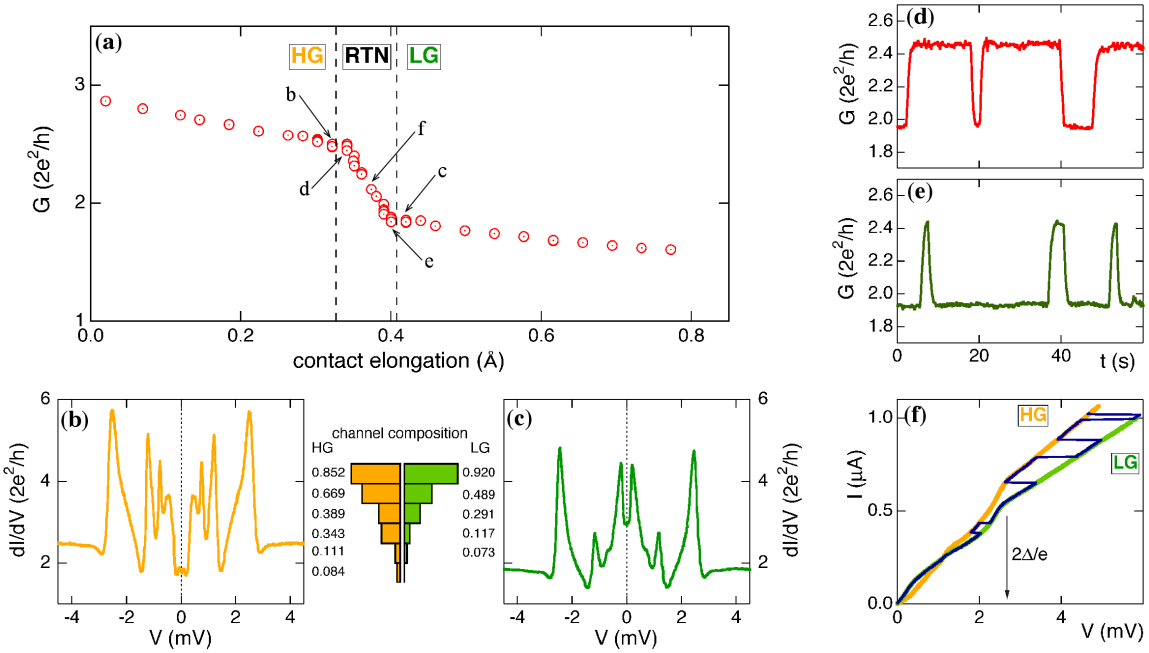


Figure 68: (a): Zoomed view of the RTN region from the previous figure. (b) and (c): Here we can see differential conductance traces taken on each side of the RTN region, showing that two distinct conductance states exists; this is further confirmed by the qualitative differences in conductance channel composition for each state (i.e. the HG state has two highly conducting channels compared to only one for the LG state). (d), (e), and (f): Here, the temporal fluctuations inside the RTN region are shown in detail; the switching occurs randomly and follows a Poissonian distribution. The last figure shows the two distinct current-voltage curves of the two states, with a trace from inside the RTN superimposed to further show the switching between the two states.

In all, this type of conductance noise has been seen in 18 contact realizations from 5 different microfabricated samples. Generally speaking, the RTN manifests around $2.4\pm0.15\mathrm{G}_0$ as the contact is elongated, continuing over a distance of approximately one angstrom until finally plateauing at the lower conductance value. Flanking the RTN region are two well defined conductance states whose differential conductance plots and typical channel compositions can be seen in the lower panels of Fig. 68. These two conductance states are termed the HG and LG state which correspond to a high conductance and a low conductance respectively. The HG and LG state are distinct in appearance due to the quantitative differences between the small bias regions of the differential conductance. Further, concerning the channel composition of the two states, the HG state always has at least two conductance channels whose transmission coefficient, $\tau_i$, is greater than 0.6, whereas the LG state always only has one channel with a transmission that high. Moreover, the one LG conductance channel whose transmission coefficient is greater than 0.6, $\tau_{LG,max}$, is greater than any channel of the HG state (i.e. $\tau_{LG,max} > \tau_{HG,max}$). This observation explains why the differential conductance for the LG state is greater at low bias than the HG state.

Looking at the HG state more closely, Fig. 69 shows the result of sweeping the HG state with both temperature and the piezo. For the piezo sweep, the HG state undergoes small structural changes as the contact is elongated. These alterations are not sufficient to change the overall character of the differential conductance curve, only modify the total conductance through the contact. If the contact were to collapse to the LG state, a drastic change in the differential conductance trace would be seen. This same behavior is seen in the thermal sweep of the HG state, where now the structure of the curve changes due to MAR features; as the temperature is increased, the superconducting gap parameter is reduced from its zero temperature value, as seen in Fig. 17. Since the multiple Andreev reflection process follows the temperature dependence of the gap, the MAR features must move inward as the temperature is raised; as well, the amplitude of the features must decrease to zero. However, beyond the small change in total conductance and the compression of the MAR features, the HG state remains in tact as the temperature is increased.

These two measurements were done on the LG state as well, which can be seen in Fig.

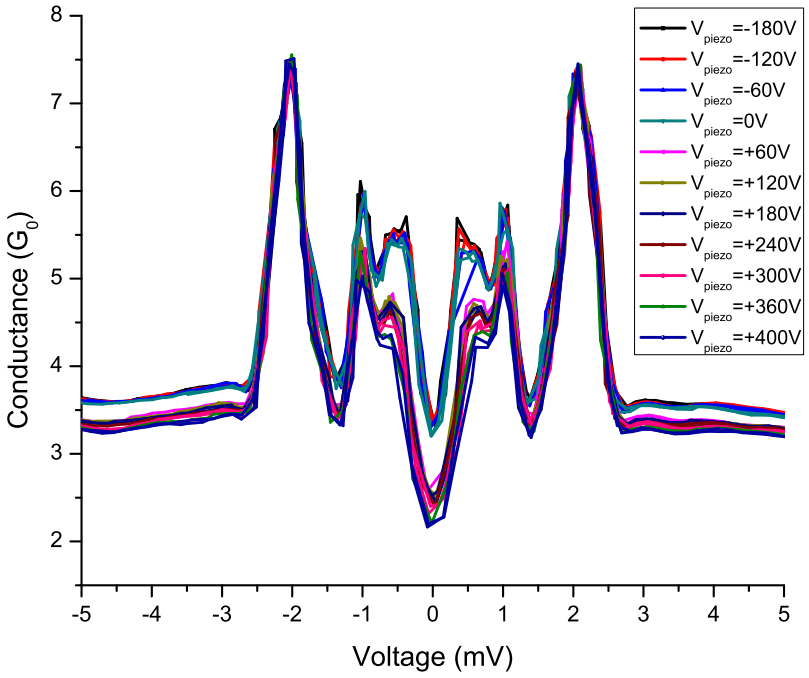


(a)

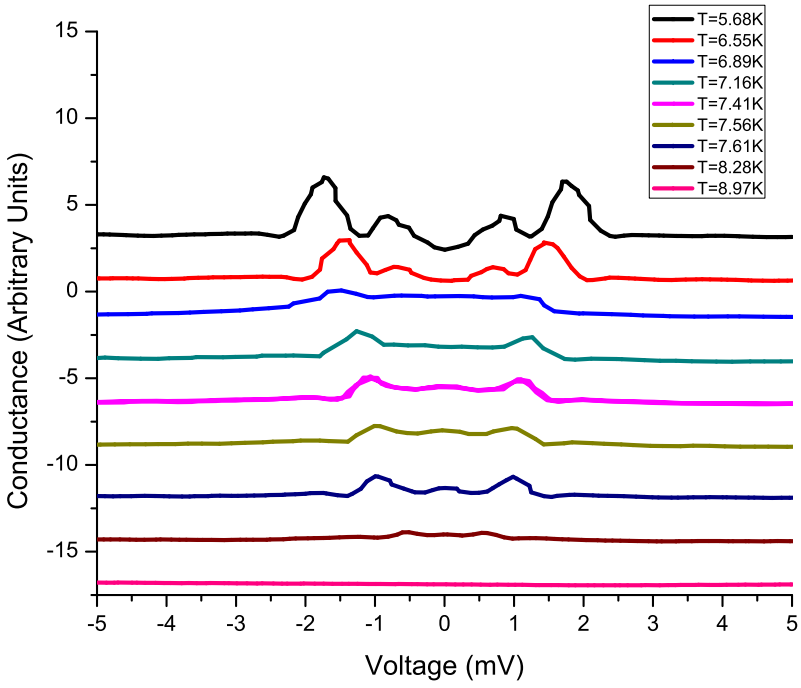


(b)

Figure 69: (a): Shown here are conductance traces of the HG state as the piezo elongates the sample. As the contact is stretched, the dimer undergoes small configuration changes which alter its conductance; eventually, this stretching results in a collapse to the LG state. (b): Shown here are conductance curves for the HG state as the temperature is raised, offset for clarity. During the temperature ramp, the MAR features move inward due to their dependence on the gap parameter; as well, thermal expansion of the contact causes the nanowire to alter its structure and conductance. The change in conductance is reflected by the non-uniform offset of each curve (i.e. each curve was manually offset by a constant amount, thus any non-uniformities result from changes in the contact's conductance).

70; the LG state shows similar behavior to both the piezo and temperature sweep. As the contact is elongated, the LG state undergoes small modifications which decrease the overall conductance; furthermore, the amplitudes of the MAR features are suppressed as well. This behavior is indicative of the LG state slowly approaching a tunnel junction where only one pair of MAR features exists (at V=2$\Delta$). If the piezo were extended further, eventually the middle region of the curve would become flat, with the only distinguishing features being the two symmetrically placed MAR peaks, as in the upper right panel of Fig. 67. In contrast to the temperature dependence of the HG state, the LG state shows significant changes as the temperature is decreased from the critical value. Specifically, the characteristic conductance suppression at low biases does not appear until the temperature has been lowered to almost 5 K; this again is due to the MAR features which obscure this depression for higher temperatures. At higher temperatures, the MAR peaks move inward and the two lowest merge into one peak; however, as the temperature is lowered and the peaks move outward, the low bias suppression feature can be fully resolved.

Thus, there exists an intrinsic two state system which forms during the last stages of elongation before breakup of the contact for niobium point contacts. However, transport measurements are only able to determine that a two state system exists, they provide no definitive information on the nature of the system itself or what it corresponds to physically. Hence, theory and simulation must be used to determine what atomic configurations the HG and LG state refer to; this work was done in collaboration with Dr. Chung Zhang, Dr. Robert N. Barnett, and Prof. Uzi Landman from the School of Physics at Georgia Tech, who have performed Density Functional Theory (DFT) structural simulations [79, 71, 124, 184, 123] along with Non-Equilibrium Green's Function (NEGF) transport calculations [56, 57, 58, 117] in order to investigate the structure of niobium nanowires and elucidate the nature of the HG and LG state.

### 4.2.3 Connection with DFT/NEGF Simulations

Knowing that a two state system exists in niobium point contacts, a combination of DFT structure simulations [20] combined with NEGF transport simulations [45, 36, 217] were

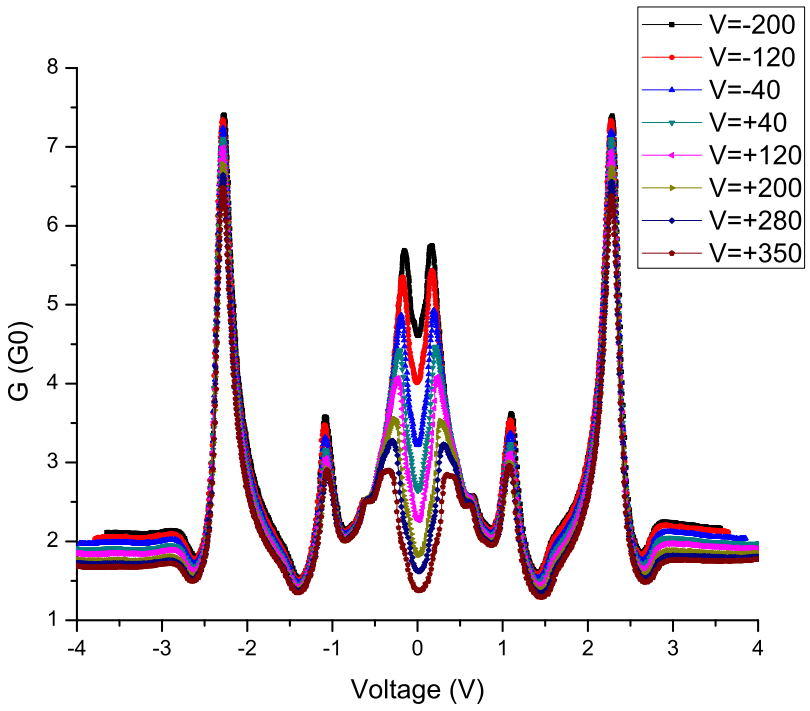


(a)

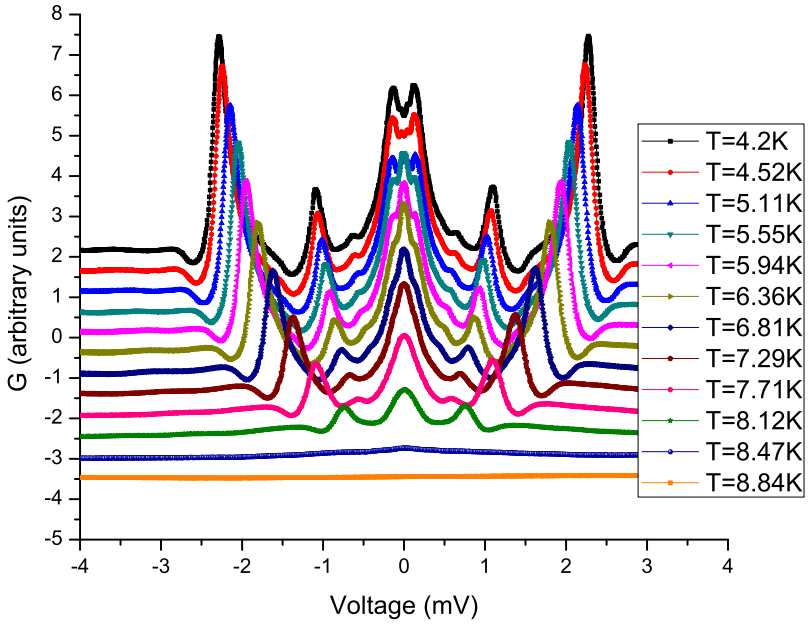


(b)

Figure 70: (a): Shown here are conductance traces of the LG state as the piezo voltage, and thus the elongation, is increased. The curves are not offset, rather, the conductance of the LG state is very sensitive to changes in the electrode spacing due to its asymmetric nature. Furthermore, as the contact is stretched, the amplitudes of the MAR peaks consistently decrease, showing signs of the LG state turning into a tunnel junction. (b): Shown here are conductance curves taken during a temperature sweep where the curves are offset for clarity. As the temperature is decreased from $T_c$, the curves takes on its characteristic shape with a conductance depression at zero bias.

used in order to probe the bonding, atomic arrangements, structural transitions, and electronic transport in niobium nanowires as the contact was elongated. In applying the DFT formalism, the generalized gradient approximation (GGA) [186] was employed, along with a plane wave basis (kinetic energy cutoff $E_{cut}$=68Ry) and norm-conserving, soft pseudopotentials [221]. Additionally, in the construction of the pseudopotential, a reference configuration of [Kr] $4s^2 4p^6 4d^5 5s^0$ was used, which uses 13 valence electrons per atom as described elsewhere [94]; thus, the electronic configuration of the niobium atom is given correctly to be [Kr] $4s^2 4p^6 4d^4 5s^1$ in this scheme.

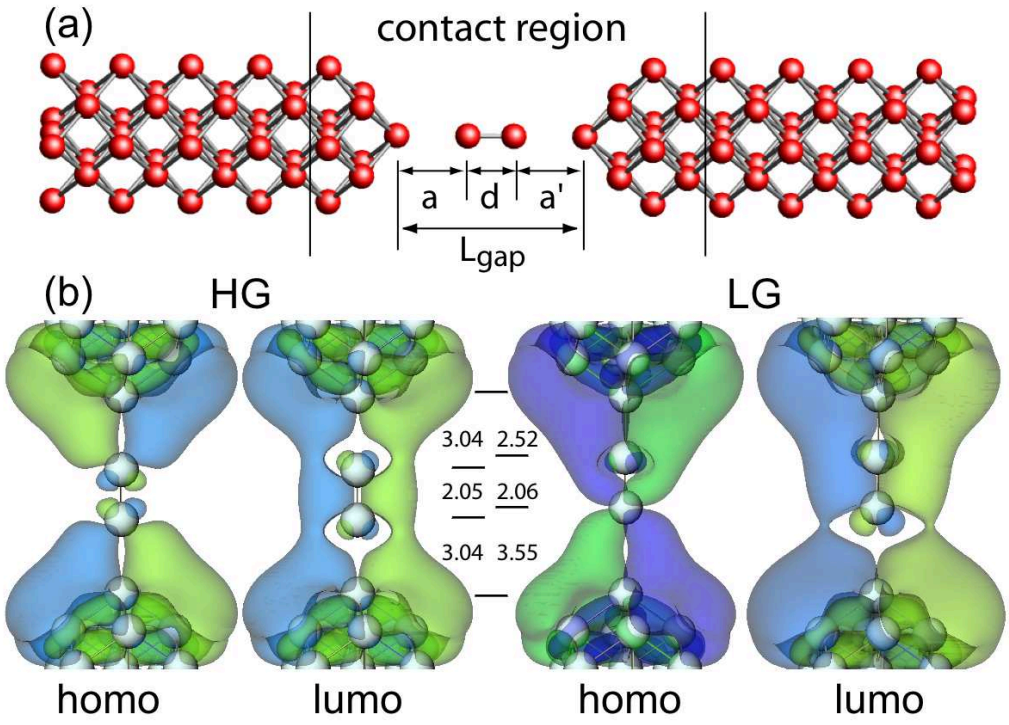


Figure 71: (a): Shown here is the niobium nanowire system in the symmetric state, as used in the DFT simulations. (b): Given here are the calculated HOMO and LUMO states for both the HG and the LG states. The blue and green areas of the wave function correspond to regions where the value is positive or negative, respectively.

For all of the structural optimizations done on niobium nanowire configurations, the system is initially configured similarly to the top panel of Fig. 71 where there are two niobium leads whose atoms are held at the bulk lattice positions for the duration of the calculation. In addition, there is a contact region where the atoms are completely free to

relax to a new equilibrium position. This contact region encompasses not only the nanowire, but also those nearest neighbor atoms whose positions are most likely to be altered from the bulk lattice position. However, though the specific configuration of the nanowire will affect the nearest neighbor atoms in different ways, simulations have shown that changes in the distance between electrodes manifest entirely through variations of only the gap region.

Once the structural relaxation is complete, the resulting atomic positions are used as the starting point for conducting NEGF transport calculations to verify whether a certain atomic configuration faithfully reproduces the experimental findings. For these NEGF calculations, the contact region was coupled to semi-infinite BCC (100) leads (consisting of BCC stacked, alternating four or five atom layers). Further, these simulations used an atomic basis with the same 10 orbitals per atom as those used in the construction of the pseudopotential; these orbitals are then subsequently expanded in a plane wave basis with $E_{cut}$=68Ry.

Due to the fact that there is no *a priori* knowledge of what atomic configuration the nanowire should take or what the HG and LG state corresponds to structurally, many different nanowire configurations were simulated and compared to the experimental data for verification. These trial structures included the simplest possible configuration consisting of two electrodes sharing a common vertex atom, which yielded a conductance of approximately $5G_0$. As well, a configuration where the two electrodes were coupled through a single atom bridging the gap was investigated which gave a conductance of approximately $4.8G_0$. Furthermore, in addition to not giving the correct conductance values, these systems were unable to reproduce the two level behavior seen in the experimental data. Thus, increasingly complex configurations were investigated, in the hopes that extra degrees of freedom would more accurately reproduce the experimental observations. Specifically, the simplest system which does not utilize one atom between the electrodes would be a system consisting of two niobium atoms bridging the gap in a dimer configuration. Even before DFT calculations were done on this nanowire configuration, this configuration is promising in that previous first principles molecular dynamics simulations predicted the existence of gold dimers suspended between opposing electrodes [98]. In this study, it was shown that

elongation of the contact leads to the eventual breakup of the dimer, with each atom from the molecule bonding to a different electrode. Furthermore, the formation of gold atomic chains has been previously reported in break junction experiments [237]. As well, these chains have been imaged via HRTEM as bridges connecting areas of thin gold films which have been perforated by the impact of energetic electrons [175, 192].

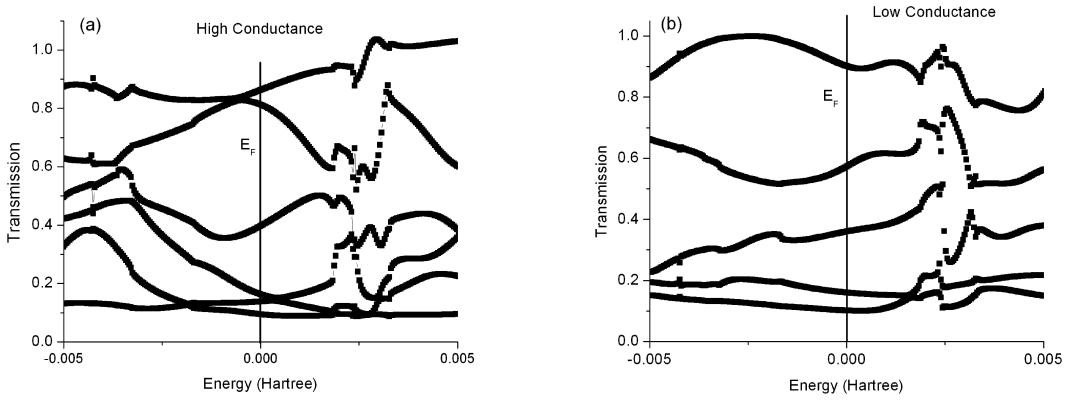


(a) (b)

Figure 72: (a): The transmission coefficients of the HG state are plotted as a function of applied voltage. Because the experimental work was done at low biases, only the region around zero (E=$E_F$) is of interest. This calculation confirms the previous assertion that the HG state is characterized by having two high transmission channels. (b): Here, the same plot is done for the LG state; again, this calculation confirms the observation that the LG state consists of one highly transmitting channel (higher than any HG channel), followed by much more weakly transmitted channels.

In fact, among the systems simulated and compared with the experimental data, the only configuration capable of accurately reproducing the observed experimental behavior is that of a niobium dimer bridging the two leads. Not only do the DFT/NEGF simulations produce the correct value for the conductance of the structure, but they also confirm the existence of a two state system during the final stages of elongation [54]. Specifically, it was found that the HG state corresponds to a dimer placed symmetrically between the two niobium leads, whereas the LG state corresponds to an asymmetrically placed dimer between the electrodes, as can be seen in Fig. 71. The figure shows not only the structure of the dimer, but also the resulting wave functions for both the HOMO and LUMO states which consist primarily of d-states which extend over the dimer and the electrodes, enabling

strong coupling between the two leads [38].

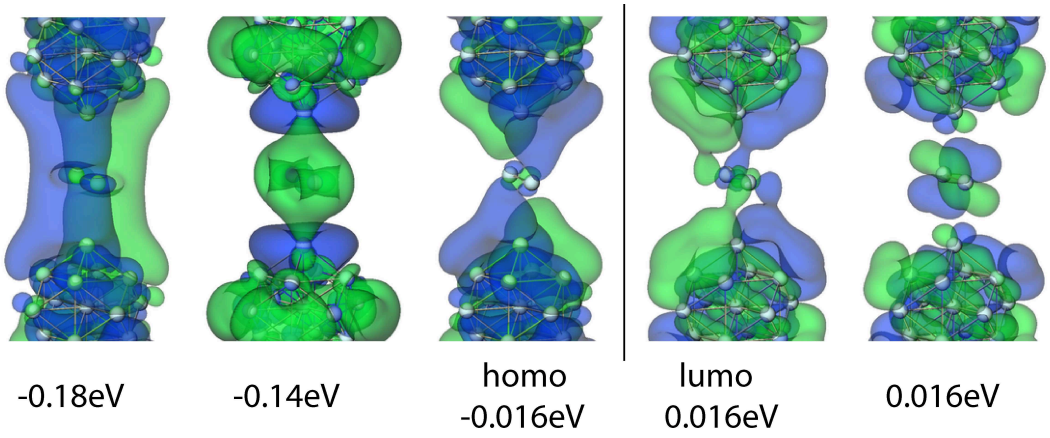


Figure 73: A configuration of the Nb nanowire corresponding to $L_{gap} = 6.63\mathring{A}$ is seen with isosurfaces of the highest (lowest) occupied (unoccupied) molecular orbitals superimposed, as well as several other orbitals with energies close to the Fermi level (the energies in the figure are with respect to the Fermi energy). Note the d-character of the orbitals and their extended nature. In this configuration, the axis of the suspended Nb dimer makes an angle of 94 degrees with the line connecting the two tip atoms of the electrodes. In addition, the distance between the two Nb atoms in the gap is d = 2.15 $\mathring{A}$, and the distance between a dimer atom and the nearest Nb tip atom is $3.42\mathring{A}$, which yields an overall conductance of $3.5G_0$.

To complement the DFT structural calculations, the resulting NEGF transport calculations for the dimer are shown in Fig. 72. Here, plots of the transmission coefficients as a function of energy are seen for both the HG and the LG state. An important point to note is the existence of two highly transmitting channels for the HG state, whereas the LG contains only one such channel; further, this single highly transmitting LG channel is more transparent than any of the HG channels. Thus, the DFT/NEGF calculations not only capture the qualitative features of the experimental data, but are also able to quantitatively confirm the existence of a dimer corresponding to the HG and LG states.

Interestingly, in addition to the HG and LG states, DFT simulations show an additional state consisting of a tilted dimer which is shown in Fig. 73. This tilted configuration makes an angle of 94° with respect to the axis joining the two electrodes. Additionally, this structure has a conductance of approximately $3.5G_0$ and occurs at a gap distance of $6.63\mathring{A}$ during compression of the contact, rather than during elongation as in our experiments. Thus, it is within our experimental capacity to confirm this result, and experiments are

underway to do such measurements.

## *4.3 Vibronic Coupling in Niobium Nanowires*

### 4.3.1 Vibrational Modes of a Niobium Dimer

With the HG and LG state characterized as being a dimer placed either symmetrically or asymmetrically with respect to the two leads, niobium nanowires clearly present unique advantages in terms of testing for vibronic coupling because niobium naturally forms a molecule during the final stages of contact elongation, niobium nanowires can serve as an ideal testbed for testing vibronic coupling between superconducting electrodes, without having to artificially introduce a molecule into the junction. To this end, our collaborators have extended the structural DFT calculations of the HG state to include the lowest vibrational frequencies of the system, the results of which are seen in Fig. 74. For these calculations, the gap between the electrodes was $L_{gap}$=8.42$\mathring{A}$ and the distance from one dimer atom to the nearest electrode was a=a'=3.17$\mathring{A}$ [150]. The lowest vibrational frequency corresponds to a

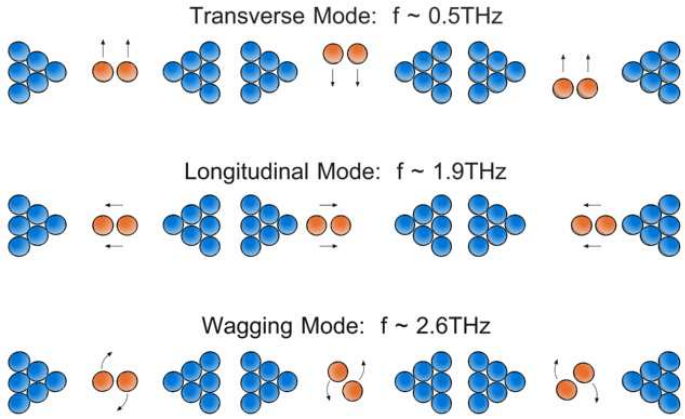


Figure 74: Shown above are the three lowest vibrational frequencies for the HG state and the corresponding vibrational motion which is induced. By plugging these frequencies into the Josephson relation, resonant coupling is expected to occur at the following voltages: $V_1$=1.0 mV, $V_2$=3.9 mV, and $V_3$=5.4 mV. It should be noted that this analysis is valid only for the HG state; due to the anisotropy of the potential for the LG state, the lowest vibrational modes are slightly different than those given here.

transverse mode and has a frequency of approximately $f_t$=0.5 THz, the next highest mode is the longitudinal mode whose frequency is approximately $f_l$=1.9 THz, followed by the

third mode which consists of a wagging motion and whose vibrational frequency is approximately $f_w$=2.6 THz. These relatively low vibrational frequencies reflect the strong d-orbital coupling between the nanowire and electrodes, thereby making the potential energy surface inside the gap region very shallow along the axis connecting the leads. For comparison, further DFT simulations show that the intra-dimer stretching frequency is given to be approximately 11.1 THz, over four times greater than the frequency of the wagging mode and beyond the high frequency limit of the AC Josephson effect. Thus, the low curvature of the potential energy surface is experimentally advantageous, allowing possible measurements of not only the fundamental frequency of these vibrational modes, but also higher harmonics up to approximately 8 THz.

In addition to these DFT studies, further simulations have given the dependence of the HG state vibrational frequencies on the contact elongation. These results have shown that by compressing the nanowire to a distance of $L_{gap}$=7.73 $\AA$, the dimer tilts with respect to the electrode axis by $\theta = 27.5°$ and the resulting vibrational frequencies are calculated as $f_t$=0.3 THz, $f_l$=2.2 THz, and $f_w$=2.6 THz. Thus, the dimer's vibrational frequencies are not strongly dependent on the electrode spacing, further reflecting the low curvature of the potential energy surface inside of the gap. However, upon further compression of the nanowire beyond this point, abrupt changes in atomic configurations result with the dimer being highly tilted with respect to the electrode axis. Similarly, further elongation of the nanowire beyond the initial gap value of $L_{gap}$=8.83 $\AA$ results in highly stretched asymmetric configurations which precede the eventual breakup of the dimer. Clearly for these cases, the resulting transport and vibrational properties deviate significantly from those calculated above due to the drastic changes in atomic structure for these cases.

Returning to the vibrational frequencies for the non-tilted dimer configuration, as seen in Fig. 74, the Josephson relation can be applied to these frequencies to determine the resonance voltage for which peaks in the differential conductance should be visible, if vibronic coupling does exist for this system. Specifically, by using the relation, $V_{res} = hf_J/2e$, the three lowest resonance voltages should be approximately 1.0 mV, 3.9 mV, and 5.4 mV. Hence, if coupling between the vibrational modes of the niobium nanowire and the AC

Josephson effect exists, peaks in the differential conductance are expected to be at these voltages, as well as multiples of these voltages which correspond to higher harmonics of the vibrational modes. However, it should be noted that for voltages below the superconducting gap $V < 2\Delta/e$, there are additional peaks due to multiple Andreev reflection which serve to mask evidence of vibronic coupling.

### 4.3.2 Experimental Results

For high quality niobium thin films, the superconducting gap is typically 1.2meV, meaning that additional structure in the differential conductance trace is expected due to multiple Andreev reflections for voltages less than 2.4 mV. These conductance peaks are observed at voltages which correspond to the condition, $V_{mar} = 2\Delta/ne$. Specifically for the n=2 peak, a conductance feature is expected at approximately 1.14mV, very close to the predicted resonance voltage of the transverse mode ($V_f = 1.0$ mV); thus, fully resolving the proposed transverse peak may be unattainable due to the presence of MAR peaks. In fact, Fig. 75 shows a differential conductance trace for the HG state at low biases taken at 4.2 K. In addition to the MAR peaks, which are marked with dashed lines, there is an additional peak at 1 mV which is due to vibronic coupling to the transverse mode of the dimer. The peak cannot be fully resolved due to the strongly nonlinear background; however, the peak itself is clear and reproducible in many contact realizations through the use of mechanical adjustments. However, though the transverse peak suffers from the additional nonlinearity induced by MAR peaks, the other two lowest vibrational frequencies are both above the subgap region and thus should not be obscured. Fig. 76 shows another HG state differential conductance curve which has a much broader range than the figure above; this data was taken at three different temperatures, one below the critical temperature and two above it. For the superconducting curve, the subgap structure is clearly visible at low voltages due to MAR; however, in addition to these peaks, there is considerable structure above the voltage corresponding to $2\Delta$, which is referred to as the over-the-gap (OGS) region. This structure exists for both polarities of the voltage, though upon raising the temperature above $T_c$, the peaks disappear and leave a base curve whose structure is dependent on

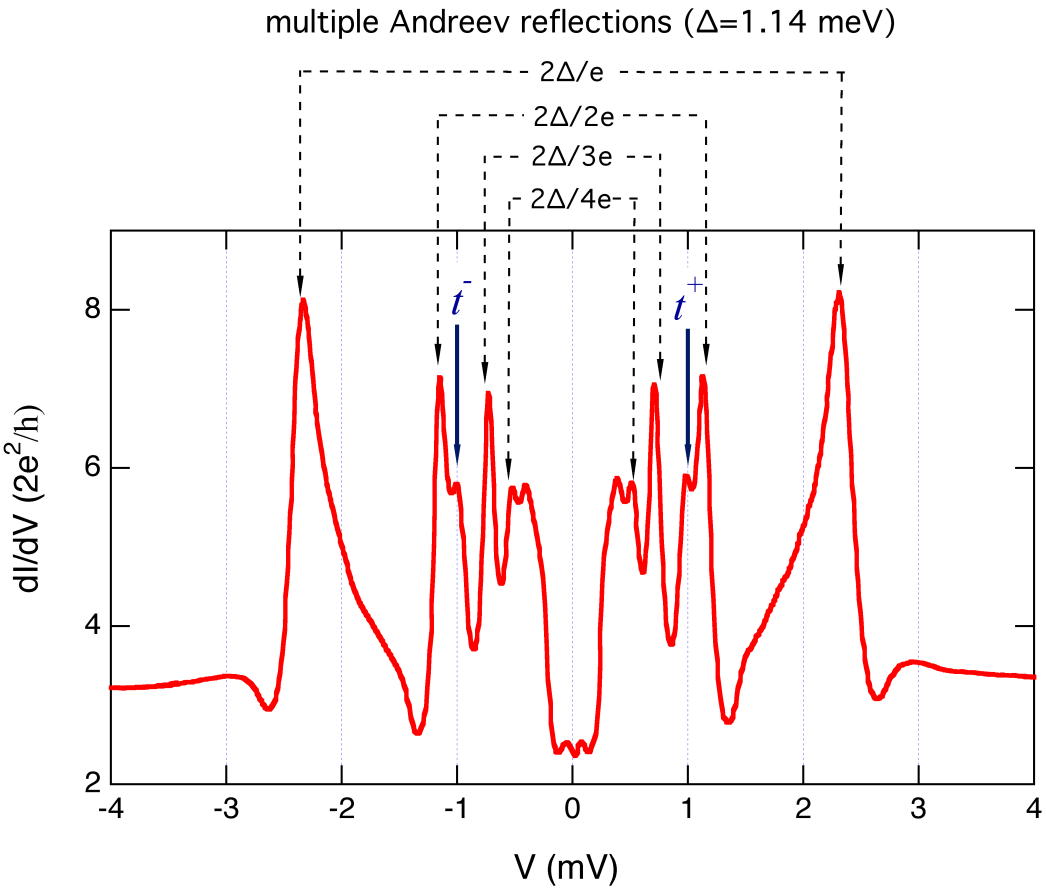


Figure 75: Shown here is a differential conductance trace for the HG state, where the focus is on the subgap structure due to multiple Andreev reflections. Among all the MAR peaks which occur at well defined voltages, there are two symmetric peaks which are partially resolved at 1.0 mV against the strongly non-linear background. This voltage corresponds to the transverse mode of the niobium dimer, thus showing that vibronic coupling does occur in niobium nanowire systems.

quantum interference effects [148, 223, 155]. Moreover, this type of behavior was seen for both the HG and LG state in over 80 contact realizations from 6 separate microfabricated samples, though the characteristics of the two OGS structures are somewhat different. More importantly, no OGS peaks are observed in either tunnel junctions or bulk contacts, though features which are consistent with the onset of longitudinal and transverse phonon modes at approximately 16mv and 24mv [112, 171] are resolved for bulk contacts (this is the point contact spectroscopy regime).

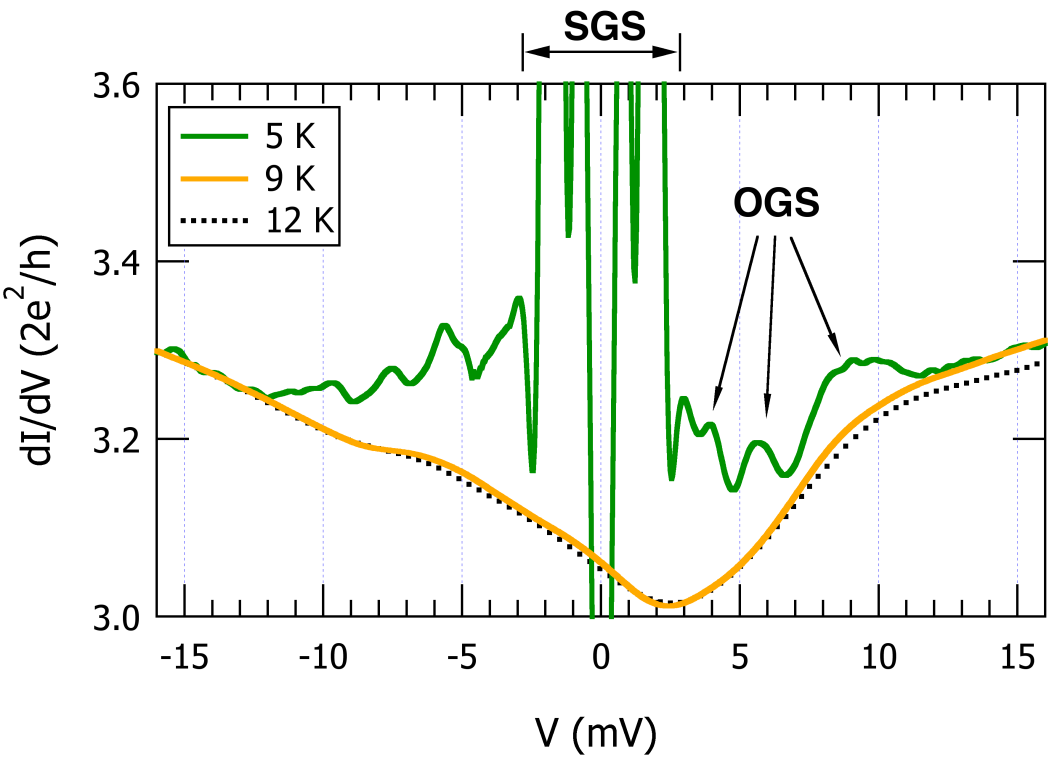


Figure 76: Shown here are three differential conductance traces for the same contact, but at different temperatures; for temperatures below the superconducting critical temperature, new peaks are observed in the differential conductance which correlate to the expected vibronic peaks. Because this effect is due to superconductivity, these peaks disappear above the critical temperature, leaving only a background curve which is due to backscattering of normal electrons in the leads.

The type of quantum interference which creates the base curve is due to electron waves being transmitted through the contact, then subsequently being backscattered at defect or impurity sites in the electrodes. This reflected wave is able to interfere with other incoming electron waves, thus modifying the transport properties of the system. Thus, the asymmetry

of the base curve reflects the fact that the distribution of scattering centers in the electrodes are different. Further, it has been shown [223] that even small changes in contact elongation can significantly affect the structure of the base curve, even though the total conductance of the point contact may remain the same. Additionally, the same study showed that the base curve varies with temperature due to the changing coherence length of the transmitted electron waves; as the coherence length decreases, there is less chance of coherent scattering off defects in the electrodes, thus smoothing out the structure of the base curve. As an additional point of interest, these quantum interference effects are still manifested at room temperature for many atomic contacts due to both long coherence lengths of some materials, as well as the nanometer scale constriction of the contact region.

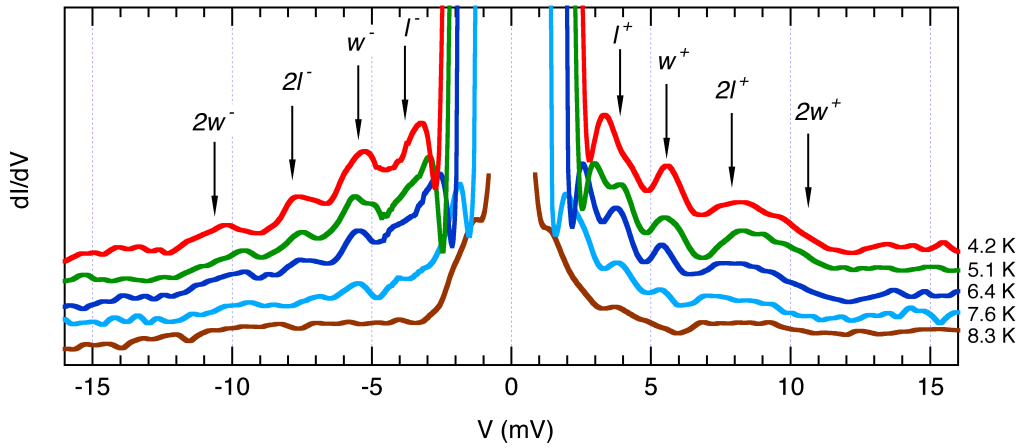


Figure 77: Shown here are multiple differential conductance traces for the same contact but at different temperatures; as the temperature is increased, the amplitudes of the OGS peaks steadily decrease until they become zero above the critical temperature. This implies that the vibrational modes of the system couple to a superconducting degree of freedom; furthermore, the positions of the peaks do not shift with temperature, as do multiple Andreev reflection peaks. Thus, another mechanism must create this resonance and it is proposed that this is due to vibronic coupling.

To understand the OGS structure, Fig. 77 shows a series of differential conductance curves for increasing temperatures which are displaced from each other for clarity; peaks for both the longitudinal and wagging mode are seen, as well as higher harmonics of both modes. No higher harmonics for the transverse mode are seen because with each harmonic,

the amplitude of the conductance peak decreases and since the first two harmonics of the transverse peak reside inside of the subgap structure, no OGS structure can be resolved for the transverse mode. From the figure, the amplitudes of the OGS peaks decrease with increasing temperature until they become zero at the critical temperature. Furthermore, even though the amplitudes are significantly affected by temperature, the positions of the peaks do not shift with increasing temperatures. In addition to not shifting with temperature, our experiments have shown that for elongations of this contact by up to 0.6 $\mathring{A}$, the resonant voltages do not shift within our experimental accuracy. Our resolution of the OGS peaks is limited by the width of the peak itself, which is approximately 0.8 mV, and corresponds to a frequency resolution of 0.4 THz. This insensitivity to temperature of the OGS peaks is in stark contrast to MAR peaks which are dependent on the superconducting gap parameter; as the temperature is increased, MAR peaks move to lower voltages which correspond to the decrease in magnitude of the superconducting gap parameter,as noted in Chapter II. Hence, the OGS peaks are most definitely not related to the MAR features which are present in point contacts at low bias voltages. Thus, a superconducting degree of freedom, not related to the mechanism of multiple Andreev reflection, is capable of coupling to the vibrational modes of a suspended niobium nanowire and exciting the lowest vibrational modes of the system.

These results are seen in the LG state as well, as can be seen in Fig. 78. The left panel of the figure shows the OGS peaks for the LG state as the piezo voltage is ramped. It is evident from the figure that the OGS peaks do not shift or change in any appreciable way during large changes in the distance between the electrodes; this is in contrast to the second panel of the figure which shows a temperature sweep for LG OGS peaks. Here, the peaks can be seen to move inward with increasing temperature. However, the shift in the peaks does not follow the gap temperature dependence, as the MAR features do. Fig. 79 shows the shift in peak placement as a function of temperature with the gap parameter's temperature dependence superimposed for comparison; clearly, the shift is too slow to be caused by any changes in the gap parameter. Moreover, as shown previously for the LG state and is further confirmed by this figure, the LG state is not destroyed by cycling the temperature;

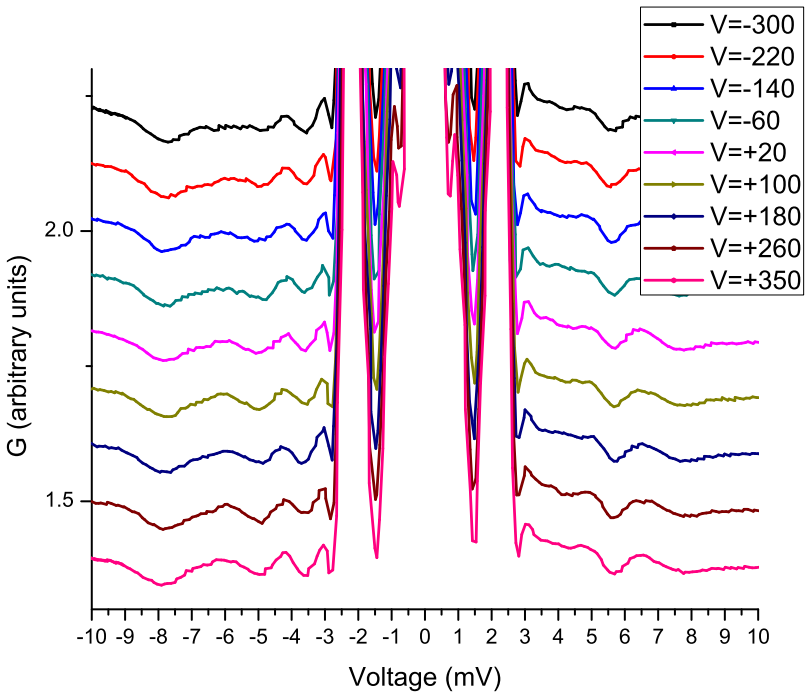


(a)

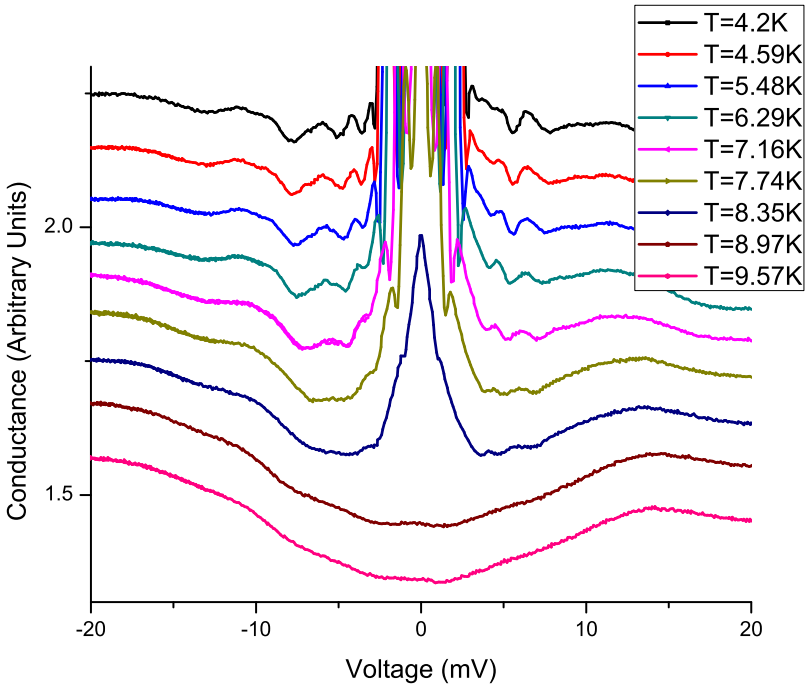


(b)

Figure 78: (a): LG OGS structure as the piezo voltage is ramped; the OGS for the LG state is similar in appearance to the HG state, though the resonant voltages are slightly different due to the asymmetric potential which the LG state resides inside. More importantly, the OGS structure shows no noticeable change in voltage as the contact is elongated, further showing the relatively shallow nature of the potential energy surface inside the gap region. (b): Temperature sweep of the LG OGS peaks; here, a noticeable shift inward for the OGS peaks is seen as the temperature is increased. This shows that changes in temperature affect the curvature of the potential energy surface more than changes in the distance between electrodes.

this means that the changes in resonant frequency must be due to slight changes in the LG state. As such, the shifts in resonance frequency which are seen in Fig. 79 are attributed to thermal expansion of the dimer which slightly changes the structure of the dimer.

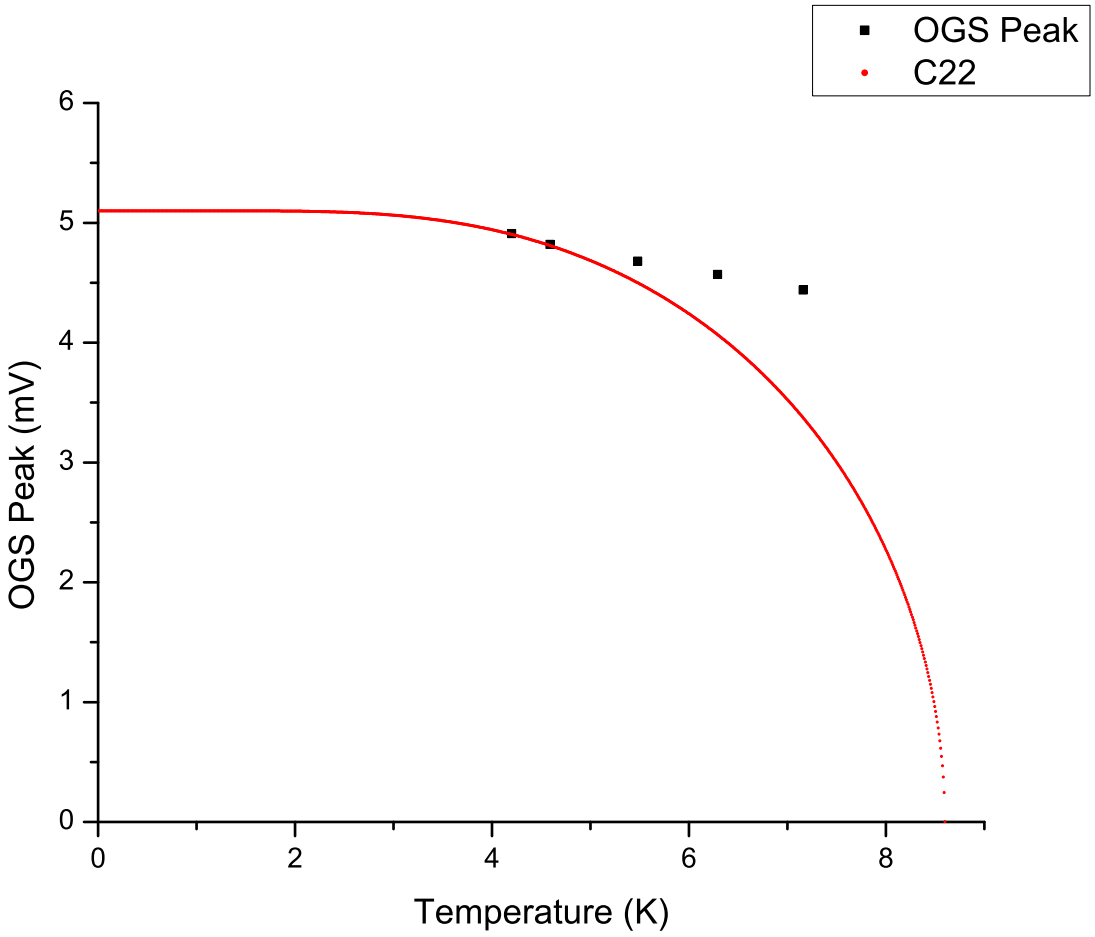


Figure 79: Shown here is the variation of the resonant voltage in the LG state as a function of temperature, along with the BCS result for the temperature dependence of the gap parameter. Clearly, the LG OGS peak varies much more slowly than the gap at high temperatures, implying that the variation is not due to superconductivity; instead, a likely explanation is that thermal expansion of the contact at higher temperatures causes the shift in peak voltage.

### 4.3.3 Future Work

Thus, it is possible to use the AC Josephson effect to excite vibrational modes of nanowires. Here it was specifically shown for the intrinsic niobium dimer which is formed during the final stages of elongation of the contact. With the intrinsic test completed, we now hope to expand our experimental capabilities to include the embedding of organic molecules into the

junction for further testing,as seen schematically in Fig. 81. As well, by introducing different gases into the sample space, various niobium nanowires can be created and investigated; for instance, by allowing oxygen to react with the dimer, it is anticipated from DFT simulations that a new structure, as in Fig. 80, will be created.

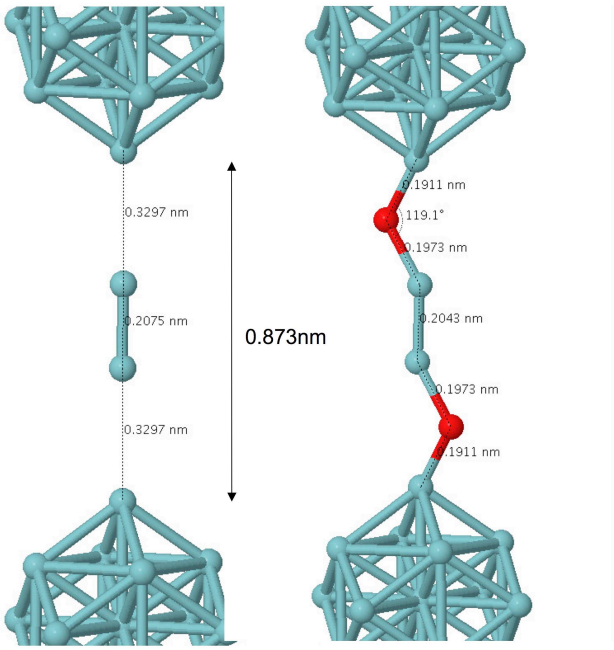


Figure 80: Here, the result of a DFT calculation is shown where oxygen is introduced into the sample space; it can be seen that the addition of the gas bridges the electrodes, thus drastically changing the conductance features of the device.

In addition, we are working on a similar project which would incorporate two point contact junctions in order to perform spectroscopic measurements on molecules, as seen in Fig. 82. Here, one of the point contacts will act as an emitter of Josephson radiation, while the other acts a detector. If a molecule is embedded between the two junctions, it will absorb a characteristic spectrum of radiation and thus spectroscopic measurements can be done by measuring the incident radiation profile from the receiver junction [27]. In order to extract the radiation profile from the transport measurements, a technique known as Hilbert Transform Spectroscopy will be utilized [129, 66, 67]. In this technique, measurement of the transport properties of both the un-radiated and radiated junctions are used to determine the spectral nature of the incident radiation. This type of spectroscopy has the distinct

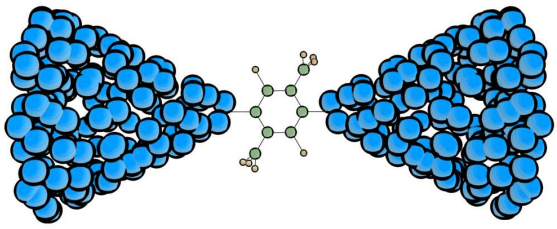

Figure 81: Shown here is a mock-up of a point contact junction which is bridged with an organic molecule; we hope in the near future to incorporate the ability to embed various molecules into point contact break junctions for further spectroscopic measurements.

advantage of being applicable to electromagnetic radiation of any arbitrary spectrum, in contrast to many other spectroscopic methods. Additionally, the system theoretically has a broad bandwidth, a high sensitivity, and a short time constant.

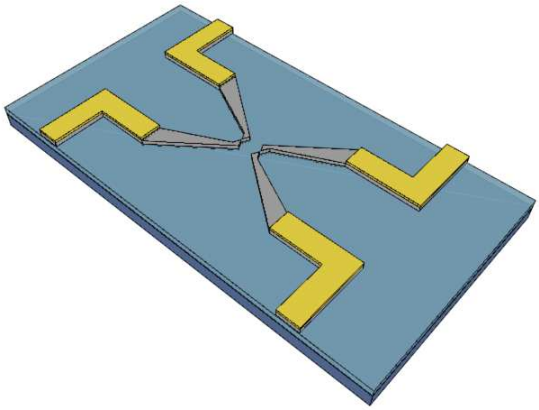

Figure 82: Shown here is a mock-up of the point contact spectrometer. The device uses one point contact to transmit a certain spectrum of radiation, while the other acts as a receiver; if a molecule is embedded between the two point contacts, the received spectrum will be different from the transmitted one, allowing a determination of the spectra of different molecules.

Lastly, another avenue of interest is depicted in Fig. 84 which shows the effect of periodic modulation of the piezo on the HG and LG states. In general, the HG and LG state occupy a double well potential of the form shown in Fig. 83, where the quantity $\Delta V$ denotes the energy barrier between the two states. As the contact is elongated, the

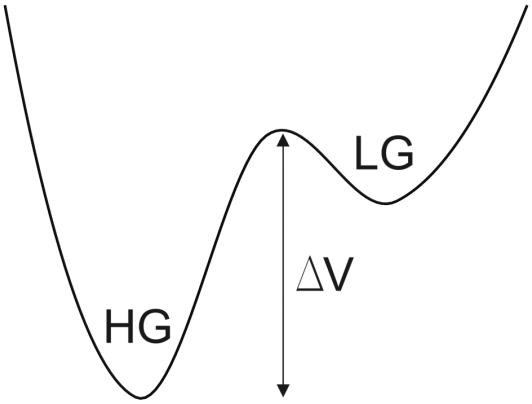


Figure 83: A generic model of the double well potential of the HG and LG state. The energy barrier which prevents state crossing has a magnitude given by ΔV.

double well potential which contains the HG and LG states is shifted preferentially toward the LG state, decreasing ΔV; eventually, the contact is elongated to the point that the LG state becomes the global minimum of the system, reversing the initial configuration of the potential. Similarly, as the contact is retracted, the HG state can again become the preferred state. However, it is possible for the system to jump from one state to the other through the energy added to the system due to background noise; the rate for this type of process is known as Kramer's rate [130], $r_K$, and is given by:

$$r_K = \frac{\omega_0 \omega_b}{2\pi\gamma} e^{-\frac{\Delta V}{D}}. \tag{151}$$

An interesting effect [83][84][115] known as Stochastic Resonance (SR) occurs when noise of a very specific type is added to this a double well potential which is subject to a weak periodic force. If the average waiting time between two noise induced events, $T_K = 1/r_K$, is comparable to half the period of the forcing, $T_\Omega$, then an enhancement of the interwell transition rate occurs; this is known as the time-matching condition:

$$2T_K = T_\Omega. \tag{152}$$

Thus, stochastic resonance is defined as the statistical synchronization between noise-induced interwell transitions of a double well potential. It is expected that the HG and LG state will exhibit stochastic resonance inside of the RTN region due to the presence of the

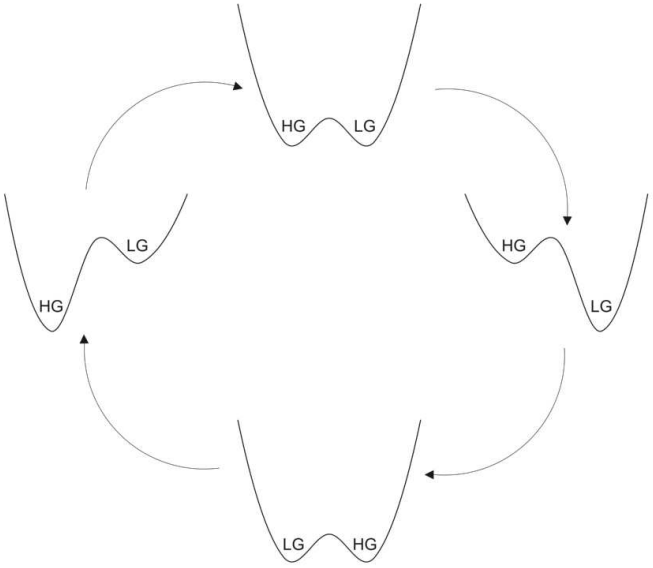


Figure 84: Effect of the double well potential on elongation and retraction of the contact. As the contact is elongated, the LG eventually becomes preferred over the HG state; conversely, the HG returns to being the preferred state if the contact is retracted.

thermal noise; as the temperature of the sample is raised, the corresponding transition rate can be measured and is expected to show a peak corresponding to stochastic resonance.

# CHAPTER V

# SUPPRESSION OF SUPERCONDUCTIVITY AT HIGH BIASES

This chapter focuses on the behavior of point contacts at large voltage biases (10's of mV); in this regime, the contact is expected to behave as a normal metal and have a flat conductance curve. However, our experiments have shown that in reality there is some structure to the current-voltage curve beyond the expected linear behavior; specifically, a cusp appears on the current-voltage curve where a transition to a lower current takes place. To describe this effect, a model is introduced which is capable of reproducing the functional dependencies of this feature on the contact resistance of the device and temperature, as well as quantitatively predicting the correct value for the suppression feature. The model relies on a coupling of two different effects: magnetism and temperature. Specifically, as the current is increased through the contact, both the magnetic field surrounding the contact and its temperature are increased. Furthermore, both of these external influences are capable of reducing or even eliminating superconductivity due to a suppression of the pair potential, $\Delta$; as such, it is anticipated that at high biases, the combined effect of the induced magnetic field and temperature is sufficient to destroy Josephson coupling between the two superconducting sides of the SNS junction. In other words, if there is no overlap of the superconducting wave functions, the phase difference on each side of the junction will be random (not locked as in a Josephson junction) and thus no supercurrent will be able to flow through the junction. This implies that the suppression feature results from the elimination of supercurrent through the junction which is brought on by a reduction of the pair potential to a point where the phase difference across the junction cannot be well defined.

## 5.1 The Excess Current

Up to this point, the effect of Andreev reflection on charge transport has only been considered for the range of voltages below $2\Delta$ (i.e. $|eV| \leq 2\Delta$); however, there remains a non-zero probability for Andreev reflection for voltages above this value, as seen in Fig. 24. Thus, two mechanisms exist for charge transport for voltages above $2\Delta$: quasiparticle transfer and Andreev reflection. Because the onset of the quasiparticle current creates dissipation in the system, the branch of the current-voltage curve above $2\Delta$ is termed the dissipative branch; this region of the current-voltage curve has an ohmic character, though it does not extrapolate to zero current for zero voltage as a purely ohmic conductor would. Instead, there is a non-zero offset to the dissipative branch due to the constant transfer of Cooper pairs through Andreev scattering; this extra current has been termed the excess current [31] and can be seen in Fig. 85. From the figure, one can see that the current-voltage curves are modified by the addition of the excess current, but that the differential conductance is not altered since the excess current is constant.

In order to understand the excess current, the BTK model [31] can be employed; this model replaces the true nature of an SNS device with that of Fig. 23, which uses two delta function barriers at the N-S interfaces and neglects the complexities of the proximity effect. These delta function barriers are characterized through a strength parameter, Z, which is zero for purely ballistic contacts.

Generally speaking, the excess current can be written as the difference between the current calculated through a N-S barrier and that of a N-N barrier:

$$I_{exc} = (I_{NS} - I_{NN})|_{eV \gg 2\Delta}, \tag{153}$$

where the large voltage condition must be met for this expression to be valid. In the BTK model which uses the parameters A,B,C,D to model the dynamics of the N-S interface, this expression for the excess current can be put in the following form:

$$I_{exc} = \frac{1}{eR_N[1 - B(\infty)]} \int_0^\infty [A(E) - B(E) + B(\infty)]dE, \tag{154}$$

where A(E) and B(E) are both functions of Z and B($\infty$) is the normal state reflection

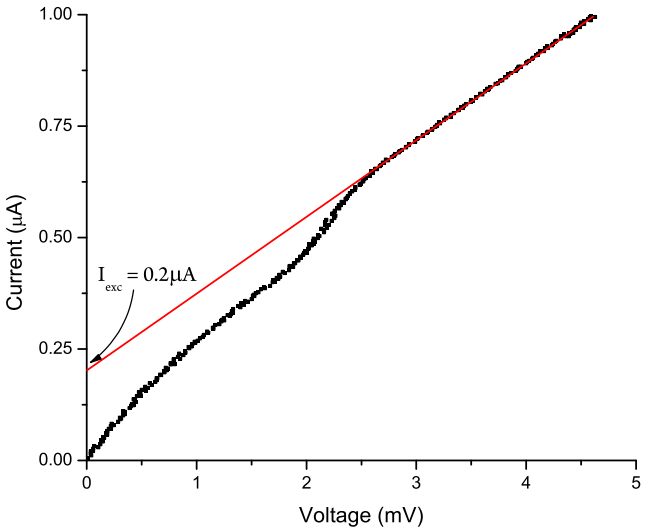


(a)

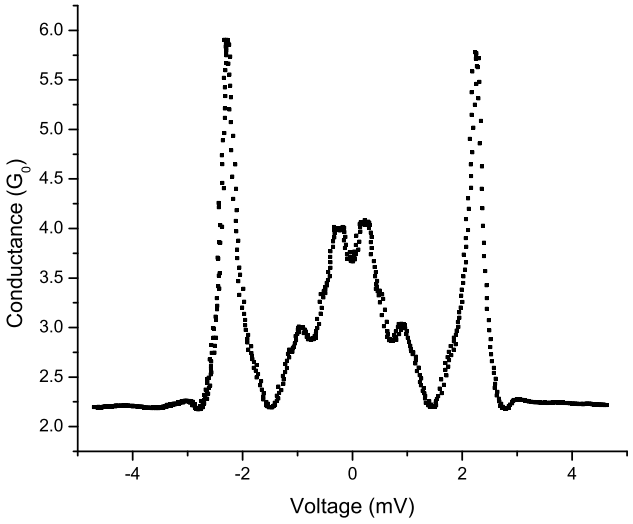


(b)

Figure 85: (a): Current-voltage curve for a niobium point contact; once the voltage exceeds $2\Delta$, quasiparticles are able to undergo transmission from one superconducting electrode to the other, adding a dissipative current to the already present supercurrent. At these higher voltages, the supercurrent is independent of voltage and thus adds a constant offset to the ohmic characteristic of the normal current; thus, the linear portion of the current-voltage curve does not extrapolate to zero. Instead, the extrapolated value is that of the excess supercurrent which exists above $2\Delta$. (b): Differential conductance trace for the data presented above. Here, the curve shows significant non-linearities at low bias voltages due to multiple Andreev reflections; however, the conductance plateaus at voltages above $2\Delta$ when the curve reaches the dissipative branch.

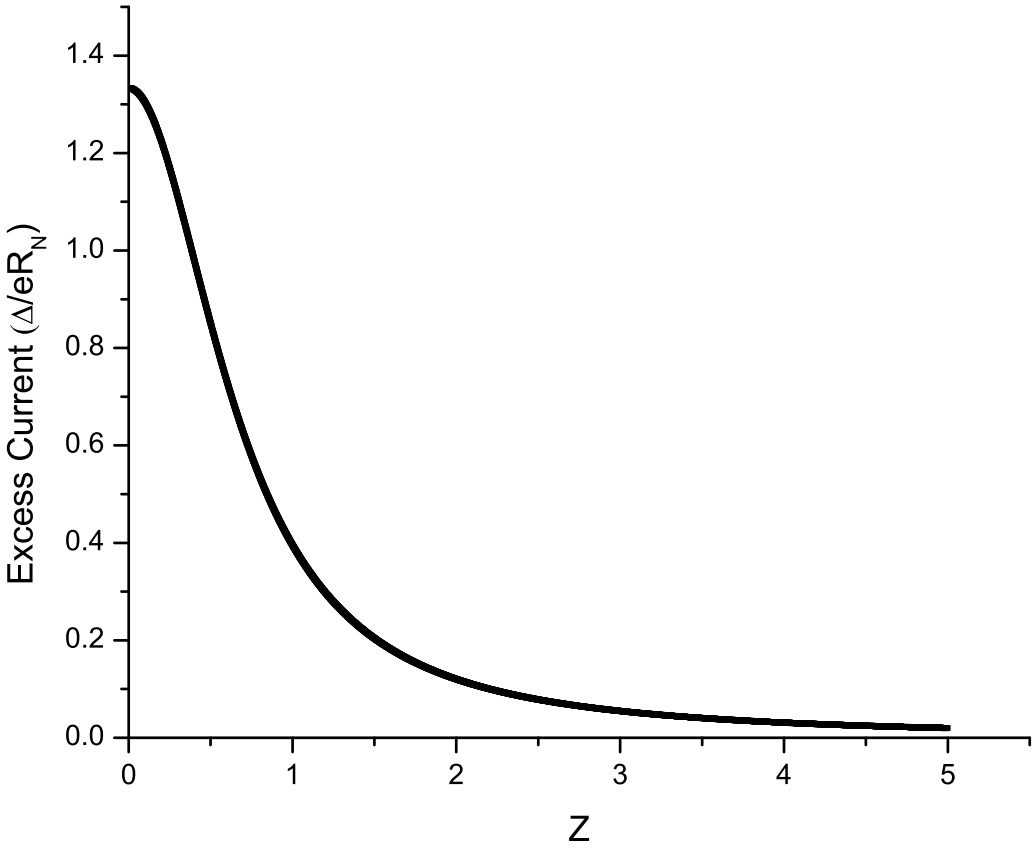


Figure 86: Plotted here is the relationship between the barrier strength, Z, and the excess current at high bias voltages. For most point contacts, the BTK model predicts that the device will operate ballistically, implying that the barrier strength will be small and the normalized current will be approximately one; as such, the amount of excess current for a point contact can be estimated as $I_{exc} \approx \Delta/eR_N$.

coefficient at high biases:

$$B(\infty) = \frac{Z^2}{1+Z^2}. \tag{155}$$

The functional forms of both A(E) and B(E) are piecewise continuous and are given in Chapter III; upon solving the above equation for the excess current as a function of barrier strength, the result is given by Fig. 86. The excess current is normalized in the plot to units of $\Delta/eR_N$, making comparisons between different contact geometries easier. Furthermore, the temperature dependence of the excess current is contained entirely within the gap parameter, $\Delta$, so the curve in Fig. 86 is temperature independent. From the figure, for low to moderate values of the barrier strength, the excess current is well approximated as:

$$I_{exc} \approx \frac{\Delta}{eR_N}, \tag{156}$$

since the normalized quantity is approximately one. However, from the current-voltage and differential conductance curves, the above figure can be inverted in order to obtain the value of Z for a given contact configuration; in this way, the nature of the contact can be determined (i.e. ballistic or diffusive). As well, the value of Z is used in the BTK expression for the width of a point contact constriction:

$$a = \sqrt{\frac{4(1+Z^2)}{2\pi N(0) v_F e^2 R_N}}, \tag{157}$$

where N(0) is the quasiparticle density of states at the Fermi energy and $v_F$ is the Fermi velocity. Not only is this a useful estimate of the number of atoms in a point contact, it is also useful in that the product $a^2 R_N$ is only a function of Z. For many mesoscopic systems, the value of Z does not change appreciably from sample to sample; thus, this product can be considered a constant.

Because most of the interesting physics of SNS devices is contained at low biases ($|eV| \leq 5\Delta$), this model does not take into account factors such as heating of the normal region due to the increased quasiparticle density because at such low biases this is not an issue. However, it is clear that the excess current will not remain constant at arbitrarily high voltages; there must exist some point when it is suppressed and the slope of the current-voltage curve renormalizes to $R_N$. In order to better understand the transition to

zero supercurrent, the high voltage characteristics of superconducting point contacts were studied to determine the nature of this transition to zero excess current.

## *5.2 Experimental Results*

Fig. 87 shows the result of measuring both the current-voltage curve and the differential conductance for a superconducting niobium point contact. From the top panel of the figure, it is clear that there are two different linear regions of the current-voltage curve at high biases; one comes from the addition of the excess current to the quasiparticle current and does not extrapolate back to zero. On the other hand, above approximately 18 mV there exists change in the slope of the curve, where the line does extrapolate back to zero. This behavior is more pronounced in the differential conductance curve: in addition to the supercurrent peak at low bias voltages, the change in slope at 18 mV corresponds to a suppression of the conductance.

Furthermore, this phenomenon is present in every sample tested at large voltages, though the placement of the peak varies with the specific contact configuration, as well as with temperature. In addition, the excess current is inversely proportional to the superconducting gap, implying that the slope of the feature will change as the temperature is raised; specifically, the amount of excess current will rise with increasing temperature due to the functional dependence on the gap. This means that at higher temperatures, the current will change more drastically as the excess is suppressed, creating a more pronounced feature in the differential conductance trace; the effect of temperature on the excess current is seen in Fig. 88.

The effect of contact configuration (i.e. normal state resistance) on the suppression voltage can be easily seen in Fig. 89. As the normal state resistance of the contact increases, the suppression feature moves outward; the conductance is normalized in order to show both sets of data since they differ greatly. Furthermore, Fig. 90 shows a fit of the suppression feature versus the square root of the normal state resistance. Over multiple samples, both microfabricated and notched wire, all showed this dependence on the normal state resistance over a wide range; in the figure shown, the data is taken for normal state resistances ranging

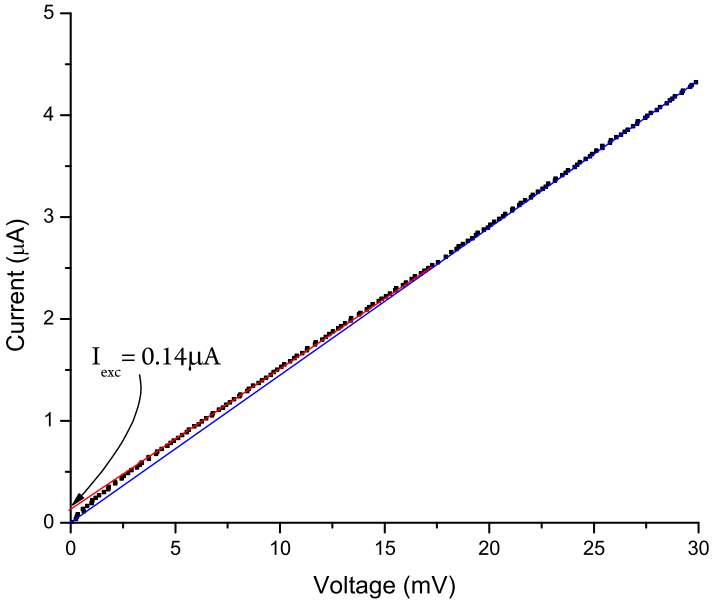


(a)

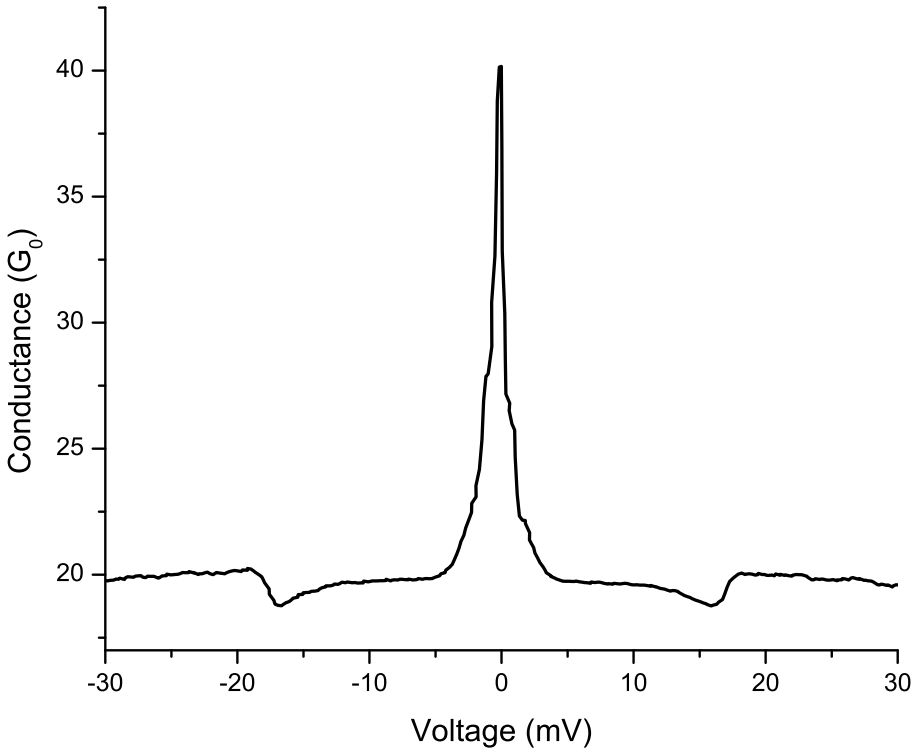


(b)

Figure 87: (a): Current-voltage characteristic at high biases for a niobium point contact. Also shown is the line which extrapolates back to the excess current of the device; this line fits the data well until approximately 18 mV, whereupon the slope of the curve changes. This change in slope is associated with the suppression of the excess current, as the slope of the new line extrapolates back to zero. (b): Differential conductance trace of the same data which shows the suppression feature more clearly.

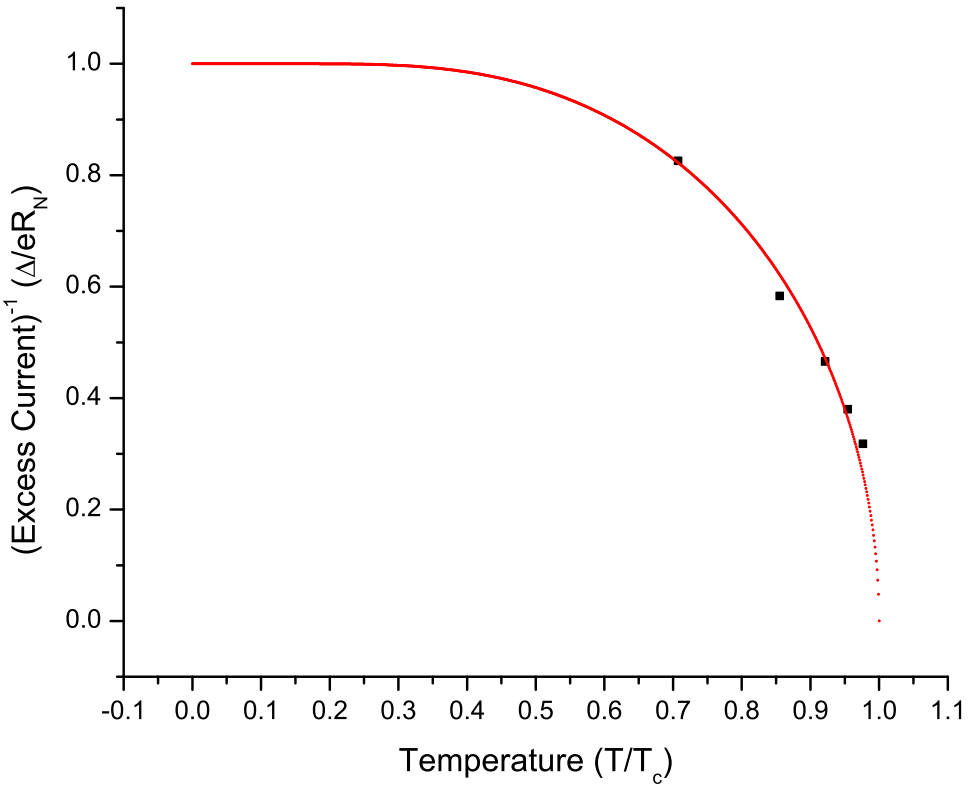


Figure 88: Shown here is a plot of the inverse excess current as a function of temperature for a given contact configuration. From the BTK model, the excess current is predicted to inversely follow the superconducting gap; as such, the inverse of the current is plotted as a function of temperature. Clearly, the data confirms the theoretically predicted temperature dependence of the excess current.

from approximately 200Ω to 3600Ω.

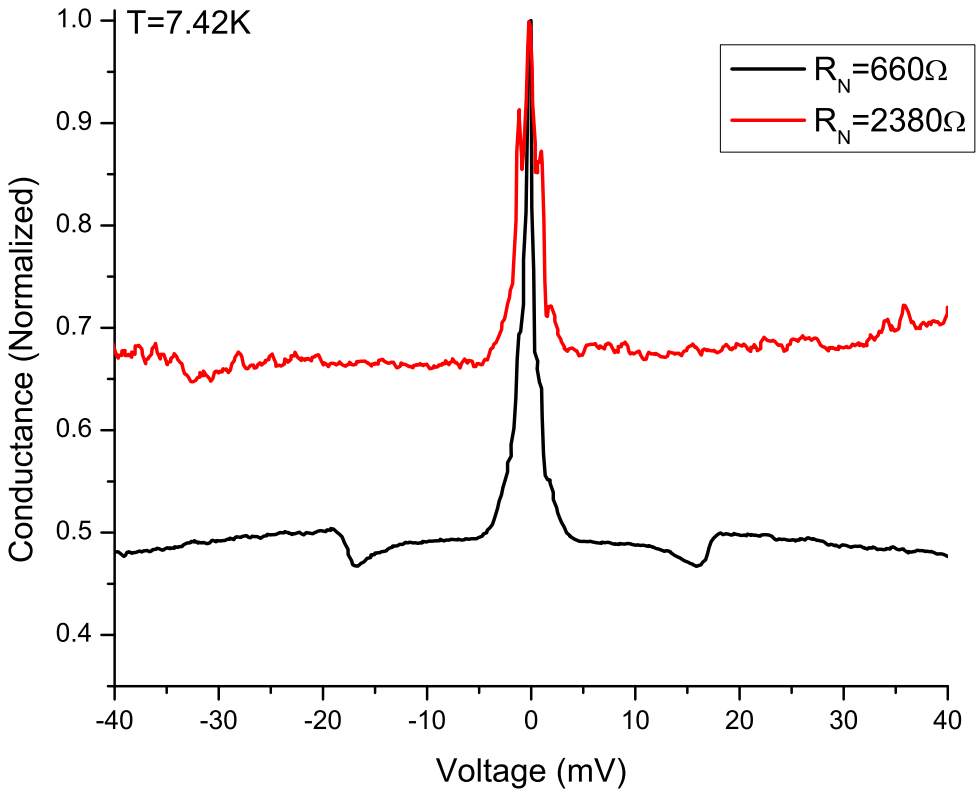


Figure 89: Shown here are two normalized differential conductance curves for different atomic configurations; as the normal state resistance of the contact is increased, the voltage at which the excess current is suppressed moves outward.

The effect of temperature on the suppression feature can be seen in Fig. 91, where the data is taken for a single contact configuration; the curves are offset for clarity with the lowest temperature curve being at the top of the graph. As the temperature is increased (as the curves move toward the bottom of the graph), the feature moves inward, slowly at first and subsequently faster as the temperature nears $T_c$. Furthermore, the slope of the suppression feature tends to become sharper as the temperature is increased, possibly implying some sort of thermal activation of the suppression. In the second panel of the figure, the normalized feature voltage is plotted against the normalized temperature for many different samples; as well, the BCS temperature dependence of the gap parameter is plotted for comparison. The reason the feature voltage was normalized is that for different

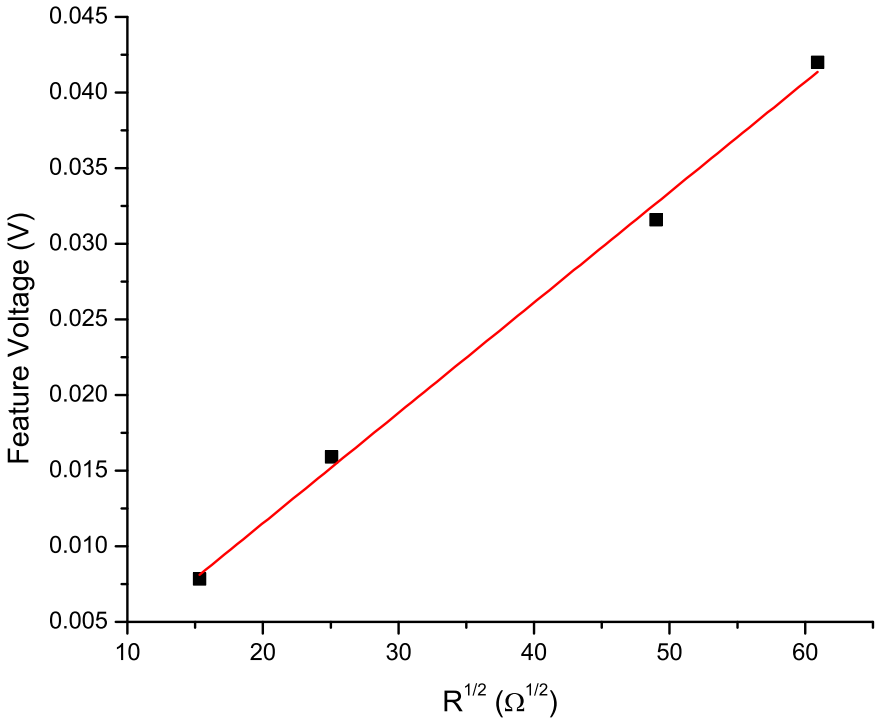


Figure 90: Here is the fit of the suppression feature as a function of the square root of the resistance; the feature follows the square root dependence of the model.

samples, the placement of the suppression feature may vary slightly; as such, the temperature dependence of each contact configuration is normalized to its zero temperature value and then was added to the plot in Fig. 91.

Clearly, the temperature dependence of the suppression feature follows the gap, implying that the effect has to do with superconductivity in some fundamental way; however, the mechanism behind the suppression of the excess current is still unclear. To account for the functional dependence of the suppression feature on the normal state resistance, as well as the temperature, a critical current model [233] is proposed; this is in contrast to other models for finite bias peaks which are inconsistent with the experimental observations in niobium point contacts. These models are are based on various assumptions such as a depairing current density [235] or increased absorption of Andreev holes [173] or a form of quantum interference similar to the type which produces the base curves in Chapter IV [96].

## *5.3 Theoretical Model*

From the discussion in Chapter II concerning the interplay between magnetism and superconductivity, it was shown that for a type II superconductor, like niobium, an applied magnetic field above $H_{c1}$ creates regions of normal material through which magnetic flux penetrates in units of $\Phi_0$; this flux penetration is accompanied by a local suppression of the Cooper pair density in the region around the vortex. Furthermore, it was also shown that vortices tend to be pinned to lattice impurities and defects; this fact, coupled with the knowledge of how lattice defects create the quasiparticle base curve shown in Chapter IV, implies that if the magnetic field is raised above $H_{c1}$ near a point contact, many vortices will be pinned in the region immediately surrounding the contact.

Thus, if it is assumed that current through the point contact travels through a radius, r=a, then it is expected that a circumferential magnetic field will be set up by this current given by:

$$\mathbf{H} = \frac{I}{2\pi a}\hat{\phi}, \tag{158}$$

where the value of the field is taken at the surface of the point contact. From this expression, it is expected that supercurrent will be able to flow only if it is less than a certain critical

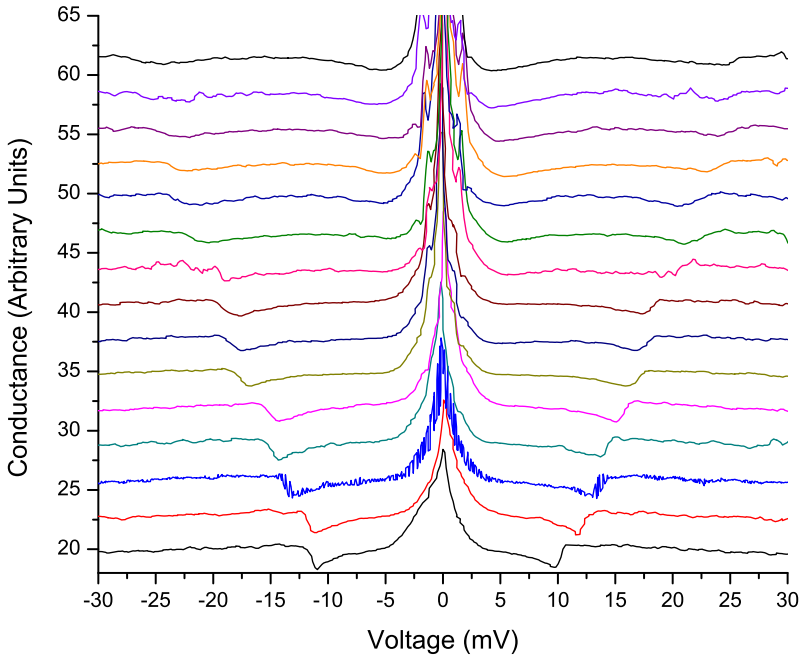


(a)

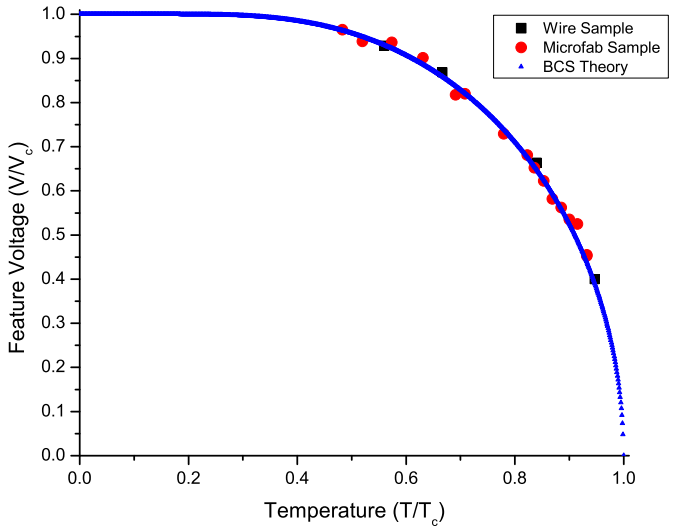


(b)

Figure 91: (a): Temperature sweep of the differential conductance for the same atomic configuration; the curves are offset for clarity and the temperature decreases as the curves go higher. As shown, the suppression feature moves inward as the temperature increases; as well, the slope of the feature tends to be greater for higher temperatures. (b): Fit of the suppression feature for multiple samples as a function of temperature; the fit of the data is provided by the temperature dependence of the BCS gap parameter, thus corroborating the superconducting nature of the feature. In addition to microfabricated samples, the data also includes notched wire samples.

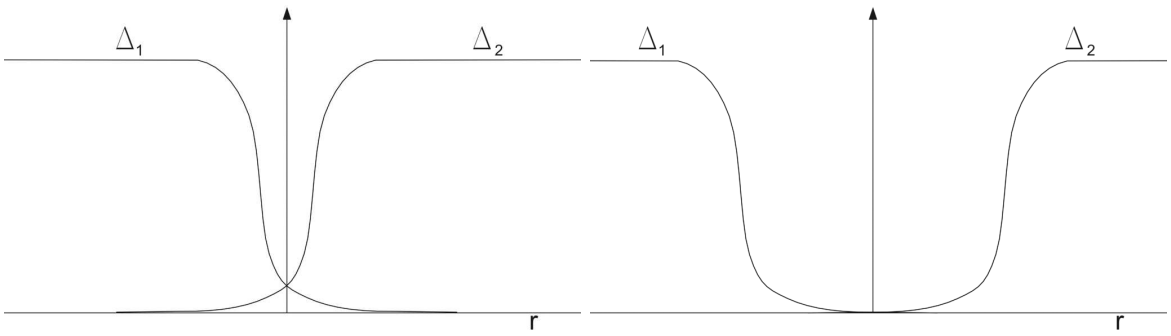


(a) (b)

Figure 92: (a): Here is a typical profile for a Josephson junction showing slight overlap of the two wave functions; this overlap is necessary for coherent effects to be possible. However, if the overlap is too great, there will be no phase difference across the normal region (the two phases will equal one another); only if weak coupling exists will the phases be able to lock relative to one another. (b): In the opposite extreme of no overlap, the phase differences are independent quantities and coherence will not be achieved.

value, $I_c$, given by:

$$I_c = 2\pi a H_{c1}. \tag{159}$$

For current higher than this, the induced magnetic field will be sufficient to destroy superconductivity locally around the point contact. Intuitively, this suppression of superconductivity implies that the overlap of the superconducting wave functions which is necessary for the Josephson effect, no longer exists. Instead of overlap between the two superconducting sides of the junction, there exists a region where $\Delta = 0$, which will prevent coherent coupling of the phase difference between the two sides; this is pictured in Fig. 92.

Because the region of interest for the suppression is at voltages much greater than $\Delta/e$, the current can be written in the general form:

$$I_{eV \gg 2\Delta} = \frac{V}{R_N} + I_{excess}. \tag{160}$$

However, since our interest lies with voltage at which the suppression feature manifests, it is more natural to solve the above equation for the voltage at high biases:

$$V_{eV \gg 2\Delta} = IR_N - I_{excess}R_N. \tag{161}$$

Now, by assuming the current, I, is equal to the critical value, $I_c$, the suppression voltage can be written as:

$$V_{peak} = 2\pi a H_{c1} R_N - I_{excess} R_N. \tag{162}$$

From the previous discussion of the excess current, it was shown that the following relation exists in the BTK model [equation (157)]:

$$a = \sqrt{\frac{4(1+Z^2)}{2\pi N(0) v_F e^2 R_N}}. \tag{163}$$

By rearranging terms, the quantity $a^2 R_N$ can be written as:

$$a^2 R_N = \frac{4(1+Z^2)}{2\pi N(0) v_F e^2}, \tag{164}$$

which is a constant, if the values of Z do not vary appreciably from sample to sample; in fact, the range of variation of Z can be upwards of 20%, though for most samples it is approximately Z=1.5. Furthermore, given a value for Z, the product of $I_{excess} R_N$ does not vary from sample to sample, as can be seen from Fig. 86. For Z=1.5, the product of $I_{excess} R_N$ is well approximated by $0.2 \cdot \Delta/e$. With these terms being constant for the purposes of the model, the expression for the peak voltage can be simplified to the following form:

$$V_{peak} = k\sqrt{R_N} + V_0, \tag{165}$$

with the definitions of k and $V_0$ being:

$$k = 2\pi H_{c1} \sqrt{\frac{4(1+Z^2)}{2\pi N(0) v_F e^2}}, \tag{166}$$

$$V_0 = 0.2 \left( \frac{\Delta}{e} \right). \tag{167}$$

One way to check the validity of this model is by solving the expression for k in terms of the critical field, $H_{c1}$; from this, one can extract the temperature of the sample which is measured independently of the transport measurements. For the data in Fig. 90, the best linear fit of the data gives the following values: $k = 0.729 mV/\sqrt{\Omega}$ and $V_0 = -3.06 mV$. Using this experimentally determined value for k, along with the density of states [156] being given as $N(0) = 5.44 \cdot 10^{28} states/(eV \cdot m^3)$, the Fermi velocity as $v_F = 1.37 \cdot 10^6$m/s,

and Z=1.5 gives that the critical field is approximately 110 G. This value of the critical field corresponds[78] to a reduced temperature (t=T/$T_c$) of 0.964, whereas the data was taken at a reduced temperature of t=0.853.

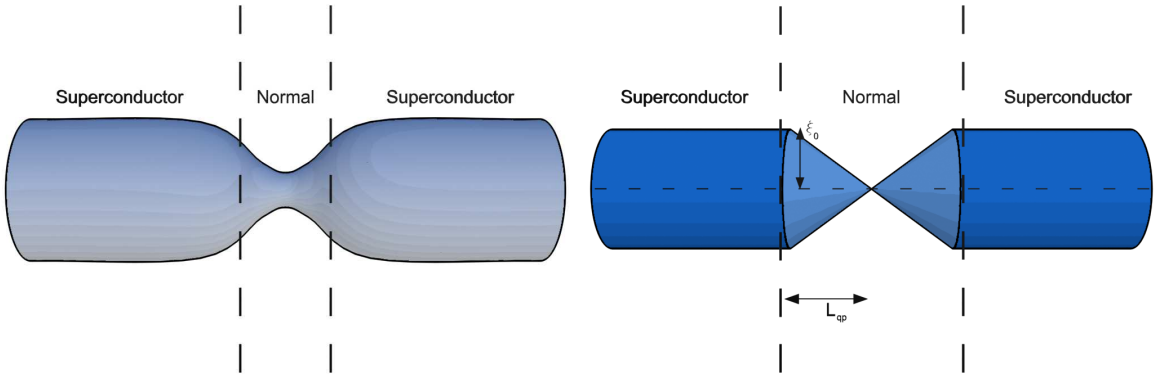


(a) (b)

Figure 93: (a): Shown here is the geometry of a SNS point contact which shows an adiabatic variation in the length of the contact. (b): For the purposes of calculation, the nanowire is assumed to be of the form shown above; here, the width of the normal region is taken to be the coherence length of the material (38 nm for niobium) and the length is assumed to be the quasiparticle diffusion length, $L_{qp}$, which is approximately 400 nm for niobium.

From these considerations, heating of the contact must be taken at high biases in order to properly account for the suppression of the excess current; to do this, the model of Fig. 93 is used. In this model, it is assumed that there is an increase in the density of quasiparticles in the normal region of the contact which raises the effective temperature of the system, accounting for the measured critical field. To set up the geometry of this region of increased quasiparticle density, it is assumed that each side of the nanowire approximates a cone; furthermore, the length of the cone is given by the quasiparticle mean free path, $L_{qp} = 400nm$ for niobium [190], which is the average distance the particle will travel before recombining in the superconductor. Moreover, the radius of the cone is assumed to be the coherence length of the superconductor, $\xi_0$, which is 38 nm for niobium [227].

With the geometry in place, the next step is to calculate the excess density of quasiparticles at the contact which lead to an local area of increased temperature, $T^*$. To do this, the first step is to calculate the power dissipated by the quasiparticles. Then, divide by the

average energy of a superconducting quasiparticle and multiply by the average lifetime of a quasiparticle, and the result is the excess number of quasiparticles. To turn this into a density requires only division by the volume of the normal region in Fig. 93. To begin, the power dissipated at the normal region when the suppression feature occurs is given simply as $V_{peak}^2/R_N$, which from the model presented above is a constant and equals approximately 400nW. Next, it is assumed that the dissipated power goes predominantly to quasiparticles and not phonons, which has been validated elsewhere [183]; thus, the entire power dissipated is transferred to the quasiparticles in the normal region. Furthermore, from the quasiparticle density of states presented in Chapter II, it is known that most quasiparticles occupy states at energies near the gap, $\Delta$. Then, given the volume of the normal region and the lifetime of a quasiparticle in niobium, $\tau = 60$ps, the excess density is given by:

$$\delta N_{qp} \approx \frac{P}{\Delta(T)} \frac{\tau}{V}. \tag{168}$$

Furthermore, it is known that the excess density at temperature, T, can be written in following form as well:

$$\delta N_{qp} = 4N(0) \left( \frac{\pi \Delta(T) k_B T}{2} \right)^{\frac{1}{2}} e^{-\frac{\Delta(T)}{k_B T}}. \tag{169}$$

By filling in the numbers given above and setting the two equations above equal to one another, the result is a reduced temperature of t=0.954, in comparison to the experimentally observed value of t=0.964, implying that not only must the effect of induced magnetic fields be taken into account when explaining the suppression feature, the increase in temperature due to the relatively large bias voltages must also be considered. This increase in temperature can be moderately large, approximately 1 K, for a niobium point contact; considering that the contact is in a thermal bath at 4.2 K, an increase in temperature of 1 K is substantial.

Thus, the experimental observations of the suppression feature (i.e. dependence of voltage on the root of the normal resistance and the temperature dependence of the feature) are explained by this critical current model which relies on a linear dependence of the suppression voltage with $H_{c1}$; the temperature dependence of $H_{c1}$ follows the superconducting gap, explaining Fig. 91. Furthermore, the square root dependence is explained by postulating

a critical current and extracting the dependence on $R_N$; in doing this, the approximation that Z is a constant among different samples is made and results in the correct functional dependence.

# REFERENCES


[1] Abrikosov, A. *Zh. Eksp. Teor. Fiz.*, vol. 32, p. 1442, 1957.

[2] Abrikosov, A. *Sov. Phys. JETP*, vol. 5, p. 1174, 1957.

[3] Abrikosov, A. A., "On the magnetic properties of superconductors of the second group," *Sov. Phys. JETP*, vol. 5, pp. 1174–1182.

[4] Abrikosov, A., *Fundamentals of the Theory of Metals*. Amsterdam: North Holland, 1 ed., 1988.

[5] Abrikosov, A., Gor'kov, L., and Dzyaloshinski, I., *Methods of Quantum Field Theory in Statistical Physics*. Englewood Cliffs: Prentice Hall, 1 ed., 1963.

[6] Adkins, C., "Two-particle tunnelling between superconductors," *Philos. Mag.*, vol. 8, pp. 1051–1061, 1963.

[7] Agrait, N., Untiedt, C., Rubio-Bollinger, G., and Vieira, S., "Electron transport and phonons in atomic wires," *Chem. Phys.*, vol. 281, pp. 231–234, 2002.

[8] Agrait, N., Untiedt, C., Rubio-Bollinger, G., and Vieira, S., "Onset of dissipation in ballistic atomic wires," *Phys. Rev. Lett.*, vol. 88, p. 216803, 2002.

[9] Agrait, N., Yeyati, A. L., and van Ruitenbeek, J., "Quantum properties of atomic-sized conductors," *Phys. Rep.*, vol. 377, pp. 81–279, 2003.

[10] Aharonov, Y. and Bohm, D., "Significance of electromagnetic potentials in the quantum theory," *Phys. Rev.*, vol. 115, pp. 485–491, 1959.

[11] Ambegaokar, V. and Baratoff, A., "Tunneling between superconductors," *Phys. Rev. Lett.*, vol. 10, p. 486, 1963.

[12] Anderson, P. and Rowell, J., "Probable observation of the josephson superconductive tunneling effect," *Phys. Rev. Lett.*, vol. 10, pp. 230–232, 1963.

[13] Andreev, A. F. *Zh. Eksp. Teor. Fiz.*, vol. 46, p. 1823, 1964.

[14] Arnold, G., "Superconducting tunneling without the tunneling hamiltonian," *J. Low Temp. Phys.*, vol. 59, pp. 143–183, 1985.

[15] Ashcroft, N. and Mermin, N., *Solid State Physics*. Massachusetts: Brooks Cole, 1 ed., 1976.

[16] Avenel, O. and Varoquaux, E., "Josephson effect and quantum phase slippage in superfluids," *Phys. Rev. Lett.*, vol. 60, pp. 416–419, 1988.

[17] Averin, D. and Bardas, A., "Ac josephson effect in a single quantum channel," *Phys. Rev. Lett.*, vol. 75, p. 1831, 1995.

[18] Bardeen, J., Cooper, L. N., and Schrieffer, J. R., "Microscopic theory of superconductivity," *Phys. Rev.*, vol. 106, pp. 162–164, 1957.

[19] Bardeen, J., Cooper, L. N., and Schrieffer, J. R., "Theory of superconductivity," *Phys. Rev.*, vol. 108, p. 1175, 1957.

[20] Barnett, R. and Landman, U., "Born-oppenheimer molecular-dynamics simulations of finite systems: Structure and dynamics of $(H_2O)_2$," *Phys. Rev. B*, vol. 48, p. 2081.

[21] Beenakker, C., "Josephson current through a superconducting quantum point contact shorter than the coherence length," *Phys. Rev. Lett.*, vol. 66, pp. 3056–3059, 1991.

[22] Beenakker, C., "Three universal mesoscopic josephson effects," in *Proceedings of the 14th Taniguchi International Symposium on Transport Phenomena in Mesoscopic Systems* (Fukuyama, H. and Ando, T., eds.), pp. 235–253, Berlin: Springer, 1992.

[23] Beenakker, C., *Quantum Mesoscopic Phenomena and Mesoscopic Devices in Microelectronics*, pp. 51–60. NATO Science Series C559, Dordrecht: Kluwer, 2000.

[24] Bhushan, B., Israelachvili, J., , and Landman, U., "Nanotribology: Friction, wear and lubrication at the atomic scale," *Nature*, vol. 374, p. 607, 1995.

[25] Binnig, G. and Rohrer, H., "Scanning tunneling microscopy," *IBM J. Res. Dev.*, vol. 30, p. 4, 1986.

[26] Binning, G., Quate, C. F., and Gerber, C., "Atomic force microscope," *Phys. Rev. Lett.*, vol. 56, p. 930, 1986.

[27] Blaney, T. G. and Bradley, C. C., "The josephson junction as a frequency analyser and mixer of submillimetre radiation sources," *J. Phys. D*, vol. 5, pp. 180–184.

[28] Blaney, T. G., Cross, N. R., and Knight, D. J. E., "Harmonic mixing and frequency measurement at 2.5 thz using josephson junctions," *J. Phys. D*, vol. 9, pp. 2175–2180, 1976.

[29] Blaney, T. G., Cross, N. R., Knight, D. J. E., Edwards, G. J., and Pearce, P. R., "Frequency measurement at 4-25 thz (70.5 $\mu$) using a josephson harmonic mixer and phase-lock techniques," *J. Phys. D*, vol. 13, pp. 1365–1370, 1980.

[30] Blaney, T. G. and Knight, D. J. E., "Direct 825th harmonic mixing of a 1 ghz source with an hcn laser in a josephson junction," *J. Phys. D*, vol. 7, pp. 1882–1886, 1974.

[31] Blonder, G., Tinkham, M., and Klapwijk, T., "Transition from metallic to tunneling regimes in superconducting microconstrictions: Excess current, charge imbalance, and supercurrent conversion," *Phys. Rev. B*, vol. 25, pp. 4515–4532, 1982.

[32] Boas, M., *Mathematical Methods in the Physical Sciences*. New York: Wiley, 2 ed., 1983.

[33] Bogachek, E., Scherbakov, A., and Landman, U., "Magnetic switching and thermal enhancement of quantum transport through nanowires," *Phys. Rev. B*, vol. 53, p. R13246.

[34] Bogoliubov, N. *Nuovo Cimento*, vol. 7, p. 794, 1958.

[35] Born, M. and Oppenheimer, R., "On the quantum theory of molecules," *Annalen der Physik*, vol. 84, pp. 457–484, 1927.

[36] Brandbyge, J., Mozos, J., Ordejon, P., Taylor, J., and Stokbro, K., "Density-functional method for nonequilibrium electron transport," *Phys. Rev. B*, vol. 65, p. 165401.

[37] Brandbyge, M., Kobayashi, N., and Tsukada, M., "Conduction channels at finite bias in single-atom gold contacts," *Phys. Rev. B*, vol. 60, p. 17064.

[38] Brandbyge, M., Sorensen, M., and Jacobsen, K., "Conductance eigenchannels in nanocontacts," *Phys. Rev. B*, vol. 56, p. 14956.

[39] Brandbyge, M., Mozos, J.-L., Ordejon, P., Taylor, J., and Stokbro, K., "Density-functional method for nonequilibrium electron transport," *Phys. Rev. B*, vol. 65, p. 165401.

[40] Bratus, E., Shumeiko, V., and Wendin, G., "Theory of subharmonic gap structure in superconducting mesoscopic tunnel contacts," *Phys. Rev. Lett.*, vol. 74, pp. 2110–2113, 1995.

[41] Buttiker, M., "Scattering theory of current and intensity noise correlations in conductors and wave guides," *Phys. Rev. B*, vol. 46, pp. 12485–12507, 1992.

[42] Buttiker, M., Imry, Y., Landauer, R., , and Pinhas, S., "Generalized many-channel conductance formula with application to small rings," *Phys. Rev. B*, vol. 31, p. 6207, 1985.

[43] Carelli, G., Moretti, A., Pereira, D., and Strumia, F., "Heterodyne frequency measurements of fir laser lines around 1.2 and 1.6 thz," *IEEE Journal of Quantum Electronics*, vol. 31, pp. 144–147, 1995.

[44] Chalmers, J. and Griffiths, P., *Handbook of Vibrational Spectroscopy*. Chichester: Wiley, 1 ed., 2002.

[45] Chang, C. and Landman, U. *to be published*.

[46] Cooper, L., "Bound electron pairs in a degenerate fermi gas," *Phys. Rev.*, vol. 104, pp. 1189–1190, 1956.

[47] Cramer, C., *Essentials of Computational Chemistry*. Wiley, 1 ed., 2002.

[48] Crommie, M., Lutz, C., and Eigler, D., "Confinement of electrons to quantum corrals on a metallic surface," *Science*, vol. 262, pp. 218–220, 1993.

[49] Cron, R., *Atomic Contacts: A Testbed for Mesoscopic Superconductivity*. PhD thesis, University of Paris VI, 2001.

[50] Cron, R., Goffman, M. F., Esteve, D., and Urbina, C., "Multiple-charge-quanta shot noise in superconducting atomic contacts," *Phys. Rev. Lett.*, vol. 86, pp. 4104–4107, 2001.

[51] Cuevas, J., Martin-Rodero, A., and Yeyati, A. L., "Hamiltonian approach to the transport properties of superconducting quantum point contacts," *Phys. Rev. B*, vol. 54, pp. 7366–7379, 1996.

[52] Cuevas, J., Yeyati, A. L., and Martin-Rodero, A., "Microscopic origin of conducting channels in metallic atomic-size contacts," *Phys. Rev. Lett.*, vol. 80, pp. 1066–1069, 1998.

[53] Dai, Z. and Marchenkov, A., "Subgap structure in resistively shunted superconducting atomic point contacts," *Appl. Phys. Lett.*, vol. 88, p. 203120.

[54] Dai, Z., Zhang, C., Barnett, R., Marchenkov, A., and Landman, U., "Structural and transport properties of niobium nanowires," *Phys. Stat. Sol. A*, vol. 204, pp. 1712–1720.

[55] Dai, Z., *Coherent and Dissipative Transport in Metallic Atomic-Size Contacts*. PhD thesis, Georgia Institute of Technology, 2006.

[56] Danielewicz, P., "Quantum theory of non-equilibrium processes," *Ann. Phys.*, vol. 152, p. 239.

[57] Datta, S., "Nanoscale device simulation: The green's function method," *Superlattices and Microstructures*, vol. 28, pp. 253–278.

[58] Datta, S., "Non-equilibrium green's function (negf) formalism: An elementary introduction," *Proceedings of the International Electron Devices Meeting (IEDM)*.

[59] Datta, S., *Electronic Transport in Mesoscopic Systems*. Combridge Universit Press: Cambridge, 1 ed., 1995.

[60] Davis, L. *Phys. Rev. B*, vol. 2, pp. 1714–1732, 1970.

[61] Dayem, A. and Grimes, C. *Appl. Phys. Lett.*, vol. 9, p. 47, 1966.

[62] de Bruyn Ouboter, R., "Superconductivity: Discoveries during the early years of low temperature research at leiden," *IEEE Trans. on Mag.*, vol. 23, pp. 355–370, 1987.

[63] de Gennes, P., *Superconductivity of Metals and Alloys*. Colorado: Westview Press, 2 ed., 1999.

[64] Deutscher, G. and de Gennes, P. G., *Superconductivity*. New York: Marcel Dekker, 1 ed., 1969.

[65] Dirac, P., "The quantum theory of emission and absorption of radiation," *Proc. Roy. Soc. London A*, vol. 114, pp. 243–265, 1927.

[66] Divin, Y. Y., Polyanski, O. Y., and Shul'man, A. Y. *Sov. Tech. Phys. Lett.*, vol. 6, pp. 454–457.

[67] Divin, Y. Y., Pavlovshi, V. V., Volkov, O. Y., Schulz, H., Poppe, U., Klein, N., and Urban, K., "Hilbert-transform spectral analysis of millimeter- and submillimeter-wave radiation with high $t_c$ josephson junctions," *IEEE Trans. Appl. Super.*, vol. 7, pp. 3426–3429.

[68] Djukic, D., Thygesen, K. S., Untiedt, C., R. H. M. Smit, K. W. J., and van Ruitenbeek, J., "Stretching dependence of the vibration modes of a single-molecule pth[sub 2]pt bridge," *Phys. Rev. B*, vol. 71, pp. 161402–161404, 2005.

[69] Dobbs, J. N., Anderson, A. C., Metzger, T. H., and Wipf, H., "Low temperature thermal expansion of niobium containing trapped hydrogen," *Phys. Rev. B*, vol. 30, pp. 6168–6169.

[70] Dobroiu, A., Yamashita, M., Ohshima, Y. N., Morita, Y., Otani, C., and Kawase, K., "The backward wave oscillator as a radiation source in terahertz imaging," in *Infrared and Millimeter Waves, 2004 and 12th International Conference on Terahertz Electronics*, 2004.

[71] Dreizler, R. and Gross, E., *Density Functional Theory*. Plenum Press: New York, 1 ed., 1995.

[72] Durig, U., Zuger, O., and Pohl, D., "Observation of metallic adhesion using the scanning tunneling microscope," *Phys. Rev. Lett.*, vol. 65, pp. 349–352, 1990.

[73] Eigler, D., Lutz, C., and Rudge, W., "An atomic switch realized with the scanning tunnelling microscope," *Nature*, vol. 352, p. 600.

[74] Elbing, M., Ochs, R., Koentopp, M., Fischer, M., von Hanish, C., Weigend, F., Evers, F., Weber, H., and Mayor, M., "A single-molecule diode," *PNAS*, vol. 102, pp. 8815–8820, 2005.

[75] Fermi, E., *Nuclear Physics*. University of Chicago Press, 1 ed., 1950.

[76] Feynman, R. P., Leighton, R., and Sands, M., *The Feynman Lectures on Physics*, vol. 3, pp. 21–14. Massachusetts: Addison-Wesley, 1965.

[77] Feynman, R., "There's plenty of room at the bottom," *Engineering and Science*, vol. 22, 1960.

[78] Finnemore, D. K., Stromberg, T. F., , and Swenson, C. A., "Superconducting properties of high purity niobium," *Phys. Rev.*, vol. 149, pp. 231–243.

[79] Fiolhais, C., Nogueira, F., and Marques, M., *A Primer in Density Functional Theory*. Springer-Verlag, 1 ed., 2003.

[80] Fossheim, K. and Sudbo, A., *Superconductivity: Physics and Applications*. New York: Wiley, 1 ed., 2007.

[81] Furusaki, A., "A unified theory of clean josephson junctions," *Physica B*, vol. 165, pp. 967–968, 1990.

[82] Galperin, M., Ratner, M., and Nitzan, A., "Molecular transport junctions: vibrational effects," *J. Phys: Conden. Matter*, vol. 19, p. 103201, 2007.

[83] Gammaitoni, L., Hanggi, P., Jung, P., and Marchesoni, F., "Stochastic resoance," *Rev. Mod. Phys.*, vol. 70, pp. 223–287.

[84] Gammaitoni, L., Marchesoni, F., Menichella-Saetta, E., and Santucci, S., "Stochastic resoance in bistable systems," *Phys. Rev. Lett.*, vol. 62, pp. 349–352.

[85] Gel'man, G. and Hellmann, H., "On a combined perturbation procedure in the problem of many electrons," *C. R. Acad. Sci. URSS N.S.*, vol. 4, pp. 442–444, 1934.

[86] Giancoli, D. C., *Physics*. New Jersey: Prentice Hall, 1995.

[87] Giessibl, F., "Advances in atomic force microscopy," *Rev. Mod. Phys.*, vol. 75, pp. 949–983, 2003.

[88] Gimzewski, J. K., Moller, R., Pohl, D., and Schlittler, R., "Transition from tunneling to point contact investigated by scanning tunneling microscopy and spectroscopy," *Surf. Sci.*, vol. 189/190, p. 15.

[89] Gimzewski, J. and Moller, R., "Transition from the tunneling regime to point contact studied using scanning tunneling microscopy," *Physica B*, vol. 36, pp. 1284–1287, 1987.

[90] Ginzburg, V. and Landau, L. *Zh. Eksp. Teor. Fiz.*, vol. 20, p. 1064, 1950.

[91] Glattli, D. C., Jacques, P., Kumar, A., Pari, P., and Saminadayar, L., "A noise detection scheme with 10 mk noise temperature resolution for semiconductor single electron tunneling devices," *J. Appl. Phys.*, vol. 81, pp. 7350–7356, 1997.

[92] Gor'kov, L. *Zh. Eksp. Teor. Fiz.*, vol. 36, p. 1364, 1959.

[93] Griffiths, D., *Introduction to Quantum Mechanics*. New Jersey: Pearson, 2 ed., 2004.

[94] Gronbeck, H., Rosen, A., and Andreoni, W., "Structural, electronic, and vibrational properties of neutral and charged $Nb_n$(n=8,9,10) clusters," *Phys. Rev. A*, vol. 58, p. 4630.

[95] Haberkorn, W., Knauer, H., and Richter, J., "A theoretical study of the current-phase relation in josephson contacts," *Phys. Stat. Sol.*, vol. 47, pp. K161–K164, 1978.

[96] Hahn, A. and Humpfner, K., "Nonequilibrium in normal-conductor/superconductor microconstrictions," *Phys. Rev. B*, vol. 51, p. 3660.

[97] Hahn, J., Lee, H., and Ho, W., "Electronic resonance and symmetry in single-molecule inelastic electron tunnelling," *Phys. Rev. Lett.*, vol. 85, pp. 1914–1917, 2000.

[98] Hakkinen, H., Barnett, R., Scherbakov, A., and Landman, U., "Nanowire gold chains: Formation mechanisms and conductance," *J. Phys. Chem. B*, vol. 104, p. 9063.

[99] Halbritter, J., "Transport in superconducting niobium films for radio frequency applications," *J. Appl. Phys.*, vol. 97, p. 083904.

[100] Hansma, P., *Tunneling Spectroscopy*. Plenum Press, New York, 1 ed., 1982.

[101] Hecht, E., *Optics*. Massachusetts: Addison Wesley, 4 ed., 2001.

[102] Heinzel, T., *Mesoscopic Electronics in Solid State Nanostructures*. New York: Wiley, 1 ed., 2007.

[103] Hekking, F. W. J., Schn, G., and Averin, D. V. in *Proceedings of the NATO Advanced Research Workshop on Mesoscopic Superconductivity*, 1994.

[104] Hipps, K. W. and Mazur, U., "The role of the crystal lattice in the electronic spectra of the hexacyanocobaltate ion, ii: Franck-condon analysis of the luminescence," *J. Phys. Chem.*, vol. 84, p. 3162, 1980.

[105] Hipps, K. W. and Mazur, U., "An inelastic electron tunneling spectroscopy study of some iron cyanide complexes," *J. Phys. Chem.*, vol. 89, p. 5459, 1985.

[106] Hipps, K. W. and Mazur, U., "Inelastic electron tunneling: An alternative molecular spectroscopy," *J. Phys. Chem.*, vol. 97, pp. 7803–7814, 1993.

[107] Hohenberg, P. and Kohn, W., "Inhomogeneous electron gas," *Phys. Rev. B*, vol. 136, pp. B864–B871.

[108] Hopkins, B. J. and Ross, K. J., "The contact potential difference between tungsten and niobium," *J. Appl. Phys.*, vol. 15, pp. 89–92, 1964.

[109] Hu, B. B. and Nuss, M. C., "Imaging with terahertz waves," *Opt. Lett.*, vol. 20, p. 1716, 1995.

[110] Humphreys, K., Loughran, J. P., Gradziel, M., Lanigan, W., Ward, T., Murphy, J., and OSullivan, C., "Medical applications of terahertz imaging: a review of current technology and potential applications in biomedical engineering," in *Proceedings of the 26th Annual International Conference of the IEEE EMBS*, pp. 1302–1305, 2004.

[111] Jackson, B. and Klapwijk, T., "The current status of low-noise thz mixers based on sis junctions," *Physica C*, vol. 372–376, pp. 368–373, 2002.

[112] Jansen, A., van Gelder, A., and Wyder, P., "Point contact spectroscopy in metals," *J. Phys. C*, vol. 13, pp. 6073–6118, 1980.

[113] Josephson, B., "Possible new effects in superconductive tunneling," *Phys. Lett.*, vol. 1, pp. 251–253, 1962.

[114] Josephson, B., *Superconductivity*, vol. 1, ch. Weakly Coupled Superconductors. New York: Marcel Dekker, 1969.

[115] Jung, P. and Hanggi, P., "Amplification of small signals via stochastic resonance," *Phys. Rev. A*, vol. 44, pp. 8032–8042.

[116] Karpov, A., Blondel, J., Voss, M., and Gundlach, K., "A three photon noise sis heterodyne receiver at submillimeter wavelength," *IEEE Trans. Appl. Supercon.*, vol. 9, p. 4456, 1999.

[117] Keldysh, L., "Diagram technique for non-equilibrium processes," *Sov. Phys. JETP*, vol. 20, p. 1018.

[118] Kim, Y. B., Hempstead, C., and Strnad, A., "Flux flow resistance in type ii superconductors," *Phys. Rev.*, vol. 139, pp. 1163–1172, 1965.

[119] Kirtley, J. *ACS Symp. Ser.*, vol. 137, p. 217, 1980.

[120] Kittel, C., *Introduction to Solid State Physics*. New York: Wiley, 8 ed., 2004.

[121] Klapwijk, T., "Proximity effect from an andreev perspective," *J. Supercond.: Incorporating Novel Magnetism*, vol. 17, pp. 593–611, 2004.

[122] Klapwijk, T., Blonder, G., and Tinkham, M., "Explanation of subharmonic energy gap structure in superconducting contacts," *Physica B*, vol. 109, pp. 1657–1664, 1982.

[123] Koch, W. and Holthausen, M. C., *A Chemist's Guide to Density Functional Theory*. Wiley-VCH, 2 ed., 2002.

[124] Kohanoff, J., *Electronic Structure Calculations for Solids and Molecules: Theory and Computational Methods*. Cambridge University Press, 1 ed., 2006.

[125] Kohn, W. and Sham, L. J., "Self-consistent equations including exchange and correlation effects," *Phys. Rev.*, vol. 140, pp. A1133–A1138.

[126] Kolesnychenko, O. Y., S., I., O., and van Kempen, H., "Calibration of the distance between electrodes of mechanically controlled break junctions using field-emission resonance," *Rev. Sci. Instrum.*, vol. 70, pp. 1442–1446, 1999.

[127] Kolesnychenko, O. Y., Shklayarevskii, O. I., and van Kempen, H., "Giant infuence of adsorbed helium on feld emission resonance measurements," *Phys. Rev. Lett.*, vol. 83, pp. 2242–2245, 1999.

[128] Kooi, J., Chan, M., Bumble, B., LeDuc, H., Schaffer, P., and Phillips, T., "230 and 492 ghz low-noise sis waveguide receivers employing tuned nb/alox/nb tunnel junctions," *Int. J. IR MM Waves*, vol. 16, p. 2049, 1995.

[129] Kosarev, E. L., Shulman, A. Y., A.Tarasov, M., and Lindstrom, T., "Deconvolution problems and superresolution in hilbert transform spectroscopy based on ac josephson efect," *Modern Trends in Computational Physics*.

[130] Kramers, H. *Physica*, vol. 7, p. 284.

[131] Kulik, I., "Macroscopic quantization and the proximity effect in s-n-s junctions," *Sov. Phys. JETP*, vol. 30, pp. 944–950, 1970.

[132] Kulik, I., Omel'yanchuk, A., and Shekhter, R., "Electrical conductivity of point microbridges and phonon and impurity spectroscopy in normal metals," *Sov. J. Low Temp. Phys.*, vol. 3, pp. 740–748, 1977.

[133] Landau, L., "The theory of a fermi liquid," *Sov. Phys. JETP*, vol. 3, pp. 920–925, 1957.

[134] Landau, L., "On the theory of a fermi liquid," *Sov. Phys. JETP*, vol. 8, pp. 70–74, 1959.

[135] Landauer, R., "Spatial variation of currents and fields due to localized scatterers in metallic conduction," *IBM J. Res. Dev.*, vol. 1, pp. 223–231, 1957.

[136] Landman, U., "On nanotribological interactions: Hard and soft interfacial junctions," *Solid State Commun.*, vol. 107, p. 693, 1998.

[137] Landman, U., Luedtke, W., , and Gao, J., "Atomic scale issues in tribology: Interfacial junctions and nano-elastohydrodynamics," *Langmuir*, vol. 12, p. 4514, 1996.

[138] Landman, U., Luedtke, W., Burnham, N., and Colton, R., "Atomistic mechanisms and dynamics of adhesion, nanoindentation, and fracture," *Science*, vol. 248, pp. 454–461, 1990.

[139] Landman, U., Luedtke, W., Salisbury, B., and Whetten, R., "Reversible manipulations of room temperature mechanical and quantum transport properties in nanowire junctions," *Phys. Rev. Lett.*, vol. 77, p. 1362, 1996.

[140] Lang, N. D., "Resistance of a one-atom contact in the scanning tunneling microscope," *Phys. Rev. B*, vol. 36, p. 8173.

[141] Lanigan, W., Murphy, J., May, R., Mahon, R., McAuley, I., Markham, C., Humphries, K., Ward, T., and Withington, S., "Quasi-optical millimetre-wave imaging with bio-medical applications," in *IRMMW-THz*, 2005.

[142] LeRoy, B. J., Lemay, S. G., Kong, J., and Dekker, C., "Electrical generation and absorption of phonons in carbon nanotubes," *Nature*, vol. 432, pp. 371–374, 2004.

[143] Likharev, K., "Superconducting weak links," *Rev. Mod. Phys.*, vol. 51, pp. 101–159, 1979.

[144] Lindsay, S. M. and Ratner, M. A., "Molecular transport junctions: Clearing mists," *Adv. Mat.*, vol. 19, pp. 23–31, 2007.

[145] Line, M. J., Pritchard, R., Pynenburg, R., Latham, R. J., and Linford, R., "Study of a zinc chloride in poly(ethylene glycol) layer on an aluminium oxide surface by inelastic electron tunneling spectroscopy," *Surf. Sci. Int. Anal.*, vol. 23, p. 565, 1995.

[146] Liu, F., Tucker, R., and Heller, P., "Nitrogen temperature superconducting ring experiment," *Am. J. Phys.*, vol. 58, pp. 211–218, 1990.

[147] London, F. and London, H., "The electromagnetic equations of the supraconductor," *Proc. R. Soc. London A*, vol. 149, pp. 71–88, 1935.

[148] Ludolph, B., Devoret, M., Esteve, D., Urbina, C., and van Ruitenbeek, J., "Evidence for saturation of channel transmission from conductance fluctuations in atomic-size point contacts," *Phys. Rev. Lett.*, vol. 82, p. 1530.

[149] Lynch, S. A., Paul, D., Townsend, P., Matmon, G., Kelsall, R., Ikonic, Z., Harrison, P., Zhang, J., Morris, D., Cullis, A., Pidgeon, C., Murzyn, C., Murdin, B., Bain, M., and Gamble, H., "Silicon quantum cascade lasers for thz sources," in *The 18th Annual Meeting of the IEEE Lasers and Electro-Optics Society*, pp. 728–729, 2005.

[150] Marchenkov, A., Dai, Z., Donehoo, B., Barnett, R., and Landman, U., "Alternating current josephson effect and resonant superconducting transport through vibration nb nanowires," *Nature Nanotech.*, vol. 2, pp. 481–485.

[151] Marder, M., *Condensed Matter Physics*. New York: Wiley, 1 ed., 2000.

[152] Martin, T. and Landauer, R., "Wave-packet approach to noise in multichannel mesoscopic systems," *Phys. Rev. B*, vol. 45, p. 1742, 1987.

[153] Martin-Rodero, A., Garcia-Vidal, F., and Yeyati, A. L., "Microscopic theory of josephson mesoscopic constrictions," *Phys. Rev. Lett.*, vol. 73, pp. 554–557, 1994.

[154] Martinis, J. M., Devoret, M. H., and Clarke, J., "Experimental tests for the quantum behavior of a macroscopic degree of freedom: The phase difference across a josephson junction," *Phys. Rev. B*, vol. 35, pp. 4682–4698, 1987.

[155] Maslov, D. L., Barnes, C., and Kirczenow, G., "Ballistic transport in a disordered environment: Why is conductance quantization observable?," *Phys. Rev. Lett.*, vol. 70, p. 1984.

[156] Mattheiss, L. F., "Electronic structure of niobium and tantalum," *Phys. Rev. B*, vol. 1, pp. 373–380.

[157] Mattis, D. and Bardeen, J., "Theory of the anomalous skin effect in normal and superconducting metals," *Phys. Rev.*, vol. 111, pp. 412–417, 1958.

[158] McDonald, D. G., Evenson, K. M., Wells, J. S., , and Cupp, J. D., "High-frequency limit of the josephson effect," *J. Appl. Phys.*, vol. 42, pp. 179–181, 1971.

[159] McDonald, D. G., Evenson, K. M., Wells, J. S., and Cupp, J. D., "High-frequency limit of the josephson effect," *J. Appl. Phys.*, vol. 42, pp. 179–181, 1971.

[160] Meissner, W. and Ochsenfeld, R., "Ein neuer effekt bei eintritt der supraleifahigkeit," *Naturwiss.*, vol. 21, pp. 787–788, 1933.

[161] Milliken, F. P., Rozen, J. R., Keefe, G. A., and Koch, R. H., "50 ohm characteristic impedance low-pass metal powder filters," *Rev. Sci. Instrum.*, vol. 78, p. 024701, 2007.

[162] Minin, I. and Minin, O., "Recent developments in active millimeter/thz waves high-quality 3d imaging for scientific, medical and homeland secuttry applications," in *5th IEEE - Russia Conference: MEMIA'2005*, 2005.

[163] Moore, G., "Cramming more components onto integrated circuits," *Electronics*, vol. 38, 1965.

[164] Moreland, J. and Ekin, J., "Electron tunneling experiments using nb-sn break junctions," *J. Appl. Phys.*, vol. 58, pp. 3888–3895, 1985.

[165] Morkoc, H., *Advanced Semiconductors and Organic Nano-Techniques*. Academics Press, New York, 1 ed., 2003.

[166] Mott, N., *Metal-Insulator Transitions*. London: Taylor and Francis, 2 ed., 1990.

[167] Mott, N. and Peierls, R. *Proc. Phys. Soc. London*, vol. 49, p. 72, 1937.

[168] Mott, N. and Peierls, R. *Proc. Phys. Soc. London A*, vol. 62, p. 416, 1949.

[169] Muller, C., van Ruitenbeek, J., and de Jongh, L., "Conductance and supercurrent discontinuities in atomic-scale metallic constrictions of variable width," *Phys. Rev. Lett.*, vol. 69, pp. 140–143, 1992.

[170] Muller, C., van Ruitenbeek, J., and de Jongh, L., "Experimental observation of the transition from weak link to tunnel junction," *Physica C*, vol. 191, pp. 485–504, 1992.

[171] Naidyuk, Y. and Yanson, I., *Point-Contact Spectroscopy*. Springer, New York, 1 ed., 2004.

[172] Negele, J. and Orland, H., *Quantum Many-Particle Systems*. Massachusetts: Addison Wesley, 1 ed., 1988.

[173] Nguyen, C., Kroemer, H., and Hu, E. L., "Anomalous andreev conductance in InAs-AlSb quantum well structures with Nb electrodes," *Phys. Rev. Lett.*, vol. 69, p. 2847.

[174] Octavio, M., Tinkham, M., Blonder, G., and Klapwijk, T., "Subharmonic energy-gap structure in superconducting constrictions," *Phys. Rev. B*, vol. 27, pp. 6739–6746, 1983.

[175] Ohnishi, H., Kondo, Y., and Takayanagi, K., "Quantized conductance through individual rows of suspended gold atoms," *Nature*, vol. 395, p. 780.

[176] Onnes, H. K. Comm. Leiden, 1908. 108.

[177] Onnes, H. K., "The disappearance of the resistivity of mercury," *Comm. Leiden*, May 1911.

[178] Onnes, H. K., "On the sudden change in the rate at which the resistance of mercury disappears," *Comm. Leiden*, November 1911.

[179] Onnes, H. K., "The resistance of pure mercury at helium temperatures," *Comm. Leiden*, April 1911.

[180] Osakabe, N., Matsuda, T., Kawasaki, T., Endo, J., Tonomura, A., Yano, S., and Yamada, H., "Experimental confirmation of aharonov-bohm effect using a toroidal magnetic field confined by a superconductor," *Phys. Rev. A*, vol. 34, pp. 815–822, 1986.

[181] Pannetier, B. and Courtois, H., "Andreev reflection and proximity effect," *J. Low Temp. Phys.*, vol. 118, pp. 599–615, 2000.

[182] Park, H., Park, J., Lim, A., Anderson, E., Alivisatos, A., and McEuen, P., "Nanomechanical oscillations in a single-$c_{60}$ transistor," *Nature*, vol. 407, pp. 57–60, 2000.

[183] Parker, W. H., "Modified heating theory of nonequilibrium superconductors," *Phys. Rev. B*, vol. 12, p. 3667.

[184] Parr, R. G. and Yang, W., *Density-Functional Theory of Atoms and Molecules*. Oxford University Press, New York, 1 ed., 1989.

[185] Pepper, D., "Time-reversed light," *Sci. Am.*, vol. 56, p. 254, 1986.

[186] Perdew, J., Burke, K., and Ernzerhof, M., "Generalized gradient approximation made simple," *Phys. Rev. Lett.*, vol. 77, p. 3865.

[187] Phillips, P., *Advanced Solid State Physics*. Colorado: Westview Press, 1 ed., 2003.

[188] Pobell, F., *Matter and Methods at Low Temperatures*. New York: Springer, 2 ed., 2002.

[189] Pothier, H., *Coulomb Blockade and Single Electron Transfer*. PhD thesis, University of Paris VI, 1991.

[190] Rachford, F. J., Wolf, S. A., and Hirvonen, J. K., "Thin film niobium squids at 20mhz and 9ghz," *IEEE Trans. Mag.*, vol. 13, pp. 875–878.

[191] Robertson, I., *Electronics for Electricians and Engineers*. New York: Industrial Press, 1987.

[192] Rodrigues, V. and Ugarte, D., "Real-time imaging of atomistic process in one-atom-thick metal junctions," *Phys. Rev. B*, vol. 63, p. 073405.

[193] Rubio-Bollinger, G., Bahn, S. R., Agrait, N., Jacobsen, K. W., and Vieira, S., "Mechanical properties and formation mechanisms of a wire of single gold atoms," *Phys. Rev. Lett.*, vol. 87, p. 026101.

[194] Rubio-Bollinger, G., Joyez, P., and Agrat, N., "Metallic adhesion in atomic-size junctions," *Phys. Rev. Lett.*, vol. 93, p. 116803.

[195] Saba, M., Pasquini, T. A., Sanner, C., Shin, Y., Ketterle, W., and Pritchard, D. E., "Light scattering to determine the relative phase of two bose-einstein condensates," *Phys. Rev. Lett.*, vol. 307, pp. 1945–1948, 2005.

[196] Sakurai, J., *Modern Quantum Mechanics*. Massachusetts: Addison-Wesley-Longman, 1 ed., 1994.

[197] Sazonova, V., Yaish, Y., Ustunel, H., Roundy, D., Arias, T., and McEuen, P., "A tunable carbon nanotube electromechanical oscillator," *Nature*, vol. 431, pp. 284–287, 2004.

[198] Scheer, E., Agrait, N., Cuevas, J., Yeyati, A. L., Ludoph, B., Martín-Rodero, A., Bollinger, G. R., van Ruitenbeek, J., and Urbina, C., "Theory of subharmonic gap structure in superconducting mesoscopic tunnel contacts," *Phys. Rev. Lett.*, vol. 74, pp. 2110–2113, 1995.

[199] Scheer, E., Agrait, N., Cuevas, J., Yeyati, A. L., Ludoph, B., Martin-Rodero, A., Bollinger, G. R., van Ruitenbeek, J., and Urbina, C., "The signature of chemical valence in the electrical conduction through a single-atom contact," *Nature*, vol. 394, pp. 154–157, 1998.

[200] Scheer, E., Joyez, P., Esteve, D., Urbina, C., and Devoret, M., "Conduction channel transmissions of atomic-size aluminum contacts," *Phys. Rev. Lett.*, vol. 78, pp. 3535–3538, 1997.

[201] Schrieffer, J. and Wilkins, J., "Two-particle tunneling processes between superconductors," *Phys. Rev. Lett.*, vol. 10, pp. 17–20, 1963.

[202] Shapiro, S. *Phys. Rev. Lett.*, vol. 11, p. 80, 1963.

[203] Sharvin, Y. *Sov. Phys. JETP*, vol. 21, p. 655, 1965.

[204] Shimozuma, T., Kikunaga, T., Sato, N., Shimawaki, H., Suzuki, T., Yokoo, K., Ono, S., Kido, G., and Terumichi, Y., "Design and the first experiment of a 1 thz gyrotron," in *Electron Devices Meeting*, pp. 375–378, 1993.

[205] Shiota, T., Mares, A. I., Valkering, A. M. C., Oosterkamp, T. H., and van Ruitenbeek, J. M., "Mechanical properties of pt monatomic chains," *Phys. Rev. B*, vol. 77, p. 125411.

[206] Smit, R., Noat, Y., Untiedt, C., Lang, N., van Hemert, M., and van Ruitenbeek, J. M., "Measurement of the conductance of a hydrogen molecule," *Nature*, vol. 419, pp. 906–909, 2002.

[207] Smith, D. P. E., "Quantum point contact switches," *Science*, vol. 269, p. 371, 1995.

[208] Smith, T. F. and Finlayson, T. R., "Thermal expansion of bcc solid solution alloys in the system zr-nb-mo-re," *J. Phys. F*, vol. 6, pp. 709–723.

[209] Stalder, A. and Durig, U., "Study of yielding mechanics in nanometer-sized au contacts," *Appl. Phys. Lett.*, vol. 68, p. 637.

[210] Stipe, B. C., Rezaei, M. A., and Ho, W., "Single-molecule vibrational spectroscopy and microscopy," *Science*, vol. 280, pp. 1732–1735, 1998.

[211] Sueur, H. and Joyez, P., "Microfabricated electromagnetic filters for millikelvin experiments," *Rev. Sci. Instrum.*, vol. 77, p. 115102, 2006.

[212] Sutton, A. and Pethica, J., "Inelastic =ow processes in nanometre volumes of solids," *J. Phys.: Cond. Mat.*, vol. 2, pp. 5317–5326, 1990.

[213] Szabo, A. and Ostlund, N. S., *Modern Quantum Chemistry*. Dover: New York, 1 ed., 1996.

[214] Taylor, B. and Burstein, E., "Excess currents in electron tunneling between superconductors," *Phys. Rev. Lett.*, vol. 10, pp. 14–17, 1963.

[215] Taylor, B., "New internationally adopted reference standards of voltage and resistance based on the josephson and quantum hall effects," in *6th IEEE Instrumentation and Measurement Technology Conference, IMTC-89*, pp. 175–177, 1989.

[216] Taylor, J., Guo, H., and Wang, J., "Ab initio modeling of open systems: Charge transfer, electron conduction, and molecular switching of a $C_{60}$ device," *Phys. Rev. B*, vol. 63, p. 121104.

[217] Taylor, J., Guo, H., and Wang, J., "Real-time imaging of atomistic process in one-atom-thick metal junctions," *Phys. Rev. B*, vol. 63, p. 073405.

[218] Terabe, K., Hasegawa, T., Nakayama, T., and Aono, M., "Quantized conductance atomic switch," *Nature*, vol. 433, p. 47.

[219] Tinkham, M., *Introduction to Superconductivity*. New York: Dover, 2 ed., 1996.

[220] Trauble, H. and Essman, U., "Flux-line arrangement in superconductors as revealed by direct observation," *J. Appl. Phys.*, vol. 39, pp. 4052–4059.

[221] Troullier, N. and Martinis, J. L., "Efficient pseudopotentials for plane-wave calculations," *Phys. Rev. B*, vol. 43, p. 1993.

[222] Tucker, J. R., "Quantum limited detection in tunnel junction mixers," *IEEE J. Quant. Elec.*, vol. 15, pp. 1234–1258, 1979.

[223] Untiedt, C., Bollinger, G. R., Vieira, S., and Agrait, N., "Quantum interference in atomic-sized point contacts," *Phys. Rev. B*, vol. 62, pp. 9962–9965.

[224] Valatin, J. *Nuovo Cimento*, vol. 7, p. 843, 1958.

[225] Valkering, A. M. C., Mares, A. I., Untiedt, C., Gavan, K. B., Oosterkamp, T. H., and van Ruitenbeek, J. M., "A force sensor for atomic point contacts," *Rev. Sci. Instrum.*, vol. 76, p. 103903.

[226] van der Post, N., Peters, E., Yanson, I., and van Ruitenbeek, J., "Subgap structure as function of the barrier in atom-size superconducting tunnel junctions," *Phys. Rev. Lett.*, vol. 73, pp. 2611–2613, 1994.

[227] van Duzer, T. and Turner, C., *Superconductive Devices and Circuits*. New Jersey: Prentice Hall, 1 ed., 1999.

[228] van Wees, B., van Houten, H., Beenakker, C., Williamson, J., Kouwenhoven, L., van der Marel, D., and Foxon, C., "Quantised conductance of point contacts in a two-dimensional electron gas," *Phys. Rev. Lett.*, vol. 60, pp. 848–850, 1988.

[229] Vion, D., Joyez, P., Esteve, D., and Devoret, M., "Miniature electrical filters for single electron devices," *J. Appl. Phys.*, vol. 77, pp. 2519–2524, 1995.

[230] von Klitzing, K., Dorda, G., and Pepper, M., "New method for high-accuracy determination of the fine-structure constant based on quantized hall resistance," *Phys. Rev. Lett.*, vol. 45, pp. 494–497, 1980.

[231] Walmsley, D. G. and Tomlin, J. L., "Compilation of inelastic electron tunnelling spectra of molecules chemisorbed on metal oxides," *Prog. Surf. Sci.*, vol. 18, p. 247, 1985.

[232] Wang, W., Lee, T., Kretzschmar, I., and Reed, M. A., "Inelastic electron tunnelling spectroscopy of alkanedithiol self-assembled monolayers," *Nano. Lett.*, vol. 4, pp. 643–646, 2004.

[233] Westbrook, P. S. and Javan, A., "Finite-bias resistance peaks in nanoscale superconductor-normal metal ta-w point contacts," *Phys. Rev. B*, vol. 59, pp. 606–611.

[234] Wu, P., Wang, H., Cheng, Q., and Xu, W., "Harmonic frequency mixing at millimeter waveband using high tc josephson junction and its applications," *Physica C*, vol. 282–287, pp. 399–402, 1997.

[235] Xiong, P., Xiao, G., and Laibowitz, R. B., "Subgap and above-gap differential resistance anomalies in superconductor-normal-metal microjunctions," *Phys. Rev. Lett.*, vol. 71, p. 1907.

[236] Yannouleas, C., Bogachek, E., and Landman, U., "Energetics, forces, and quantized conductance in jellium-modeled metallic nanowires," *Phys. Rev. B*, vol. 57, p. 4872.

[237] Yanson, A., Rubio-Bollinger, G., van der Brom, H., Agrait, N., and van Ruitenbeek, J., "Formation and manipulation of a metallic wire of single gold atoms," *Nature*, vol. 395, p. 783.

[238] Yanson, I., "Nonlinear effects in the electric conductivity of point junctions and electron-phonon interaction in metals," *Zh. Eksp. Teor. Fiz.*, vol. 74, pp. 1035–1050, 1966.

[239] Yeyati, A. L., Martin-Rodero, A., and Vidal, F. G., "Self-consistent theory of superconducting mesoscopic weak links," *Phys. Rev. B*, vol. 51, pp. 3743–3753, 1995.

[240] Zahopolis, C., Shiffman, C., and Sridhar, S., "Flux rearrangement, type ii behavior, and persistent currents in rings and disks of $Y_1Ba_2Ca_3O_y$ and $La_{1.85}Sr_{0.15}CuO_4$," *Am. Phys. Soc.*, vol. 33, p. 607, 1988.

[241] Zhitenev, N. B., Meng, H., and Bao, Z., "Conductance of small molecular junctions," *Phys. Rev. Lett.*, vol. 88, p. 226801, 2002.

[242] Zorin, A., "The thermcoax cable as the microwave frequency filter for single electron circuits," *Rev. Sci. Instrum.*, vol. 66, pp. 4296–4300, 1995.

# VITA

Brandon Donehoo was born on July 20, 1982 in Macon, Georgia, where he grew up, went to school, and eventually started college. In 2002, he transferred from Macon State College to Georgia Tech, where he completed his Bachelor's in Science in Physics by 2004. During this time, he also began working in Professor Alexei Marchenkov's lab, who would eventually become his graduate advisor. Brandon chose to remain at Georgia Tech for his graduate work and completed a Master's in Physics in 2005, as well as an additional Master's in Electrical Engineering in 2008; as well, throughout this period he continued working on research in Dr. Marchenkov's lab. Finally, on June 13th of 2008, Brandon defended his doctoral thesis and finished his schooling once and for all.